

CORROSION PROTECTION PROVIDED BY TRIVALENT CHROMIUM PROCESS
CONVERSION COATINGS ON ALUMINUM ALLOYS

By

Liangliang Li

A DISSERTATION

Submitted to
Michigan State University
in partial fulfillment of the requirements
for the degree of

Chemical Engineering – Doctor of Philosophy

2013

ABSTRACT

CORROSION PROTECTION PROVIDED BY TRIVALENT CHROMIUM PROCESS CONVERSION COATINGS ON ALUMINUM ALLOYS

By

Liangliang Li

High strength aluminum alloys are widely used in aviation and aerospace industries because of their desirable strength/weight ratio that results from the alloy addition (*e.g.*, Cu, Fe *etc.*). However, this alloy addition causes pitting corrosion of the aluminum surrounding those intermetallic inclusions. One efficient way to inhibit the corrosion is through the protective coating system that contains the topcoat, primer, and conversion coating. The conversion coating is in direct contact with the alloy surface and is expected to provide both good corrosion protection and adhesion. The chromate conversion coating (CCC) has been widely used in aviation/aerospace industry and provides excellent active corrosion protection and adhesion to aluminum alloys. Unfortunately, the Cr(VI) is toxic and chromate is a carcinogen. Therefore, a trivalent chromium process (TCP) coating was developed as a drop-in replacement of CCC.

This dissertation focuses on a fundamental understanding of the formation mechanism, chemical structure, and basic electrochemical properties of the TCP coating on three high strength aluminum alloys: AA2024-T3, AA6061-T6, and AA7075-T6. The formation of the TCP coating is driven by an increase in the interfacial pH. The coating is about 50-100 nm thick and has a biphasic structure consisting of a $ZrO_2/Cr(OH)_3$ top layer and an $AlF_6^{3-}/Al(OH)_3$ interfacial layer. The coating contains hydrated channels and or defects.

The TCP coating provides good corrosion protection to all three aluminum alloys evidenced by *e.g.*, increased R_p , decreased i_{corr} , and higher E_{pit} for the coated alloys than uncoated samples. However, the protection by TCP is increased for AA2024-T3 < AA7075-T6 < AA6061-T6. The protection mechanisms include (i) reducing oxygen reduction kinetics, (ii) partially blocking the mass transfer of dissolved O_2 and ions to the metal, and (iii) insulating the electron transfer through the non-conductive oxide layer. The TCP coating (Cr(III)/Zr-based) provides better corrosion protection compared to other non-Cr alternatives of CCC, *e.g.*, Ti/Zr- and Zn/Zr-based conversion coatings,

Another significant finding of this work is that the TCP coating provides some active corrosion protection by transiently forming Cr(VI) species (*e.g.*, CrO_4^{2-}). The formation involves two steps: (i) O_2 diffuses through the defects to the Cu-rich intermetallic sites where it is reduced to H_2O_2 ; (ii) H_2O_2 oxidizes nearby Cr(III) to Cr(VI).

The insights gained from this fundamental study provide information to improve the corrosion protection provided by TCP. For example, the coating contains defects through which dissolved O_2 and ions can still diffuse to the underlying metal. Therefore, its corrosion protection can be improved by (i) compressing the coating structure and (ii) reducing the alloy sites where defects form. The former is achieved by optimizing the curing temperature and time and the corrosion resistance is increased by ~4x; the latter is through optimization of the deoxidation/desmutting time and solution and the corrosion protection property is improved by ~5x.

ACKNOWLEDGEMENTS

My success in graduate school was made possible by the combined effort of a number of people.

I would like to first thank my advisor, Dr. Greg Swain. He continually and convincingly conveyed a spirit of adventure in regard to research and an excitement as to teaching. He provided me with a research environment that encouraged me to solve scientific problems. His understanding and patience supported me through my research. I have been awarded the Dissertation Completion Fellowship, which would have been impossible without his advising and mentoring. I enjoyed working with him and am sincerely grateful for him and his guidance.

I would also like to thank my committee professors, Dr. Scott Barton, Dr. Lawrence Drzal, and Dr. Andre Lee. They provided professional guidance and generous advice. I also thank several other great professors, Dr. Gerald Frankel and Dr. Rudy Buchheit from The Ohio State University (OSU), Dr. Mark Orazem from University of Florida, Dr. Wei Lai from Michigan State University (MSU) for their generous advice, persistent encouragement, and insightful comments. I would also like to take this opportunity to thank Dr. Robert Ofoli who was my first advisor in graduate school. Without his understanding and support during my transferring group, I could not get the chance to work in my interested research fields.

My sincere thanks also go to my past and current group members for their sharing information and experiences. Dr. Doo Young Kim and Dr. Matthew Phaner encouraged and helped train me to become the scientist I am today. I would also send

thanks to David Woodbury, Brandon Whitman, Dr. Xingyi Yang, Marion France, LeighAnn Tomaswick, Yan Zhu, Chen Qiu and Catharine Munson along with all other Swain Group member.

I would like to thank my friends I made during my graduate school. I cannot gain the success without their support, understanding, and help. I thank Xinting Lin, Huang Wu, Ruiguo Yang, Yan Li, Pitichon Klomjit (OSU), Zhicao Feng (OSU), Chao Cheng, and Heyi Hu for their academic and personal help. I thank Dr. Stanley Flegler, Carol Flegler, Abigail Tirrell, and Per Askeland for their technical support.

Finally, I would like to thank my family, especially my parents for their support and understanding when I had to decline family functions for work reasons. I cannot achieve so much without their encouragement and motivation.

TABLE OF CONTENTS

LIST OF TABLES	x
LIST OF FIGURES.....	xii
CHAPTER 1. INTRODUCTION AND BACKGROUND.....	1
1.1 Aluminum Alloys	1
1.1.1 Designation system, chemical compositions, and mechanical properties..	1
1.1.2 Applications	3
1.2 Corrosion and Corrosion Protection for Aluminum Alloys	4
1.2.1 Corrosion types.....	4
1.2.2 Corrosion protection methods.....	7
1.3 Chromate Conversion Coatings.....	12
1.4 Non-Chromate Conversion Coatings	14
1.5 Metal Surface Pretreatment	17
1.5.1 Cleaning/degreasing.....	17
1.5.2 Etching.....	17
1.5.3 Deoxidizing/desmutting.....	18
1.6 Research Objective and Aims.....	19
CHAPTER 2. EXPERIMENTAL SECTION	22
2.1 Reagents.....	22
2.2 Preparation of TCP-coated aluminum alloys.....	23
2.3 Physical and Chemical Characterization.....	24
2.3.1 Raman Spectroscopy.....	24
2.3.2 X-ray Photoelectron Spectroscopy	24
2.3.3 Auger Depth Profiling.....	25
2.3.4 Scanning Electron Microscopy / Energy-Dispersive X-ray Spectroscopy	25
2.3.5 Transmission Electron Microscopy	25
2.3.6 Atomic Force Microscopy.....	26
2.3.7 Spectroscopic ellipsometry	26
2.3.8 Contact angle measurement.....	27
2.4 Electrochemical Characterization.....	27
2.5 <i>In situ</i> pH Measurement.....	36
2.5.1 Tungsten Microelectrode Preparation.....	36
2.5.2 OCP traces of the tungsten microelectrode in buffer solutions	37
2.5.3 Calibration Curves of OCP vs. pH	38
2.6 Accelerated corrosion (degradation) tests	40
2.6.1 Full immersion test.....	40

2.6.2	Atmospheric corrosion test – humidified air	41
2.6.3	Amospheric corrosion test - moist SO ₂	41
2.6.4	Thin layer test	43
2.7	Galvanic coupling.....	44

CHAPTER 3. FORMATION, STRUCTURE, AND BASIC ELECTROCHEMISTRY OF TRIVALENT CHROMIUM PROCESS (TCP) COATINGS ON AA2024-T3 46

3.1	Introduction	46
3.2	Results.....	48
3.2.1	OCP and pH changes during formation of TCP coatings.....	48
3.2.2	AFM topography of TCP-coated alloys	52
3.2.3	Auger depth profiling of TCP coatings	53
3.2.4	Chemical structure of Cr in TCP coatings	55
3.2.5	SEM/EDAX analysis of TCP-coated aluminum alloys.....	56
3.2.6	Basic electrochemistry of TCP-coated aluminum alloys	57
3.2.7	Mass transfer inhibition	62
3.3	Discussion.....	65
3.3.1	Formation of TCP coatings	65
3.3.2	Structure of TCP coatings.....	66
3.3.3	TCP as charge transfer inhibitor	68
3.3.4	TCP as a poorly conductive barrier to ETR.....	68
3.3.5	TCP as a physical barrier that diminishes O ₂ mass transfer	69
3.4	Conclusions	71

CHAPTER 4. TRANSIENT FORMATION OF CR(VI) IN TRIVALENT CHROMIUM PROCESS COATINGS IN AA2024-T3 PROBED BY RAMAN SPECTROSCOPY 73

4.1	Introduction	73
4.2	Results.....	76
4.2.1	Raman spectra for reference Cr and mixed Cr/Al oxides.....	76
4.2.2	Transient formation of Cr(VI) caused by H ₂ O ₂	80
4.2.3	TCP-coated AA2024 samples before immersion testing.....	84
4.2.4	Transient formation of Cr(VI) during immersion testing.	87
4.2.5	Corrosion protection linked with the transient formation of Cr(VI).....	90
4.3	Discussion.....	94
4.3.1	What is the mechanism by which the Cr(VI) oxide species transiently form in the TCP coating on AA2024?	94
4.3.2	What is the chemical environment around the Cr(VI) oxide species that form? 96	
4.3.3	Does the Cr(VI) oxide species provide any active corrosion protection? .	97
4.4	Conclusion	98

CHAPTER 5. THE FORMATION, STRUCTURE AND BASIC ELECTROCHEMICAL PROPERTIES OF TCP COATINGS ON AA6061-T6 AND AA7075-T6 100

5.1 Introduction 100

5.2 Results 102

5.2.1 Formation of the TCP coating 102

5.2.2 Structure of the TCP coating 103

5.2.3 Stability of the TCP coating 108

5.2.4 Transient formation of Cr(VI) during immersion 110

5.2.5 Corrosion protection provided by the TCP coating. 112

5.3 Discussion 123

5.3.1 Formation mechanism and chemical structure 123

5.3.2 Stability of the TCP coating on AA6061 and AA7075 125

5.3.3 Transient formation of Cr(VI) 126

5.3.4 Corrosion protection 127

5.4 Conclusion 130

CHAPTER 6. STABILITY OF TCP COATINGS DURING ACCELERATED CORROSION TESTS..... 132

6.1 Introduction 132

6.2 Results and Discussion 134

6.2.1 Full immersion 134

6.2.2 Atmospheric corrosion 137

6.2.3 Thin layer mist exposure 140

6.3 Conclusion 142

CHAPTER 7. EFFECTS OF THE DEOXIDATION/DESMUTTING TIME AND SOLUTION CHEMISTRY ON THE CORROSION INHIBITION PROVIDED BY THE TCP COATING ON AA2024 143

7.1 Introduction 143

7.2 Results 146

7.2.1 Deoxidizing/desmutting in acidic fluoride Smut-Go 146

7.2.2 Deoxidizing/desmutting in alkaline halide-free 0.1 M NaOH. 150

7.3 Discussion 160

7.4 Conclusion 163

CHAPTER 8. EFFECTS OF CURING TEMPERATURE AND TIME ON THE CORROSION INHIBITION PROVIDED BY THE TCP COATING ON AA2024-T3.... 165

8.1 Introduction 165

8.2 Results 166

8.2.1 Curing temperature 166

8.2.2 Curing time. 172

8.3	Discussion.....	174
8.3.1	Effect of the curing temperature and time	174
8.3.2	Effect mechanisms	176
8.4	Conclusion	177
CHAPTER 9. CORROSION PROTECTION PROVIDED BY OTHER NON-CHROMIUM CONVERSION COATINGS ON AA2024-T3		179
9.1	Introduction	179
9.2	Results.....	180
9.2.1	Formation of Ti/Zr coatings.....	180
9.2.2	Chemical Structure	181
9.2.3	Basic Electrochemical Properties	187
9.2.4	Galvanic Couples of 5200-coated AA2024-T3 and Ti-6Al-4V fasteners.....	192
9.2.5	Accelerated Corrosion Tests.....	195
9.3	Discussion.....	196
9.3.1	Formation mechanism and chemical structure	196
9.3.2	Corrosion protection property	198
9.4	Conclusion	199
CHAPTER 10. EFFECTS OF GALVANIC COUPLING WITH SS A286 CRES AND TI- 6AL-4V FASTENERS ON CORROSION INHIBITION PROVIDED BY TRIVALENT CHROMIUM PROCESS (TCP) COATINGS ON AA2024-T3 PANELS		201
10.1	Introduction	201
10.2	Results.....	202
10.2.1	Basic electrochemical properties	202
10.2.2	Accelerated corrosion tests.....	207
10.3	Discussion.....	213
10.3.1	Corrosion protection provided by the TCP coating	213
10.3.2	Effects of Fasteners on Corrosion Protection by TCP	214
10.4	Conclusions	214
CHAPTER 11. SUMMERY AND FUTURE WORK		216
11.1	Summery.....	216
11.2	Future Work	221
BIBLIOGRAPHY.....		224

LIST OF TABLES

Table 1.1 Chemical composition of AA2024-T3, AA6061-T6 and AA7075-T6.	3
Table 1.2 Typical mechanical properties of AA2024-T3, AA6061-T6, and AA7075-T6... 3	3
Table 2.1 Major chemical compositions for non-chromate conversion coatings.....	23
Table 3.1 Best-fit parameters of the experimental EIS data for the TCP-coated and uncoated AA2024 samples in naturally aerated 0.5 M Na ₂ SO ₄ . Each datum is an average value of no less than 4 samples. The equivalent circuits used for the simulation were presented in Fig. 2 in Chapter 2.	62
Table 5.1 Electrochemical parameters for the TCP-coated and bare AA2024, 6061 and 7075 alloys during full immersion in air-saturated 0.5 M Na ₂ SO ₄ and 0.5 M Na ₂ SO ₄ + 0.05 M NaCl. $\Delta E = E_{pit} - E_{corr}$. All statistical data are reported at a 90% confidence level. Each datum is an average measurement for 4 samples.	119
Table 5.2 Best-fit parameters from experimental EIS data for TCP-coated AA2024, AA6061 and AA7075 samples in naturally aerated 0.5 M Na ₂ SO ₄ at room temperature. The equivalent circuit used for data analysis was presented in Chapter 2.....	123
Table 6.1 ASTM standard methods for accelerated corrosion testing and the electrochemical methods that are commonly used to assess the corrosion and corrosion inhibition.....	133
Table 6.2 SEM images of TCP-coated and uncoated AA2024-T3, AA6061-T6, and AA7075-T6 during full immersion in air-saturated 0.5 M NaCl for 14 days.....	136
Table 6.3 Optical images of the TCP-coated AA2024-T3 specimens after the thin-layer mist corrosion test at 55 °C for 14 days. The coated alloy panels were galvanically-coupled with either a stainless steel or a Ti alloy fastener. Samples were rinsed in ultrapure water for 30 s and dried in flowing N ₂ before images were recorded.....	141
Table 6.4 Weight loss percentage of the TCP-coated AA2024-T3 specimens after the thin-layer mist (TLM) corrosion test at 55 °C for 14 days and full immersion in naturally-aerated 3.5% NaCl at room temperature for 14 days. The coated alloy panels were galvanically-coupled with either a stainless steel or a Ti alloy fastener. Samples were rinsed in ultrapure water for 30 s and dried in flowing N ₂ before images were recorded.	141
Table 7.1 Summary of the physical properties and electrochemical paramaters measured for TCP-coated AA2024 specimens degreased and deoxidized for 2 min in either Smut-go or NaOH. The physical properties shown, as determined from optical	

profilometry, are the surface roughness (RMS), pit density, pit diameter and pit depth. The electrochemical parameters shown are E_{corr} , E_{pit} , and R_p 154

Table 7.2 Best-fit parameters, C_{CO} , R_{po} , C_{dl} , and R_p , for the EIS data obtained for TCP-coated AA2024 specimens formed after deoxidation for 2 min in either Smut-Go or NaOH. 158

Table 8.1 Best-fit parameters from experimental EIS results of the TCP-coated AA2024 after overnight curing at varied temperatures: room temperature (RT), 55, 100, and 150 °C. The measurements were conducted in naturally aerated 0.5 M Na₂SO₄ at room temperature. 170

Table 9.1 E_{corr} , R_p , and defect parameter for 5200-, TCP- and NCP-coated AA2024. The electrochemical measurements were carried out in air-saturated electrolyte solutions. Data were also recorded for the uncoated alloys (immediately after degreasing and deoxidation/desmutting) as control. The R_p values are calculated by taking the inverse of the slope of the E vs. i curves at E_{corr} (± 30 mV). Each datum is an average value of at least 3 samples. 190

Table 9.2 Best-fit parameters for the experimental EIS data for the 5200-coated and uncoated AA2024 samples in air-saturated 0.5 M Na₂SO₄. The equivalent circuits used for the simulation was presented in Chapter 2. 194

Table 9.3 Basic electrochemical parameters of the 5200-coated AA2024 panel, Ti-6Al-4V fastener, and the galvanic couples. The coupled samples were set up as shown in Chapter 2. Measurements were carried out in air-saturated 0.5 M Na₂SO₄ + 0.1% NaCl and 3.5% NaCl, respectively. Each datum is an average value of at least 3 samples. 194

Table 10.1 Basic electrochemical parameters, E_{corr} , R_p , and i_{gal} for the uncoated and TCP-coated AA2024 panels galvanically coupled with Ti-6Al-4V fasteners, and TCP-coated Al alloy panels coupled with SS A286 CRES fasteners. Measurements were conducted in 0.5 M Na₂SO₄ + 0.1% NaCl that was purged with O₂ for 30 min prior to the measurements. 205

Table 10.2 Optical images of the TCP-coated AA2024 panels before and after the thin-layer mist exposure at 50 °C and full immersion at room temperature in 3.5% NaCl for 14 days. The Al alloy panels were galvanically-coupled with SS A286 CRES and Ti-6Al-4V fasteners during the tests. 209

Table 10.3 Weigh loss data for galvanically-coupled TCP-coated AA2024 panels after full immersion at room temperature and exposure to a thin-layer mist (TLM) test at 40 °C for 14 days. The solution used for both accelerated corrosion tests was naturally aerated 3.5% NaCl. The panels were galvanically coupled with SS A286 CRES and Ti-6Al-4V fasteners. 210

LIST OF FIGURES

Figure 1.1 Optical micrograph of the cross section of the pitting corrosion of AA2024. ..	5
Figure 1.2 Cross-sectional optical micrograph of an intergranular corrosion site on AA2024-T3.	6
Figure 1.3 Optical micrograph of the cross section of SCC.	7
Figure 1.4 Schematic of a typical multi-coating system that is used to protect aluminum alloys from corrosion. The chromate, CrO_4^{2-} , in the conversion coating enables the self-healing of this multi-coating system by transporting to the scratched area and forming a passivating $\text{Cr}(\text{OH})_3$ layer. For interpretation of the references to color in this and all other figures, the reader is referred to the electronic version of this dissertation.	11
Figure 2.1 Schematic of single-compartment glass cell with working, reference, and counter electrodes.	28
Figure 2.2 The equivalent circuit model used to represent the TCP-coated alloy.	30
Figure 2.3 Simulated EIS spectra of phase shift vs. log frequency generated using the equivalent circuit shown in Fig. 2.2B. The parameter values used in the simulation were: $R_e=100 \Omega$, $Q_{po}=1 \times 10^{-6} \text{ s}^n/(\Omega \cdot \text{cm}^2)$, $n_{po}=0.85$, $Q_d=1 \times 10^{-6} \text{ s}^n/(\Omega \cdot \text{cm}^2)$, and $n_d=0.85$. Two values were varied: (A) R_{po} from 1×10^3 to $1 \times 10^4 \Omega$ and (B) R_p (or R_{ct}) from 5×10^5 to $5 \times 10^6 \Omega$	31
Figure 2.4 A model cyclic potentiodynamic polarization curve for an aluminum alloy in a chloride-containing electrolyte. Several characteristic electrochemical parameters are labeled: E_{corr} is the corrosion potential measured at the open circuit condition; E_{pit} is the pitting potential where the passivating oxide layer breaks down during the forward scan and the current density increases sharply; i_{rev} is the anodic current density limit where the scan is reversed in the active direction; E_{ptp} is the pit transition potential at the inflection point in the reversal scan; E_{rep} is the repassivation potential which is defined as the value where the current density falls to zero during the reversal scan...	35
Figure 2.5 SEM image of the conically-shaped tungsten microelectrode etched in 1 M KOH.	37
Figure 2.6 Tungsten microelectrode potential stability when in contact with solutions of different pH: 1.56, 3.68, 5.04, 7.31 and 9.14. Measurements were made at room temperature (21-27 °C).	38

Figure 2.7 The stabilized (<1 min) tungsten microelectrode potential as a function of the pH in the two different solution groups: 0.1 M phosphate buffers and model hexafluorozirconate baths.	40
Figure 2.8 Schematic of the apparatus used for the atmospheric corrosion testing in humidified air.....	41
Figure 2.9 Schematic of the “bird house” used for the moist SO ₂ atmospheric exposure tests.....	42
Figure 2.10 Schematic of the thin layer mist (TLM) testing (A) during one test cycle and (B) between two test cycles. The container was well sealed during one cycle but opened for 15 min to replace the air inside. Several sprays were carried out between cycles to ensure the sample surface was dampened.....	44
Figure 2.11 Schematic of the galvanic couples of the AA2024 panel and the fastener (A) during accelerated corrosion testing and (B) during the electrochemical measurement of the galvanic current.....	45
Figure 3.1 OCP-time profiles recorded during formation of the TCP coatings on AA2024 immediately after degreasing and deoxidizing. The profile of a high oxide AA2024 sample, immersed in boiled water for 1 min after deoxidizing, was also shown here as comparison. Coatings were formed at room temperature (21-27 °C).....	49
Figure 3.2 OCP-time profiles recorded during the formation of the TCP coating on AA2024. The two metal samples were boiled in water for 1 min to produce a hydroxide/oxyhydroxide layer. Two different strengths of the Alodine® 5900 solution were used: full strength (100%) and diluted (50%). Coatings were formed at room temperature (21-27 °C).	50
Figure 3.3 A typical pH trace at the AA2024 surface (empty squares, right y axis) before, during and after formation of the T5900 conversion (TCP) coating. The OCP of the W/WO ₃ microelectrode and the AA2024 sample (solid circles and squares, respectively, left y axis) were also recorded. The formation of the coating occurred during the 18 to 28 min period, as indicated by the grey background.....	52
Figure 3.4 <i>Ex situ</i> tapping mode AFM images of uncoated and TCP-coated AA2024 specimens. Images (10 × 10 μm ²) are presented in the height mode.....	53
Figure 3.5 Scanning Auger electron spectroscopy depth profiling analysis of TCP-coated AA2024. Depth profiling levels are shown for several important elements including Al, Zr, O, Cr, Cu, K and F. Arrows in (A) identify traces for Zr and O. Arrow in (B) identifies the F signal.....	55
Figure 3.6 XPS survey scan in the Cr 2p region for a TCP-coated AA2024 sample.....	56

Figure 3.7 (A) SEM micrograph of a TCP-coated AA2024 specimen, and (B-E) EDAX line profiles for Cu, Cr, Zr, and O, respectively, across the coating as demarked by the line in (A). 58

Figure 3.8 Potentiodynamic polarization curves for TCP-coated and uncoated AA2024 samples. Measurements were conducted in naturally aerated 0.5 M Na₂SO₄. The scan rate was 2 mV/s. 59

Figure 3.9 Corrosion potential (E_{corr}) and polarization resistance (R_p) data for TCP-coated and uncoated AA2024 specimens measured in naturally aerated 0.5 M Na₂SO₄. R_p was determined by the inverse of the slope of $E-i$ curves at E_{corr} . Each datum is an average value of no less than 4 samples. The asterisks indicate statistically significant differences at the 95% confidence level. 60

Figure 3.10 Bode plots for the TCP-coated AA2024 at E_{corr} . Measurements were made in air-saturated 0.5 M Na₂SO₄ + 0.01 M NaCl after the samples were aged in air overnight at room temperature. All samples had a geometric area of 0.2 cm² exposed to the electrolyte solution during measurements. 61

Figure 3.11 Cathodic potentiodynamic sweeps for an (A) uncoated and (B) TCP-coated AA2024 rotating disk electrode at different rotation rates in naturally aerated 0.5 M Na₂SO₄. Scan rate = 2 mV/sec..... 64

Figure 3.12 Plots of i_{lim} for the oxygen reduction reaction as a function of $w^{0.5}$ recorded using uncoated AA2024, Cu and TCP-coated AA2024 rotating disk electrodes in naturally aerated 0.5 M Na₂SO₄. The theoretical Levich plot for of the 4e⁻ reduction of oxygen is also shown for comparison. The variables in the theoretical curve were: n=4, A=0.283 cm², C_{O2}=1×10⁻⁴ M, D_{O2}=1×10⁻⁴ cm²/s, and v=0.01 cm²/s. 64

Figure 3.13 Schematic of the biphasic chemical structure of the TCP coating on AA2024. The thickness values listed are those estimated from measurements made *in vacuo*, and are likely less the true thickness..... 66

Figure 3.14 Simulated Levich plots for TCP-coated AA2024 according to Eq. (3.2) with the assumption that n=4, F=96500 As, C_{bulk}=1 × 10⁻⁴ M, v=0.01 cm²/s, D_{sol}=1 × 10⁻⁵ cm²/s, δ_{TCP}=100 nm. D_{TCP} was varied from 10⁻⁵ to 10⁻⁸ cm²/s..... 71

Figure 4.1 Raman spectra for reference chromium compounds: (a) 0.1M K₂CrO₄ solution, (b) 0.1M K₂Cr₂O₇ solution, (c) Cr₂O₃ pasted with water, (d) Cr(OH)₃ salt, (e) Cr(III)/Cr(VI) mixed oxide, (f) Al(III)/Cr(VI) mixed oxide at pH 4.2 and (g) at pH 7.8. The spectra were obtained using Chromex Raman 2000 using a 532 nm, 20 mW power

laser. The integration time was 3-10 s. The 1048 cm^{-1} peak in (d) is attributed to NO_3^- in $\text{Cr}(\text{NO}_3)_3$ that is used to prepare $\text{Cr}(\text{OH})_3$ 78

Figure 4.2 Raman band frequency of Cr(VI)-O bonds vs. pH for the mixed oxides of Al(III)/Cr(VI) and Cr(III)/Cr(VI). 79

Figure 4.3 Raman spectra for the TCP-coated samples aged (a) in air and (b) in vacuum at room temperature overnight. Spectra were acquired within the pitted areas. 81

Figure 4.4 Raman spectra for the TCP-coated samples immersed in 0.5 M NaCl (a) with and (b) without oxygen for three days. Spectra were acquired on the terrace near the pits..... 81

Figure 4.5 Raman spectra of the TCP-coated samples immersed in 0.5 M Na_2SO_4 added with H_2O_2 by (a) 1%, (b) 0.1% and (c) 0.011% (v/v). Spectra were recorded on the terrace near the pits. (d) A spectrum recorded on the terrace of a coated sample immersed in 0.5 M non- H_2O_2 Na_2SO_4 83

Figure 4.6 (A) SEM micrograph of the surface of a TCP-coated AA2024 sample. Three regions are identified as (a) a large pit (~10 μm diam.), (b) relatively smooth terrace sites with no damage and (c) several elongated precipitates (~1 μm) distributed over the undamaged terrace sites. (B) Raman spectra for (a1) in a pit with a spectrum that is featured with multiple peaks at $434, 552, 680$ and 854 cm^{-1} , (a2) in a pit that exhibits only one peak at 556 cm^{-1} , (b) on the terrace devoid of any pits, (c) on the elongated precipitates. The spectra for (d) a non-chrome 5200-coated sample and (e) a bare sample are also shown as control. 86

Figure 4.7 Raman spectra for the TCP-coated AA2024 immersed in naturally aerated 0.5 M NaCl for 3 days. They were acquired (a) in a pit that contains a Cr-rich intermetallic particle, (b) in a pit devoid of Cu and (c) at a terrace site, and (d) on an elongated precipitate. Relevant reference spectra of (e) a Cr(III)/Cr(VI) mixed oxide and (f) a bare sample are shown as control. 88

Figure 4.8 Plots of the intensity of the Cr(VI) peak as a function of immersion time in air-saturated (a) 0.5 M Na_2SO_4 , (b) 0.5 M NaCl and (c) daily-refreshed 0.5 M NaCl. Spectra were recorded on the terrace near the pits. The trend lines are drawn in solid. 90

Figure 4.9 Profiles of pit density and band areas of Cr(VI)-O vs. immersion time on the TCP-coated AA2024 samples immersed in the air-saturated 0.5 M NaCl for 15 days. . 91

Figure 4.10 (A) Video micrograph of a scratched TCP-coated AA2024 sample after 1-day immersion in 0.5 M NaCl + 0.01% (v/v) H_2O_2 solution. Afterwards, the scratched sample was rinsed in tap water for 10 s and dried in air at room temperature for 30 min

before spectra recording. (B) Raman spectrum of the scratched sample before immersion and spectra after immersion (a) on the coated area, (b) in or near the pitted area in the scratched area and (c) at the terrace site in the scratched area..... 93

Figure 4.11 Schematic illustration of the mechanism for the transient formation of Cr(VI) in the TCP coating during immersion in the air-saturated solution. 99

Figure 5.1 E_{corr} vs. time profiles recorded during the formation of the TCP coating on AA6061 and AA7075 at room temperature (20-25 °C). Full strength (100%) Alodine® 5900 RTU solution was used with the sample under full immersion. 103

Figure 5.2 Auger depth profiles for the TCP coatings on (A) AA6061 and (C) AA7075. The elemental profiles are enlarged in (B) AA6061 and (D) AA7075. Dashed lines are approximate boundaries between the hydrated zirconia overlayer and the interfacial layer at the alloy surface. 105

Figure 5.3 (A) An SEM image, (B) EDX spectrum at the Al matrix site, and (C) elemental line profiles across an Fe and Si-rich intermetallic particle in the TCP-coated AA6061. Profiles were recorded after overnight aging in air. White features in the image are elongated precipitates of the TCP coating..... 107

Figure 5.4 (A) An SEM image, (B) EDX spectrum on the Al matrix site, and (C) elemental line profiles across two intermetallic sites in the TCP-coated AA7075. Profiles were recorded on a film after overnight aging in air. 108

Figure 5.5 (A) Pit density vs. time profiles of the TCP-coated AA6061 and AA7075 recorded before and after the deoxidizing pretreatment step, and during full immersion testing in naturally aerated 0.5 M Na₂SO₄ for 14 days at room temperature. The pit density of the coated AA2024 is also shown here for comparison. All data represent averages and standard errors for 3 samples of each alloy. (B) Backscattered SEM images of AA6061 and AA7075 samples before and after deoxidizing. Bright features indicate the higher-atomic-weight intermetallic particles relative to Al matrix; dark features indicate pits due to attack during deoxidizing (some are pointed by arrows). 109

Figure 5.6 Pit density vs. time profiles recorded during full immersion testing of TCP-coated AA2024, AA6061 and AA7075 in air-saturated 0.5 M NaCl for 14 days at room temperature. Data represent averages and standard errors for 3 samples of each alloy. 110

Figure 5.7 Raman spectra recorded at (a) an Fe-rich intermetallic site and (b) the terrace near but outside the pit on the TCP-coated AA6061, (c) a Cu-rich intermetallic site and (d) the terrace outside the pit on the coated AA7075, all after full immersion in naturally aerated 0.5 M NaCl for 15 days. Spectra for (e) the Cr(III)/Cr(VI) mixed oxide and (f) the Al(III)/Cr(VI) mixed oxide (pH 7.40) are also shown for comparison. 111

Figure 5.8 Cr(VI) peak intensity vs. time for the three TCP-coated alloys that were immersed in the naturally aerated 0.5 M NaCl for about 30 days. Spectra were

recorded on the terrace near the pits. Data represent averages and standard deviations for 3 samples of each alloy..... 112

Figure 5.9 Potentiodynamic scans for bare and TCP-coated AA6061 and AA7075 recorded in two different naturally aerated electrolyte solutions: (A) AA6061 and (B) AA7075 in 0.5 M Na₂SO₄, and (C) AA6061 and (D) AA7075 in 0.5 M Na₂SO₄ + 0.05 M NaCl. Scan rate = 2 mV/s..... 114

Figure 5.10 Corrosion potentials (E_{corr}) for TCP-coated AA2024, AA6061 and AA7075 in naturally aerated (A) 0.5 M Na₂SO₄ and (B) 0.5 M Na₂SO₄ + 0.05 M NaCl. E_{corr} values were also recorded for the bare alloys (degreased and deoxidized) as controls. Each datum is an average value of no less than 4 samples. The asterisks indicate statistically-significant differences at the 95% confidence level..... 116

Figure 5.11 Polarization resistance (R_p) for TCP-coated AA2024, AA6061 and AA7075 in naturally aerated (A) 0.5 M Na₂SO₄ and (B) 0.5 M Na₂SO₄ + 0.05 M NaCl. R_p values were also recorded for the uncoated alloys (degreased and deoxidized) as controls. Each datum is an average value of no less than 4 samples. The asterisks indicate statistically- significant differences at the 95% confidence level. 117

Figure 5.12 Bode plots for the TCP-coated alloys (AA2024, AA6061 and AA7075) at E_{corr} . Measurements were made in naturally aerated 0.5M Na₂SO₄ after the samples were aged in air overnight at room temperature. All samples had a geometric area of 0.2 cm² exposed to the electrolyte solution during measurements. 122

Figure 5.13 Proposed mechanism for transient formation of Cr(VI) on the TCP-coated aluminum alloys during immersion in naturally aerated electrolyte solution. 127

Figure 6.1 Polarization resistance data, R_p , for the TCP-coated AA2024, AA6061, and AA7075 during full immersion in naturally aerated 0.5 M Na₂SO₄ for 14 days. 135

Figure 6.2 R_p for TCP-coated AA2024, AA6061, and AA7075 at different time points during a 14-day atmospheric exposure test in humidified air (RH=100%) at (A) room temperature and (B) 55 °C for 1, 7, and 14 days..... 138

Figure 6.3 Optical images for the (A) TCP-coated and (D) uncoated AA2024-T3 after exposure in moist SO₂ atmosphere (RH=100%) at 40 °C for 14 days. The alloy panels were galvanically coupled with Ti-6Al-4V fasteners. SEM images of the corroded areas (solid black circles) in (A) and (D) are shown in (B) and (E), respectively. Images of the dashed black circles in (B) and (E) are shown in (C) and (F) with a higher magnitude. 139

Figure 7.1 Proposed conversion coating structure on (A) an alloy pretreated to minimize surface roughening and pitting and (B) an alloy pretreated in a manner that increases surface roughening and pitting. 145

Figure 7.2 Profilometry contour plots (left) of AA2024 specimens before and after deoxidation in Smut-Go for different times. SEM micrographs (right) of TCP-coated AA2024 specimens prepared by deoxidation for different times in Smut-Go. Red arrows indicate the pits and damage sites, whereas yellow ones indicate the visible intermetallics. 147

Figure 7.3 Plots of the (A) surface roughness (RMS), (B) pit density, (C) pit depth and (D) equivalent pit diameter for AA2024 specimens treated in Smut-go for different times. Values for the alloy before deoxidation are also shown for comparison (\diamond). Data were obtained from the analysis of profilometry contour plots. Only the pits of $7 \mu\text{m}^2$ or greater in area and $0.5 \mu\text{m}$ or greater in depth were regarded as significant. (E) Plot of the TCP coating thickness, as determined from ellipsometry, on AA2024 specimens treated in Smut-go for different times. Each datum is an average value of 3 spots on each sample. Asterisk indicates significant difference from the values for the untreated controls (0-min treatment). 149

Figure 7.4 (A) Corrosion potential, E_{CORR} and (B) polarization resistance, R_p , for TCP-coated AA2024 specimens after deoxidation times of 0.5, 2, 6, and 12 min. All measurements were made in naturally aerated $0.5 \text{ M Na}_2\text{SO}_4 + 0.01 \text{ M NaCl}$. Each datum is an average of three replicates with the standard error revealed by the bars. 150

Figure 7.5 SEM micrographs of the uncoated AA2024 after (A) degreasing, (B) degreasing and deoxidizing for 2 min in 0.1 M NaOH and (C) degreasing and deoxidizing for 2 min in Smut-Go. The micrographs were taken with the samples tilted by 54° towards the secondary electron detector. These intermetallic compounds contain Al, Cu, Fe, and Mn according to EDAX analysis data that are not shown here. 151

Figure 7.6 SEM micrograph and EDAX elemental line profiling data for the TCP-coated AA2024 formed after degreasing and a deoxidation time of 2 min in 0.1 M NaOH 153

Figure 7.7 Representative electrochemical impedance spectra (EIS) for TCP-coated AA2024 specimens prepared using a 2-min deoxidation in either Smut-Go or NaOH at room temperature. Curves for the TCP-coated sample without deoxidation ($-\Delta-$) are also shown for comparison. Measurements were conducted at E_{CORR} in naturally aerated $0.5 \text{ M Na}_2\text{SO}_4 + 0.01 \text{ M NaCl}$ 158

Figure 7.8 Representative potentiodynamic polarization curves for TCP-coated AA2024 formed after deoxidizing (2 min) in Smut-Go ($-\bullet-$) or NaOH ($-\square-$). Curves for the TCP-coated substrates formed without any deoxidation step ($-\Delta-$) are shown for comparison. Measurements were conducted in naturally aerated $0.5 \text{ M Na}_2\text{SO}_4 + 0.01 \text{ M NaCl}$. Scan rate = 2 mV/s 160

Figure 8.1 Weight loss of a TCP coating during thermogravimetric analysis under an N₂ atmosphere. The sample was obtained by carefully scraping the coatings from three TCP-coated AA2024 specimen surfaces using a sharp blade. 167

Figure 8.2 (A) Polarization resistance, R_p , and (B) corrosion current density, i_{corr} data for the TCP-coated (■) and uncoated (□) AA2024 after overnight curing in air at varied temperatures: room temperature (RT), 55, 100, and 150 °C. The measurements were conducted in naturally aerated 0.5 M Na₂SO₄. Each datum is an average value of 3 samples..... 168

Figure 8.3 Bode plots for the TCP-coated AA2024 at E_{corr} after overnight curing at the various temperature: room temperature (RT, ■), 55 (○), 100 (▲), and 150 °C (□). Three measurements were made in naturally aerated 0.5M Na₂SO₄. 170

Figure 8.4 (A) Defect parameter, (B) coating thickness, and (C) contact angle of static water on the TCP-coated (■) and uncoated (□) AA2024 after overnight curing in air at various temperatures: room temperature (RT), 55 and 100 °C. Each datum is an average of 3 measurements. The open squares in (B) represent the thickness of Al-oxide layers. 171

Figure 8.5 Effects of curing period on the physical and chemical properties of the TCP-coated AA2024 during curing in air at room temperature (RT): (A) thickness of TCP coatings for the coated samples (■) and that of Al oxide films for the uncoated samples (□), and (B) contact angle of static water on the uncoated (□), TCP-coated (■) and non-Cr TCP-coated (▲) samples. Each datum is an average of 3 measurements. 173

Figure 8.6 Effects of curing periods on the electrochemical properties of the TCP-coated (■) AA2024 during curing in air at room temperature (RT): (A) E_{corr} and (B) R_p . Data of the uncoated (□) is shown as control. Each datum is an average of 3 measurements. 174

Figure 9.1 Open circuit potential of the AA2024 sample (dark marks) and the interfacial pH (open marks) at the alloy surface recorded during formation of the 5200 coating (grey background). The pH traces with the white background reflect the value of the coating solution. The coating was formed by immersion at room temperature (21-27 °C). 181

Figure 9.2 An (A) SEM image, (B) EDX spectrum at the Al terrace site (boxed area), and (C) elemental line profiles across two Cu-rich intermetallic compounds in the 5200-coated AA2024. Profiles were recorded after overnight aging in air..... 182

Figure 9.3 An (A) SEM image and (B-F) elemental line profiles for Cu, Zr, O, Zn, and F across the Cu-rich intermetallic compounds in the NCP-coated AA2024. Profiles were recorded after overnight aging in air..... 184

Figure 9.4 Auger depth profiles of several characteristic elements in the (A) 5200 and (B) NCP coatings on AA2024. Dashed lines are approximate boundaries between the coatings and Al matrix at the alloy surface. Data courtesy of Dr. Wayne Jennings from Case Western Reserve University (Swagelok Center for Surface Analysis of Materials).

..... 185

Figure 9.5 TEM images of the cross section of the (A) 5200 and (B) NCP coatings at the Al terrace site, and (C) the 5200 coating at the Cu-rich intermetallic sites on AA2024. The Pt layer is to protect the coating from deformation during TEM specimen preparation using FIB milling. Data courtesy of Mr. Hendrik Colijn from The Ohio State University.

..... 186

Figure 9.6 Slow-scan potentiodynamic polarization curves recorded for 5200-coated AA2024 in air-saturated 0.5 M Na₂SO₄. Data were also recorded for the uncoated (immediately after degreasing and deoxidation/desmutting) sample, a TCP-coated samples and an NCP-coated sample, for comparison. The scan rate was 2 mV/s. The measurement of the NCP-coated sample was performed in 0.5 M Na₂SO₄ + 0.1% NaCl.

..... 188

Figure 9.7 Bode plots of the 5200-coated and uncoated AA2024 in air-saturated 0.5 M Na₂SO₄.

..... 192

Figure 9.8 Optical images of the 5200-coated AA2024 galvanically coupled with Ti-6Al-4V fasteners (A) before any accelerated corrosion testing, and after 14-day (B) full immersion in air-saturated 0.5 M Na₂SO₄ + 0.1% NaCl and (C) exposure in moist SO₂ at 40 °C. The image of (D) an uncoated AA2024 sample galvanically coupled with the Ti alloy fastener is also shown as control.

..... 196

Figure 10.1 Galvanic current density (*i_{gal}*) vs. time profiles for TCP-coated and uncoated AA2024-T3 panels when coupled with fasteners made of SS A286 CRESSS A286 CRES and Ti-6Al-4V. The current density was normalized to the geometric area of the Al alloy panels. Measurements were conducted in naturally aerated 0.5 M Na₂SO₄ + 0.1% NaCl after 30-min purging with O₂.

..... 203

Figure 10.2 (A) Cathodic and (B) anodic polarization curves for the isolated fasteners, the TCP-coated AA2024 panels, and the galvanically-coupled TCP-coated panels. Fasteners include SS A286 CRES and Ti-6Al-4V. The currents were normalized to the geometric area of the fasteners and Al alloy panels. Measurements were conducted in 0.5 M Na₂SO₄ + 0.1% NaCl after a 30-min purge with O₂. The scan rate was 1 mV/s.

..... 206

Figure 10.3 Polarization curves for galvanically-coupled TCP-coated AA2024 panels with Ti-6Al-4V fasteners before and after (A) full immersion in 3.5% NaCl at room temperature and (B) exposure to moist SO₂ at 40 °C, both for 14 days. The

electrochemical measurements were conducted in naturally aerated 0.5 M Na₂SO₄ + 0.1% NaCl for the samples after full immersion testing while naturally aerated 0.5 M Na₂SO₄ was used for the samples after the moist SO₂ test. The scan rate was 1 mV/s. 211

Figure 10.4 (A) Cathodic and (B) anodic polarization curves for the isolated fasteners and TCP-coated AA2024 panels, and the galvanic couples. Fasteners include SS A286 CRES and Ti-6Al-4V. The currents were normalized to the geometric area of the fasteners and Al alloy panels. Measurements were conducted in 0.5 M Na₂SO₄ + 0.1% NaCl that was purged with O₂ for 30 min before measurements. The scan rate was 1 mV/s. 212

CHAPTER 1. INTRODUCTION AND BACKGROUND

1.1 Aluminum Alloys

The aerospace industry used materials with high strength and low weight. Aluminum is one of these materials facing these challenges. Alloying of aluminum with other metallic (e.g., Cu, Fe, Mn, etc.) or semi-metallic (e.g., Si) elements strengthens the alloys' mechanical properties. The high strength aluminum alloys are used in a large number of aerospace applications, ranging from simple components through to primary load bearing structures. Among these alloys, 2024-T3, 6061-T6, and 7075-T6 are the three heat-treated types that are sometimes referred to as the group of "aerospace alloys".

1.1.1 Designation system, chemical compositions, and mechanical properties

The three heat-treated aluminum alloys, AA2024-T3, AA6061-T6, and AA7075-T6, belong to the wrought alloy family that are designated by the 4 digits and thermal treatment T followed with a digit.¹⁻² The first digit indicates the principal alloy elements. The second single digit, if different from 0, indicates a modification of the specific alloy. The third and fourth digits are arbitrary numbers given to identify a specific alloy in the series. The aluminum alloys are strengthened by the thermal treatment T. This process consists of three steps: (i) heat treating, (ii) rapidly quenching to a lower temperature, and (iii) aging.^{1, 3} During the heattreatment, the aluminum is heated to a temperature that is high enough to liquify the metal and allow the introduction of the alloying elements. After holding at the heat treating temperature for a period of time, solute atoms diffuse into the solvent matrix. The alloy is then quenched to a lower temperature (e.g., room

temperature) to keep the alloying elements trapped in solution. During aging, the alloying elements trapped in solution precipitate to form a uniform distribution of very fine particles. The natural aging indicates a hardening process for a few days at room temperature, while the artificial aging is by heating the alloys to an intermediate temperature. If it is cold worked during heat treatment, it is designated as the T3 condition (solution heat treated, cold worked, and then naturally aged), If it is aged by reheating to an intermediate temperature, it is designated as T6 (solution heat treated and artificially aged). As an example of the aforementioned designations, the designation 2024-T3 would indicate that alloy 24 (which defines the specific chemistry) belongs to the original 2xxx series of wrought alloys and is strengthened by solution heating, cold working, and then naturally aging. On reheating to an intermediate temperature, the host metal rejects the alloying element in the form of an extremely fine precipitate only several angstroms in diameter. The fine precipitate creates matrix strains in the lattice that act as barriers to the motion of dislocations and provide resistance to slip, thereby increasing the strength and hardness.⁴

The elemental compositions of AA2024-T3, AA6061-T6 and AA7075-T6 are presented in Table 1.1.⁵ The composition in weight percent is provided by the Aluminum Association.

The typical mechanical properties of these three alloys are shown in Table 1.2.^{1,}
⁶ These values can differ depending on the alloy size and method of manufacture. The data are intended for comparing alloys and tempers.

Table 1.1 Chemical composition of AA2024-T3, AA6061-T6 and AA7075-T6.

wt.%	Cu	Fe	Mg	Mn	Si	Zn	Ti	Cr	Al
2024-T3	3.8-4.9	0.5	1.2-1.8	0.3-0.9	0.5	0.25	0.15	0.1	Bal.
6061-T6	0.15-0.4	0.7	0.8-1.2	0.15	0.4-0.8	0.25	0.15	0.04-0.35	Bal.
7075-T6	1.2-2	0.5	2.1-2.9	0.3	0.4	5.1-6.1	0.2	0.18-0.28	Bal.

Table 1.2 Typical mechanical properties of AA2024-T3, AA6061-T6, and AA7075-T6.

	Tensile strength (MPa)	Yield strength (MPa)	Elongation at break (%) ^a
2024-T3	483	345	18
6061-T6	310	276	12
7075-T6	572	503	11

^a 1.6mm thickness

1.1.2 Applications

AA2024-T3 is a high strength, high performance alloy that is often used for aerospace applications. It has excellent strength over a wide range of temperatures. However, AA2024-T3 is considered non-weldable by arc welding because of its susceptibility to hot cracking and stress corrosion cracking. Therefore, it can be welded only through friction welding.⁶⁻⁷

AA6061-T6 is found widely throughout the welding fabrication industry, is used predominantly in the form of extrusions, and is incorporated in many structural

components. This alloy is naturally solidification crack sensitive, and for this reason, it should be arc welded with adequate amounts of filler material (4xxx and 5xxx filler materials) during the process.⁷⁻⁸

AA7075-T6 is one of the highest strength aluminum alloys. It is often used in high performance applications, such as aircraft, aerospace, and competitive sporting equipment. Like AA2024-T3, AA7075-T3 is considered an unsuitable candidate for arc welding but can be welded by the friction stir welding (FSW) joining technique.⁶⁻⁸

1.2 Corrosion and Corrosion Protection for Aluminum Alloys

1.2.1 Corrosion types

The improved strength of the aluminum alloys leads to compromised elastic strain, electrical and thermal conductivity because of crystalline defects.^{1, 4} Fatigue sensitivity is increased through deformation and propagation of crystal defects that create crack failure. Metal homogeneity is reduced, which increases the quantity of interstitial defects and permeability to atoms or small molecules. Moreover, contact of the aluminum with dissimilar metals or with other alloying elements causes galvanic coupling that leads to electrochemical corrosion. Corrosion can be categorized according to four types:^{1, 4, 6}

Pitting corrosion is normally encountered with all aluminum alloys because of the galvanic coupling between the more noble intermetallic metals and the aluminum.⁹⁻¹⁰ It initiates locally at second-phase particles as shown in Figure 1.1. For example, the Al

phase acts as an anode when in contact with a Cu-rich inclusion that serves as the cathode. Al is oxidized to Al^{3+} that is dissolved in the electrolyte solution, while Cu-rich inclusions are the sites for the reduction of dissolved O_2 . Pitting can be accelerated by presence of chloride ions, which causes severe pitting at potentials above the pitting potential E_{pit} .¹⁰ A guide for examination and evaluation of pitting corrosion can be seen in ASTM G46.¹¹



Figure 1.1 Optical micrograph of the cross section of the pitting corrosion of AA2024.

Intergranular corrosion (IGC) occurs mostly at the grain boundaries.^{4, 9} It usually occurs randomly over the entire surface due to the compositional differences between precipitates on the boundaries, the solute depleted grain margins, and the higher solute grain interiors shown in Figure 1.2.¹² IGC usually reaches a self-limiting depth due to limiting transport of O_2 down the narrow corroded path. When the self-limited depth is reached, IGC spreads laterally. However, if IGC results in splitting or exfoliation, the corrosion will not be self-limiting. Therefore, IGC has a more damaging contribution to corrosion fatigue than pitting corrosion. IGC and its occurrence on aluminum alloys can be assessed according to ASTM G110.¹³

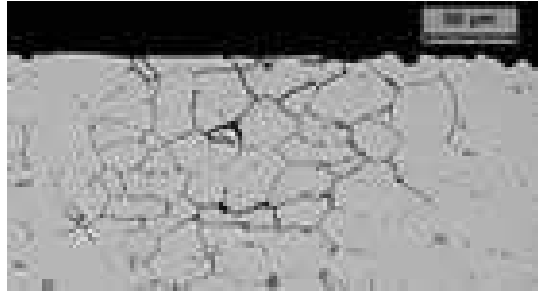


Figure 1.2 Cross-sectional optical micrograph of an intergranular corrosion site on AA2024-T3.

Exfoliation corrosion occurs in aluminum alloys that have a highly directional grain structure.^{4, 9} The corrosion is initiated by the lateral intergranular corrosion and occurs on subsurface grain boundaries parallel to the metal surface. The entrapped corrosion products produce internal stresses that tend to lift off the overlying metal. The spalling off of the metal creates fresh metal surfaces for continued corrosion. In other words, the exfoliation corrosion does not become self limiting. The method for visual assessment of the exfoliation corrosion on aluminum alloys can be found in ASTM G34.¹⁴

Stress corrosion cracking (SCC) in aluminum alloys occurs mostly at intergranular boundaries.^{1, 4, 9} Cross sections of SCC frequently are evidenced by branched cracks as shown in Figure 1.3. It requires the interaction of a metallurgically susceptible material, a corrosive environment, and sustained tensile stress. There is generally a threshold stress above which SCC is initiated. This threshold stress is dependent on the environment, the test specimen and part configuration, and the method of loading (e.g., bending, extension, and constant loading, etc.). The initiation period increases as the applied stress is decreased and can be varied from a few hours

to many years. Once SCC begins, the crack grows linearly at a constant rate independent of the applied stress. This cracking continues until either unstable crack growth occurs leading to rapid failure, or the applied stress falls below the threshold required for crack propagation. The standard test method for SCC is seen in ASTM G47.¹⁵



Figure 1.3 Optical micrograph of the cross section of SCC.

1.2.2 Corrosion protection methods

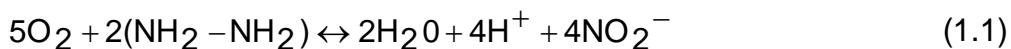
Several methods have been used to protect aluminum alloys from corrosion. The essential idea is to passivate the alloy surface through isolating the metallic surface from contact with the environment (moisture, salts, acids, oxygen, etc.).¹⁶

Corrosion inhibitors. A corrosion inhibitor is a chemical substance which, when added in small concentrations to an environment, minimizes or prevents corrosion.¹⁷

Corrosion inhibitors are used to protect metals from corrosion, including temporary protection during storage or transport as well as localized protection. An effective

inhibitor is compatible with the environment, is economical for application, and produces the desired effect when present at low concentrations.

Inhibitor selection is based on the metal and the environment. Inhibitors can be classified into environmental conditioners and interface inhibitors. The environmental conditioners remove the corrosive species in the medium and decrease corrosivity of the medium by scavenging the aggressive substances. For example, in near neutral and alkaline solutions, hydrazine can be used to decrease the oxygen content that leads to a reduction in the oxygen reduction reaction, as shown in the following equation:¹⁸



Interface inhibitors control corrosion by forming a film at the metal/environment interface. They can be classified into cathodic, anodic and mixed inhibitors, depending on whether they inhibit the anodic, cathodic, or both electrochemical reactions. Anodic inhibitors are usually used in near-neutral solutions where sparingly soluble corrosion products, such as oxides, hydroxides, or salts, are formed. They passivate the alloy surface and inhibit the anodic metal dissolution reaction. Cathodic inhibitors, such as phosphates, silicates, and borates, form protective films that decrease the cathodic reactions rate by blocking the oxygen chemisorption and or limiting the diffusion of oxygen to the metal surface in near-neutral and alkaline solutions. The mixed inhibitors are most organic compounds that adsorb on the metal surface physically or chemically, or form a polymeric film.

Coatings. The application of coatings to metal is the oldest means of corrosion control.¹⁵ It was assumed that protection with paint films was based simply on isolation of the metal from the corrosive environment, specifically water and oxygen.¹⁹⁻²⁰ However, in the late 1940s several other anticorrosive pigments were introduced and these advances led to a more organized understanding of corrosion control by coatings.²¹⁻²² Corrosion control by coatings can be subclassified into three techniques:

(i). The barrier coating protects the metal substrate by acting as an ionic filter. It ensures that the paint film has a high electrical resistance to mitigate current transfer between anodic and cathodic sites.^{19-20, 23} In addition, the barrier can also inhibit the oxygen transport to the metal, thus reducing the rate and impede the cathodic reaction.²⁴⁻²⁵ Whether protecting by an ionic filter or oxygen deprivation, the fundamental requirements of a barrier system are that the coating should be impermeable to ionic moieties and to oxygen, and should maintain adhesion with the metal under wet service conditions.¹⁵ Impermeability to ionic solutions and oxygen is thought to be rate determining for corrosion beneath barrier films, while permeability of the film to water is generally thought to have greater direct consequence on de-adhesion, leading subsequently to corrosion.²⁶⁻²⁷

(ii). The sacrificial coating protects a metal substrate by preventing current discharge from the metal to the environment.²⁸ This cathodic protection effect is accomplished by applying a film pigmented with a more anodic metal (usually zinc, for

protecting aluminum and its alloys).²⁹⁻³⁰ Loadings of the anodic zinc dust pigment must be high enough to ensure a continuous current flow through the film itself and across the interface (*i.e.*, between anodic film and cathodic metal substrate).^{18, 30} All discharge occurs to the zinc pigment, and as long as the conductivity of these sacrificial pigments is sufficient to just sustain current flow from the coating to the environment, the substrate metal remains protected.

(iii). Inhibitory primers control corrosion by modifying the interfacial (primer/metal) environment so that passivation (or inhibition) of the metal substrate may be achieved and maintained.³¹ In this case, the primer's formulation promotes moisture permeation of the coating, such that soluble inhibiting pigments in the coating film can be transported to the metal where they react to form passive (or inhibitory) films. This requires (i) a relatively high volume concentration of a soluble pigment and sufficient water absorption into the film, and (ii) an ionic impermeability with that have favorable passivator (pigments) / depassivator (O_2 , ions) ratios. This design ensures release of soluble inhibitive ions by the pigment that are then carried to the metal surface beneath the primer where passive films may be established, but little permeability of the depassivating ions (chloride, sulfates, *etc.*) into the film from the environment.

In the aerospace industry, one of the most effective strategies for corrosion protection is through the application of multi-coating system.¹⁶ Topcoats are usually applied over primers and render additional service, that is, either enhanced impermeability to moisture, oxygen, and ionic species or improved weathering resistance.

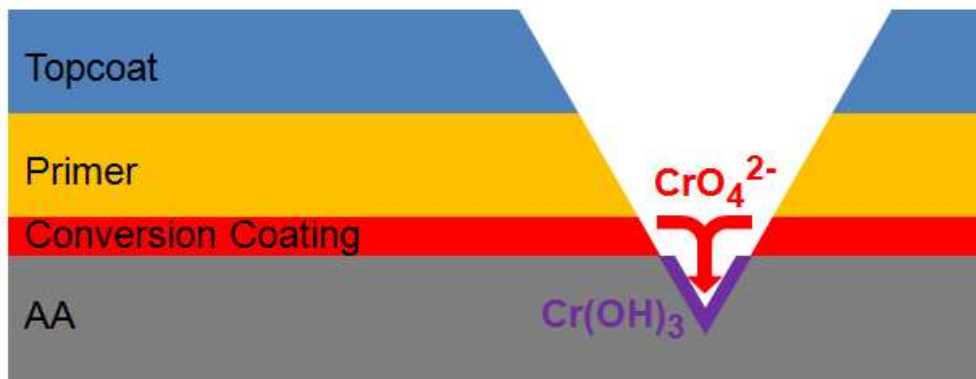


Figure 1.4 Schematic of a typical multi-coating system that is used to protect aluminum alloys from corrosion. The chromate, CrO_4^{2-} , in the conversion coating enables the self-healing of this multi-coating system by transporting to the scratched area and forming a passivating Cr(OH)_3 layer. For interpretation of the references to color in this and all other figures, the reader is referred to the electronic version of this dissertation.

However, inhibitory primers and topcoats neither adhere well to nor protect the underlying aluminum because of the native oxide layer that is a polar and weakly binds with polymer primers.^{1, 32} Therefore, “conversion coatings” are applied to properly condition the metal for interaction with the primers and topcoats, as shown in Figure 1.4. Such coatings provide corrosion inhibition and promotes adhesion of the primer.³¹ Conversion coatings commonly used with aluminum alloys include phosphate-, cobalt-, titanium-, zirconium-, manganate-, silicate-, chromate-, and other rare earth-based systems. They all produce a coating that provides not only a defensive layer against corrosion but also promotes adhesion that is required for a stable performance of the organic primers and the topcoats. In addition, scratching may occur on the aircraft during service. For the multi-coating system containing a conversion coating that can self-heal, as shown in Fig.1.4, the mobile ions (e.g., CrO_4^{2-} , VO_4^{3-})^{34, 54-57} are

transported to the scratched area and get reduced to form a insoluble oxide layer (e.g., Cr(OH)_3 , V_2O_3). This passivates the corroding surface.

1.3 Chromate Conversion Coatings

The most widely used conversion coating in the aerospace industry is the chromate conversion coating (CCC) under the trade names Alodine® from Henkel³³ or Iridite® from MacDermid³⁴. It provides stable and consistent corrosion protection on aluminum alloys for as long as 1,400 h during neutral salt spray testing according to ASTM B117.³⁵⁻³⁶ The formation, structure, and corrosion protective properties were thoroughly studied from late 1990s to early 2000s by an interdisciplinary research team lead by Dr. Gerald Frankel at The Ohio State University.³⁷⁻⁴³ Formation of CCC involves several sequential steps: (i) etching of the native aluminum oxide film layer by fluoride to activate the metal surface, (ii) reduction of Cr(VI) in the coating bath to Cr(III) accelerated by a $\text{Fe(CN)}_6^{-4/-3}$ mediator and (iii) polymerization of Cr(III)-O-Cr(VI) mixed oxide and adsorption of chromate onto the backbone.³⁶ The resulting CCC is a Cr(VI)/Cr(III) mixed oxide with a 3:1 Cr(III):Cr(VI) molar ratio. The coating is generally 0.1 to 1 μm thick depending on the coating time. CCC provides active, self-healing corrosion protection to aluminum alloys by inhibiting transport of dissolved O_2 and ions from the environment through the coating, blocking cathodic intermetallic sites for O_2 chemisorption and anodic Al sites where corrosion initiates and chloride adsorb, and reducing the tunneling rate of electrons through the coating film. Furthermore, the

outstanding corrosion protection provided by CCC is also attributed to its “self healing” capability that was studied by Frankel *et al* using an artificial scratch cell.⁴⁴ In this mechanism, the mobile chromate stored in the coating leaches into the solution, migrates to nearby uncoated, defective areas, adsorbs at the actively corroding sites where it gets reduced to form an insoluble layer of passivating Cr(III) hydroxide. CCC meets military specification, MIL-DTL-5541F.³⁶ It is an approved material to produce Class 1A coating, which indicates maximum corrosion protection whether painted or unpainted. CCC also improves adhesion of paint finish systems on aluminum and its alloys.³⁵

However, hexavalent chromium is carcinogenic to humans and represents key environmental pollutant.⁴⁵⁻⁴⁷ It causes lung cancer by chronic inhalation, exacerbate dermatitis by contact with chromate-dyed textiles or chromate-tanned leather shoes, and irritation or even ulcers in the stomach and intestines through ingestion. Hexavalent chromium is transported into cells via the sulfate transport mechanisms due to the similarity of chromate and sulfate in terms of their structure and charge.⁴⁶ Inside cells, Cr(VI) is reduced to Cr(V) by vitamin C and other reducing agents. The damage is caused by hydroxyl radicals generated during reoxidation of the pentavalent chromium by hydrogen peroxide in cells.

1.4 Non-Chromate Conversion Coatings

Due to the toxic and carcinogenic nature of hexavalent chromium, an increasingly stringent legislation regarding their use and waste disposal has been established. The Occupational Safety and Health Administration (OSHA) published its final standard for Cr(VI) compounds in 2006, regulating a permissive exposure limit (PEL) of $5 \mu\text{g}/\text{m}^3$ for airborne exposure.⁴⁸ The National Institute for Occupational Safety and Health (NIOSH) proposed a recommended exposure limit (REL) of $0.2 \mu\text{g}/\text{m}^3$ for airborne exposure.⁴⁹ Therefore, great efforts have been focused on development of alternative pretreatment conversion coatings that contain no hexavalent chromium but exhibit equally good corrosion protection of aluminum alloys and primer/paint adhesion as CCCs.

To this end, in the mid 1990's, Sanchem Inc. designed the permanganate- and silicate-based conversion coatings for an aluminum alloy (AA1100). In the late 1990's, Henkel Corp. developed a cobalt conversion coating that provided good primer/paint adhesion and electrical contact resistance, but failed salt spray corrosion tests. Since early 2000's, Dr. O'Keefe and his research group from University of Missouri at Rolla have been working on development of a cerium conversion coating (CeCC) of which the electrodeposited version has promised good corrosion protection on multiple aluminum alloys and paint adhesion.⁵⁰⁻⁵⁴ The coating forms a Ce(III)/Ce(VI) mixed oxide and its thickness is in the range of several hundreds of nanometers depending on the preparation process (e.g., degreasing temperature). Salt spray tests showed that CeCC provided some good corrosion protection to aluminum alloys. However, it is crucial to

control the processing parameters for different substrate alloys, which decreases the usage of this coating. Moreover, a vanadate conversion coating (VCC) was also proposed by several research groups.⁵⁵⁻⁵⁸ Similar to CCC, VCC forms through hydrolysis, condensation and polymerization and consists of vanadium in several oxidation states. The coating increases resistance to pitting, suppresses oxygen reduction reactions and provides some active corrosion protection. However, vanadium is known to produce some adverse health effects even though it is not a cancer-causing agent in mammals. This is the main reason why VCC is not widely used.

A promising replacement for CCC is the trivalent chromium process (TCP) coating that has gained wide acceptance recently. It was first developed by Agarwala and colleagues who coated aluminum alloys by immersing the samples in aqueous solutions containing $\text{Cr}_2(\text{SO}_4)_3$ and Na_2SiF_6 or NaF .⁵⁹ Later, The Naval Air Systems Command (NAVIAR) has developed a zirconium-based TCP coating that is different in nature and has improved corrosion protection and adhesion properties.⁶⁰ TCP is currently one of the leading non-chromate conversion coatings on the market. Its baths is similar to fluorozirconate solutions (H_2ZrF_6 or K_2ZrF_6) except that the former contains soluble Cr(III) salts (< 5 wt%) but no Cr(VI), which makes TCP less toxic and environmental-friendly than CCC.⁶¹ Because of TCP's increasing usage as a common pretreatment for aluminum alloys, great efforts have been focused on a fundamental understanding of its formation, structure, and corrosion protection properties on aluminum alloys.

Several other fluorozirconate coatings have also been developed and are sold commercially. For example, there is a Zr/Ti-based coating that consists of fluorozirconate and fluorotitanate in the coating bath. Henkel developed it in early 1980s and is known by Alodine® 5200⁶² or 5700⁶³. Alodine® 5700 is a ready-to-use or diluted version of 5200 (concentrated). The coatings can be applied by immersion, spray, and wipe, *etc.* Previous studies have shown that Alodine® 5200-coated AA2024 suffered corrosion within 48 h during a neutral salt fog test (ASTM B 117).⁶⁴ However, it is interesting to note that the 5200 coating provides respectable performance in corrosion resistance and adhesion when bonded with other chromate-free primers (*e.g.*, Mil-PRF-85582 N, Mil-PRF-53030, *etc.*)⁶⁵ This is attributed to its excellent adhesion properties. Some AA2024 panels coated with 5200 and primers (*i.e.*, Mil-PR-53030) and topcoats (*i.e.*, Mil-C-53039) even exceeded performance of CCCs in terms of corrosion resistance. However, little is known about its chemical structure and if there is any corrosion protection provided by only the 5200 coating.

Another member in the fluorozirconate coating family is the Zr/Zn-based conversion coating. Studies have shown that Zn^{2+} is an effective soluble inhibitor at acidic and neutral pH.⁶⁶ Therefore NAVAIR paired the inhibitor Zn^{2+} with the fluorozirconate barrier coating by adding zinc sulfate to the fluorozirconate coating bath. It is currently under development in NAVAIR. Therefore, characterization of its structure, stability, and corrosion protective property is needed for a fundamental understanding of the Zr/Zn-based conversion coating.

1.5 Metal Surface Pretreatment

Prior to application of various types of conversion coatings on aluminum alloys, it is essential to clean the metal surface by removing contaminants, and to expose bare metal by deoxidizing the native oxide films. Thorough studies have shown that these surface pretreatments are critical for the corrosion protection performance of conversion coatings.

1.5.1 Cleaning/degreasing

Oils and contaminants come from the fabrication lubricants. They can prevent the assembly and adhesion of a uniform conversion coating on the metal surface. A non-uniform coating may lead to localized areas of high cathodic or anodic activity, both of which enhance corrosion. Therefore, aluminum alloys are always cleaned/degreased before coating.⁶⁷ Cleaner/degreasers are classified as alkaline, neutral, and acidic, and are selected for use based on the alloy composition, the presence of a passating oxide layer or smut, and the presence of other complex contaminants.

1.5.2 Etching

Many of the oils and lubricants can be removed by a cleaning/degreasing step. An alkaline solution treatment can be used to remove the remaining grease contamination with possible etching of the alloy surface that is dependent on the alkalinity of the solution and the immersion time.⁶⁷ The alkaline etchants tend to remove the more active aluminum but leave behind the more noble metals, such as copper. Enhanced surface copper concentrations may lead to greater corrosion sensitivity for aluminum. Therefore, selectively reducing copper content is usually a goal

of the pretreatment process to improve corrosion resistance. For example, the metasilicate dissolved in alkaline solution can inhibit surface etching leading to a lower copper concentration at the aluminum alloy surface.¹ Studies have shown that the silicate salt inhibits formation of some conversion coatings, e.g. the TCP coating. In addition, no universal etchant could, for instance, clean both aluminum and copper alloys effectively.⁶⁸ However, these two first steps, cleaning and etching, appear universal for most aluminum alloy cleaning pretreatments.

1.5.3 Deoxidizing/desmutting

Smut is a general term describing residues from either a metal working step, such as a lubricant, or the etching pretreatment, such as the precipitate metal oxide. Deoxidizing/desmutting is the chemical removal of any residues, mainly oxide films for aluminum alloys, in order to expose the underlying metal surface.⁶⁷ The alloy surface is reconstructed to produce a durable interface for proper adhesion of the conversion coating. Deoxidizers may be alkaline utilizing hydroxide and/or ammonia to dissolve the surface oxide layer. However, acidic deoxidizer is more commonly used due to their greater solubilizing power of metals and their oxides. Several acid baths are used including sulfuric acid, nitric acid, and hydrofluoric acid. Sulfuric acid is less aggressive than the other two acids and thus requires a higher operating temperature or longer treatment for proper deoxidation. Nitric acid is less aggressive than those halo acids and is usually used for active metals, e.g., pure aluminum or wrought aluminum-magnesium. Hydrofluoric acid is the strongest deoxidizer/desmutter and is used to

dissolve the metasilicate deposits formed during alkaline etching.¹ These baths can also be used as mixtures, in which the concentration of the halogen determines the surface reactivity and the deoxidizing rate. Excessive deoxidizing can cause pitting corrosion that is an undesired result. Additives are added to inhibit the dissolution process preventing excessive deoxidation. Mixtures of deoxidizers with these additives help to regulate their aggressiveness. For example, the zincate solution is usually added to the deoxidizer and retards excess surface dissolution or corrosion.

1.6 Research Objective and Aims

The overall goal of this research was to develop a fundamental understanding of the mechanisms by which the trivalent chromium process (TCP) conversion coatings form and protect various aluminum alloys (2024-T3, 6061-T6, and 7075-T6) from corrosion. The TCP coating was a Henkel product named Alodine® T5900. Specifically, we investigated the coating structure and chemical composition, the role of the substrate surface structure and chemistry on the coating structure, and the degree of corrosion inhibition (mechanism and kinetics) provided by the coating during different accelerated degradation tests. This Zr/Cr(III)-based TCP coating was also compared with other commercial non-chromated conversion coatings, *e.g.*, the Ti/Zr-based Alodine® 5200, the Zn/Zr-based non-chromate pretreatment (NCP) coating. The importance of the work is that it provides scientists and engineers with information about the conditions under which the TCP coating studied in this research provides corrosion protection as well as information about the corrosion inhibition mechanism and kinetics. This scientific insight will be useful for development of improved corrosion mitigation

strategies. A number of important issues related to these non-chromate conversion coatings were researched:

Aim 1: To investigate the formation mechanism, chemical composition and structure of the several non-chromated conversion coatings on aluminum alloys. A home-made tungsten microelectrode was used to record the pH increase in the interfacial region during coating formation. Scanning electron microscopy (SEM), energy-dispersive x-ray spectroscopy (EDAX) and several other analytical techniques were used to investigate the physical and chemical structure of the coating.

Aim 2: To assess the native corrosion inhibition provided by these conversion coatings on three different aluminum alloys (2024-T3, 6061-T6, and 7075-T6) and to investigate the mechanisms by which the coatings inhibit the corrosion. Various electrochemical methods were used to assess the corrosion inhibition including the corrosion potential (E_{corr}), polarization resistance (R_p), Tafel slopes, corrosion current (i_{corr}) and pitting potential (E_{pit}) in different electrolyte solutions. The coating structure was characterized by SEM/EDAX, scanning auger electron spectroscopy and Raman spectroscopy..

Aim 3: To determine if any transient formation of Cr(VI) species occurs in trivalent chromium process (TCP) coatings and, if so, by what mechanism does this occur. Raman spectroscopy was used to probe the coatings before and after different environmental corrosion tests for the Cr(III)-O vibration mode near 540 cm^{-1} and the Cr(VI)-O mode near 865 cm^{-1} .

Aim 4: To assess the chemical stability of the conversion coatings and the corrosion inhibition they provide (mechanisms and kinetics) during different accelerated corrosion tests. Coated specimens were exposed to fully immersed in high concentration salt solutions, to humidified SO₂ atmosphere, and a thin layer mist of concentrated salt solutions at elevated temperature.

Aim 5: To understand how substrate surface pretreatment and post treatment of the coated specimens affects the corrosion inhibition provided by the conversion coating. This work included investigating the effects of the deoxidation/desmutting chemistry and treatment time, and post-formation heat treatment and aging on the conversion coating structure and performance.

Aim 6: To investigate the conversion inhibition provided by the coatings alloy specimens galvanically-coupled with a metal fastener (Ti-6Al-4V or stainless steel CRES A296) during the different accelerated corrosion tests. Various electrochemical methods were used to determine parameters such as E_{corr} , R_p , Tafel slopes, i_{corr} , and R_{pit} in different electrolyte solutions. The coating structure was characterized by SEM/EDAX, scanning auger electron spectroscopy and Raman spectroscopy. Optical microscopy was used to determine the extent of corrosion (pitting and surface damage). Gravimetric analysis was performed to quantify the mass loss.

CHAPTER 2. EXPERIMENTAL SECTION

2.1 Reagents

All chemicals used were analytical grade quality or better. Sodium sulfate (Na_2SO_4), sodium chloride (NaCl) and hydrogen peroxide (H_2O_2) were purchased from CCI Chemical (Vernon, CA); potassium chromate (K_2CrO_4) was purchased from JT Baker Reagent (Center Valley, PA); potassium dichromate ($\text{K}_2\text{Cr}_2\text{O}_7$), chromium oxide (Cr_2O_3), aluminum nitrate ($\text{Al}(\text{NO}_3)_3$) and chromium nitrate ($\text{Cr}(\text{NO}_3)_3$) were purchased from Sigma-Aldrich (St. Louis, MO); and sodium hydroxide (NaOH) was purchased from Spectrum Chemical (New Brunswick, NJ). The Turco® 6849 and Turco® Liquid Smut-Go NC solutions were provided by Henkel Corp. (Madison Heights, MI). Both were diluted with ultrapure water to 20% (v/v) before use. The Cr(III)/Zr (TCP) bath, Alodine® 5900 RTU obtained from Henkel Corp. was used as received.⁶¹ The Ti/Zr-based coating solution was Alodine® 5200 from Henkel Corp. and was used after diluted by 20% v/v.⁶² The Zn/Zr-based coating (NCP) was applied by NAVAIR and the Si/Zr coating (Boegel)⁶⁹ was obtained from Boeing. Table 2.1 lists the primary chemical composition of each coating solution. All solutions were prepared using ultrapure water (Barnstead) with a resistivity of $\sim 17 \text{ M}\Omega\cdot\text{cm}$.

Table 2.1 Major chemical compositions for non-chromate conversion coatings.

Coating solutions	Product Name	Compositions	Description
Cr(III)/Zr (TCP)	Henkel Alodine® T 5900	K ₂ ZrF ₆ , Cr ₂ (SO ₄) ₃ , H ₂ SO ₄ , HBF ₄	Ready to use (RTU)
Ti/Zr	Henkel Alodine® 5200	K ₂ ZrF ₆ , H ₂ TiF ₆	Diluted by 20% v/v
Zn/Zr	NAVIAR NCP	K ₂ ZrF ₆ , ZnSO ₄	Coated by NAVAIR
Si/Zr	Boegel	-	Coated by Boeing

2.2 Preparation of TCP-coated aluminum alloys

The metal samples were obtained as a 2 mm-thick sheets. They were cut into 1 cm² squares and polished to smooth and clean surface. Mechanical grinding by hand was performed wet on 1500 grit alumina paper initially. Samples were then polished to a mirror-like finish on separate felt pads using alumina grit (0.3 μm diam.) slurred with ultrapure water. Each polishing step lasted for 10 min and was followed by a 10-min ultrasonic cleaning in ultrapure water. The polished samples were then degreased in 20% (v/v) Turco® 6849 at 55 °C for 10 min, followed by rinsing with tap water for 2 min. The degreased samples were then deoxidized in 20% (v/v) Turco® Liquid Smut-Go NC for 2 min at room temperature (21-27 °C). This was followed by rinsing with tap water for another 2 min. Finally, the cleaned and deoxidized samples were immersed in full strength Alodine® T 5900 RTU for 10 min at room temperature. The TCP-coated samples were then rinsed with tap water for 2 min and air dried at room temperature overnight in a covered dish.⁷⁰ For the 5200 coating, deoxidized samples were

immersed in Alodine® 5200 (20% v/v) for 2 min and then rinsed in ultrapure water for 30 s.⁷¹ This was followed by curing overnight at room temperature in a covered petri dish.

2.3 Physical and Chemical Characterization

2.3.1 Raman Spectroscopy

A Chromex Raman 2000 spectrograph (Bruker) equipped with a Nd:YAG laser (500 mW) was used to record the transiently formed Cr(VI)-O species in the trivalent chromium process (TCP) coating. This was accomplished by monitoring the Cr(III)-O vibrational mode near 540 cm^{-1} and the Cr(VI)-O mode near 860 cm^{-1} . The laser source with an output at 532 nm along with a 1200 line/mm grating were used to obtain all spectra. The spectrograph also consisted of a charge-coupled device (CCD) detector cooled to $-38\text{ }^{\circ}\text{C}$. In addition to a holographic band rejection filter, a notch filter was positioned at the entrance slit of the spectrograph for improved source light rejection. An Olympus 40x/0.80 W objective lens provided a laser spot size of 3-5 μm with a laser power of 17 mW at the sample ($\sim 80\text{ kW/cm}^2$). The Logitech QuickCam was used for recording images of the sample surface. Wavenumber calibration was accomplished using a naphthalene solid standard.

2.3.2 X-ray Photoelectron Spectroscopy

X-ray photoelectron spectra (XPS) were recorded using a Perkin-Elmer PHI 5400 ESCA system with a magnesium $\text{K}\alpha$ X-ray source (1254 eV). A take-off angle of 45° was used for all measurements at a base pressure less than 5×10^{-9} Torr. The

spectrometer was calibrated using the C1s line of graphite at 284.6 eV. The XPS can be used to quantify Cr(III) and Cr(VI) species. However, it should be noted that the Cr(VI) deeper in the coating than the escape depth of 2-10 nm would not be detected.

2.3.3 Auger Depth Profiling

The scanning auger electron measurements were made at the Swagelok Center for Surface Analysis of Materials (Case Western Reserve University) using a Perkin-Elmer PHI-680 scanning Auger microprobe. Inert gas sputtering (PHE-06-350) was used to remove surface contaminants and coating materials from a small area for depth profiling. The ion gun was operated with argon gas at ca. 1 keV.

2.3.4 Scanning Electron Microscopy / Energy-Dispersive X-ray Spectroscopy

Scanning electron micrographs (SEM) were obtained using a field-emission scanning electron microscope (JSM-7500F, JEOL, Ltd., Tokyo, Japan). Energy dispersive X-ray spectroscopy (EDS) was used for the elemental line-scan analysis. Data were analyzed using INCA software.

2.3.5 Transmission Electron Microscopy

An FEI Nova Dual Beam SEM/FIB instrument was used to prepare cross-sectional samples from coated specimens. FIB milling was conducted with a 30 keV Ga ion beam and a 5 keV electron beam. A layer of Pt with a thickness of $\sim 1.5 \mu\text{m}$ was sputter deposited on the area of interest to protect the coating from milling. Electron transparent foils with dimensions of $15 \mu\text{m} \times 5 \mu\text{m}$ were produced by FIB and finally thinned to a thickness of $\sim 100 \text{ nm}$. The extraction of foils was performed using a micromanipulator with a Pyrex needle ($\sim 1 \mu\text{m}$ in diameter) under an optical microscope.

Then the thin foils were placed on a 200-mesh Ni grid with a carbon support film for TEM examination.

An FEI Tecnai F20 microscope was used to characterize the cross-sectional foils at high magnification. EDX line profiles were acquired at 200 kV. FEI/Emispec TIA software was used to analyze the data.

2.3.6 Atomic Force Microscopy

Atomic force microscopy (AFM) was performed in air using a Nano Scope IIIa scanning probe microscope (Veeco Instruments Inc., CA). In the contact mode, pyramidal-shaped Si₃N₄ tips, mounted on gold cantilevers (100 μm legs, 0.38 N/m spring constant), were used for obtaining the topographical images. In the tapping mode, RTESP tips (125 μm leg, 40 N/m spring constant, 300 kHz resonant frequency, 8 nm tip radius) were used.

2.3.7 Spectroscopic ellipsometry

The thicknesses of coatings and the Al oxide layer were determined using *ex situ* ellipsometry.⁷²⁻⁷³ The ellipsometer measured a change in the light polarization as the probing beam reflects or transmits at the sample surface in terms of a phase difference Δ and an amplitude ratio Ψ . The data were then fit to a model to calculate the optical properties and thickness of the thin-film coatings. Our ellipsometric data were acquired on a VASE (J.A. Woollam Co., NE) instrument from 300 to 2500 nm. The experimental data were fit to the Cauchy's equation shown below:⁷²⁻⁷⁴

$$n = A + \frac{B}{\lambda^2} + \frac{C}{\lambda^4} \quad (2.1)$$

where n is the refractive index, λ is wavelength of incident light, and A , B , and C are the Cauchy fit parameters.

2.3.8 Contact angle measurement

The wettability of the coated alloy surface was assessed by measuring the static contact angle of ultrapure water on the specimen.⁷⁵ One droplet (ca. 0.05 mL) of ultrapure water was dropped on the alloy surface and its contact angle was measured using a video system (FTA200, First Ten Angstroms, Inc., VA).

2.4 Electrochemical Characterization

All electrochemical measurements were conducted in a single-compartment glass cell using a CH Instruments potentiostat (Model CHI 650A, Austin, TX) shown in Figure 2.1. The coated sample was mounted at the bottom of the cell with an o-ring defining the exposed geometric area (0.2 cm^2). The counter electrode was a Pt wire sealed in glass that was placed in a separate glass tube with an attached porous glass frit. The reference was an Ag/AgCl electrode (4 M KCl, $E^0 = 0.197 \text{ V}$ vs. NHE) that was housed in a Luggin capillary with a cracked glass tip. All measurements were made in air-saturated Na_2SO_4 or NaCl electrolyte solutions at room temperature (21-27 °C).

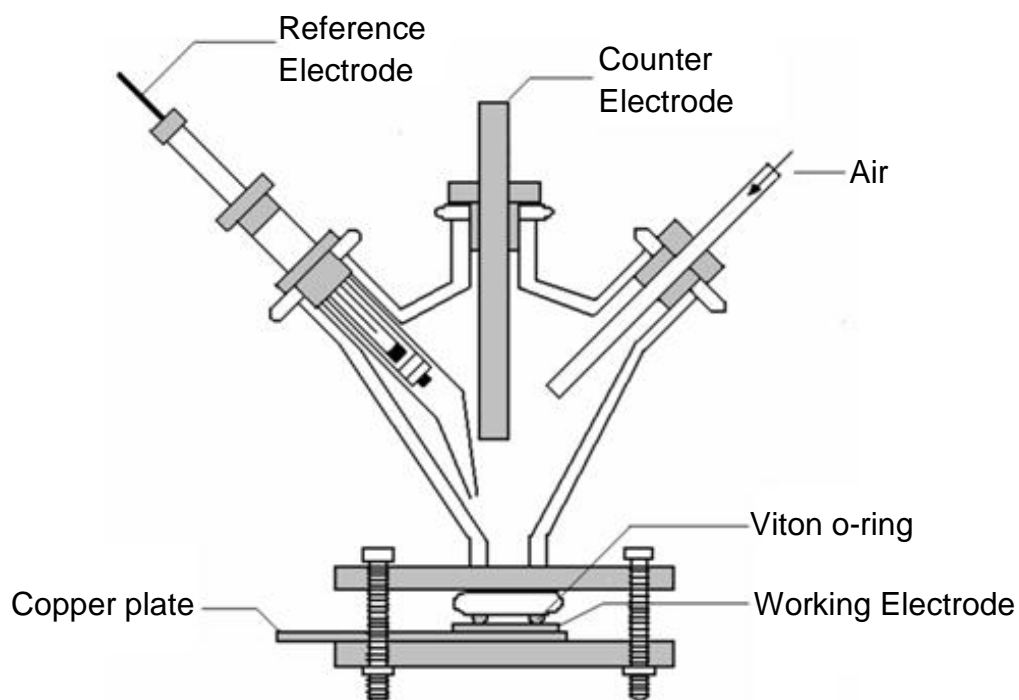


Figure 2.1 Schematic of single-compartment glass cell with working, reference, and counter electrodes.

The electrochemical testing proceeded as follows: (i) measurement of the open circuit (OCP) or corrosion potential (E_{corr}) for 30 min; (ii) performing electrochemical impedance spectroscopy (EIS) analysis from 10^6 to 10^{-2} Hz at E_{corr} ; (iii) recording linear polarization curves ± 20 mV vs. E_{corr} to determine the polarization resistance, R_p and (iv) recording a potentiodynamic cathodic scan from E_{corr} to a cathodic limit of -1.1 V vs Ag/AgCl, allowing E_{corr} to be re-established, and then recording an anodic scan from E_{corr} to 0.6 V vs. Ag/AgCl. The potentiodynamic scans were recorded at 2 mV/s. The EIS measurements were made using a 10 mV rms AC sine wave at E_{corr} .

Figure 2.2 shows the equivalent circuits and models used to evaluate and interpret the impedance data.⁷⁶ We modeled the uncoated alloy surface using the circuit in Fig. 2.2A, while the TCP coating acts as a thin-film barrier layer that contains some pores or hydrated channels through which the electrolyte solution can penetrate and reach a small portion of the metal surface as shown in Fig. 2.2B. In these equivalent circuits, R_{el} is the resistance of the bulk electrolyte, R_{po} and R_p (also called R_{ct}) represent the resistance of the electrolyte in the pores and the polarization resistance of the metal to corrosion, respectively. CPE_{co} is a constant phase element that represents the potential-dependent coating capacitance, and CPE_{dl} represents the potential-dependent electrolyte-metal interfacial capacitance in the coating defects and pores. The CPE components are expressed by mathematical parameters, Q and n , that are used to calculate the effective coating capacitance by $C_{po} = Q^{1/n} R^{1/n-1}$.⁷⁶⁻⁷⁷ For statistical analysis, all measurements on a sample type were replicated at least 3 times.

Figure 2.3 shows the simulated phase shift vs. log frequency plots generated using the equivalent circuit shown in Fig. 2.2B. Most of the parameters were held constant in the simulations (R_e , Q_{po} , n_{po} , Q_{dl} , and n_{dl}) except for two: R_{po} and R_p . As seen, the phase angle of the higher-frequency peak increases with increasing R_{po} . This indicates that the higher-frequency time constant is associated with the hydrated channels and defects of the coating. Similarly, the lower-frequency peak becomes wider

with a maximum that shifts to lower frequency with increasing R_p . This indicates that the lower-frequency time constant is associated with the underlying metal corrosion reaction.

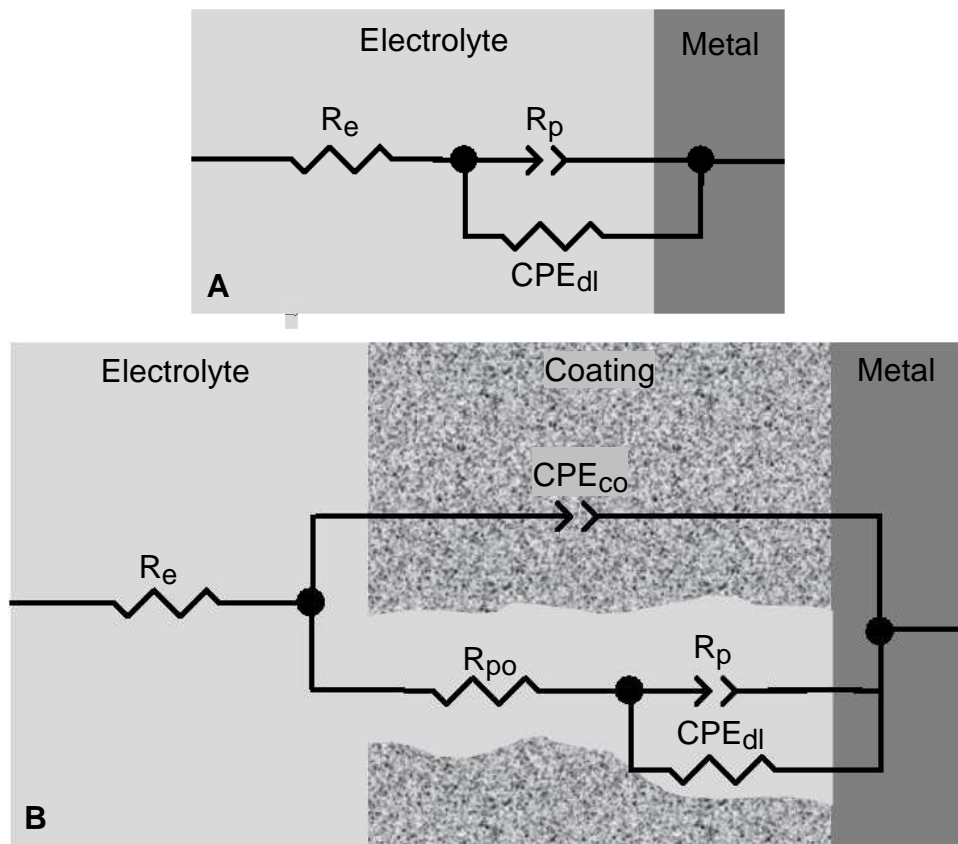


Figure 2.2 The equivalent circuit model used to represent the TCP-coated alloy.

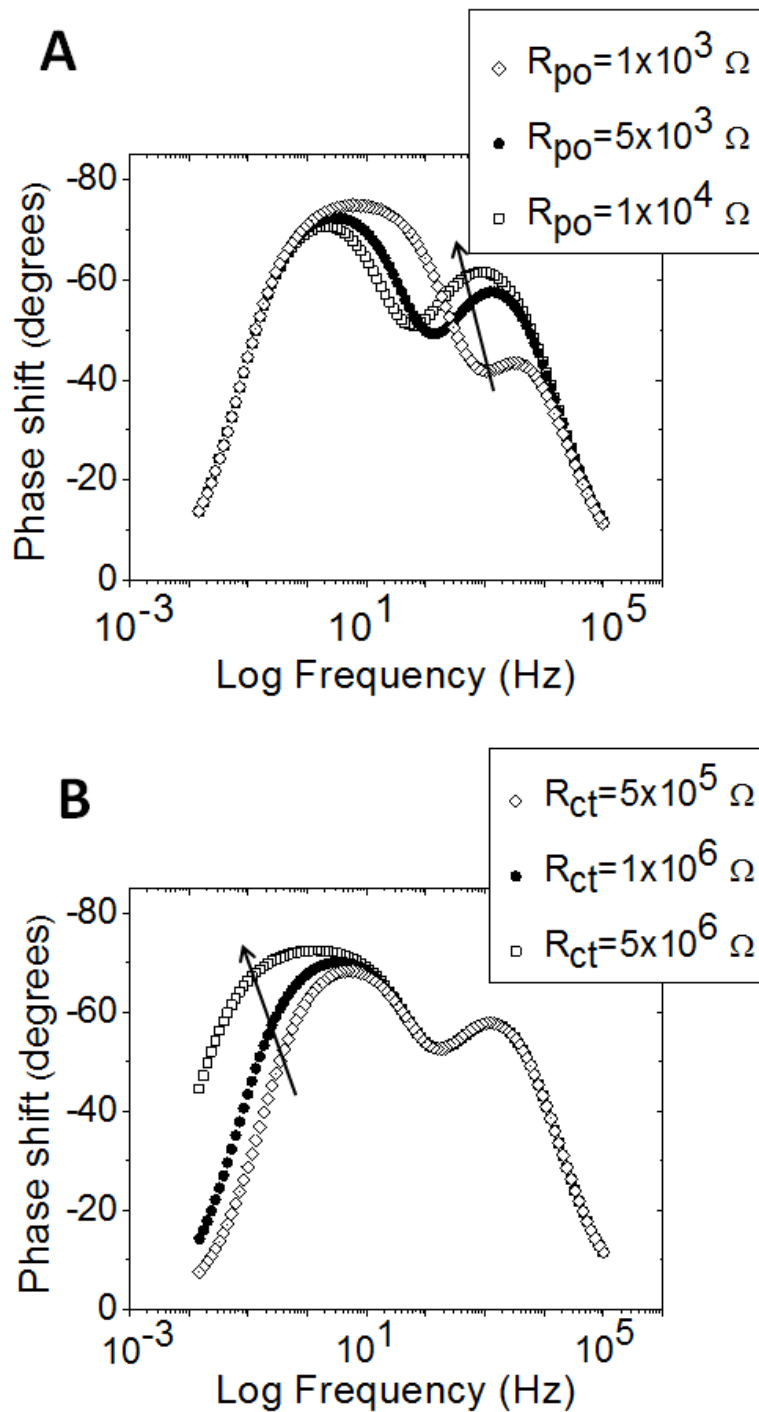


Figure 2.3 Simulated EIS spectra of phase shift vs. log frequency generated using the equivalent circuit shown in Fig. 2.2B. The parameter values used in the simulation were: $R_e=100 \Omega$, $Q_{po}=1 \times 10^{-6} \text{ s}^n/(\Omega \cdot \text{cm}^2)$, $n_{po}=0.85$, $Q_{dl}=1 \times 10^{-6} \text{ s}^n/(\Omega \cdot \text{cm}^2)$, and $n_{dl}=0.85$. Two values were varied: (A) R_{po} from 1×10^3 to $1 \times 10^4 \Omega$ and (B) R_p (or R_{ct}) from 5×10^5 to $5 \times 10^6 \Omega$.

The polarization resistance (R_p) at E_{corr} was determined by linear polarization curves according to the following equation:

$$R_p = \frac{\Delta E}{\Delta i} \quad \Delta E \rightarrow 0 \quad (2.2)$$

where ΔE is the variation about ± 20 mV around E_{corr} and Δi is the resulting current. R_p values determined by linear polarization curves were comparable to values determined from the low frequency EIS data.

The corrosion current density (i_{corr}) is a measurement of the corrosion rate at E_{corr} based on the assumption of steady corrosion. It can be used to calculate an apparent uniform corrosion rate (e.g., weight loss per year) by Faraday's Law:

$$\text{Corrosion rate} = \frac{M}{nF\rho} i_{corr} \quad (2.3)$$

where M is the molecular weight of the corroding metal ($M_{Al}=27.0$ g/mol), n is the number of electron in the corrosion reaction ($n_{Al}=3$), F is the Faraday constant ($F=96500$ C/mol), and ρ is the density of the metal ($\rho_{Al}=2.70$ g/cm³). The corrosion current density (i_{corr}) at E_{corr} was determined by Tafel analysis of the potentiodynamic curve data.⁷⁸ For large cathodic overpotentials ($E_{appl} - E_{corr}$), the Butler-Volmer equation can be simplified to the following,

$$\log i = \log i_{corr} + \frac{\eta}{b_c} \quad (2.4)$$

where $\eta = E_{app} - E_{corr}$ is cathodic overpotential, and b_c is the cathodic Tafel slope. i_{corr} was also be calculated using the R_p data according to the following equation (Stern-Geary equation):

$$i_{corr} = 2.303 \frac{b_a b_c}{b_a + b_c} \left(\frac{1}{R_p} \right) \quad (2.5)$$

where b_a is the anodic Tafel slope.

The TCP coating is an electrical insulator and is electrochemically inert at low anodic overpotentials. These property allow one to estimate the apparent coating porosity, which we refer to as a defect parameter, from dc polarization data using the following equation:⁷⁹

$$P = \frac{R_{p,bare}}{R_{p,TCP}} \times 10^{\frac{-|\Delta E_{corr}|}{b_a}} \quad (2.5)$$

where $R_{p,bare}$ and $R_{p,TCP}$ is the polarization resistance of bare and TCP-coated alloys, respectively; ΔE_{corr} is the difference of E_{corr} for the bare and TCP-coated alloys.; b_a is the anodic Tafel slope for the bare alloy. This method of calculating an apparent porosity parameter has been used by several research groups for plasma vapor

deposited (PVD) ceramic coatings on steels.⁷⁹⁻⁸⁰ We applied this parameter to the conversion-coated samples.

Potentiodynamic polarization curves were the primary tool used to determine the electrochemical parameters that reflect the corrosion status of the specimens. Figure 2.4 shows a model cyclic potentiodynamic polarization curve for an aluminum alloy in a chloride electrolyte solution. E_{corr} is the equilibrium potential of the specimen with no net current flowing. The forward potentiodynamic scan starts at E_{corr} with the applied potential being changed in the positive direction (noble direction) at a slow scan rate until the current density reaches a pre-selected limit i_{rev} . During this positive scan, the critical pitting potential is reached, E_{pit} , where the passivating oxide film breaks down and pitting commences.⁸¹⁻⁸² At E_{pit} , the current density shows a sharp increase above the background passive current density. The i_{rev} is linearly related to the charge passed during pit growth and therefore can be used as one method to assess the extent of pitting severity on the forward scan.⁸³ Once the current density reaches i_{rev} , the scan is reversed in the negative or active direction. The alloy undergoes severe pitting until the pit transition potential, E_{ptp} , is reached, shown as the inflection point in the reversal scan. E_{ptp} is usually indicative of the first stages of pit repassivation.⁸³ The total charge passed from E_{pit} to E_{ptp} is a direct measure of the extent of pitting during the entire cyclic potentiodynamic scan.⁸⁴⁻⁸⁶ The surface fully repassivates as the scan reaches

the repassivation potential, E_{rep} , which can also be considered as the potential above which pits can grow. E_{rep} is defined as the potential at which the current density intercepts with the cathodic scan in this study. More positive E_{pit} values reflect greater inhibition to pitting corrosion. E_{rep} values that are more negative of E_{corr} means that the alloy is susceptible to pitting corrosion. E_{rep} values more positive than E_{corr} means that under open circuit conditions, the alloy is stable against pitting corrosion.

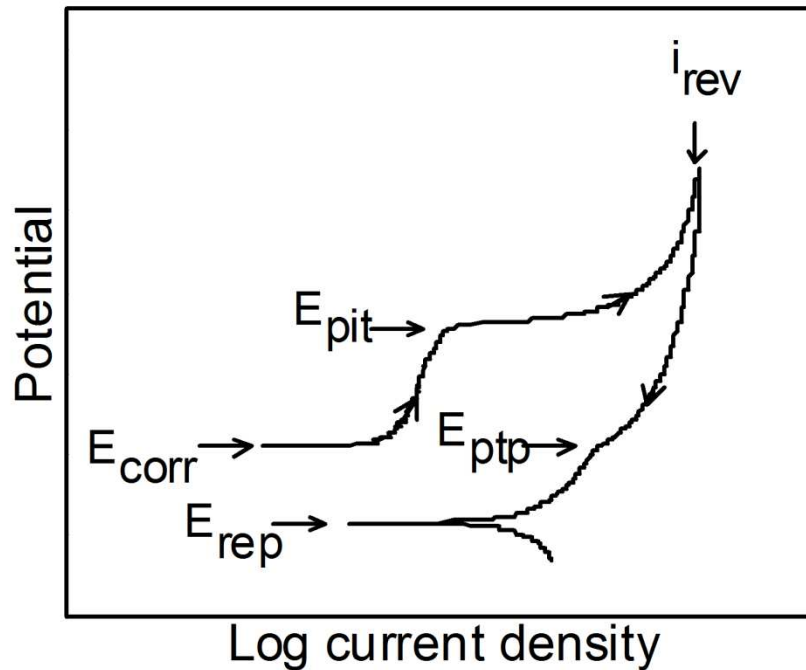


Figure 2.4 A model cyclic potentiodynamic polarization curve for an aluminum alloy in a chloride-containing electrolyte. Several characteristic electrochemical parameters are labeled: E_{corr} is the corrosion potential measured at the open circuit condition; E_{pit} is the pitting potential where the passivating oxide layer breaks down during the forward scan and the current density increases sharply; i_{rev} is the anodic current density limit where the scan is reversed in the active direction; E_{ptp} is the pit transition potential at the inflection point in the reversal scan; E_{rep} is the repassivation potential which is defined as the value where the current density falls to zero during the reversal scan.

2.5 *In situ* pH Measurement

A method of locally measuring the interfacial pH change during formation of the non-chromate conversion coatings (*i.e.*, TCP and Zr/Ti-based coatings) involves the use of a tungsten microelectrode positioned near the alloy surface.⁸⁷ The potential of a tungsten electrode is pH sensitive (Nernstian, ~ -60 mV/pH) due to the natural formation of a surface oxide layer.⁸⁷⁻⁸⁹

2.5.1 Tungsten Microelectrode Preparation

The tungsten wire (0.01" diameter, FHC Inc., Bowdoin, ME) was cut into 2-cm lengths. Electrical connection was made by attaching a longer Cu wire to one end of the tungsten wire with conductive silver epoxy and super glue. The two wires were then insulated with polypropylene from a heated pipette tip, leaving about 0.5-cm of the tungsten wire exposed.⁹⁰ The exposed tungsten was then electrochemically etched in 1 M KOH by applying a 12 V AC relative to a carbon counter electrode. This process formed a conically-shaped tip. The voltage was applied using a variable autotransformer (Staco Energy Products, Dayton, OH). The wire was etched until visible gas evolution ceased (*ca.* 30 s). The sharpened microelectrodes were then ultrasonically cleaned in ultrapure water for 10 min while suspended vertically to avoid tip damage. The resulting microelectrode was conically shaped with a tip about 30 μm in diameter and the cylinder about 80 μm wide. The exposed cone length was about 500 μm . A scanning electron micrograph of a typical microelectrode is shown in Figure 2.5.

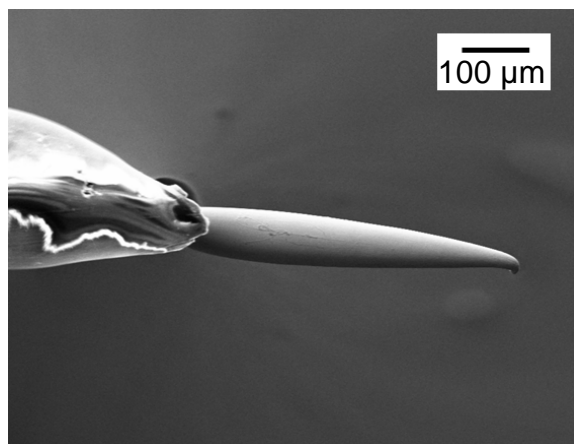


Figure 2.5 SEM image of the conically-shaped tungsten microelectrode etched in 1 M KOH.

2.5.2 OCP traces of the tungsten microelectrode in buffer solutions

The open circuit potential (OCP) of W/WO_3 can be used to measure the local solution pH.⁸⁷ Figure 2.6 shows the tungsten microelectrode potential as a function of time during full immersion in solutions of variable pH. The mock coating solutions were prepared by dissolving 1 g potassium hexafluorozirconate (K_2ZrF_6), 0.28 g chromium nitrate ($Cr(NO_3)_3$) in 50 mL ultrapure water, and using 0.1 M H_2SO_4 and 0.1 M NaOH to adjust the solution pH. The solution pH was verified using a conventional glass pH electrode (FB-5, Fisher Scientific Inc.). These solutions were designed to mimic the chemical composition of the 5900 and 5200 baths. After each measurement, the microelectrode was rinsed in ultrapure water. As can be seen in Fig. 2.6, the microelectrode potential quickly stabilized at each pH. The short response time is noteworthy and is important for measuring the transient pH change that occurs during the conversion coating formation (see below).

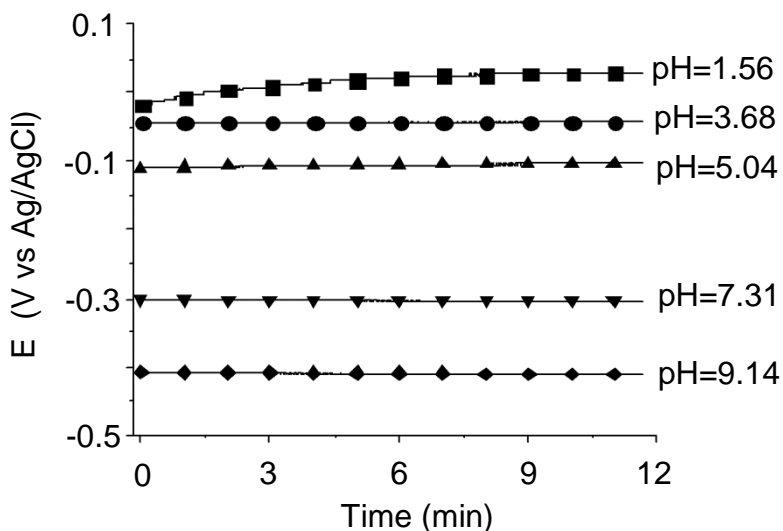


Figure 2.6 Tungsten microelectrode potential stability when in contact with solutions of different pH: 1.56, 3.68, 5.04, 7.31 and 9.14. Measurements were made at room temperature (21-27 °C).

2.5.3 Calibration Curves of OCP vs. pH

Figure 2.7 shows the tungsten microelectrode potential plotted as a function of the solution pH for the hexafluorozirconate model solutions and for 0.1 M phosphate buffers of variable pH that were used as controls. The true pH values were determined using a conventional glass pH electrode that was carefully calibrated and only exposed to the aggressive F^- -containing hexafluorozirconate solutions for brief periods of time. For a pH sensing electrode at equilibrium, a Nernstian response of -59 mV/pH at 25 °C is predicted.^{87, 91-92} However, deviation from this theoretical value occurs for the W/WO_3 electrode.⁹¹⁻⁹² This is because the electrode surface exhibits a mixed potential resulting from a balance between anodic oxidation of tungsten and cathodic hydrogen reduction as shown below:⁸⁷⁻⁸⁸



Our measurements revealed a near-Nernstian response for the tungsten electrode in phosphate buffer solutions with a slope of -64 mV/pH. Phosphate buffers have been widely used in pH-relevant studies as the phosphate anion does not strongly interact the tungsten surface within the measurement periods.⁹³⁻⁹⁴ A near-Nernstian electrode response was also observed in the hexafluorozirconate solutions with a slope of -63 mV/pH. In other words, the aggressive chemicals (e.g., hexafluorozirconate, Cr(III) salts) in the model coating solutions do not appear to interact strongly with the tungsten surface to alter the pH response. Two additional tungsten microelectrodes were also tested (data not shown here). For all three microelectrodes, identical pH-potential responses were found at 61.8 ± 0.6 . These results reveal that the potential of the tungsten microelectrode is affected primarily by the H^+ activity, and not by the other chemical constituents in the 5900 or 5200 baths. The curves in Fig. 2.7 allow us to calculate the interfacial pH near the aluminum alloy surface during the formation of the conversion coating.

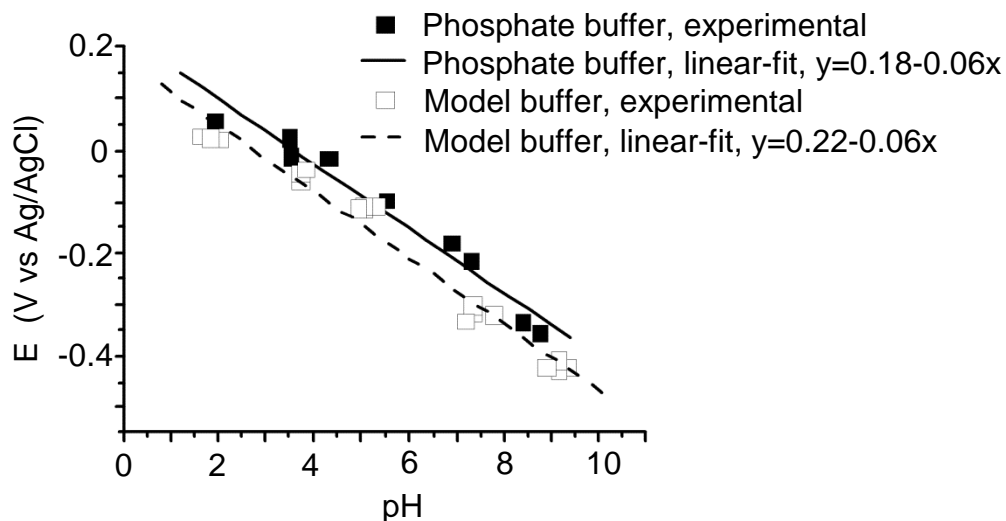


Figure 2.7 The stabilized (<1 min) tungsten microelectrode potential as a function of the pH in the two different solution groups: 0.1 M phosphate buffers and model hexafluorozirconate baths.

2.6 Accelerated corrosion (degradation) tests

2.6.1 Full immersion test

One accelerated corrosion test was a full immersion one. Specimens were fully immersed in 10 mL naturally aerated electrolyte solutions (e.g., Na₂SO₄, NaCl) in glass vials (20 mL) continuously for 1, 7 and 14 days at room temperature.⁹⁵ Each vial contains one sample. The glass vials were sealed during the test with replacement of the air in the container every 24 h. The replenishment was achieved by simply opening the lid and exposing the solution to the open air for 30 min. At the end of the test period, the specimens were removed from the glass vials and then rinsed with flowing ultrapure water before examinations.

2.6.2 Atmospheric corrosion test – humidified air

Specimens were exposed to humid natural air (RH=100%) continuously for 1, 7 and 14 days at 55 °C.⁹⁶ This was achieved by placing the specimens on a platform above a 0.5 M Na₂SO₄ solution in a well sealed container, as shown in Figure 2.8. One test cycle lasted 24 h at which time the air in the container is replenished by open air exposure. After the test, the specimens were rinsed with ultrapure water for 10 s and dried under N₂ prior to any spectroscopic and or electrochemical measurements.

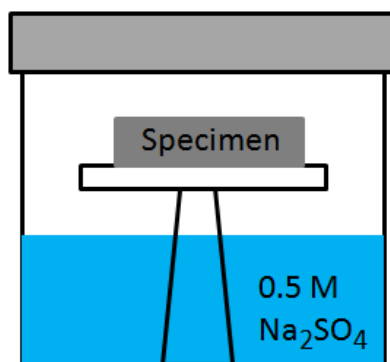


Figure 2.8 Schematic of the apparatus used for the atmospheric corrosion testing in humidified air.

2.6.3 Atmospheric corrosion test - moist SO₂

The moist SO₂ exposure test was used to mimic urban environment conditions. This test was carried out according to ASTM G87.⁹⁷ Figure 2.9 shows a “bird house” that was used as the test chamber temperatured at 40 ± 3 °C in a heated oven. The chamber has a roof pitch of about 14/12 that keeps condensed moisture at the ceiling slide down along the chamber walls without falling on the specimens. The inlet of sulfur dioxide is controlled by a valve and the outlet leads to an alkaline solution ensuring no

leakage of SO₂ into atmosphere. The chamber has a specimen support island that holds 12-30 samples at one time depending on the sample size. The island surface is fabricated with notches that specimens can be positioned in a near vertical orientation (~20° from vertical). Distilled water (~500 mL) is introduced into the base of chamber.

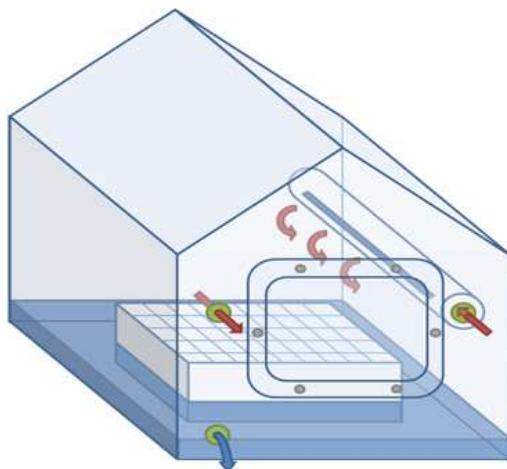


Figure 2.9 Schematic of the “bird house” used for the moist SO₂ atmospheric exposure tests.

One test cycle was 24 h during which period the specimens were continuously exposed to the SO₂/H₂O environment. Water in the chamber and SO₂ in the air of the chamber are replaced before each 24-h cycle begins. The whole test lasts for 14 cycles (*i.e.*, 14 days). At the end of the test period, the specimens were removed and cleaned by rinsing in flowing ultrapure water for 10-30 s. The specimens were then air dried or dries under a stream of N₂ prior to any additional measurements.

2.6.4 Thin layer test

Aircrafts experience humid environments in service. In some cases, these environments can contain high salt content, such as service at sea on an aircraft carrier. Moisture condenses on surfaces with high salt content. The thickness of the electrolyte layer is usually on the order of low millimeter down to micrometers. To assess the protective properties of the non-chromate coatings in these conditions, we developed a thin-layer mist (TLM) test accomplished by spraying a 3.5% NaCl aerosol on the specimen surface, as shown in Figure 2.10. The specimen was positioned horizontally on a platform above ultrapure water in a sealed container. The temperature was maintained at 55 °C that kept the relative humidity (RH) at 100% during the test. One test cycle was 24 h during which period the specimens were continuously exposed. The air in the container and the electrolyte mist were replenished each 24-h cycle by opening the container to the natural air for 15 min and spraying the 3.5% NaCl mist to wet the alloy surface. The whole test lasted for 14 cycles (*i.e.*, 14 days). At the end of the period, the electrolyte layer was rinsing away with flowing ultrapure water for 10-30 s. The specimens were then dried in flowing N₂ before follow-up examinations.

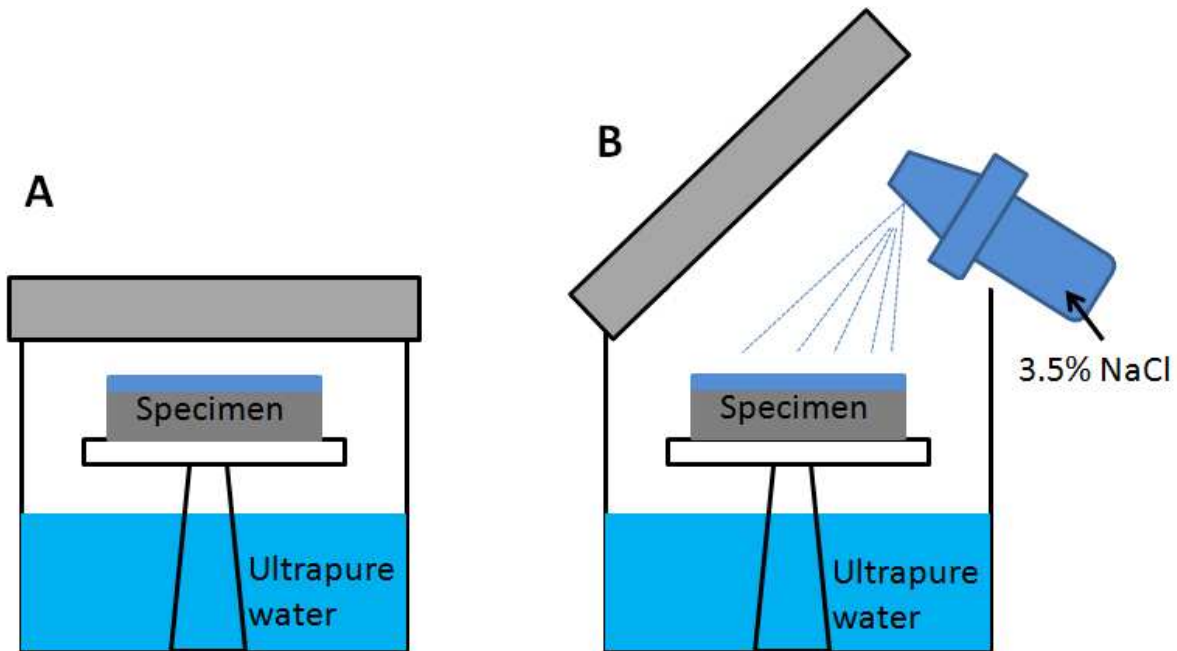


Figure 2.10 Schematic of the thin layer mist (TLM) testing (A) during one test cycle and (B) between two test cycles. The container was well sealed during one cycle but opened for 15 min to replace the air inside. Several sprays were carried out between cycles to ensure the sample surface was dampened.

2.7 Galvanic coupling

Due to the difficulties of welding high strength aluminum alloys, they are joined together by fasteners⁹⁸ that are usually made of stainless steels, titanium alloys, and carbon steels. The stainless steel (SS) and Ti alloy fasteners are usually more noble than aluminum alloy components and act as the cathode in the galvanic couple while the Al alloys are the anode. This galvanic interaction can drive the corrosion of the Al alloys and cause severe failure.

During the accelerated corrosion tests, the SS A286 CRES and TTi-6Al-4V fasteners were galvanically coupled with the Al alloy panels as shown in Figure 2.11. A hole (6 mm diam.) was drilled first through the Al alloy panel at the center. Then the

panel was coated and coupled with the fastener (100 in-oz torque). During the accelerated corrosion testing, the fastener was in direct contact with the alloy panel (Fig. 2.11A). However, during the electrochemical measurement, the fastener was isolated with the alloy panel using nonconductive o-rings, electrical and Teflon tape as shown in Fig. 2.11B. This design is to measure the galvanic current between the fastener and alloy panel.

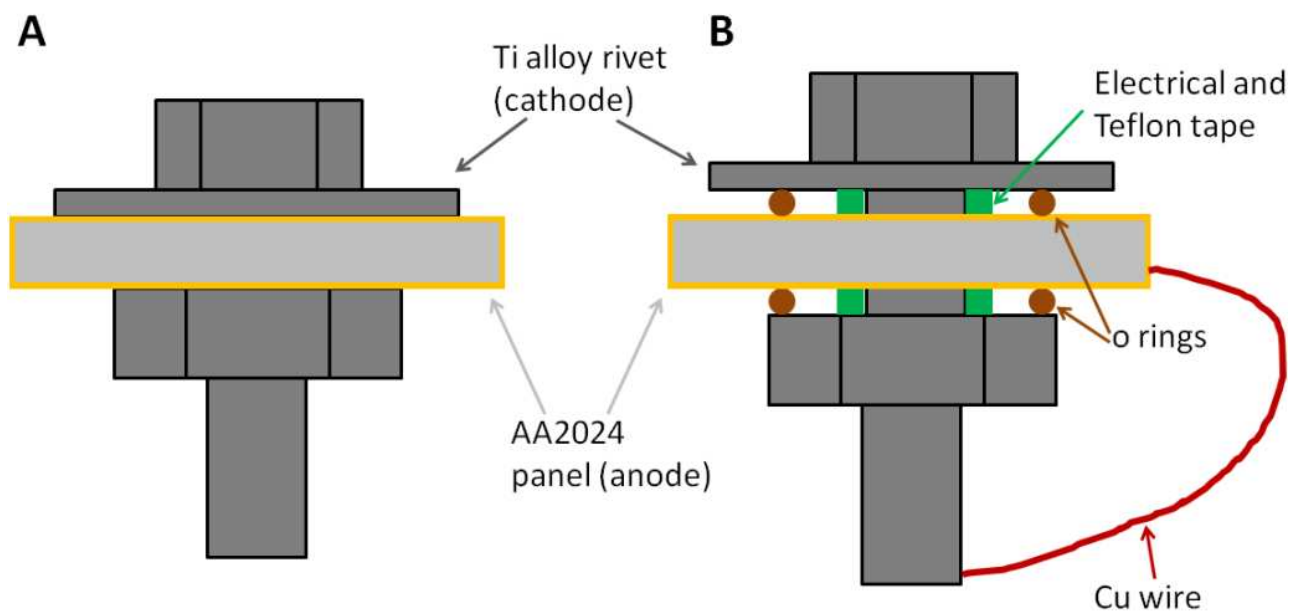


Figure 2.11 Schematic of the galvanic couples of the AA2024 panel and the fastener (A) during accelerated corrosion testing and (B) during the electrochemical measurement of the galvanic current.

CHAPTER 3. FORMATION, STRUCTURE, AND BASIC ELECTROCHEMISTRY OF TRIVALENT CHROMIUM PROCESS (TCP) COATINGS ON AA2024-T3

3.1 Introduction

Chromate conversion coatings (CCCs) have been widely used a protective coating on high strength aluminum alloys for the last decades.⁹⁹ The formation and structure of CCCs on aluminum alloys were extensively studied by McCreery and colleagues.¹⁰⁰⁻¹⁰⁸ Formation of CCC initiates by the reduction of Cr(VI) species in the coating bath to Cr(III),; a process is catalyzed by ferri/ferrocyanide at Al matrix sites.¹⁰¹⁻¹⁰³ Cr(III) binds to Cr(VI) species in the bath to form an insoluble Cr(III)/Cr(VI) mixed oxide that has an approximate molar ratio of Cr(VI) : Cr(III) = 1: 3.^{103, 109} Studies have shown that this binding is reversible and that the Cr(III)/Cr(VI) mixed oxide can leach Cr(VI) into the aqueous solution.^{100, 107-108} At the intermetallic sites, such as Cu-rich particles, the reduction of Cr(VI) at the metal surface is spontaneous and is self-limiting to approximately one Cr(III) monolayer due to the ohmic resistance of the layer.^{103, 109} This monolayer likely interacts with Cr(VI) species in the coating bath to forms a mixed Cr(III)/Cr(VI) oxide. In other words, at the early stage, CCC forms preferentially at the Cu-rich intermetallic sites, which process is self limited due to the inhibition of electron transfer by the Cr(III) monolayer; afterwards, reduction of Cr(VI) on the Al matrix sites are accelerated by ferri/ferrocyanide; eventually, CCC forms a mixed oxide layer of several micrometers on Al matrix and a monolayer of Cr(III) on the Cu-rich intermetallic compounds. These layers are effective at reducing both anodic and cathodic reaction

kinetics on the Al matrix and intermetallic compounds, respectively.¹⁰³ The corrosion mechanism involves (i) blocking active sites, especially for O₂ adsorption, (ii) reducing the electronic transport through the poorly conductive mixed oxide film, and (iii) suppressing diffusion of dissolved O₂ and ions to the metal surface.¹¹⁰ In presence of Cl⁻, adsorbed Cr(VI) lowers the zeta potential and the pH of zero charge of Al oxide films which inhibits chloride adsorption.¹¹¹

Unfortunately, CCCs contain Cr(VI) that is toxic and a potent carcinogen. Current research is directed toward the identification and or development of alternate non-chromate coatings that are less toxic, but equally as effective as CCCs. The new trivalent chromium process (TCP) coating has been developed at NAVAIR as a drop-in alternative for the chromate conversion coating (CCC).¹¹²⁻¹¹³ The TCP coating bath contains no toxic and carcinogenic Cr(VI) species. It has recently gained a wide acceptance as a promising replacement for CCC for providing excellent corrosion protection on high strength aluminum alloys.¹¹³ For example, TCP-coated AA2024-T3 exhibited no evidence of corrosion after 2-week exposure to a neutral salt fog (ASTM B117).⁶⁴⁻⁶⁵ Beach exposure for 30 days also revealed that the TCP coating inhibits corrosion on Al alloys.⁶⁴ While the coating provides corrosion inhibition, little is known about the mechanism of this protection. In this chapter, data are presented that support the corrosion inhibition mechanism by the conversion coating. The mechanism is dependent on the aluminum alloy. In addition, little fundamental insight exists regarding

the formation mechanisms and structure of TCP coatings on aluminum alloys. The results presented and discussed herein also address the formation mechanism, composition and structure of the TCP coating on AA2024-T3.

3.2 Results

3.2.1 OCP and pH changes during formation of TCP coatings

Figure 3.1 shows the open circuit potential (OCP) versus time profiles recorded during the formation of a TCP coating on a degreased and deoxidized AA2024 specimen. The immersion lasted 10 min. Curves for two coatings solutions are presented: (i) the “ready to use (RTU)” 100% full-strength Alodine® T5900 RTU solution and (ii) the RTU solution diluted by 50% (v/v) with ultrapure water. The OCP transients are similar in shape and magnitude for both solutions. The TCP bath is very aggressive toward the alloy surface as evidenced by the cathodic shift in the OCP to *ca.* -0.95 V vs Ag/AgCl within the first 60 s. The fluoride in the solution facilitates the dissolution of the oxide layer on these surfaces. The oxide layer dissolution exposes the bare aluminum (activates the metal) is an essential first step in the formation of the TPC coating.¹¹⁴ The OCP transient then goes through a minimum before a slight positive increase to -0.90 V within the first 100-200 s. Afterwards, the potential stabilizes at this value for the duration of the immersion period.

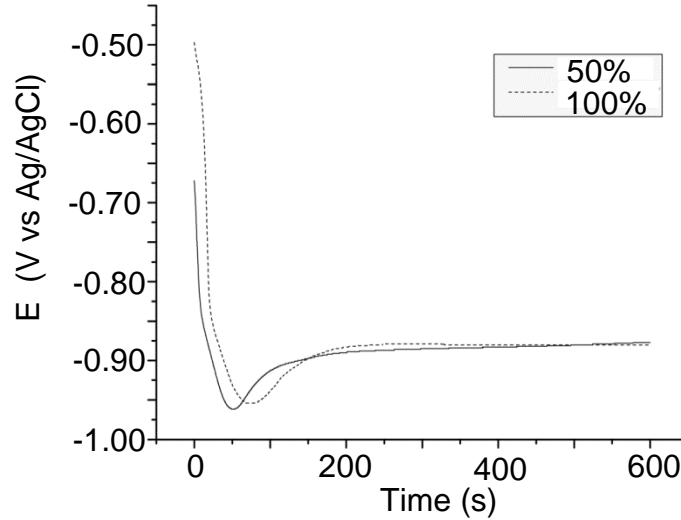


Figure 3.1 OCP-time profiles recorded during formation of the TCP coatings on AA2024 immediately after degreasing and deoxidizing. The profile of a high oxide AA2024 sample, immersed in boiled water for 1 min after deoxidizing, was also shown here as comparison. Coatings were formed at room temperature (21-27 °C).

The importance of the initial oxide layer dissolution during the coating formation process is illustrated in Figure 3.2. In this figure, OCP-time transients are shown for high oxide AA2024 samples in 50 and 100% Alodine® T5900. The samples were prepared by degreasing and deoxidation, followed by immersion in boiling water for 1 min. This leads to formation of a thicker Al oxide film layer on the alloy surface. For this high oxide AA2024, there is a slower cathodic shift in the OCP to -0.9 V vs Ag/AgCl as compared to the low oxide sample in Fig. 3.1. This reflects an extra time needed to dissolve the thicker oxide and expose bare Al. The cathodic limit of ca. -0.9 V is reached after about 500 s on the high oxide samples as compared to the 100 s seen for the low oxide surfaces. Once the oxide film is dissolved, then the TCP formation is in an identical manner on all of the surfaces, based on the similarity in the OCP values. The increase in the surface pH due to hydrogen discharge and oxygen reduction reaction drives the

hydrolysis of hexafluorozirconate to form hydrated zirconia that precipitates on the surface according to the following reaction:

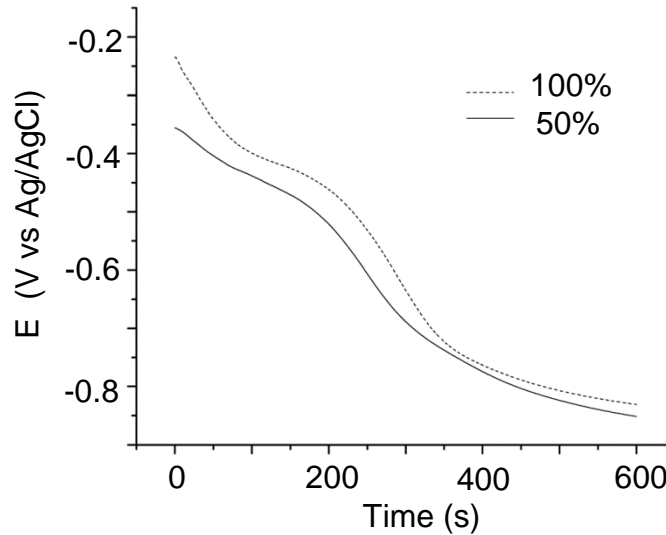
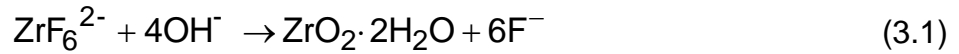


Figure 3.2 OCP-time profiles recorded during the formation of the TCP coating on AA2024. The two metal samples were boiled in water for 1 min to produce a hydroxide/oxyhydroxide layer. Two different strengths of the Alodine® 5900 solution were used: full strength (100%) and diluted (50%). Coatings were formed at room temperature (21-27 °C).

Figure 3.3 presents a typical in situ pH trace at the surface of an AA2024 sample (empty squares) recorded before, during and after formation of the TCP conversion coating.¹¹⁵ The pH values were obtained by converting the tungsten microelectrode potentials using the linear regression equation for the model buffer solutions in Fig. 3.3B. The microelectrode potential (solid circles) and OCP of the AA2024 substrate (solid squares) were recorded simultaneously during the coating formation for comparison. First, the tungsten microelectrode was fully immersed in the TCP bath for 10 min. The microelectrode potential reached a constant potential of -0.06 V vs. Ag/AgCl within the first few seconds of immersion. This value corresponds to a pH of 3.9 for the bulk TCP

bath. The microelectrode was then repositioned close to the AA2024 sample surface followed by adding the coating solution. Immediately when both the microelectrode and the alloy sample were fully immersed in the solution, the OCP measurement started. Parallel with the cathodic shift of the AA2024 OCP during the first 2 min, the tungsten microelectrode potential also decreased rapidly. The decrease in tungsten electrode potential is an indication of an increase in the local solution pH according to Fig. 3.3B. As the oxide layer on the aluminum alloy gets dissolved in the coating bath, the OCP for the alloys shifts considerably cathodic. This cathodic shift is reflective of the increased rate of cathodic reactions needed to balance the increased rate of corrosion due to the dissolution of the passivating oxide. The cathodic reactions consume H^+ ions: (i) oxygen reduction and (ii) hydrogen evolution. A H^+ concentration gradient develops at the alloy surface relative to the solution bulk. The interfacial pH shifts from 3.9 to near 7 during the initial stages of coating formation. The variation in the response period is due to a lag time needed for development of the concentration gradient of H^+ from the alloy surface to the microelectrode.

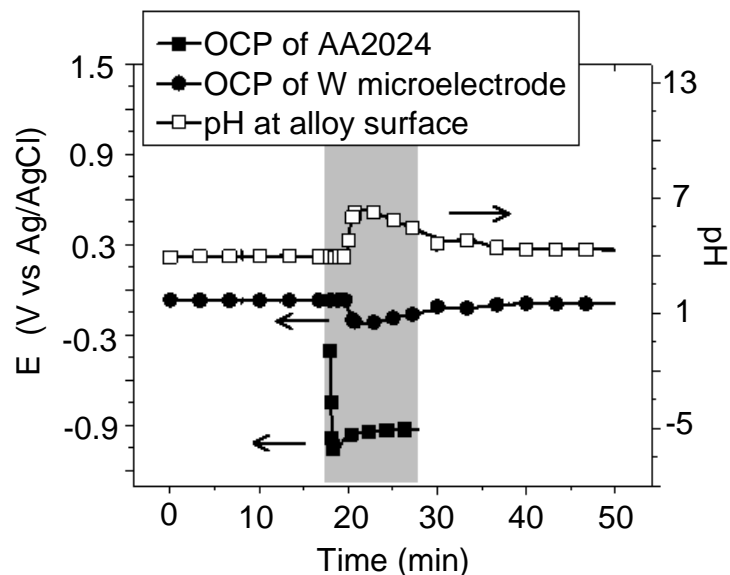


Figure 3.3 A typical pH trace at the AA2024 surface (empty squares, right y axis) before, during and after formation of the T5900 conversion (TCP) coating. The OCP of the W/WO₃ microelectrode and the AA2024 sample (solid circles and squares, respectively, left y axis) were also recorded. The formation of the coating occurred during the 18 to 28 min period, as indicated by the grey background.

3.2.2 AFM topography of TCP-coated alloys

Figure 3.4 shows *ex situ* tapping-mode AFM images of polished, degreased and deoxidized AA2024 surfaces before and after TCP coating. Height mode images are shown over a 10 × 10 mm² area. The uncoated surface (Fig. 3.4A) is relatively smooth with no intermetallics or defects in the imaged area. The roughness is 20.9 nm (root mean square, rms) over the 100 mm² area. The image of the coated surface (Fig. 3.4B) reveals a nodular morphology. The film conforms to the underlying surface topography as a similar nominal roughness of 21.3 nm (rms) is found over the same geometric area. On these length scales, the coating conforms to the underlying metal topography and appears devoid of large-scale cracks and imperfections.

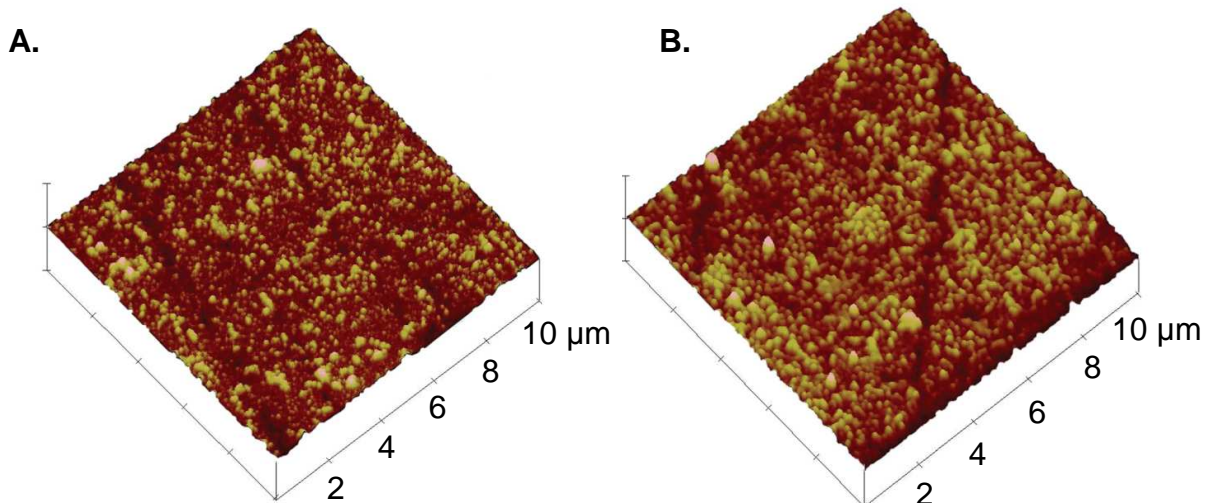


Figure 3.4 *Ex situ* tapping mode AFM images of uncoated and TCP-coated AA2024 specimens. Images ($10 \times 10 \mu\text{m}^2$) are presented in the height mode.

3.2.3 Auger depth profiling of TCP coatings

Figure 3.5 presents elemental depth profiling data for TCP-coated AA2024 samples obtained by scanning auger microprobe analysis. Tracking the Al signal with depth indicates the film is on the order of 50 nm thick (*in vacuo*). Further evidence that the immersion coating is about 50 nm thick comes from tracking the Cu signal with depth. This Cu signal arises from intermetallic particles at the alloy surface and should not be affected by the aggressive TCP coating solution. As can be seen, the Cu signal intensity starts to increase at about 50 nm into the coating. Recently reported ellipsometric data of a hydrated coating, formed in a manner similar to our coatings, revealed a nominal film thickness of 90 nm for a 10 min immersion coating.⁷² Therefore, we suppose the true (hydrate) thickness of our TCP coating is on the order of 90-100 nm. Cracks in the coating are observed from time to time during SEM imaging, consistent with tensile stress caused by a reduction in film volume in vacuum. A

noteworthy observation in Fig. 3.5 is that the Zr atomic concentration tracks the O rather than the F concentration. The Zr and O levels are relatively constant with depth into the coating with the atomic concentration ratio (O/Zr) of is about 2:1. This is consistent with the empirical formula of dehydrated zirconia, ZrO_2 . The zirconia layer is on the order of 30 nm thick and it interfaces with a 20 nm, or so, thick AlF_3 -rich layer at the alloy surface. The conclusion is based on the fact that the K and F atomic concentrations are elevated in the interfacial region making up this AlF_3 -rich zone. We suppose that this AlF_3 -rich region consists of K_3AlF_6 (fluoroaluminate). When the Al-rich matrix undergoes oxidation during the coating process, corrosion products form in the F⁻-rich solution that gets precipitated as a K_3AlF_6 -rich layer (fluoroaluminate) on the metal surface. Therefore, the initial increase in the Al atomic concentration with depth likely originates from this precipitated interfacial layer. Figure 3.5 reveals that the increased Al concentration actually begins to increase about 20-30 nm into the coating. Another explanation for the elevated K level in the interfacial region is that the cation is there to charge compensate the excess F⁻ from the coating arising from the hydrolysis of the hexafluorozirconate. Finally, the all important Cr concentration is elevated near the alloy surface but the element does not appear to be distributed uniformly throughout the coating thickness. The Cr level is comparatively low at about 4–5 atom % but comparable to the solution concentration, <5 wt %.

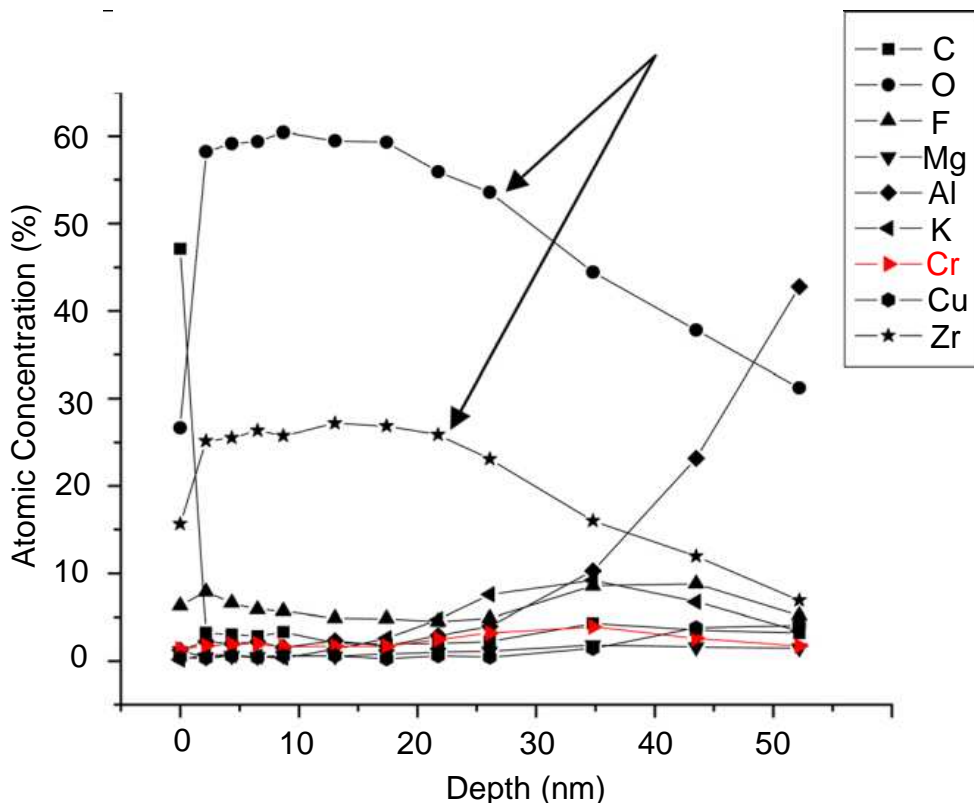


Figure 3.5 Scanning Auger electron spectroscopy depth profiling analysis of TCP-coated AA2024. Depth profiling levels are shown for several important elements including Al, Zr, O, Cr, Cu, K and F. Arrows in (A) identify traces for Zr and O. Arrow in (B) identifies the F signal.

3.2.4 Chemical structure of Cr in TCP coatings

Additional evidence for the presence of Cr species in the coating comes from XPS data. Figure 3.6 shows the Cr 2p region of the survey scan for TCP-coated AA2024. XPS is useful for assessing the oxidation state of the Cr in the coating. There are two peaks in the spectrum at *ca.* 576 and 586 eV. They represent Cr 2p_{3/2} and 2p_{1/2} photoelectrons, respectively. The 2p_{3/2} peak is sensitive to the Cr oxidation state and can be fit with two peaks when both Cr(III) and Cr(VI) are present in a mixed oxide: 576.7 eV for Cr(III) and 579.3 eV for Cr(VI). A narrow Cr 2p_{3/2} peak is seen for the TCP coating with no higher binding energy tail. Therefore, the coating as formed appears to

consist of mainly Cr(III) species ($\text{Cr}(\text{OH})_3$, Cr_2O_3 and or CrOOH). In other words, the freshly prepared coating contains chromium in a trivalent rather than a hexavalent oxidation state. It should be noted that the samples used for XPS measurements were coated and dried for 1-2 h before placement in the vacuum chamber for elemental analysis.

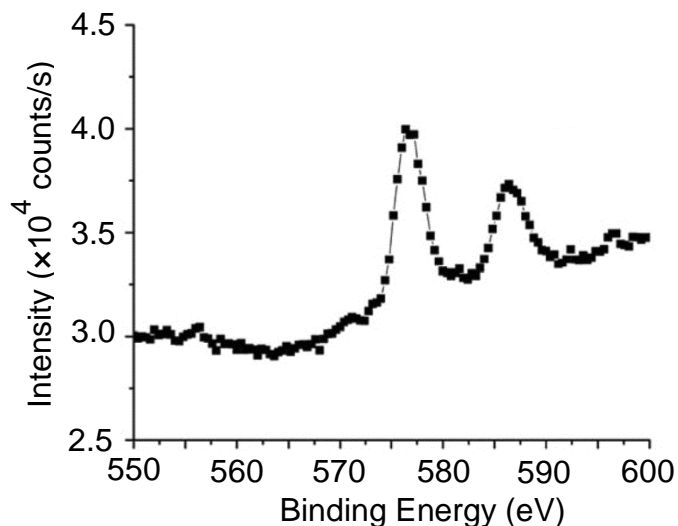


Figure 3.6 XPS survey scan in the Cr 2p region for a TCP-coated AA2024 sample.

3.2.5 SEM/EDAX analysis of TCP-coated aluminum alloys

Figure 3.7A presents an SEM image of a pitted region of a TCP-coated AA2024 sample, along with an x-ray line profile across several Cu-rich intermetallic particles and pits. A $\sim 90 \mu\text{m}$ line profile is demarked in the image. The pit diameters range from 1 to about $10 \mu\text{m}$ and likely form during the coating process. Figures 3.7B-E shows energy-dispersive x-ray analysis (EDS) line profiles for Cu, Zr, O and Cr recorded across the pitted areas. In Fig. 3.7B, the profile for Cu (Ka) shows elevated metal levels in two of the pits at the 18, 48 and $75 \mu\text{m}$ points of the profile. The Cr (Ka), Zr (La) and O (Ka) signal intensities shown in Figs. 3.7C-E are reflective of the presence of TCP. It can be

seen that the signal intensities for all three elements are higher near the pit edges than on the terraces surrounding the pits. This is a common observation from probing numerous pit areas on TCP-coated AA2024. The Zr and O signals arise from the hydrated zirconia, $ZrO_2 \cdot 2H_2O$, that precipitates during the immersion process. The Cr signal arises from Cr(III) localized within the coating, likely Cr_2O_3 . Based on the x-ray signal intensities, the levels of Cr regionally in the coating are less than the Zr or O levels, as expected.

3.2.6 Basic electrochemistry of TCP-coated aluminum alloys

Figure 3.8 presents the potentiodynamic polarization curves for TCP-coated and uncoated AA2024 specimens measured in naturally aerated 0.5 M Na_2SO_4 . The presence of the coating does not cause a significant shift in the corrosion potential (E_{corr}). However, the coating produces attenuated anodic and cathodic currents around the E_{corr} . For example, the anodic current density at 0.1 V is about a factor of 10× lower for the TCP-coated alloy compared to the uncoated sample. Attenuated current is also seen for the cathodic scan from E_{corr} to about -1.0 V vs Ag/AgCl. The cathodic current in this potential region is arises from oxygen reduction and the inhibition by TCP may result from the blockade of at least some of the Cu-rich intermetallic sites.

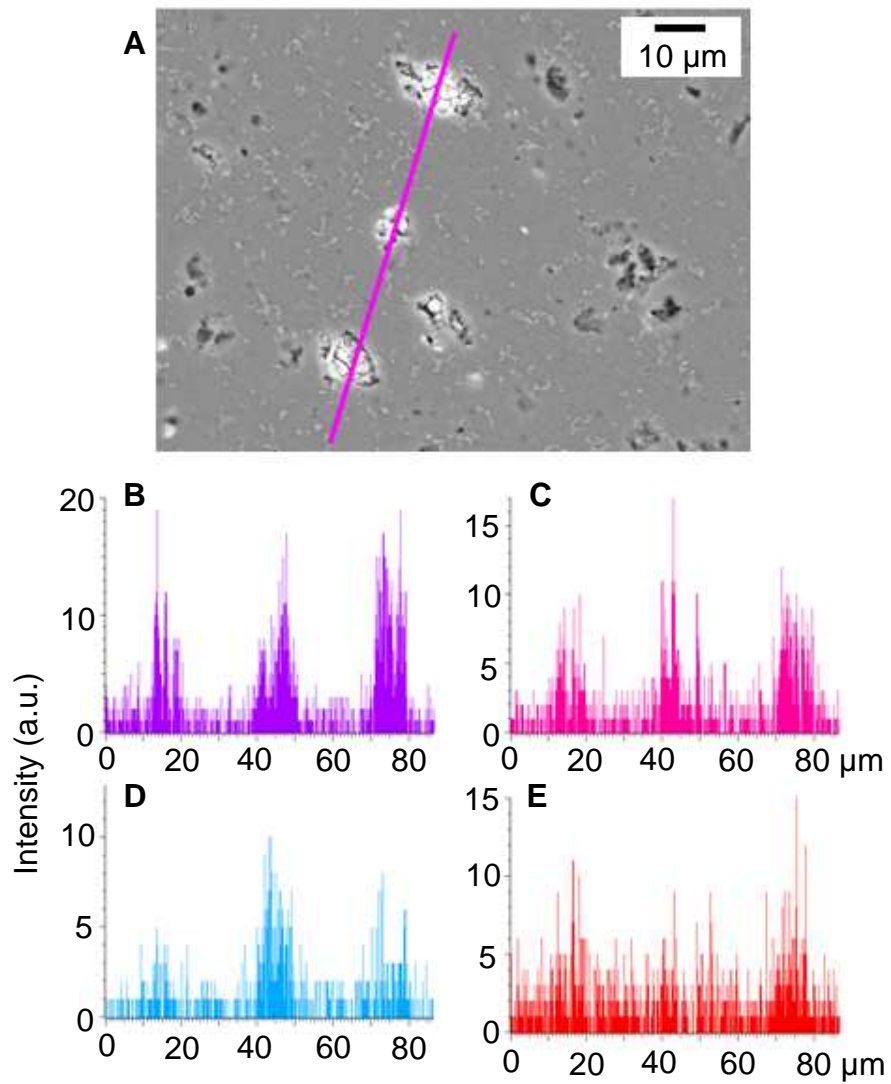


Figure 3.7 (A) SEM micrograph of aTCP-coated AA2024 specimen, and (B-E) EDAX line profiles for Cu, Cr, Zr, and O, respectively, across the coating as demarked by the line in (A).

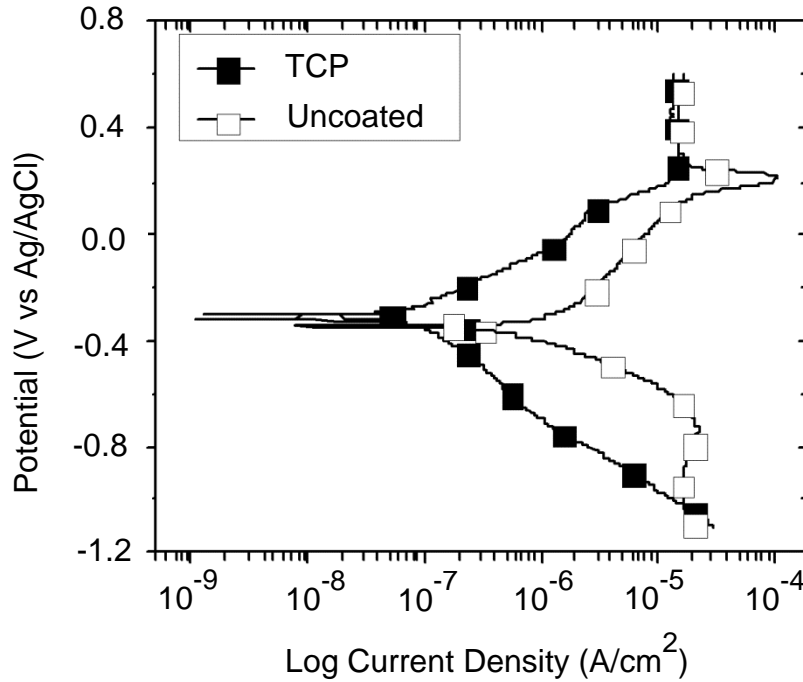


Figure 3.8 Potentiodynamic polarization curves for TCP-coated and uncoated AA2024 samples. Measurements were conducted in naturally aerated 0.5 M Na₂SO₄. The scan rate was 2 mV/s.

Figure 3.9 presents corrosion potential, E_{corr} , and polarization resistance, R_p , data for TCP-coated and uncoated AA2024 alloys measured in naturally aerated 0.5 M Na₂SO₄. The R_p values were calculated from the slope of linear sweep polarization curves recorded at ± 30 mV vs. E_{corr} (Chapter 2). The TCP coating provides a $\sim 10\times$ increase in R_p for AA2024-T3 ($4.03 \pm 0.61 \times 10^5 \Omega\cdot\text{cm}^2$ vs. $5.42 \pm 0.60 \times 10^4 \Omega\cdot\text{cm}^2$ for the uncoated samples). It should be noted that R_p is only $10^5 \sim 10^6 \Omega\cdot\text{cm}^2$ rather than $\sim 10^9 \Omega\cdot\text{cm}^2$ value that would reflect full barrier properties.¹¹⁴ Therefore, the TCP

coating, while partially passivating the alloy, likely consists of hydrated channels/pores and or defects.

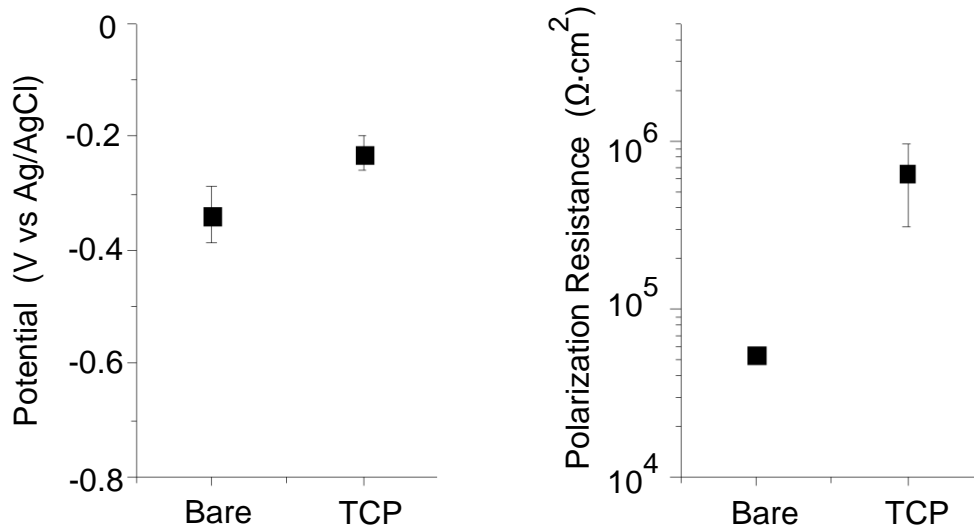


Figure 3.9 Corrosion potential (E_{corr}) and polarization resistance (R_p) data for TCP-coated and uncoated AA2024 specimens measured in naturally aerated 0.5 M Na_2SO_4 . R_p was determined by the inverse of the slope of $E-i$ curves at E_{corr} . Each datum is an average value of no less than 4 samples. The asterisks indicate statistically significant differences at the 95% confidence level.

Figure 3.10 shows the typical Bode plots for the TCP-coated AA2024 specimens at E_{corr} . Measurements were conducted in naturally aerated 0.5 M Na_2SO_4 + 0.01 M NaCl. Table 1.1 presents the best-fit parameters for these EIS data to the equivalent circuits shown in Figure 2 of Chapter 2. The uncoated AA2024-T3 shows one time constant that is attributed to the interfacial capacitance at the metal surface, while the TCP-coated sample exhibits two time constants due to its microporous or defect structure. The higher frequency time constant corresponds to the coating and the lower frequency one that is attributed to the double layer at the uncoated metal region

(Chapter 2). The fitted R_p for both TCP-coated and uncoated AA2024-T3 are consistent with the values shown in Fig. 2. In addition, the effective coating capacitance (C_{co}) is $5.9 \pm 0.6 \mu\text{F}/\text{cm}^2$ that was calculated using Q_{po} and n_{po} by $C_{po} = Q^{1/n} R^{1/n-1}$ where $R=R_{po}$. The coated sample exhibits a larger capacitive reactance over a wider frequency range which is consistent with greater corrosion inhibition.

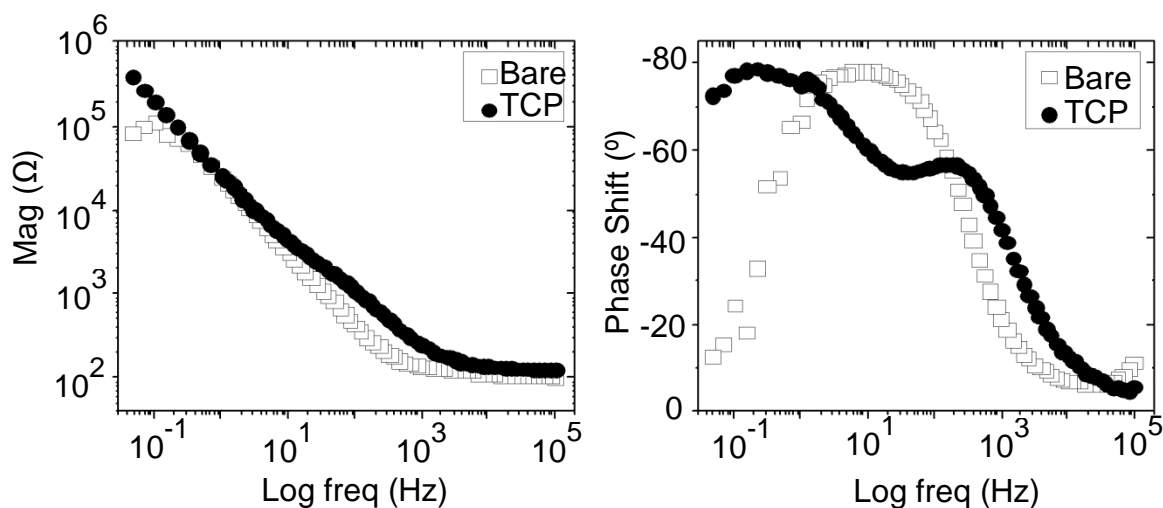


Figure 3.10 Bode plots for the TCP-coated AA2024 at E_{corr} . Measurements were made in air-saturated 0.5 M Na_2SO_4 + 0.01 M NaCl after the samples were aged in air overnight at room temperature. All samples had a geometric area of 0.2 cm^2 exposed to the electrolyte solution during measurements.

Table 3.1 Best-fit parameters of the experimental EIS data for the TCP-coated and uncoated AA2024 samples in naturally aerated 0.5 M Na₂SO₄. Each datum is an average value of no less than 4 samples. The equivalent circuits used for the simulation were presented in Fig. 2 in Chapter 2.

	R_{el} (Ω)	Q_{co} ($\times 10^{-6}$ $s^n/(\Omega \cdot cm^2)$)	n_{co}	R_{po} ($\Omega \cdot cm^2$)	Q_{dl} ($\times 10^{-6}$ $s^n/(\Omega \cdot cm^2)$)	n_{dl}	R_p ($\times 10^4$ $\Omega \cdot cm^2$)
TCP	118 ± 4	28.9 ± 2.1	0.8 ± 0.0	152 ± 57	24.2 ± 3.3	0.9 ± 0.0	18.8 ± 5.1
Bare	131 ± 12	-	-	-	55.5 ± 7.9	0.8 ± 0.0	4.9 ± 0.2

3.2.7 Mass transfer inhibition

Figure 3.11 shows cathodic potentiodynamic sweeps for an (A) uncoated and (B) TCP-coated AA2024 rotating disk electrode that were recorded at various electrode rotation rates in the naturally aerated 0.5 M Na₂SO₄. For the uncoated alloy, the cathodic current for oxygen reduction increases as expected with the rotation rate. The current profile exhibits a peak at -0.4 V due to oxygen reduction and then becomes stable at more negative potentials. In contrast for the TCP-coated alloy, the current is 10× lower than that recorded for the uncoated alloy and there is no increase with rotation rate. In other words, the reaction rate is insensitive to the flux of oxygen to the electrode surface, which is consistent with the coating providing barrier protection and inhibiting mass transport.

Figure 3.12 shows the Levich plots of the oxygen reduction current at different applied potentials for the uncoated and TCP-coated AA2024 alloys. Data for an

uncoated Cu rotating disk electrode are also presented for comparison. The i_{lim} data for the uncoated and TCP-coated AA2024-T3 at -0.7 V vs Ag/AgCl are plotted against the rotation rate^{1/2}. For the uncoated alloys, the potentiodynamic curves show a similar trend that is the current density increases from OCP and reaches a peak at about -0.4 V vs Ag/AgCl. The curves then decrease slightly before approaching a plateau. Moreover, in the mass-transfer controlled region (e.g., from -0.4 to -1.0 V vs Ag/AgCl), the current density increases as the rotating rate increases. However, the i_{lim} value is smaller on the uncoated AA2024 compared to the uncoated Cu, which is attributed to the greater ORR active areas on the Cu electrode than that on AA2024. The slope of the curve for uncoated AA2024 is less than the expected value for the case with the oxygen reduction reaction (n=4) is proceeding under diffusion control. The lower slope is likely due to formation of a passivating oxide layer at both the Al and the Cu-rich intermetallic sites. The passivating oxide layer functions as a barrier for both electron transfer from the underlying metal and mass transport of oxygen. Therefore the higher angular velocity does not increase i_{lim} to the level expected for n=4. In contrast, the TCP-coated AA2024-T3 exhibits i_{lim} (e.g., -0.01 $\mu\text{A}/\text{cm}^2$) that is smaller by about one order of magnitude than that for the uncoated sample (e.g., -0.2 to -0.6 $\mu\text{A}/\text{cm}^2$) throughout this potential window shown in Fig. 4B. The curves have no plateau or peaks, which indicates a mass transfer inhibition of the dissolved O₂. It is also noted that there is no significant change in the current density as the rotating rate increases. This independence of i_{lim} to $w^{0.5}$ (Fig. 5) is attributed to both the mass transfer inhibition

provided by the TCP coating and the fact that this coating contains ZrO_2 , $Cr(OH)_3$, and $Al(OH)_3$ which are poorly conductive materials.

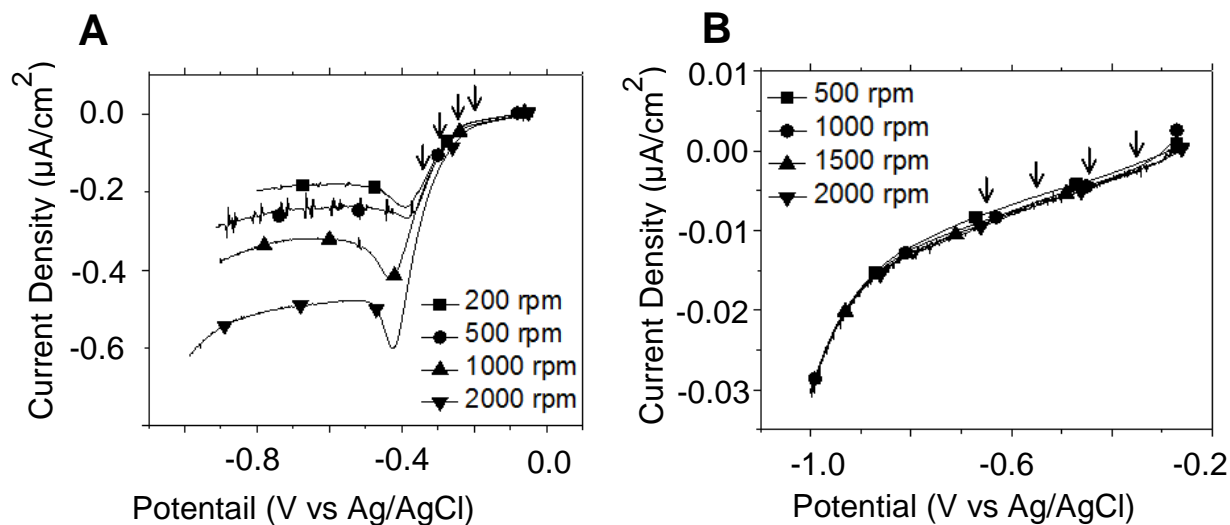


Figure 3.11 Cathodic potentiodynamic sweeps for an (A) uncoated and (B) TCP-coated AA2024 rotating disk electrode at different rotation rates in naturally aerated 0.5 M Na_2SO_4 . Scan rate = 2 mV/sec.

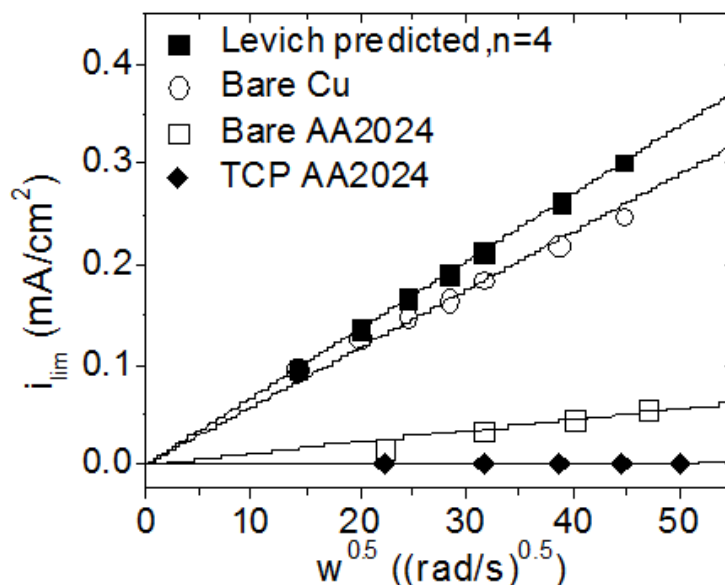


Figure 3.12 Plots of i_{lim} for the oxygen reduction reaction as a function of $w^{0.5}$ recorded using uncoated AA2024, Cu and TCP-coated AA2024 rotating disk electrodes in naturally aerated 0.5 M Na_2SO_4 . The theoretical Levich plot for of the $4e^-$ reduction of oxygen is also shown for comparison. The variables in the theoretical curve were: $n=4$, $A=0.283\text{ cm}^2$, $C_{O_2}=1\times 10^{-4}\text{ M}$, $D_{O_2}=1\times 10^{-4}\text{ cm}^2/\text{s}$, and $\nu=0.01\text{ cm}^2/\text{s}$.¹¹⁰

3.3 Discussion

3.3.1 Formation of TCP coatings

The formation of TCP immersion coatings occurs by a series of chemical steps, initially driven by an increase in the interfacial pH. The initial chemical step involves dissolution of the native oxide layer, as evidenced by the negative shift in the OCP (Fig. 3.1). This is in agreement with recent observations made by Dong *et al.* and Jaworowski *et al.*¹¹³ The hydrogen discharge that accompanies the oxidation and dissolution of the Al alloy consumes protons and causes an interfacial pH increase (Fig. 3.3). Oxygen reduction is also a counterbalancing cathodic reaction that occurs at the Cu-rich intermetallics and contributes to the interfacial pH increase. The increased pH up to ca. 7 at the metal surface, as well as an OCP of the alloys of ca. -0.9 V vs Ag/AgCl, lead to hydrolysis of hexafluorozirconate to form a hydrated zirconia layer. Energy-dispersive x-ray spectroscopy (EDX) analysis revealed that TCP coating consists of Zr and O, consistent with the formation of zirconia (Fig. 3.5), and that the coating is present over most regions of the alloy surface (Fig. 3.7). EDX data were also consistent with a biphasic coating consisting of an outer $\text{ZrO}_2 \cdot 2\text{H}_2\text{O}$ layer and an interfacial $\text{K}_x\text{AlF}_{3+x}$ -rich layer (fluoroaluminate, AlF_6^{3-}). This is based on the elevated levels of Al, F and K detected at the interface of coatings and alloys using Auger electron spectroscopy (AES) depth profiling (Fig. 3.5). Once the oxide layer is dissolved, the exposed aluminum undergoes oxidation in the fluoride-rich coating solution (pH 3.8-4) forming AlF_6^{3-} ions. The fluoride at the metal surface originates from the hydrolysis of hexafluorozirconate and the HBF_4 in the coating solution. Al^{3+} formation is promoted by the presence of F^- .

We suppose that this leads to the formation of a fluoroaluminate interfacial layer. The $\text{Cr}(\text{OH})_3$, CrOOH and or Cr_2O_3 appear to co-precipitate along with the hydrated ZrO_2 .

3.3.2 Structure of TCP coatings

Figure 3.13 illustrates the proposed biphasic chemical structure of the immersion coating. The interfacial layer is comprised of $\text{K}_x\text{AlF}_{3+x}$ that forms through dissolving the Al surface by F^- in the coating baths. The overlayer is an inert ZrO_2 film that forms by hydrolysis of ZrF_6^{-2} as the surface pH increases from 3.8 to 7. For a 10-min full immersion in the TCP baths, the apparent thickness of the coating is on the order of 50 nm for AA2024. We refer to this as an apparent thickness because the AES data used to estimate the thickness were all taken *in vacuo*. Coating shrinkage is expected so the true thickness is on an order of 100 nm for AA2024.¹¹³

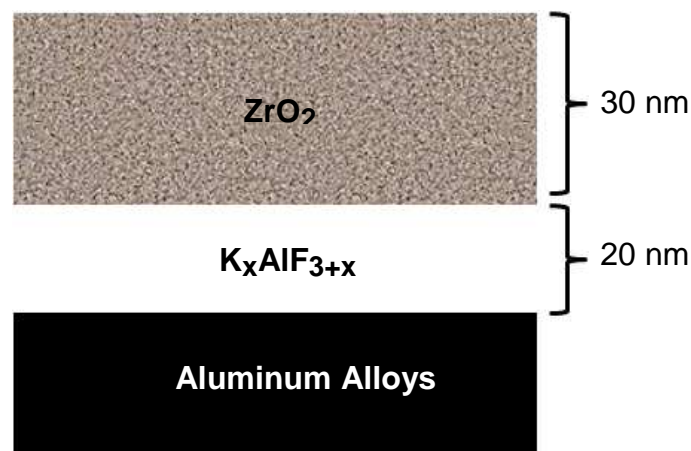


Figure 3.13 Schematic of the biphasic chemical structure of the TCP coating on AA2024. The thickness values listed are those estimated from measurements made *in vacuo*, and are likely less the true thickness.

Line profiling x-ray analysis revealed the coating forms on most areas of the aluminum alloy and enriched at the intermetallic sites (Fig. 3.7). Furthermore, the immersion coating does not form an impermeable barrier on the alloy surface. This conclusion is based on the fact that the polarization resistance is 10^5 - $10^6 \Omega\cdot\text{cm}^2$ in air-saturated 0.5 M Na_2SO_4 rather than $\sim 10^9 \Omega\cdot\text{cm}^2$, as expected for more impermeable barrier coatings on aluminum alloys. We suppose the biphasic coating is hydrated and contains channels and pathways through which dissolved O_2 and ions can diffuse to reach the underlying metal surface. This leads to localized corrosion on the coated surface.

Cr is incorporated but its distribution does not appear uniform throughout the coating. Cr levels are elevated in and around pits based on EDX analysis (Fig. 3.7). A steeper pH gradient likely exists near these sites during the coating formation and this may be a driver for the formation of Cr(III) oxide. Several elongated precipitates were seen on the surface of the coated alloys (Fig. 3.7). This is attributed to the pH increase (Fig. 3.3) that leads to precipitation of Cr(III) oxide species, *e.g.*, Cr_2O_3 , $\text{Cr}(\text{OH})_3$, and or CrOOH , during formation of the coatings. Cr exists as Cr(III) oxides in the TCP coating after the overnight aging in air at room temperature (Fig. 3.6). Some Cr(VI) was seen in the pit around the intermetallic compounds, which is attributed to transient formation of Cr(VI) at the Cu- or Fe-rich intermetallic sites where is not completely dried after overnight aging. More details of transient formation of Cr(VI) in the TCP coating will be discussed in the next chapter.

3.3.3 TCP as charge transfer inhibitor

R_p is calculated at E_{corr} as shown in Chapter 2. Therefore, the increased R_p indicates a charge transfer inhibition effect by the TCP coating. The corrosion for both anodic and cathodic reactions are reduced by blocking the active sites for Al oxidation and O_2 reduction. For example, the suppressed Cu stripping peak shown in Fig. 3.8 indicates that fewer Cu sites are exposed for the coated alloy sample and the O_2 reduction is inhibited. In addition, it should be noted that the coating does not block all the active sites completely since R_p is only $\sim 10^6 \Omega \cdot \text{cm}^2$ rather than $\geq 10^9 \Omega \cdot \text{cm}^2$ that is expected for a completely inert surface. The TCP-coated alloy shows a two time constant spectrum with the high-freq time constant indicating a porous structure of the coating (Fig. 3.10). Therefore, the coating blocks some active sites for Al oxidation and O_2 reduction but does not completely passivate the alloy surface due to the existence of hydrated channels and or defects.

3.3.4 TCP as a poorly conductive barrier to ETR

A thin layer of oxide naturally forms on Al when exposed to the atmosphere (~ 10 nm thick) after deoxidation.. Furthermore, the oxide layer on Cu intermetallic sites may not be dissolved depending on the chemical nature of the deoxidizer used. . These oxide layers are poorly conductive and act as electronic barriers that inhibit electron transfer (ETR).^{103, 110} This leads to an i_{lim} that is weakly dependent of $w^{0.5}$ and the Levich slope that is much smaller than the predicted value when $n=4$ (Fig. 3.12). The same applies to the TCP coating that also contains poorly conductive oxides, such as

ZrO₂, Cr(OH)₃, and Al(OH)₃. Scully *et al.* compared the oxygen reduction current at rotating disk electrodes made of Cr and Au.¹¹⁰ The Cr electrode forms a hydrated Cr oxide layer (e.g., Cr(OH)₃) on the surface naturally when exposed to air and shows an independent i_{lim} vs. $w^{0.5}$ relationship. In contrast, the Au electrode has no oxide film and shows a Levich slope consistent with that expected when $n=4$. This indicates that the TCP coating functions partially as an ETR barrier that inhibits the electron transfer through the coating. Since the thickness of the coating is greater, the Levich slope is smaller than that for the Al oxide layer on the uncoated samples.

3.3.5 TCP as a physical barrier that diminishes O₂ mass transfer

The independence of the i_{lim} on $w^{0.5}$ (Fig. 3.11 and 3.12) can also be attributed to the inhibition of the mass transfer of dissolved O₂ through the hydrated channels and or defects to the underlying metal. The dissolved O₂ transports through the coating in a much slower rate than in the bulk electrolyte solution. Therefore, the ORR is hampered and controlled by the diffusion of the dissolved O₂ within the TCP coating. For the mass transport limited ORR, the limiting current density is given by the following equation:¹¹⁷

$$i_l = \frac{nFC_{bulk}}{\delta_{sol}} = nFC_{bulk} \frac{1}{1.61v^{1/6}w^{1/2}/D_{sol}^{2/3}} \quad (3.1)$$

where δ_{sol} is the O₂ diffuse layer thickness, D_{sol} is the O₂ diffusion coefficient, n is the number of electrons in the reduction of 1 mol O₂, F is the Faraday constant, C_{bulk} is the

bulk concentration of the dissolved O₂, ν is the viscosity constant of the solution, and w is the rotation rate of the RDE. If the transport of dissolved O₂ through the TCP coating is taken into consideration, Eq. (3.1) becomes:

$$i_l = \frac{nFC_{\text{bulk}}}{\delta_{\text{sol}}/D_{\text{sol}} + \delta_{\text{TCP}}/D_{\text{TCP}}} = nFC_{\text{bulk}} \frac{1}{1.61\nu^{1/6}w^{1/2}/D_{\text{sol}}^{2/3} + \delta_{\text{TCP}}/D_{\text{TCP}}} \quad (3.2)$$

where δ_{TCP} is the length of the pathways that dissolved O₂ diffuse from the electrolyte/coating interface to the coating/metal interface. D_{TCP} is the diffusion coefficient of dissolved O₂ in the TCP coating. With the assumption that $n=4$, $F=96500$ As, $C_{\text{bulk}}=1 \times 10^{-4}$ M, $\nu=0.01$ cm²/s, $D_{\text{sol}}=1 \times 10^{-5}$ cm²/s,¹¹⁰ and δ_{TCP} is taken as the thickness of the TCP coating (e.g., 100 nm¹¹³), the simulated Levich plots are shown in Figure 3.14 as D_{TCP} is varied between 10⁻⁵ and 10⁻⁸ cm²/s. It can be seen that the TCP coating suppress ORR rates below the Levich predictions and i_{lim} becomes weakly dependent on the $w^{0.5}$. Therefore, the behavior of the TCP-coated AA2024 electrode in Fig. 3.11B and 3.12 can be explained in part by the mass transfer inhibition of the dissolved O₂ within the TCP coating.

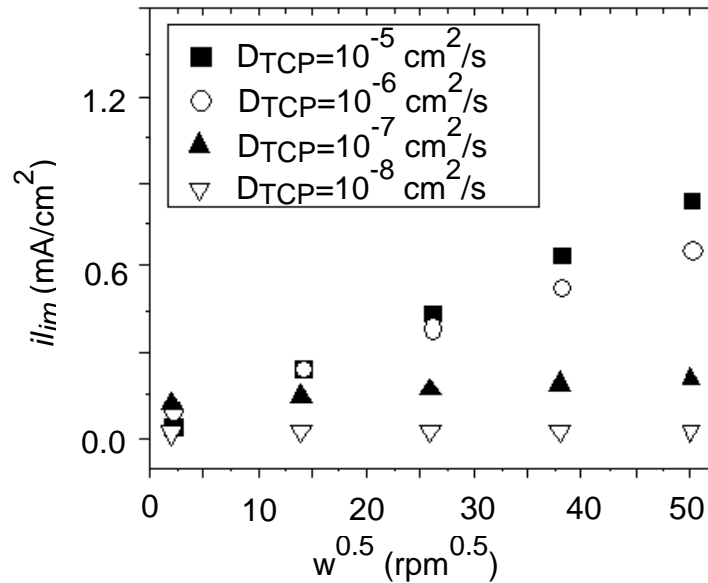


Figure 3.14 Simulated Levich plots for TCP-coated AA2024 according to Eq. (3.2) with the assumption that $n=4$, $F=96500$ As, $C_{bulk}=1 \times 10^{-4}$ M, $\nu=0.01$ cm²/s, $D_{sol}=1 \times 10^{-5}$ cm²/s, $\delta_{TCP}=100$ nm. D_{TCP} was varied from 10^{-5} to 10^{-8} cm²/s.

3.4 Conclusions

Trivalent chromium process (TCP) coatings were formed on AA2024 samples that were first degreased and deoxidized. The TCP coating in vacuum is approximately 50 nm thick and forms over most of the Al alloy surface. The true coating thickness (hydrated conditions) is on the order of 90-100 nm. The formation of the hydrated zirconia ($ZrO_2 \cdot 2H_2O$) coating is driven by an increase in the interfacial pH caused by (i) dissolution of the oxide layer and (ii) localized oxygen reduction at Cu-rich intermetallic sites. The coating composition is biphasic consisting of a hydrated zirconia overlayer and a K- and F-rich fluoroalumininate interfacial layer (K_3AlF_6). At least initially, $Cr(OH)_3$

is coprecipitated with the hydrated zirconia. The Cr-rich regions of the coating are in and around pits. The TCP coating provides both anodic and cathodic protection by physically blocking Al-rich sites (oxidation) and Cu-rich intermetallics (reduction). This is evidenced by the 10× greater polarization resistance for the TCP-coated alloys.

In addition, this chapter characterized the electrochemical properties of the TCP coating on AA2024-T3 and investigated the mechanisms by which the TCP coating inhibits corrosion. The TCP coating provides both cathodic and anodic protection as evidenced by suppressed current density at potentials around E_{corr} compared to those for the uncoated samples. The TCP-coated AA2024-T3 exhibits an R_p that is ~10× greater than that for the uncoated alloys, which indicates an open circuit protection. The TCP coating protects the alloy by providing an ohmically resistant layer and serving as a barrier to O₂ diffusion to the underlying metal. However, it should be noted that the TCP coating is not a perfect barrier layer and contains hydrated channels/pores and or defects that allow diffusion of some dissolved O₂ the underlying metal.

CHAPTER 4. TRANSIENT FORMATION OF CR(VI) IN TRIVALENT CHROMIUM PROCESS COATINGS IN AA2024-T3 PROBED BY RAMAN SPECTROSCOPY

4.1 Introduction

Chromate conversion pretreatment coatings (CCCs) are effective inhibitors of localized pitting corrosion on high strength aluminum alloys.⁹⁹⁻¹⁰⁸ As a consequence, they have been widely employed in the aerospace industry.⁹⁹ Research has revealed that CCCs possess “self-healing” capability and provide “active” corrosion protection to the alloys, which is attributed release of a soluble Cr(VI) species (*i.e.* chromate) from the coating, its transport through the solution and its action at nearby corroding sites. Unfortunately, hexavalent Cr is highly toxic and, therefore, is a tightly-regulated environmental pollutant. Its toxicity and carcinogenicity creates a risk to human health and to the environment. As a consequence, there has been a focus in recent years on developing alternate, less-toxic pretreatment coatings that provide equally effective corrosion protection as CCCs.

The Trivalent Chromium Process (TCP) coating is the leading CCC replacement and it provides corrosion protection to aerospace aluminum alloys, including AA2024-T3.^{99, 113, 118} TCP coatings are formed by solution immersion in a bath containing hexafluorozirconate (H_2ZrF_6 or K_2ZrF_6), trivalent chromium salts (*e.g.* $\text{Cr}_2(\text{SO}_4)_3$), and a fluoroborate salt (BF_4^-). The bath pH is maintained between 3.8 and 4.0 using hydrofluoric (HF) or sulfuric acid (H_2SO_4).^{112, 119} Chapter 3 covered the formation,

structure, basic electrochemical properties of the TCP coating on AA2024-T3. The formation of the coating is a pH-increase driven process that leads to hydrolysis of the dissolved fluorozirconate precursor to form a hydrated zirconia ($\text{ZrO}_2 \cdot 2\text{H}_2\text{O}$) coating. The soluble Cr(III) salt in the bath also reacts with hydroxide at elevated pH to form Cr(III) oxides (e.g. Cr_2O_3 , $\text{Cr}(\text{OH})_3$, and or CrOOH) that are coprecipitated with the hydrated zirconia.

While the coating bath contains no Cr(VI) species, a point of concern is whether there is any transient formation of Cr(VI) in the coating during exposure to the environment. In this work, Raman spectroscopy was used to probe for the transient formation of Cr(VI) oxide species in the coating during full immersion testing.

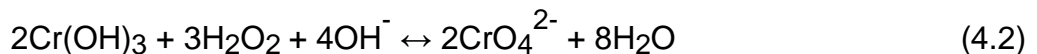
Raman spectroscopy is extensively used in the material science community. Spectral data are produced that serve as a “fingerprint” for the identification of lattice structures in a solid and the chemical composition of a coating. The method is quite useful for characterizing coatings that contain Cr oxide species, like CCC or TCP. Since the Raman cross-section for Cr(VI)-O is about 3 orders of magnitude larger than that for Cr(III)-O, the technique is sensitive to the presence of Cr(VI).¹²⁰ Another advantage of the method is that the band positions are reflective of the molecular structure and local chemical environment. For example, the characteristic bands for Cr(VI)-O and Cr(III)-O are easily distinguished by their peak positions: Cr(III)-O in the range of $520\text{-}580\text{ cm}^{-1}$ and Cr(VI)-O in the $840\text{-}904\text{ cm}^{-1}$ range. The Cr(III)-O band position shifts between $520\text{ - }580\text{ cm}^{-1}$ depending on the state of hydration.¹²¹⁻¹²³ Analogously, the Cr(VI)-O peak

position shifts depending on the interaction with other metals, such as Al, Mg, Mn, etc. to form mixed-metal oxides.¹²³

In this chapter, research was conducted to answer three questions:

- (1) Do Cr(VI) oxide species transiently form in the TCP and, if so, by what mechanism do they form in the coating on AA2024?
- (2) When does it form and what is the chemical environment around the Cr(VI) oxide species ?
- (3) Does the Cr(VI) oxide species provide any active corrosion protection on AA2024?

Our hypothesis regarding the formation is that dissolved oxygen is reduced at the Cu-rich intermetallic sites to hydrogen peroxide, H₂O₂, and that this H₂O₂ diffuses to nearby Cr-rich sites in the coating where it oxidizes native Cr(III) in the coating to Cr(VI). H₂O₂ is produced from the two-electron reduction of dissolved oxygen, as shown below.²⁰ Therefore, we suppose the conversion of Cr(OH)₃ transiently to chromate (CrO₄²⁻) involves the following two steps:



4.2 Results

4.2.1 Raman spectra for reference Cr and mixed Cr/Al oxides.

Figure 4.1 presents Raman spectra for several reference chromium oxides both as solid samples and salts dissolved in solution. Several standard solid compounds were prepared and used to qualitatively correlate the Raman spectral features with the chemical composition. A Cr(III)/Cr(VI) mixed oxide standard was prepared by dissolving 4.0 g $\text{Cr}(\text{NO}_3)_3 \cdot 9\text{H}_2\text{O}$ and 0.5 g $\text{K}_2\text{Cr}_2\text{O}_7$ in 50 mL H_2O and then adding 1.0 M NaOH dropwise into the stirred solution until the pH exceeded 4.5. The precipitate was then filtered, rinsed with H_2O , and dried in air at room temperature. The Al(III)/Cr(VI) mixed oxide was prepared by adding 1.0 M NaOH dropwise to a 50 mL solution containing 0.2 M $\text{Al}(\text{NO}_3)_3$ and 0.03M $\text{K}_2\text{Cr}_2\text{O}_7$. A precipitate formed at a pH above about 3. The precipitates were filtered at different pH as the NaOH solution continued to be added. Chromate (CrO_4^{2-}) and dichromate ($\text{Cr}_2\text{O}_7^{2-}$) are easily distinguished when dissolved in 0.1 M solutions (Fig. 4.1-a, b). Both exhibit a strong Cr(VI)-O peak in the 840-904 cm^{-1} range. The Cr(VI)-O band frequency shifts depending on the local environmental pH.¹²⁴ For example, at high pH (pH=9.36 for 0.1 M K_2CrO_4), Cr(VI) exists primarily as CrO_4^{2-} that is characterized by a peak at 847 cm^{-1} (Fig. 4.1-a). At low pH (pH=4.10 for 0.1M $\text{K}_2\text{Cr}_2\text{O}_7$), Cr(VI) exists as $\text{Cr}_2\text{O}_7^{2-}$ with a characteristic peak at 904 cm^{-1} (Fig. 4.1-b). At even lower pH (pH=2-5) and with a low total concentration (below 0.002 M) of chromate, Cr(VI) exists predominantly in HCrO_4^- that has a peak at 899 cm^{-1} .¹⁰⁷

Although the equilibrium distribution of CrO_4^{2-} , HCrO_4^- and $\text{Cr}_2\text{O}_7^{2-}$ is complex and depends on the local pH, the Cr(VI)-O bands are positioned in the $840\text{-}904\text{ cm}^{-1}$ range, which easily distinguishes them from the Cr(III)-O bands in the range of $520\text{-}580\text{ cm}^{-1}$. Cr_2O_3 and $\text{Cr}(\text{OH})_3$ are the two possible Cr(III) oxides in the TCP coating. Fig. 4.1-c shows a peak at 540 cm^{-1} for the reference Cr_2O_3 and Fig. 4.1-d shows a broad peak at 530 cm^{-1} for $\text{Cr}(\text{OH})_3$. The difference in band shape and peak position is due to differential states of hydration.^{101, 121, 123} The 1048 cm^{-1} peak in Fig. 4.1-d is attributed to the N-O bond in the $\text{Cr}(\text{NO}_3)_3$ salt that was used to prepare the solid.¹²¹ It should be noted that Raman scattering cross-section for Cr(III)-O is considerably smaller than that for Cr(VI)-O.¹²⁰ Therefore, the relative intensity of Cr(III)-O to Cr(VI)-O peaks is not a quantitative indicator of the Cr(III)/Cr(VI) ratio. These reference spectra were used as “fingerprints” to identify and distinguish Cr(III)-O and Cr(VI)-O species spatially in the TCP coating.

Spectra for two mixed oxides, Cr(III)/Cr(VI) and Al(III)/Cr(VI), were also recorded and are shown in Fig. 4.1-e and f. These mixed oxides were prepared as described in the Experimental section. The Cr(III)/Cr(VI) mixed oxide is the main chemical constituent in the CCC, while the Al(III)/Cr(VI) mixed oxide is considered to be the corrosion product in the CCC-coated alloys.¹⁰⁷ For the Cr(III)/Cr(VI) mixed oxide, the Cr(VI)-O peak is centered at 860 cm^{-1} and does not shift with pH. The pH independence of this band position can be used to distinguish a Cr(III)/Cr(VI) from

Al(III)/Cr(VI) mixed oxide. Figure 4.1-f presents a spectrum for Al(III)/Cr(VI) at pH 5.3. The Cr(VI)-O peak at 874 cm^{-1} shifts to lower frequency with increasing pH (e.g. 847 cm^{-1} at 7.8 in Fig. 4.1-g).

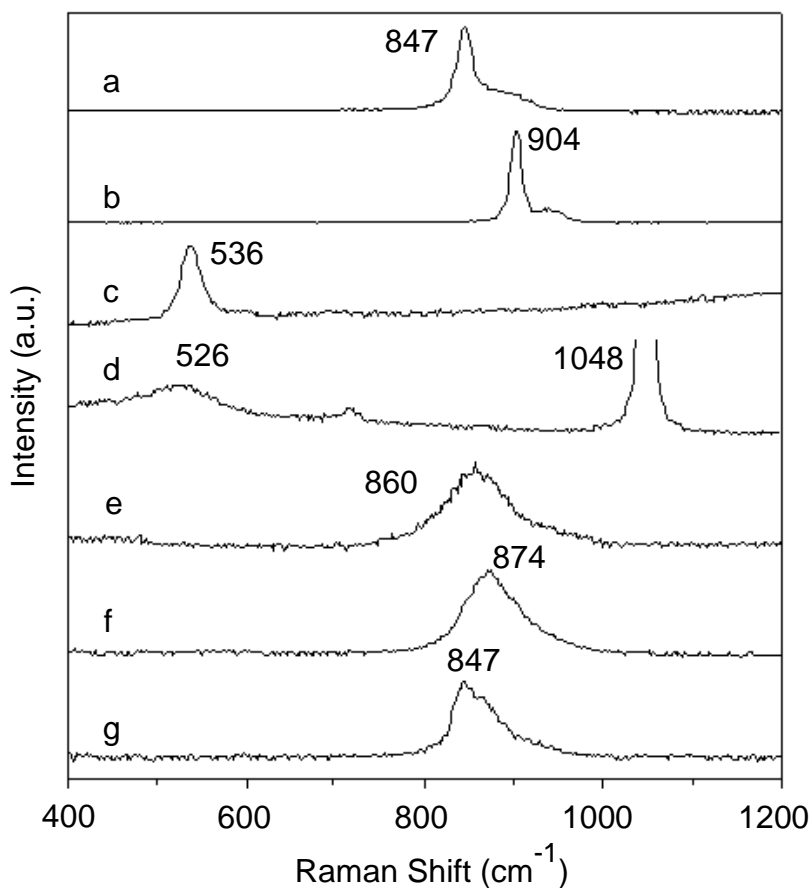


Figure 4.1 Raman spectra for reference chromium compounds: (a) 0.1M K_2CrO_4 solution, (b) 0.1M $\text{K}_2\text{Cr}_2\text{O}_7$ solution, (c) Cr_2O_3 pasted with water, (d) $\text{Cr}(\text{OH})_3$ salt, (e) Cr(III)/Cr(VI) mixed oxide, (f) Al(III)/Cr(VI) mixed oxide at pH 4.2 and (g) at pH 7.8. The spectra were obtained using Chromex Raman 2000 using a 532 nm, 20 mW power laser. The integration time was 3-10 s. The 1048 cm^{-1} peak in (d) is attributed to NO_3^- in $\text{Cr}(\text{NO}_3)_3$ that is used to prepare $\text{Cr}(\text{OH})_3$.

Figure 4.2 shows the pH dependence of the Cr(VI)-O peak position for mixed oxides of Al(III)/Cr(VI) and Cr(III)/Cr(VI). These were formed by dropwise addition of NaOH, as described in the Experimental section. For Al(III)/Cr(VI), the Cr(VI)-O peak position shifts from 904 cm^{-1} to 847 cm^{-1} as the pH is increased from 3.5 to 7.8. In contrast, the Cr(VI)-O peak for Cr(III)/Cr(VI) is independent of pH at 860 cm^{-1} . It has been reported that the Cr(VI)-O peak for Al(III)/Cr(VI) has multiple components at 847, 874 and 904 cm^{-1} whose intensities vary with the pH.¹⁰⁷ It was observed in our work that the position of the predominant peak shifts from 904 to 847 cm^{-1} with increasing pH with an asymmetric band shape for the Al(III)/Cr(VI) mixed oxide.

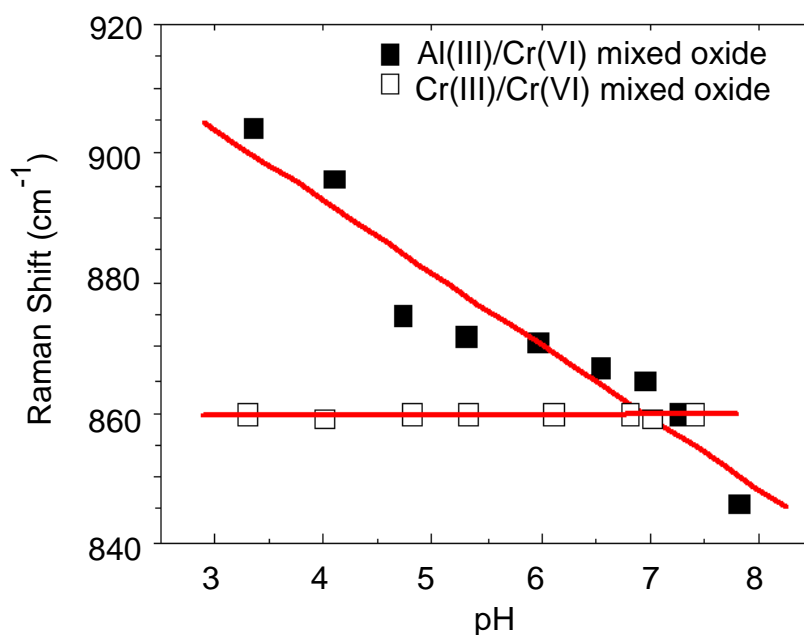


Figure 4.2 Raman band frequency of Cr(VI)-O bonds vs. pH for the mixed oxides of Al(III)/Cr(VI) and Cr(III)/Cr(VI).

4.2.2 Transient formation of Cr(VI) caused by H₂O₂.

An important question to answer is by what chemical reaction does the Cr(VI)-O species form from the Cr(III) oxide in the coating. We hypothesized that Cr(III) is oxidized to Cr(VI) by H₂O₂ that is produced by the two-electron reduction of dissolved oxygen at nearby Cu-rich intermetallic sites. To determine if this reaction is possible, we coated two AA2024 samples with TCP. One was aged one overnight under a vacuum while the other aged in the laboratory air for the same period of time. Both samples were aged at room temperature. Our hypothesis was that if O₂ availability was limited (*in vacuo*) then the corresponding level of H₂O₂ would be limited in the hydrated coating and there would be little oxidation of Cr(III) to Cr(VI)-O. In other words, no Cr(VI)-O peak was expected in the Raman spectrum for the sample aged *in vacuo*.

Multiple spectra were acquired across the TCP-coated surfaces and two representatives are shown in Figure 4.3. The Cr(VI)-O peak, centered at 854 cm⁻¹ was often detected in and around the pits on the sample aged in air while no such peak was found in the coating aged *in vacuo*. For the latter, only the Cr(III)-O peak at 538 cm⁻¹ was observed. The 438 and 680 cm⁻¹ peaks are associated with Cu-O bonds of the Cu-rich intermetallic compound.¹²⁵⁻¹²⁷ No evidence of any Cr(VI)-O species was found when probing the coated sample aged in vacuum. This confirms the involvement of dissolved oxygen in the transient formation of Cr(VI), likely through the production of H₂O₂.

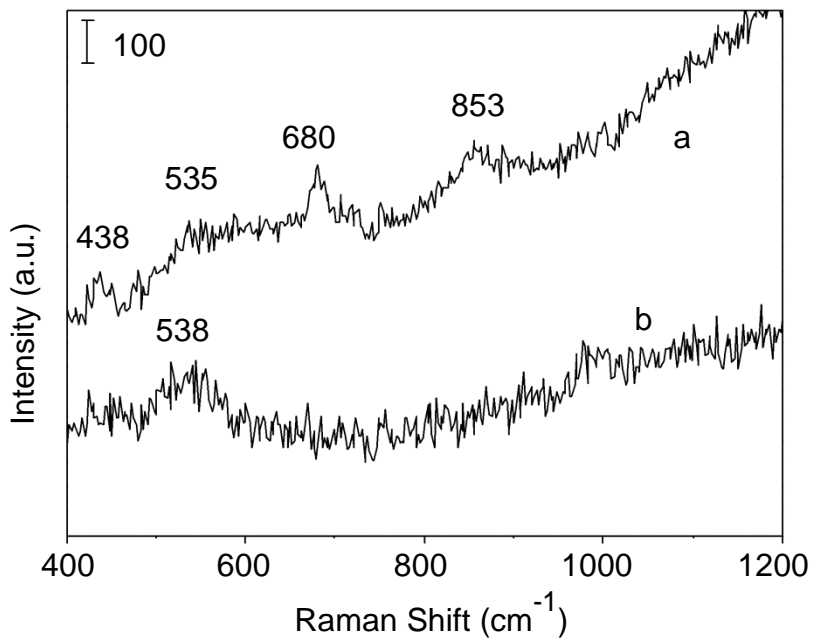


Figure 4.3 Raman spectra for the TCP-coated samples aged (a) in air and (b) in vacuum at room temperature overnight. Spectra were acquired within the pitted areas.

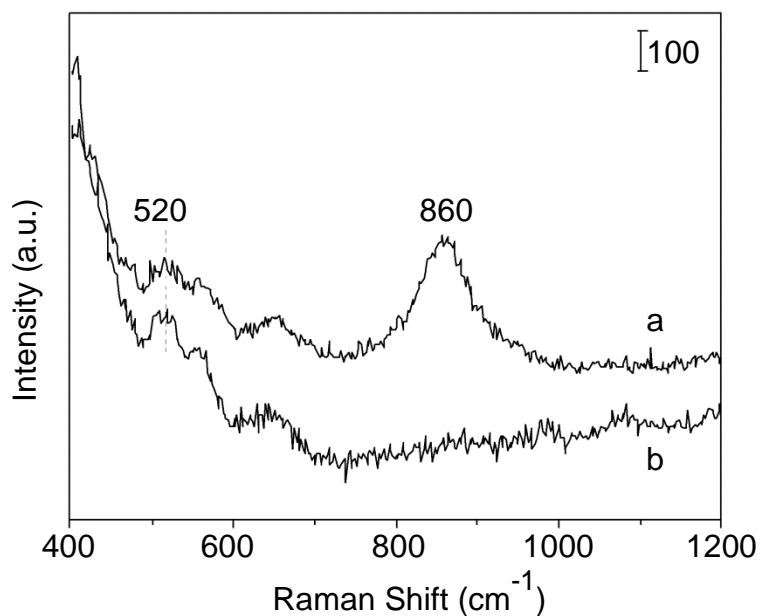


Figure 4.4 Raman spectra for the TCP-coated samples immersed in 0.5 M NaCl (a) with and (b) without oxygen for three days. Spectra were acquired on the terrace near the pits.

To further confirm the importance of dissolved O₂ in the conversion of Cr(III)-O to Cr(VI)-O, we coated another two samples and immersed them for 3 days in 0.5 M NaCl, with and without dissolved O₂. After immersion and prior to Raman analysis, the samples were rinsed for 10 s in ultrapure water. The sample immersed in the air-saturated solution was then dried in the laboratory air (room temperature) for 30 min. The sample immersed in the O₂-free solution was dried for the same period of time *in vacuo* at room temperature. Figure 4.4-a shows that the 860 cm⁻¹ Cr(VI)-O band forms during immersion in the air-saturated solution but does not in the deaerated solution. For the sample immersed in the air-saturated electrolyte, both the Cr(VI)-O peak and the Cr(III)-O peak are present, consistent with the formation of a mixed oxide. In contrast, the spectrum for the sample immersed in the deaerated electrolyte shows only the Cr(III)-O peak at 520 cm⁻¹. These results further confirm the necessary role of dissolved oxygen in the transient formation of Cr(VI) in the TCP coating

To test how effective (kinetically) H₂O₂ is at oxidizing Cr(III) to Cr(VI), we coated three alloys and immersed each in an air-saturated 0.5 M Na₂SO₄ containing a different concentrations of H₂O₂ (0.01, 0.1 and 1% (v/v)). Our hypothesis was that the Cr(VI)-O peak intensity would increase proportionally with the H₂O₂ solution concentration if this oxidant acts rapidly to oxidize Cr(III)-O. The immersion period was 1 h in each solution. A TCP-coated sample immersed in H₂O₂-free 0.5M Na₂SO₄ for the same period of time was used as the control. Before acquiring Raman spectra, the

samples were removed from the immersion solution, rinsed in tap water for 30 s and aged in the in air for 30 min. Spectra were acquired on the terrace sites near pits about 10 μm in diameter Figure 4.5 shows that the Cr(VI)-O peak at 860 cm^{-1} increases proportionally with the H_2O_2 concentration. The sample immersed in H_2O_2 -free Na_2O_4 solution has no significant Cr(VI)-O peak intensity. These results confirm the ability of H_2O_2 to rapidly oxidize Cr(III) to Cr(VI) in the coating.

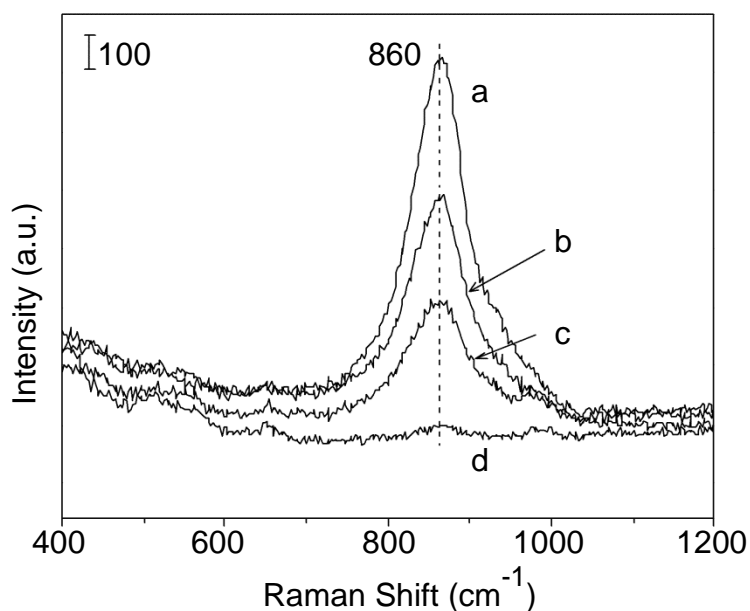


Figure 4.5 Raman spectra of the TCP-coated samples immersed in 0.5M Na_2SO_4 added with H_2O_2 by (a) 1%, (b) 0.1% and (c) 0.011% (v/v). Spectra were recorded on the terrace near the pits. (d) A spectrum recorded on the terrace of a coated sample immersed in 0.5 M non- H_2O_2 Na_2SO_4 .

4.2.3 TCP-coated AA2024 samples before immersion testing.

After coating with TCP, samples were aged overnight in air at room temperature. It is supposed that coatings are hydrated during the aging period, which aids facilitates O_2 dissolution into the coating. This is followed by reduction of at least some of the O_2 to H_2O_2 at the Cu intermetallic sites and this product then locally oxidizes Cr(III) in the coating to Cr(VI). Figure 4.6A shows a SEM micrograph of a coated AA2024 sample after overnight aging. The surface, typical of all coated samples investigated ($n > 10$), is characterized by three distinct features: (a) a large pit ($\sim 10 \mu\text{m}$ diam.), (b) relatively smooth terrace sites with no damage and (c) several elongated precipitates ($\sim 1 \mu\text{m}$) distributed over the undamaged terrace sites. Raman spectra were recorded from each of these three sites and representative ones are shown in Figure 4.6B. The TCP-coated AA2024 sample contains two types of pits. One type contains Cu-rich intermetallic compounds and the other is devoid of Cu.¹²⁸⁻¹²⁹ There is a characteristic spectrum for each. Figure 4.6B-a1 shows the spectrum acquired at a Cu-rich pit. The two sharp peaks at 434 and 680 cm^{-1} are attributed to Cu-O vibrations.¹²⁵⁻¹²⁷ The broad peak at 556 cm^{-1} is attributed to a Cr(III)-O bond from either Cr(OH)_3 or $\alpha\text{-CrOOH}$. This is evidence that the TCP coating forms on at least some of the Cu-rich intermetallic sites, consistent with our previously reported EDX results (Chapter 3). The 854 cm^{-1} peak arises from a Cr(VI)-O bond presumably produced from the oxidation of Cr(III) in the coating by H_2O_2 . Figure 4.6B-a2 is the spectrum acquired from a pit devoid of Cu. Consequently, there are no 434 or 680 cm^{-1} peaks seen. The weak 556 cm^{-1} peak is

attributed to Cr(III)-O. A spectrum recorded from a terrace site is shown in Figure 4.5B-b and contains only the Cr(III)-O peak at 520 cm^{-1} . Figure 4.6B-c shows a typical spectrum acquired at one of the elongated precipitate particles. The broad peak at 536 cm^{-1} is due to the hydrated Cr(III) oxide in the TCP coating. Both Cr(OH)_3 and $\alpha\text{-CrOOH}$ have an amorphous structure.¹³⁰⁻¹³¹ The length of Cr(III)-O bond varies as OH or H_2O is incorporated. Thus, Cr(VI) can even transiently form near the Cu-rich intermetallic phases during overnight aging. Spectra for AA2024 samples, bare and coated with the non-chrome containing Alodine® 5200, are also presented in Figs. 4.6B-d and 4.6B-e for comparison. Both are featureless within the spectral window, as expected. The take-home message is that Cr(VI) oxide species can transiently form in the TCP coating even during overnight aging. However, the Cr(VI) species are localized near Cu-rich intermetallic sites presumably due to the confined nature of the pockets of water in the hydrated coating.

Spectra for the TCP-coated samples aged in the laboratory air for 15 days were also studied (data not shown here). Spectral features similar to those shown in Figure 4.6 were found. The Cr(VI)-O peak in the $840\text{-}904\text{ cm}^{-1}$ range always accompanied the Cu-O peaks at 434 and 680 cm^{-1} . Spectra from the coating in pits devoid of Cu and on the Al terrace sites contain only the Cr(OH)_3 or $\alpha\text{-CrOOH}$ peak in the $520\text{-}580\text{ cm}^{-1}$ range.

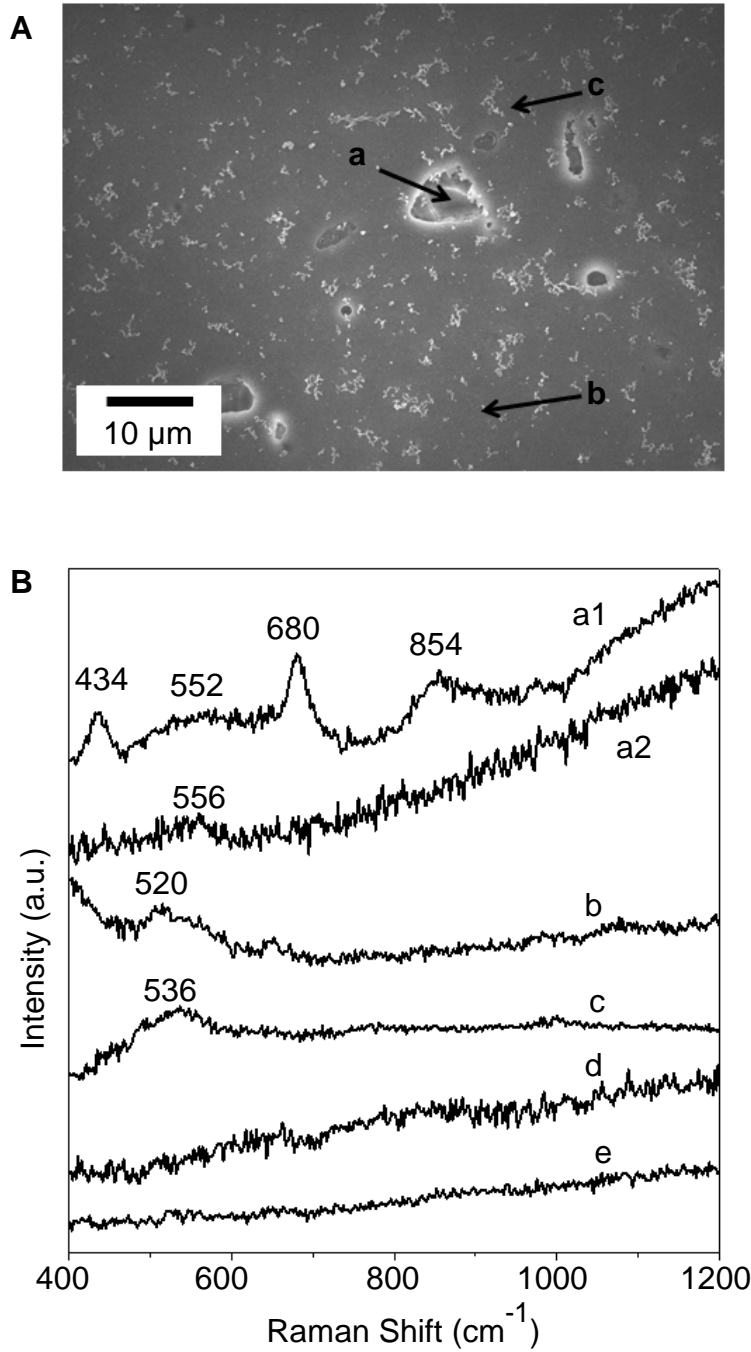


Figure 4.6 (A) SEM micrograph of the surface of a TCP-coated AA2024 sample. Three regions are identified as (a) a large pit (~10 μm diam.), (b) relatively smooth terrace sites with no damage and (c) several elongated precipitates (~1 μm) distributed over the undamaged terrace sites. (B) Raman spectra for (a1) in a pit with a spectrum that is featured with multiple peaks at 434, 552, 680 and 854 cm⁻¹, (a2) in a pit that exhibits only one peak at 556 cm⁻¹, (b) on the terrace devoid of any pits, (c) on the elongated precipitates. The spectra for (d) a non-chrome 5200-coated sample and (e) a bare sample are also shown as control.

4.2.4 Transient formation of Cr(VI) during immersion testing.

After the typical overnight aging in air at room temperature, the TCP-coated samples were then immersed in air-saturated 0.5 M NaCl solution for 30 days. Spectra were recorded at different times during the immersion period. At the time of measurement, each sample was removed from the solution, rinsed with tap water for 10 s and dried in air for 30 min. Figure 4.7 shows representative spectra acquired at a pit and on the terrace sites after 3 days. The spectrum in Figure 4.7-a has multiple peaks reflective of the formation of both Cr(OH)₃ or α-CrOOH (556 cm⁻¹) and Cr(VI)-O (847 cm⁻¹) near a Cu-rich intermetallic site (434 and 680 cm⁻¹). In contrast, in pits devoid of Cu, the spectrum has only the Cr(VI)-O peak at 860 cm⁻¹, as shown in Figure 4.7-b. Contrary to the samples aged in air, the Cr(VI)-O peak is found in most pits regardless of the presence of Cu during full solution immersion. Spectra in Figure 4.7-c and d were acquired at a terrace site and from an elongated precipitate particle (Fig. 4.6), respectively. Both exhibit both a Cr(III)-O peak at 520 cm⁻¹ and a Cr(VI)-O peak at 860 cm⁻¹, which is the suggestion of a mixed oxide. Figure 4.7-e shows a spectrum for the mixed Cr(III)/Cr(VI) oxide that contains a symmetric peak at 860 cm⁻¹. As a control, an uncoated AA2024 sample was immersed in the air-saturated 0.5M NaCl for 30 days, removed and rinsed with tap water for 10 s, and then dried under flow N₂ at room temperature. Figure 4.7-f is a spectrum for this sample. No peaks are present, as expected. These results indicate that under full immersion, Cr(VI)-O and mixed Cr(III)/Cr(VI) oxides can form in areas outside of the immediate Cu-rich intermetallic

region. The bulk solution allows H_2O_2 produced locally at the Cu-rich intermetallic sites to diffuse away from these sites and oxidize Cr(III) in the coating at locations remote of the intermetallic.

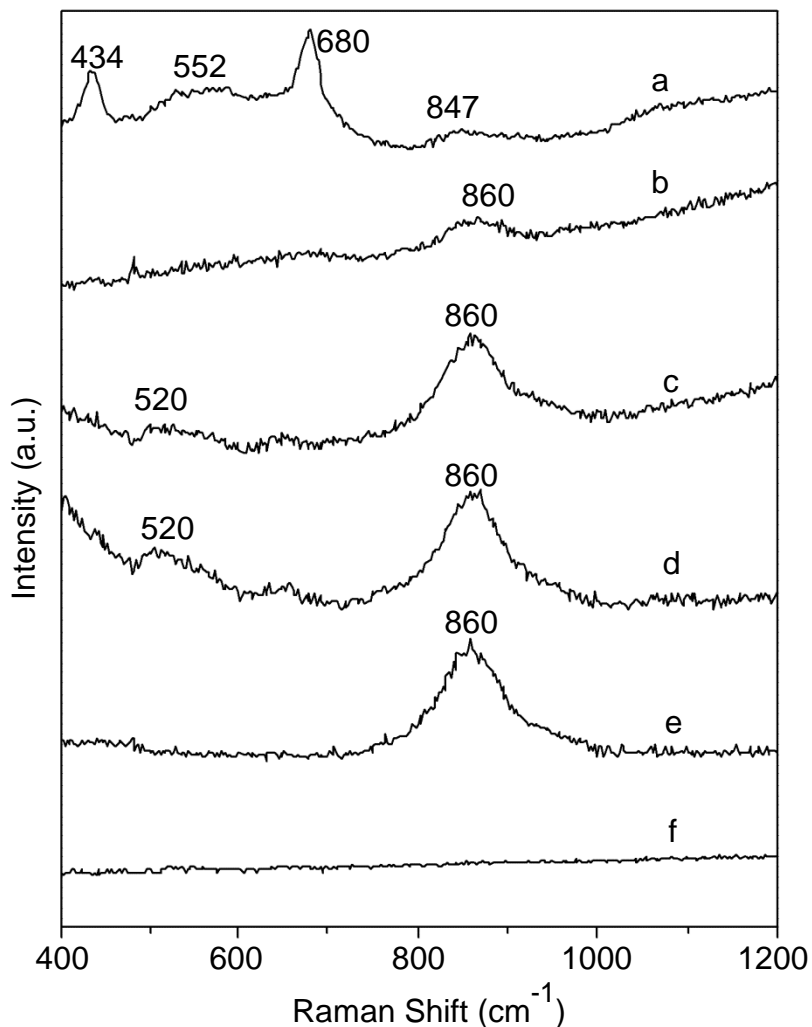


Figure 4.7 Raman spectra for the TCP-coated AA2024 immersed in naturally aerated 0.5 M NaCl for 3 days. They were acquired (a) in a pit that contains a Cr-rich intermetallic particle, (b) in a pit devoid of Cu and (c) at a terrace site, and (d) on an elongated precipitate. Relevant reference spectra of (e) a Cr(III)/Cr(VI) mixed oxide and (f) a bare sample are shown as control.

Figure 4.8A shows the Cr(VI)-O 860 cm^{-1} peak area for TCP-coated AA2024 as a function of the immersion time in (a) air-saturated 0.5 M Na_2SO_4 , (b) air-saturated 0.5 M NaCl and (c) a 0.5 M NaCl solution that was re-oxygenated daily. Prior to recording the spectra, a sample was removed from the immersion solution, rinsed with tap water for 10 s and then aged in air for 30 min. Each datum represents the average and standard deviation of spectral recordings from 5 different locations on a sample. The spectra were recorded at terrace sites near to but outside of pits. Two trends are seen for all the samples: (i) the Cr(VI)-O peak area increases rapidly within the first five days of immersion before reaching a relatively constant level for the remainder period, and (ii) the peak intensity is larger for the sample immersed in 0.5 M NaCl than the sample in 0.5M Na_2SO_4 . Additionally, the sample immersed in a 0.5 M NaCl solution that was refreshed with dissolved O_2 daily exhibits the largest Cr(VI) peak area (*i.e.*, greatest coating content) over the immersion period. The stability of the peak area after the first five days suggests that the transiently formed Cr(VI) content in the coating is stable at least under these immersion test conditions.

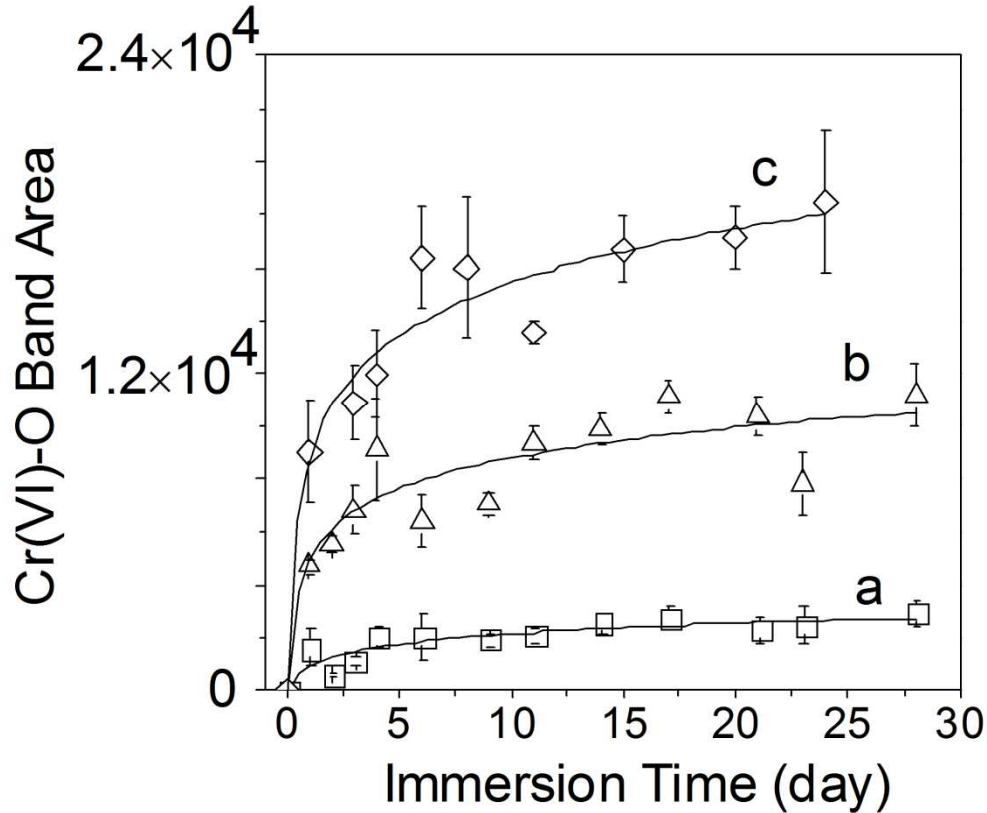


Figure 4.8 Plots of the intensity of the Cr(VI) peak as a function of immersion time in air-saturated (a) 0.5 M Na₂SO₄, (b) 0.5 M NaCl and (c) daily-refreshed 0.5 M NaCl. Spectra were recorded on the terrace near the pits. The trend lines are drawn in solid.

4.2.5 Corrosion protection linked with the transient formation of Cr(VI).

Figure 4.9 shows how the Cr(VI)-O peak area (860 cm^{-1}) in the TCP-coated samples correlates with the pitting of samples immersed in the air-saturated 0.5M NaCl for 15 days. Raman spectra were recorded at terrace sites between pits. The pit density for the uncoated samples increased in a near linear fashion with immersion time from $\sim 1 \times 10^5$ to 2.5×10^5 pits/cm². The polished and cleaned (degreased and deoxidized) sample has some surface damage and pitting to begin with. The Smut-Go (deoxidizing solution) is rich in F⁻ and, therefore, is aggressive to the alloy surface. In contrast, the pit

density on the coated samples remained relatively constant at $\sim 1 \times 10^5$ pits/cm². The Cr(VI)-O peak area (860 cm⁻¹) increased with time but the pit density remained relatively constant. The results suggest there is a correlation between the formation of Cr(VI)-O species and pitting resistance.

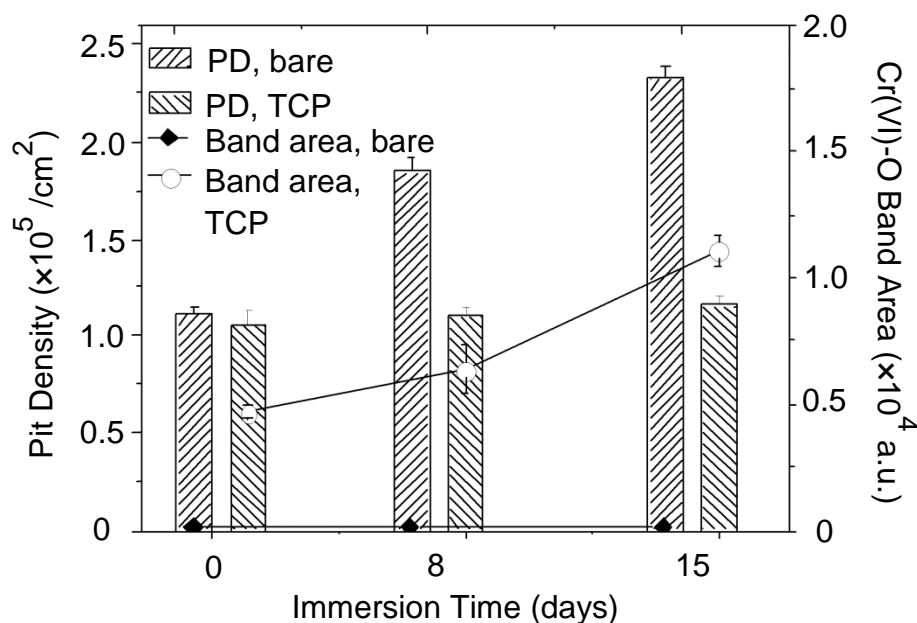


Figure 4.9 Profiles of pit density and band areas of Cr(VI)-O vs. immersion time on the TCP-coated AA2024 samples immersed in the air-saturated 0.5 M NaCl for 15 days.

A question to consider though is, does the transiently formed Cr(VI) species actively protect the surface? This was probed by scratch testing a TCP-coated sample. Figure 4.10A shows an optical micrograph of a TCP-coated region of the AA2024 surface adjacent to an uncoated area. The uncoated region was produced by scratch removal of the TCP coating with a sharp blade. The sample was then immersed in air-saturated 0.5 M NaCl + 0.01% (v/v) H₂O₂ for 24 h. Due to absence of the coating, the

uncoated area corroded during immersion and a resulting circular pit (region c) with a ~ 20 μm diameter is seen (Fig. 4.10A-b). Spectra from the three different spots were recorded and are presented in Fig. 4.10B. As seen in Fig. 4.10B, the spectrum from the scratched area prior to full immersion is featureless with no Cr(III)-O or Cr(VI)-O peaks. In the coated area (region b), a strong 861 cm^{-1} peak is evident and attributed to the formation of Cr(VI) by H_2O_2 (Fig. 4.10B-b). In or near the circular pit (region c), the spectrum features a broad Cr(III)-O peak at 587 cm^{-1} and a Cr(VI)-O peak at 856 cm^{-1} (Fig. 4.10B-c), consistent with the formation of a mixed Cr(III)/Cr(VI) oxide. The origin of the 976 cm^{-1} peak is unknown but the literature shows this mode is present in the Raman spectrum for a CrO_3 reference compound. The Cr(III) and Cr(VI) species detected on the scratched surface are consistent with active transport of Cr(VI). Figure 4.10B-d shows the spectrum obtained at a terrace site in the scratched area between the circular pit and the coated area. It has weak intensity for Cr(III)- or Cr(VI)-O. In summary, it seems that the Cr(III) in the coating is transiently oxidized to Cr(VI) (e.g., CrO_4^{2-}) by locally produced H_2O_2 . The Cr(VI) species has some mobility and can be released into the solution. Solution CrO_4^{2-} species in the nearby solution phase can then react at corroding sites on the aluminum alloy to produce $\text{Cr}(\text{OH})_3$ or $\alpha\text{-CrOOH}$ that is reflected as a broad peak at 587 cm^{-1} .^{107, 124} The following reaction is proposed:



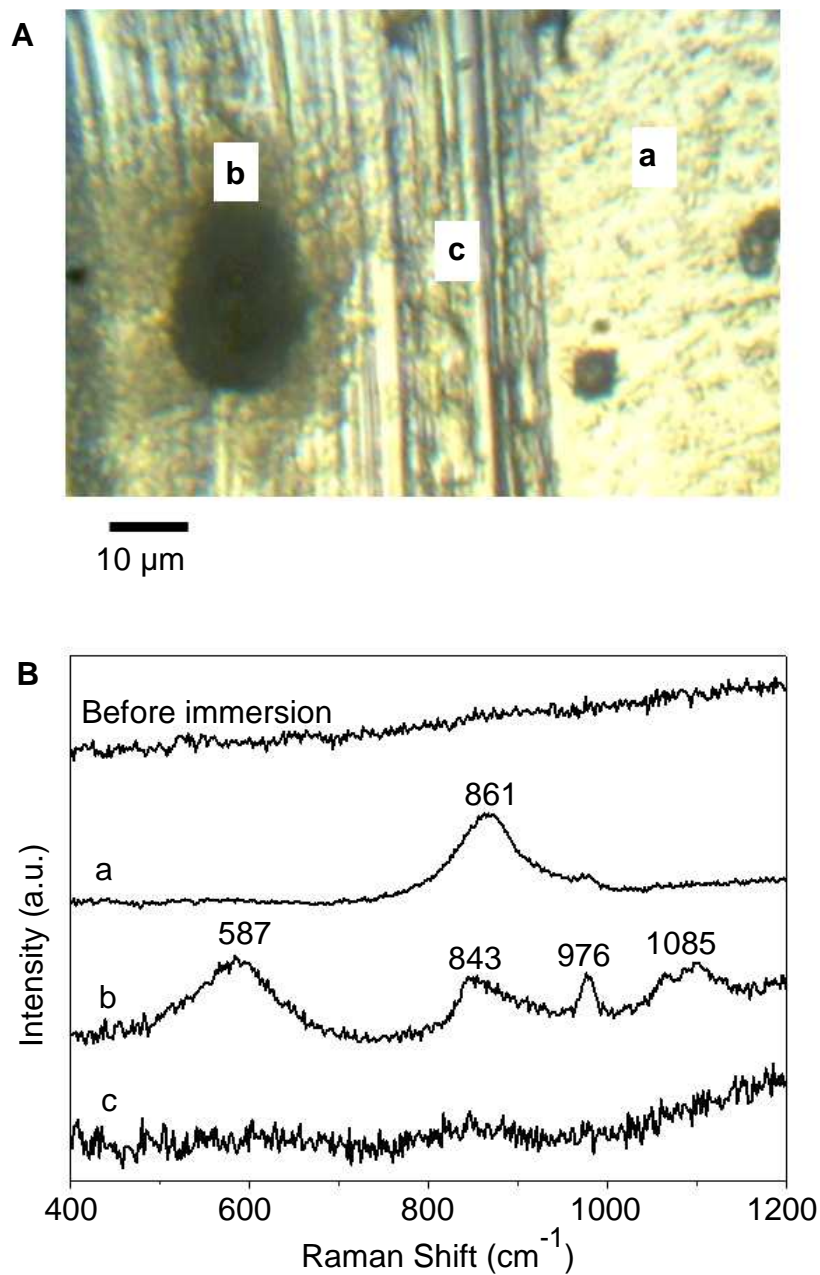


Figure 4.10 (A) Video micrograph of a scratched TCP-coated AA2024 sample after 1-day immersion in 0.5 M NaCl + 0.01% (v/v) H₂O₂ solution. Afterwards, the scratched sample was rinsed in tap water for 10 s and dried in air at room temperature for 30 min before spectra recording. (B) Raman spectrum of the scratched sample before immersion and spectra after immersion (a) on the coated area, (b) in or near the pitted area in the scratched area and (c) at the terrace site in the scratched area.

4.3 Discussion

We found that Cr(VI)-O species transiently form in TCP coatings on AA2024 during immersion testing or even aging in the humidified air. Raman spectroscopy confirmed the formation of hexavalent chrome in the TCP coating. Furthermore, we tested the hypothesis that the oxidation of Cr(III)-O species native to the coating is caused by H₂O₂ produced via the 2e⁻ reduction of dissolved O₂ (See Introduction for chemical reactions).

4.3.1 What is the mechanism by which the Cr(VI) oxide species transiently form in the TCP coating on AA2024?

While we do not have any direct evidence for the formation H₂O₂, results are presented that support the proposed model implicating this oxidant in the formation of Cr(VI). Hexavalent chrome formation requires the generation of H₂O₂ from the 2e⁻ reduction of dissolved O₂, a reaction that occurs at the Cu-rich intermetallic sites. Our experiments showed that if there is no dissolved O₂ (either aging the coated samples overnight *in vacuo* or immersion in deoxygenated solution), then there is little or no Cr(VI)-O modes detected by Raman, even around Cu-rich intermetallics. In contrast, significant Cr(VI)-O Raman intensity was detected on samples immersed in oxygenated solution or aged in the humidified laboratory air. The H₂O₂ produced then diffuses to nearby sites in the coating where Cr(III) can be oxidized to Cr(VI). Evidence was presented showing that H₂O₂ can rapidly oxidize Cr(III) in the coating to Cr(VI). When the coated samples were aged in air, the formation of Cr(VI) was localized around the

Cu-rich intermetallics. Support for this is the fact that the Raman spectra from these sites almost always contain the 860 cm^{-1} Cr(VI)-O band as well as the two Cu-O bands at 434 and 680 cm^{-1} for the Cu intermetallic. When aged in air, the coating likely contains isolated pockets of water with some of these pockets being located around Cu-rich intermetallic particles. The isolated nature of the water limits how far from the generation site the H_2O_2 can diffuse and react. The situation is different under full immersion as a bulk water layer exists. Under these conditions, the diffusion of H_2O_2 is not confined, hence Cr(VI)-O and mixed Cr(VI) oxide species were detected by Raman spectroscopy over most areas of a coated surface, not just to regions around a Cu intermetallic compound.

It would appear that the direct oxidation of Cr(III) to Cr(VI) by dissolved O_2 is too slow kinetically to account for the observed trends in Cr(VI) formation. Several researchers reported that this oxidation reaction rate is slow.¹³² H_2O_2 is a stronger oxidant than O_2 (1.76 vs 1.23 V vs SHE). Pettine et al. studied the oxidation of Cr(III) in solutions with H_2O_2 and concluded that this reaction controls the rate of oxidation.¹³³ H_2O_2 is presumably produced from the reduction of dissolved O_2 by a two-electron process. Normally, O_2 reduction occurs by a four-electron pathway to water on Cu.¹³⁵ However, Unwin *et al.* have shown that the two-electron pathway to H_2O_2 can be favored on Cu under conditions of O_2 high flux.¹³⁶ They demonstrated this by SECM

measurements of O₂ reduction on Cu nanoparticles of varying size. We previously reported that the TCP coating on AA2024 has a biphasic structure consisting of a hydrated zirconia (ZrO₂·2H₂O) overlayer and a K₃AlF₆ interfacial layer (Chapter 3). We suppose the biphasic coating is hydrated and contains channels through which dissolved O₂ can diffuse and reach the Cu sites. In addition, we found that the Cu-rich intermetallic sites are partially coated with defects that are on the order of several nanometers. High rates of mass transport might be achieved at nanoscopic domains of partially-coated Cu intermetallics.

4.3.2 What is the chemical environment around the Cr(VI) oxide species that form?

A variety of Cr(VI) oxides and mixed oxides are formed in the coating during immersion testing or even aging in air. On the terrace sites, the Cr(III) oxide (Cr(OH)₃ or α-CrOOH) making up the elongated precipitates of the TCP coating are oxidized to Cr(VI) or mixed Cr(III)/Cr(VI) oxides. The Cr(VI) species appears to be primarily chromate, CrO₄²⁻. Near pits that contain no Cu-rich intermetallic compound, Cr(VI) or a mixed Cr(III)/Cr(VI) oxide is also produced.

In and around pits that contain a Cu-intermetallic, the chemical environment of the chromate is quite different. Nearby Al behaves as the anode and gets oxidized to Al³⁺. The O₂ reduction reaction at the Cu-rich site consumes protons and increases the local pH in the pit. This pH change drives the hydrolysis of Al³⁺ to form Al(OH)_x^{3-x}. We

suppose the Al(OH)_x^{3-x} interacts with the transiently formed Cr(VI) in or near the pits, mediated by H_2O_2 , and forms a mixed oxide of Al(III)/Cr(VI). Spanos *et al.* studied the interaction of chromate and aluminum hydroxide, and found that in the pH range of 6.1 to 7.5, an Al(III)-O-Cr(VI) covalent bond forms when Al(OH)_x^{3-x} and chromate (CrO_4^{2-}) interact.¹³⁷ However, in a lower pH range (< 6.0) the Al(OH)_x^{3-x} is protonized to form $\text{Al(OH}_2)_x^{3+}$ that electrostatically bind anionic chromate (CrO_4^{2-}).¹³⁷ The mixed oxide of Al(III)/Cr(VI) mainly exists in the pits and may function as a reservoir for the transiently formed Cr(VI). We suppose another storage site is on the terrace where a mixed oxide of Cr(III)/Cr(VI) forms. The spectrum in Fig. 4.3-c features a Cr(III)-O peak at 520 cm^{-1} and a Cr(VI)-O peak at 860 cm^{-1} . Both Cr(OH)_3 or $\alpha\text{-CrOOH}$ and chromate (CrO_4^{2-}) are expected to co-exist in the coating.

4.3.3 Does the Cr(VI) oxide species provide any active corrosion protection?

The soluble chromate (CrO_4^{2-}) is expected to be more mobile during solution immersion than the relatively insoluble Cr(OH)_3 or $\alpha\text{-CrOOH}$ at neutral pH. The active protection provided by the chromate (CrO_4^{2-}) in the chromate conversion coatings (CCCs) has been discussed by Frankel *et al.*¹⁰⁸ To elucidate the mechanism of action, they performed tests in an artificial scratch cell in which a bare sample and a CCC-coated sample are connected by a thin layer of electrolyte solution (1.8 mm gap). The CrO_4^{2-} released from CCC populates the solution phase and can then react at

corroding metal sites several millimeters away. Similar to CCCs but with a much lower concentration of Cr(VI), the transiently formed CrO_4^{2-} also appears to be released into the solution phase.¹⁰⁸ After the sample was immersed in a NaCl + H_2O_2 solution, the Cr(VI)-O species were detected in the coating (Fig. 4.9B-a) due to the oxidation of Cr(III) to the Cr(VI) species by H_2O_2 . Cr(VI)-O Raman bands were detected on the uncoated samples consistent with some active corrosion protection. We suppose, similar to CCCs, the stored chromate (CrO_4^{2-}) can be released into the solution phase. It can diffuse to and react at corroding sites where it gets reduced to passivating $\text{Cr}(\text{OH})_3$ or $\alpha\text{-CrOOH}$. Future studies will focus on developing a greater understanding of how chromate released from the TCP coating can actively protect aluminum alloys from corrosion.

4.4 Conclusion

Raman spectroscopy was employed to study the transient formation of Cr(VI) in a TCP coating on AA2024-T3. The Cr(VI) formation occurs when the coated alloy is immersed in naturally aerated electrolyte solutions or even during exposure to humid air (aging). The formation involves two steps (Fig. 4.11). Oxygen diffuses through the hydrated channels to the Cu-rich intermetallic sites where it gets reduced to H_2O_2 . The H_2O_2 is a strong oxidant and diffuses to nearby sites to oxidize native Cr(III) in the coating to Cr(VI). In samples aged in the laboratory air, the Cr(VI) formation is localized to intermetallic areas where the H_2O_2 is formed. When fully immersed, the locally

produced H_2O_2 can diffuse to sites remote from the pits and oxidize the Cr(III) . The Cr(VI) exists mainly in the form of chromate (CrO_4^{2-}). It combines Al^{3+} or Al(OH)_x to form a mixed oxide of Al(III)/Cr(VI) in the pits. Some chromate (CrO_4^{2-}) leaks into the solution, diffuses to the terrace and binds Cr(III) to form a Cr(III)/Cr(VI) mixed oxide. The covalent, polymeric Cr(III)/Cr(VI) mixed oxide accounts for the chemical stability of the TCP coating. Although it is still not clear if the TCP coating provides an active corrosion protection, but the leaking of chromate might occur during the immersion in solutions. While there is clear transient formation of Cr(VI) in the TCP conversion coating, it is unknown if there would be formation of this species when the conversion coating is used in combination with a primer and topcoat (e.g., paint). Future work will address this issue.

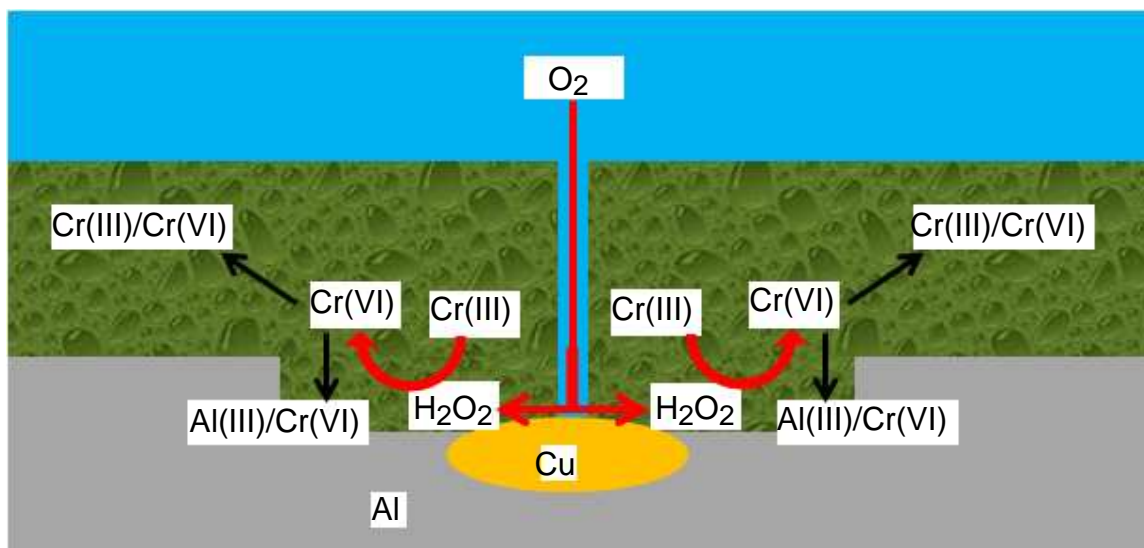


Figure 4.11 Schematic illustration of the mechanism for the transient formation of Cr(VI) in the TCP coating during immersion in the air-saturated solution.

CHAPTER 5. THE FORMATION, STRUCTURE AND BASIC ELECTROCHEMICAL PROPERTIES OF TCP COATINGS ON AA6061-T6 AND AA7075-T6

5.1 Introduction

AA6061-T6 and AA7075-T3 are high strength aluminum alloys that are widely used in the aerospace industry. Their desirable mechanical properties result from the combination of alloy addition and heat treatment. The regions around the Cu- and Fe-rich intermetallic compounds are particularly prone to localized pitting corrosion. For example, AA6061 contains mainly Fe-Si intermetallics, while AA7075 has several intermetallic compounds including Al-Cu, Al-Fe, Al-Cu-Fe, and Al-Cu-Fe-Mg-Si, *et al.*¹³⁸⁻¹⁴⁰ These intermetallic phases commonly exhibit distinct cathodic activity, as compared the surrounding Al matrix, and this renders the local Al susceptible to corrosion.¹⁴⁰⁻¹⁴² For example, pitting corrosion generally begins near a noble intermetallic phase, which acts as a cathodic site for the reduction reaction (*e.g.* O₂ reduction), while the local Al functions as an anode with the metal being oxidized to Al³⁺. In the early stage of corrosion, the nearby Al matrix is attacked and circumferential pits appear peripheral to the intermetallics.¹⁴³ Intermetallic dealloying can also occur and this can induce secondary corrosion where the dissolved Cu redeposits on the surface.¹⁴³⁻¹⁴⁴

The Trivalent Chromium Process (TCP) coating (immersion), one of the leading replacement alternatives for the Cr(VI)-containing chromate conversion coatings, has been studied on AA2024-T3 as reported in the previous chapters. In Chapter 3, it was

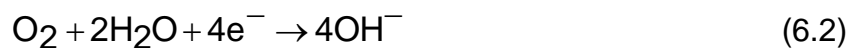
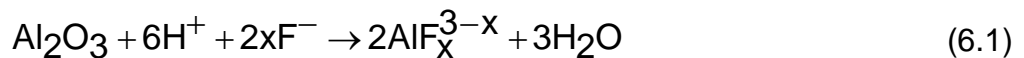
shown that the formation of the TCP coating is initiated by an interfacial pH increase. It drives hydrolysis of hexafluorozirconate in the bath to a hydrated zirconia layer that precipitates on top of a K_3AlF_6 interfacial layer on the Al matrix. The biphasic coating is on the order of 100 nm thick. The TCP coating forms across the entire sample surface and is often enriched around the Cu-rich intermetallic sites. In Chapter 4, it was shown that transient formation of Cr(VI) occurs in the TCP coating on AA2024 during full immersion in corrosive electrolyte solutions. The mobile Cr(VI) species (e.g., CrO_4^{2-}) provide some active protection. In Chapter 3, the basic electrochemical properties of TCP coatings on AA2024 were discussed. The results revealed that the TCP coating provides both cathodic and anodic protection by serving as a barrier layer inhibiting contact of dissolved oxygen and solution species with the underlying metal surface. Little information exists for TCP coatings on other high strength aluminum alloys. We addressed this knowledge gap by the work, and present data on the formation, structure and electrochemical properties of TCP coatings formed on AA6061-T6 and AA7075-T6. Several key questions were addressed in this chapter:

- (1) What is formation mechanism and chemical structure of the TCP coating on AA6061 and AA7075?
- (2) Is there any evidence for transient formation of Cr(VI) species under full immersion testing and if so at what sites?
- (3) Does the TCP coating provide any corrosion protection to AA6061 and AA7075 in mild and aggressive aqueous electrolyte solutions?

5.2 Results

5.2.1 Formation of the TCP coating

The open circuit potentials (OCP) of AA6061 and AA7075 alloy samples were recorded during immersion formation of the TCP coating, and are presented in Figure 5.1. The profiles for both alloys are similar to each other and to the typical profile for AA2024 (Chapter 3). The OCP for both alloys shifts cathodically to between -1.2 and -1.3 V vs. Ag/AgCl soon after immersion. Both profiles pass through a minimum before stabilizing at a slightly less negative potential. The cathodic shift of the alloy potential occurs because of dissolution of the passivating oxide by the H^+ and F^- ions in the bath. This dissolution activates the metal surface by exposing the underlying aluminum. With the metal unpassivated, corrosion of the aluminum occurs. The metal potential shifts cathodic because of the increased rates of counterbalancing cathodic reactions: dissolved oxygen reduction and hydrogen evolution. Both reactions consume protons and increase in the interfacial pH. The following two reactions represent the oxide dissolution and oxygen reduction reactions that likely occur:



The increased interfacial pH causes the hydrolysis of hexafluorozirconate and Cr(III) in the coating bath to form a precipitating layer of $ZrO_2 \cdot 2H_2O$ and $Cr(OH)_3$. The balance between the surface processes and the precipitation of hydrated zirconia seems to stabilize after 2-6 min, with the response being longer for AA6061. The longer period

before OCP stabilization of AA6061 (ca. 6 min) is probably due to a more homogeneous and thicker passivating oxide layer than that exists on AA7075.

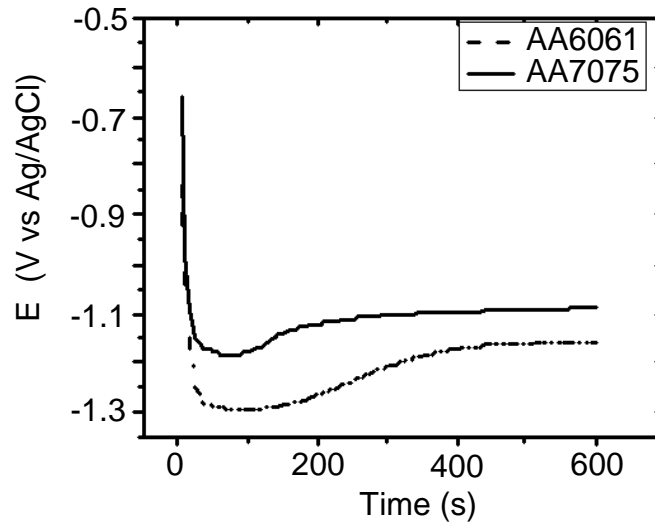


Figure 5.1 E_{corr} vs. time profiles recorded during the formation of the TCP coating on AA6061 and AA7075 at room temperature (20-25 °C). Full strength (100%) Alodine® 5900 RTU solution was used with the sample under full immersion.

5.2.2 Structure of the TCP coating

Figure 5.2 presents the Auger electron spectroscopy depth profiles through the TCP coating on each alloy. The depth profiles into the TCP-coated AA6061 and AA7075 are shown in Fig. 5.2A and C, respectively. The profiles are shown on an enlarged scale in Fig. 5.2B (AA6061) and D (AA7075). For both coated alloys, the characteristic coating elements, e.g., Zr, Cr, O, and K (elevated in the interfacial region), are detected. As was the case for AA2024, the TCP coating on these two alloys has an apparent biphasic structure (Chapter 3). For the first ca. 30 nm into the coating, Zr tracks the O signal with an atomic concentration ratio (O/Zr) of about 2:1. This is consistent with the empirical formula of dehydrated zirconia, ZrO_2 . In the interfacial

region between the zirconia and the alloy, the K and Al signals increase, consistent with a K_3AlF_6 interfacial layer. This interfacial region appears to be between 25-75 nm. The overall coating thickness is greater for AA6061 than AA7075. As Fig. 5.2B and D show, the Cr content appears to be enriched for the first 30-40 nm which is consistent with the ZrO_2 overlayer. The Cr signal then decreases with depth through the K^+ -rich interfacial layer. Since the Cr signal comes from the TCP coating, the decreased Cr signal intensity at ca. 100 nm into the TCP-coated AA6061 can be used as an indicator of the approximate coating thickness on AA6061 (*in vacuo*). Similarly, the coating on AA7075 appears to be about 80 nm thick. Evidence for the thickness of the coating comes from tracking the Ca signals. The Ca signal presumably results from the tap water rinse used in the coating formation. We suppose that the TCP coating both on AA6061 and AA7075, similar to the coating on AA2024 (Chapter 3), contains hydrated channels that allow Ca^{2+} to penetrate the coating. It should be noted that these measurements were made *in vacuo* and this causes the coating to shrink due to water loss. Therefore, the true (hydrated) thickness on both alloys is expected to be several tens of nanometers larger than the values estimated from these measurements.

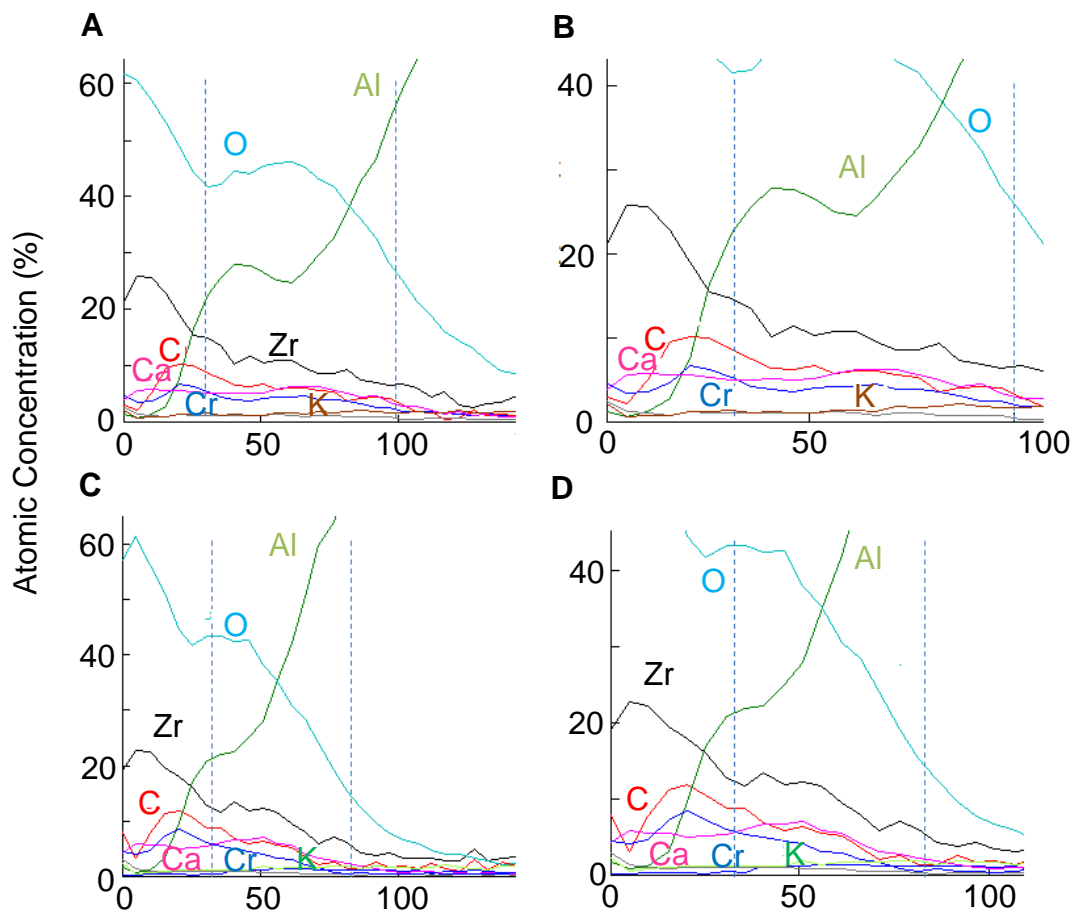


Figure 5.2 Auger depth profiles for the TCP coatings on (A) AA6061 and (C) AA7075. The elemental profiles are enlarged in (B) AA6061 and (D) AA7075. Dashed lines are approximate boundaries between the hydrated zirconia overlayer and the interfacial layer at the alloy surface.

Figure 5.3 presents (A) an SEM micrograph of a TCP-coated AA6061 sample, along with (B) energy dispersive X-ray (EDX) spectra for the coated and uncoated alloy, and (C) line profiles for several elements across a coating. The micrograph shows that the coated surface is fairly smooth with the exception of several elongated precipitate particles. The line profile in this image crosses an intermetallic compound and multiple elongated precipitate particles that are characteristic of the TCP coating (*i.e.*, likely precipitates from the coating solution). The intermetallic compound (left of image) consists of mainly Fe and Si, as evidenced by elevated elemental intensities at ca. 3 μm

(Fig. 5.3C). This intermetallic compound is about 3 μm in diameter. The signals for the characteristic elements of the TCP coating, e.g. Zr, O, Cr and F, are present. Their intensity tracks the Fe and Si intensities indicating the TCP coating forms on and around the intermetallic compound. The spectrum (Fig. 5.3B) was acquired within the red square in the micrograph, away from the intermetallic site or any elongated precipitates. The TCP-coated sample (red) exhibits significantly stronger signals of Zr, Cr, O, and F elements compared to a bare sample (black). The presence of these elements indicates that coating forms across the Al matrix in between the intermetallic compounds. Compared to the Zr and Cr signals in the line scans, the TCP coating appears to be enriched at the intermetallic site. The Zr and O signals arise from the zirconia and the Cr signal comes from Cr(III) oxide (see Raman spectroscopy results below). The F signal is attributed to FeF_x or SiF_x that forms from the attack by F^- on the Fe-rich intermetallic during immersion in the F^- -rich TCP bath.

Figure 5.4A presents (A) an SEM micrograph of a TCP-coated AA7075 sample along with (B) energy dispersive X-ray (EDX) spectra for the coated and uncoated alloy, and (C) line profiles for several elements across an intermetallic compound and the elongated precipitate particles of TCP. The coating on AA7075 consists of smooth features with fewer of the elongated precipitates than are typically present in the coating on AA6061. Two types of intermetallic compounds and surrounding features are apparent from the data. One intermetallic is a Cu-rich one, as seen by the increased Cu signal at 10 μm (Fig. 5.4C). A surrounding trench where the Al matrix has been corroded is detectable. The signal intensities for Zr, O and Cr all track the Cu signal

indicating the coating forms on the intermetallic compound. The other type of intermetallic compound that exists is a relatively smooth one that is rich with Fe. See the X-ray profile for Fe at the at 28 μm mark along the line profile. The Zr and O signal intensities are constant over this intermetallic phase suggestive of the same coating thickness. In contrast, the signal intensities for Cr and F are elevated at this phase. The spectrum (Fig. 5.4B) of the TCP-coated sample shows signals for Zr, Cr, O, and F that are attributed to the coating. This indicates that the coating forms over both the intermetallic compounds and Al matrix in between. The apparent enrichment of F might be due to reactivity of the anion with the Fe-rich intermetallic phase.

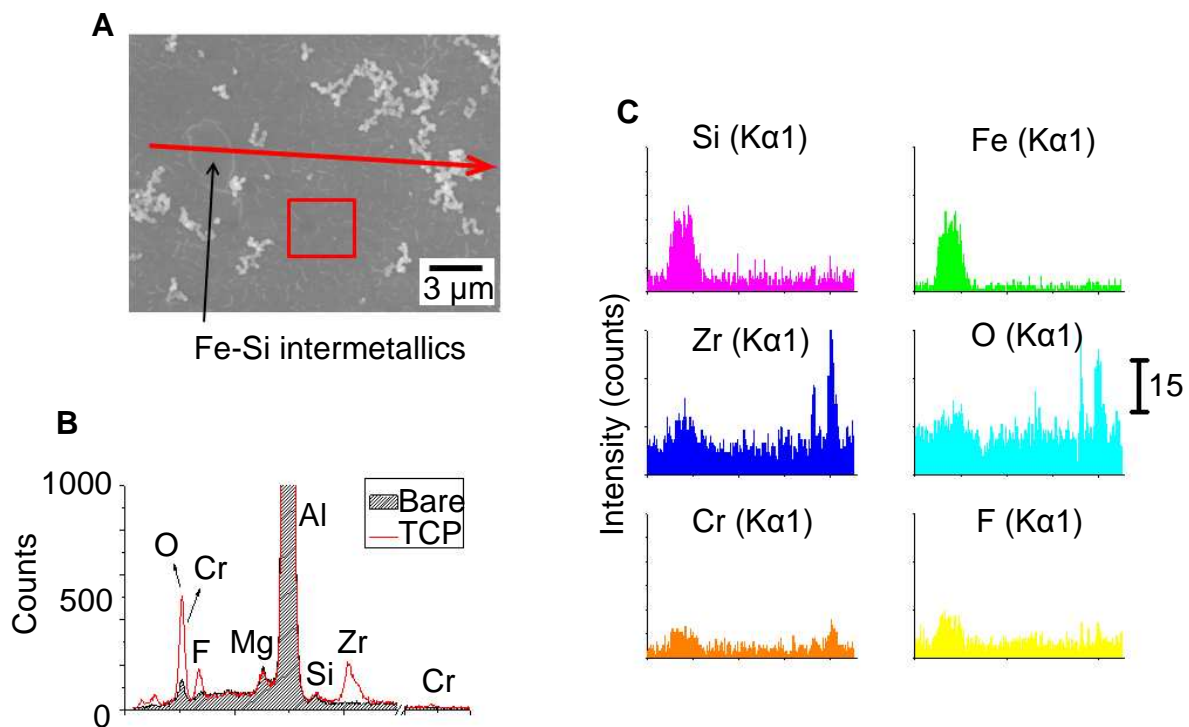


Figure 5.3 (A) An SEM image, (B) EDX spectrum at the Al matrix site, and (C) elemental line profiles across an Fe and Si-rich intermetallic particle in the TCP-coated AA6061. Profiles were recorded after overnight aging in air. White features in the image are elongated precipitates of the TCP coating.

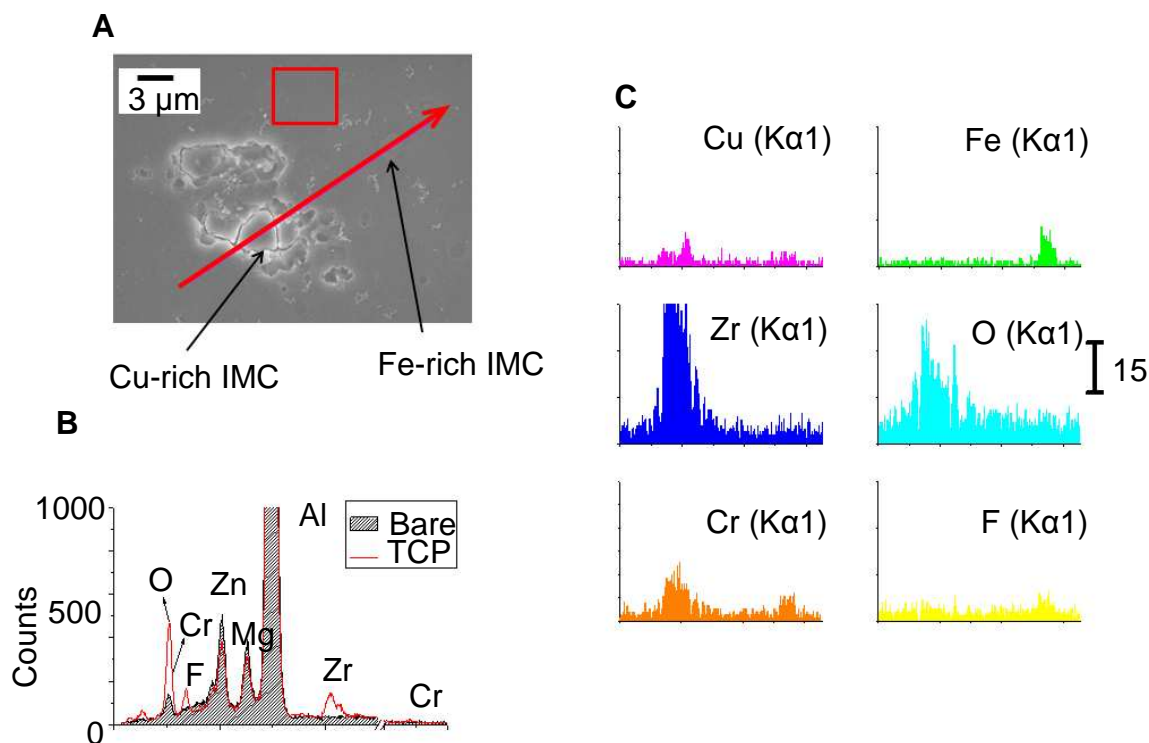
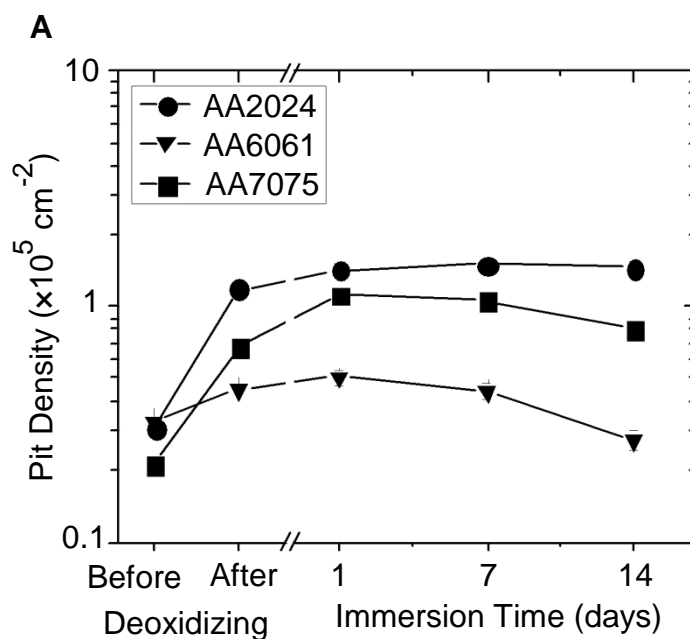


Figure 5.4 (A) An SEM image, (B) EDX spectrum on the Al matrix site, and (C) elemental line profiles across two intermetallic sites in the TCP-coated AA7075. Profiles were recorded on a film after overnight aging in air.

5.2.3 Stability of the TCP coating

We assessed the structural stability of the TCP-coated AA6061 and AA7075 alloys by measuring pit densities periodically during a 14-day full immersion in the naturally aerated 0.5M Na₂SO₄. The results are shown in Figure 5A. Three samples of each alloy type were immersed and removed for characterization at the 1-, 7- and 14-day time points. Constant pit densities were seen for all three alloys during full immersion indicating good TCP coating stability. It is noteworthy that all of the alloys have significant pit densities prior to immersion and this is because of the aggressive nature of the Turco® Smut-Go deoxidizing solution. Fig. 5.5B shows backscattered SEM micrographs of AA6061 and AA7075 samples before and after deoxidizing. A greater number of pits are seen for the samples after deoxidizing.



B

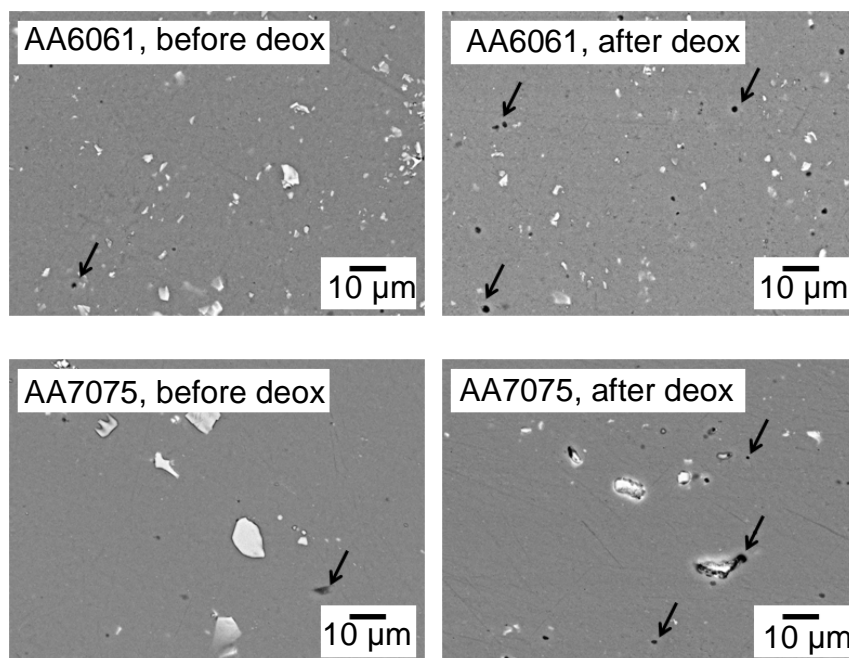


Figure 5.5 (A) Pit density vs. time profiles of the TCP-coated AA6061 and AA7075 recorded before and after the deoxidizing pretreatment step, and during full immersion testing in naturally aerated 0.5 M Na₂SO₄ for 14 days at room temperature. The pit density of the coated AA2024 is also shown here for comparison. All data represent averages and standard errors for 3 samples of each alloy. (B) Backscattered SEM images of AA6061 and AA7075 samples before and after deoxidizing. Bright features indicate the higher-atomic-weight intermetallic particles relative to Al matrix; dark features indicate pits due to attack during deoxidizing (some are pointed by arrows).

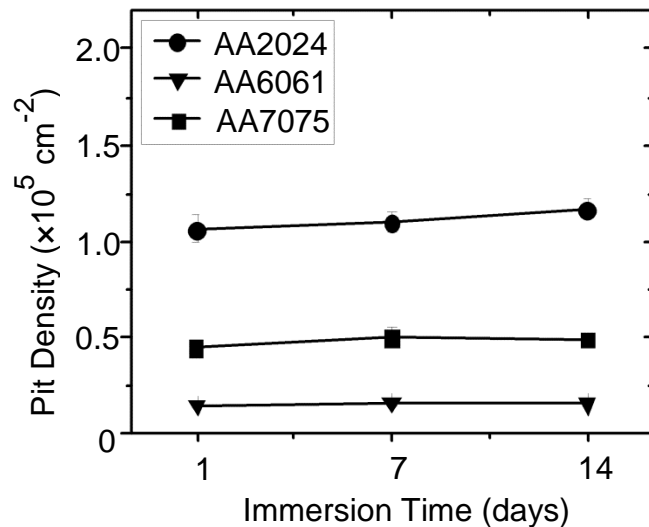


Figure 5.6 Pit density vs. time profiles recorded during full immersion testing of TCP-coated AA2024, AA6061 and AA7075 in air-saturated 0.5 M NaCl for 14 days at room temperature. Data represent averages and standard errors for 3 samples of each alloy.

5.2.4 Transient formation of Cr(VI) during immersion

In Chapter 4, it was shown that Cr(VI) can transiently form on TCP-coated AA2024 during full solution immersion. The same holds true for TCP-coated AA6061 and AA7075. Three samples of each alloy were immersed in the air-saturated 0.5 M NaCl for 15 days. Spectra were collected at five spots on each sample. Figure 7 presents typical spectra acquired at a Fe-rich intermetallic site and on the terrace site away from pit area of coated AA6061 and AA7075. The spectra acquired near an intermetallic and on the terrace away from any intermetallic on AA6061 consists of a symmetric 860 cm^{-1} peak (Fig. 5.7-a, b), which indicates the presence of a mixed Cr(III)/Cr(VI) oxide (Fig. 5.7-e). The same applies for the spectrum acquired at a terrace site on AA7075 (Fig. 5.7-d). In contrast, the spectrum acquired at a Cu-rich intermetallic

site on AA7075 consists of an asymmetric peak centered at 850 cm^{-1} (Fig. 5.7-c). Additionally, there are peaks at 437 and 678 cm^{-1} that are attributed to Cu-O bonds associated with the Cu-rich intermetallic compound.¹²⁵⁻¹²⁶ The varied Cr(VI)-O peak position is caused by the interaction of the Cr(VI)-O species with Al oxides.^{107, 121, 145} The 850 cm^{-1} Cr(VI) peak in Fig. 5.7-c is identified as the Al(III)/Cr(VI) mixed oxide at pH 7.40 (Fig. 5.7-f).

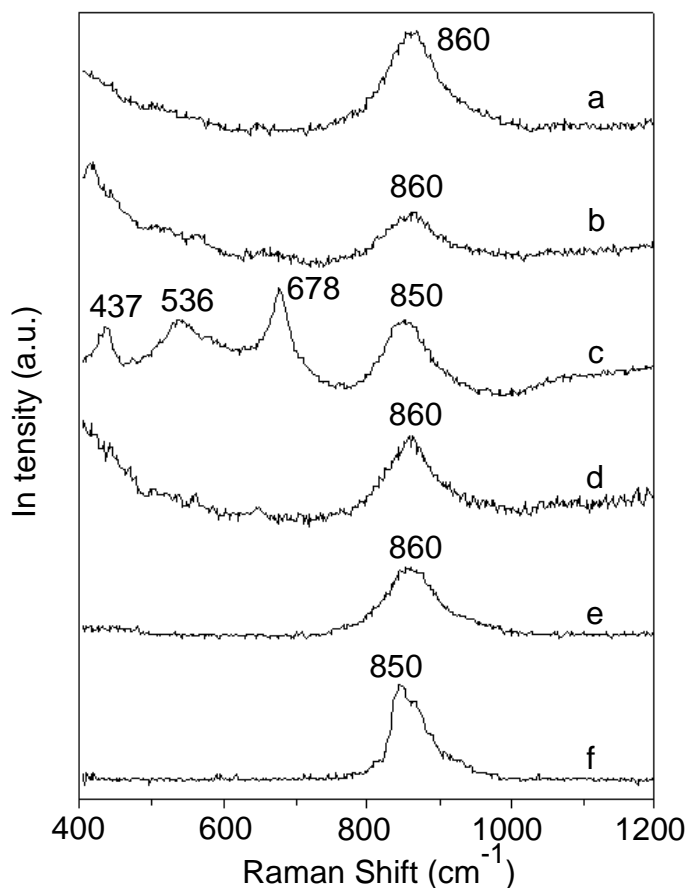


Figure 5.7 Raman spectra recorded at (a) an Fe-rich intermetallic site and (b) the terrace near but outside the pit on the TCP-coated AA6061, (c) a Cu-rich intermetallic site and (d) the terrace outside the pit on the coated AA7075, all after full immersion in naturally aerated 0.5 M NaCl for 15 days. Spectra for (e) the Cr(III)/Cr(VI) mixed oxide and (f) the Al(III)/Cr(VI) mixed oxide (pH 7.40) are also shown for comparison.

Figure 5.8 presents the 860 cm^{-1} peak area as a function of immersion time for both coated alloys. Each datum represents the average of spectral recordings from 5 different locations on each sample. Three samples for each alloy were tested. The Cr(VI)-O peak area increases rapidly within the first 5 days of immersion before reaching a relatively constant level for the remainder period. The coated AA7075 sample exhibits larger Cr(VI)-O peak areas than AA6061 during the immersion period. The stability of the peak area after the first five days reflects the chemical stability of the transiently formed Cr(VI) species on the surface.

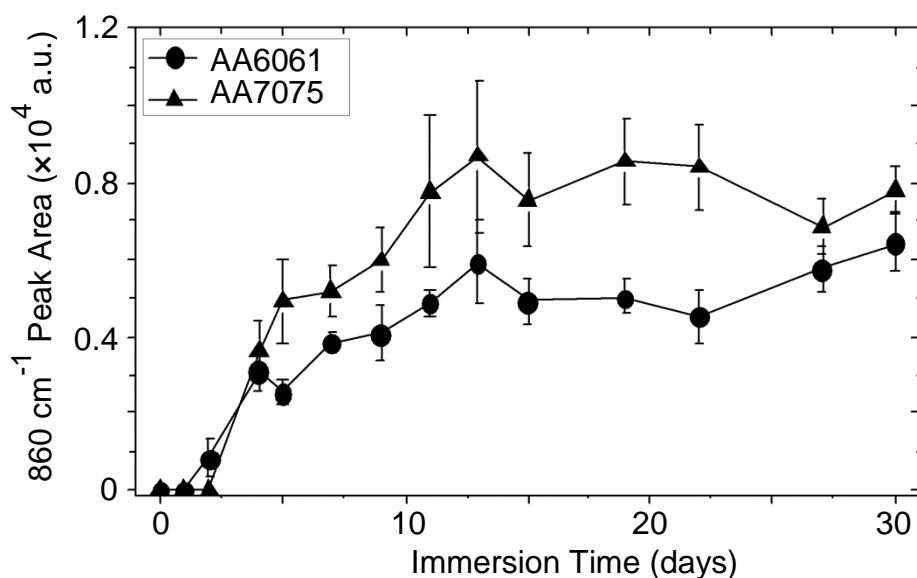


Figure 5.8 Cr(VI) peak intensity vs. time for the three TCP-coated alloys that were immersed in the naturally aerated 0.5 M NaCl for about 30 days. Spectra were recorded on the terrace near the pits. Data represent averages and standard deviations for 3 samples of each alloy.

5.2.5 Corrosion protection provided by the TCP coating.

The electrochemical properties of the TCP-coated AA6061 and AA7075 were evaluated in air-saturated 0.5 M Na_2SO_4 or 0.5 M Na_2SO_4 + 0.05 M NaCl at room

temperature. The bare samples were tested immediately after being deoxidized and dried with a stream of N₂, while the coated samples were aged overnight in the laboratory atmosphere prior to testing.

Figure 5.9A presents slow-scan potentiodynamic polarization curves for bare and TCP-coated AA6061 in air-saturated 0.5 M Na₂SO₄. The presence of the coating causes a *ca.* 500 mV cathodic shift of E_{corr} . An attenuated cathodic current by about 10x is seen around E_{corr} (e.g., at -0.9 V vs Ag/AgCl), as compared to the curve for the bare sample. Moreover, the anodic currents were also suppressed by about 5x, for example, at -0.2 V vs Ag/AgCl (*ca.* 5.58 $\mu\text{A}/\text{cm}^2$ the bare sample while 1.67 $\mu\text{A}/\text{cm}^2$ the coated sample). The cathodic shift of E_{corr} is consistent with the coating providing better cathodic than anodic inhibition. Anodizing of the Al matrix forms Al oxide films that leads to the similar current densities between the coated and bare samples as the potential approached 0.4 V vs Ag/AgCl. Figure 9B shows polarization curves for TCP-coated and bare AA7075. A much smaller difference is seen in E_{corr} after coating (also in Figure 5.10). Reduced anodic and cathodic currents are seen around E_{corr} for the TCP-coated sample. The anodic current is reduced by about 10x for the coated sample around E_{corr} . A smaller Cu oxidation peak ¹³⁵ current (+0.2 V vs Ag/AgCl) is seen for TCP-coated AA7075 than that for the bare sample. The cathodic current for the coated AA7075 sample is over 10x smaller than the current for the bare sample, e.g. at -0.65 V vs. Ag/AgCl. The cathodic current in this potential region arises from oxygen reduction and

the inhibition by TCP results primarily from the physical blockade of some of the Fe-rich (AA6061 and AA7075) and or Cu-rich (AA7075) intermetallic sites. The reduced anodic current results from passivation of the Al matrix by the TCP coating in the vicinity of the intermetallic compounds.

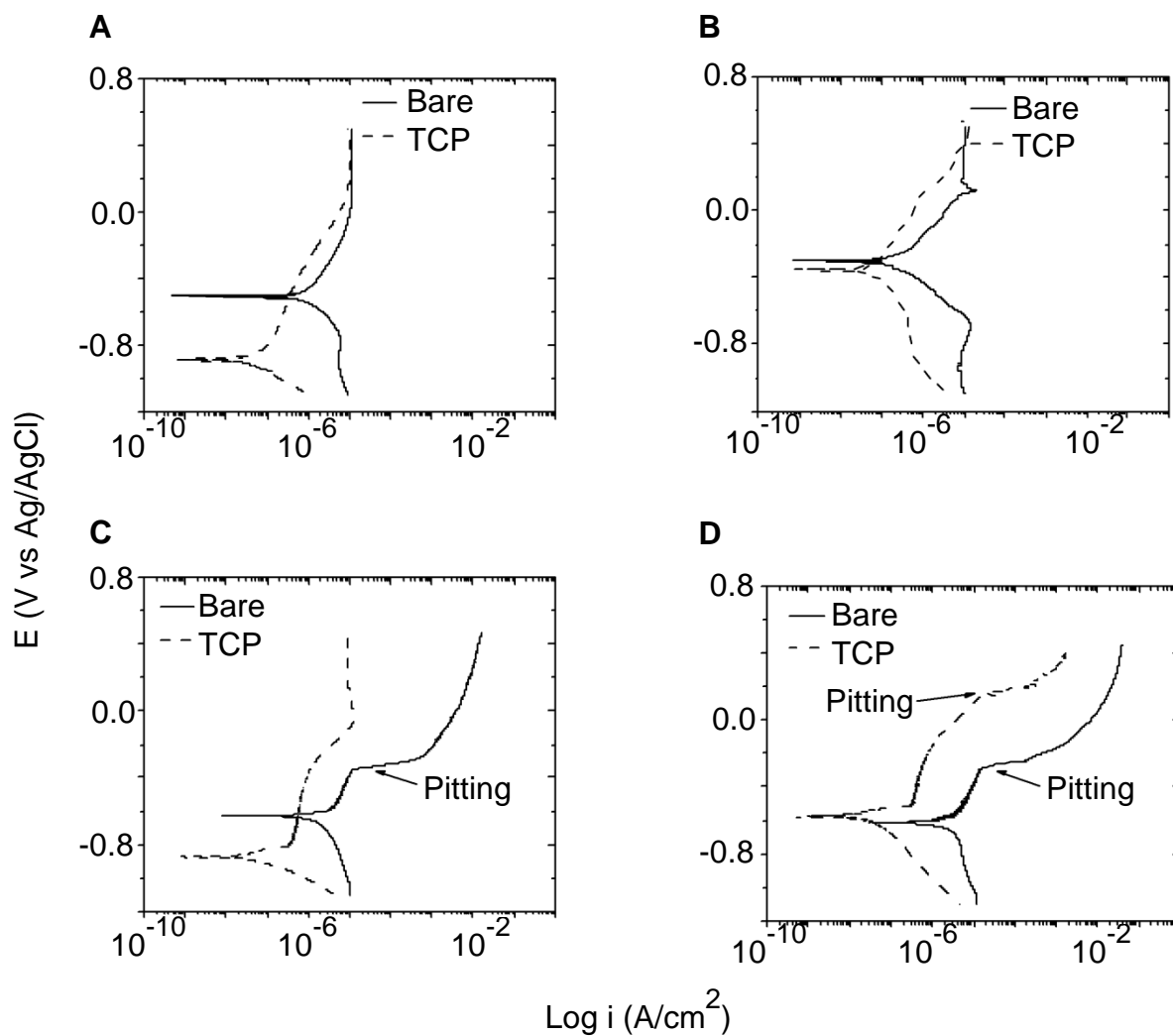


Figure 5.9 Potentiodynamic scans for bare and TCP-coated AA6061 and AA7075 recorded in two different naturally aerated electrolyte solutions: (A) AA6061 and (B) AA7075 in 0.5 M Na₂SO₄, and (C) AA6061 and (D) AA7075 in 0.5 M Na₂SO₄ + 0.05 M NaCl. Scan rate = 2 mV/s.

Polarization curves for the two alloys were also recorded in naturally aerated 0.5 M Na₂SO₄ + 0.05 M NaCl, as shown in Figure 5.9C for AA6061 and Figure 5.9D for AA7075. Similar to the Na₂SO₄ results, the cathodic and anodic currents for the coated alloys are suppressed around E_{corr} by about 10x or more. In addition, due to the presence of Cl⁻, the alloys are susceptible to pitting. The bare alloy samples have pitting potentials, E_{pit} , of -0.343 V vs Ag/AgCl for AA6061 and -0.269 V vs. Ag/AgCl for AA7075. At potentials slightly positive of E_{pit} , the current densities for both bare alloys increase rapidly by 3 orders of magnitude. Importantly, the TCP coating provides some inhibition to pitting by Cl⁻. For example, E_{pit} for TCP-coated AA7075 is positively-shifted by ~400 mV to ca. 0.171 V vs Ag/AgCl. Furthermore, TCP-coated AA6061 shows no evidence of pitting up to an anodic limit of 0.5 V vs. Ag/AgCl for all tested samples.

Figure 5.10 presents E_{corr} for the TCP-coated and bare alloy samples. These values were collected after the samples were fully immersed in the air-saturated electrolyte solutions for 30 min. The data for AA2024 in Na₂SO₄ are taken from our previous report (Chapter 3). The coated AA2024 and AA7075 samples have E_{corr} values that are not significantly different from the bare samples in both Na₂SO₄ and Na₂SO₄ + NaCl, according to an unpaired *t*-test. In contrast, E_{corr} for the TCP-coated AA6061 samples is about 400 mV negative of the value for the bare samples in Na₂SO₄. E_{corr} for the coated sample is about 200 mV negative of that for the bare alloy in

Na₂SO₄ + NaCl. In the presence of Cl⁻, the E_{corr} values are more negative for all three uncoated alloys than they are in the Cl⁻-free electrolyte solution. This is attributed to attack by Cl⁻ on the Al, which then leads to an increased anodic current. The E_{corr} shifts cathodically to counterbalance the increased anodic current.

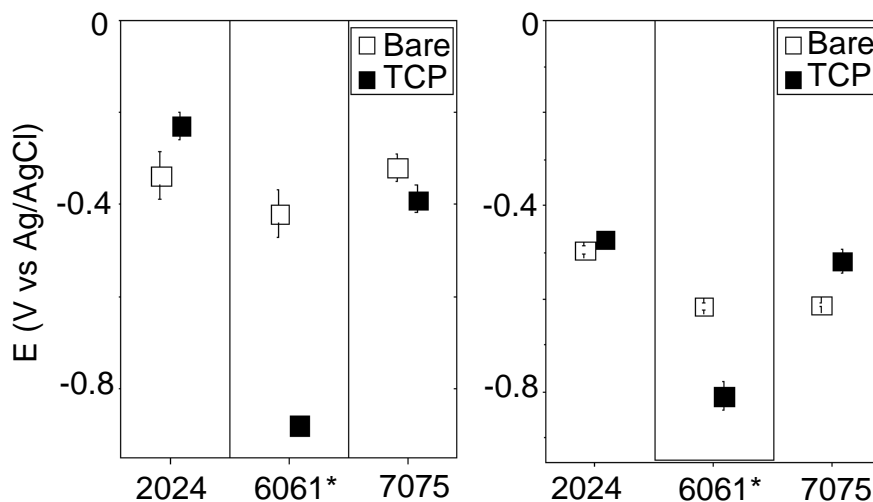


Figure 5.10 Corrosion potentials (E_{corr}) for TCP-coated AA2024, AA6061 and AA7075 in naturally aerated (A) 0.5 M Na₂SO₄ and (B) 0.5 M Na₂SO₄ + 0.05 M NaCl. E_{corr} values were also recorded for the bare alloys (degreased and deoxidized) as controls. Each datum is an average value of no less than 4 samples. The asterisks indicate statistically-significant differences at the 95% confidence level.

Figure 5.11 presents polarization resistance, R_p , data for the bare and TCP-coated alloys in both electrolyte solutions. These data were calculated from the slope of linear sweep polarization curve data recorded at ± 50 mV vs. E_{corr} . Similar R_p values were obtained from the low frequency impedance (0.01 Hz) data in Bode plots (see Figure 5.12). The TCP coating provides a nearly 100x increase in R_p for AA6061 (1.15

$\pm 0.26 \times 10^6$ vs. $2.85 \pm 0.60 \times 10^4 \Omega\text{-cm}^2$) and 7075 ($1.26 \pm 0.23 \times 10^6$ vs. $4.58 \pm 0.97 \times 10^4 \Omega\text{-cm}^2$). In contrast, R_p for the coated AA2024 samples ($6.43 \pm 0.33 \times 10^5 \Omega\text{-cm}^2$) is only 10x greater than the uncoated controls ($5.42 \pm 0.32 \times 10^4 \Omega\text{-cm}^2$). The results for AA2024 are in agreement with the previously reported 8-10x increase in R_p after coating (Chapter 3). When Cl^- is added to the electrolyte, the bare alloys exhibit decreased R_p values compared to the values in the Cl^- -free electrolyte (Na_2SO_4). The coating provides some barrier protection to both of the alloys given the R_p of $\sim 10^6 \Omega\text{-cm}^2$. However, the coating likely consists of hydrated channels and defects.

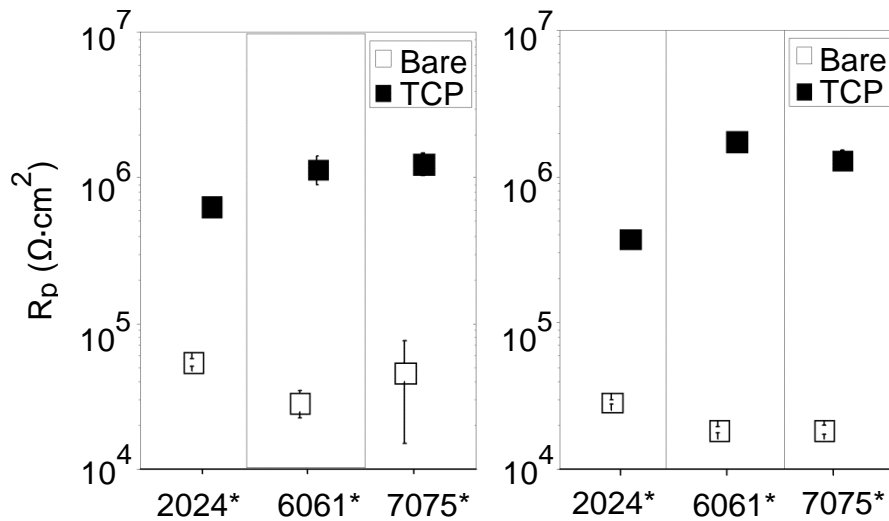


Figure 5.11 Polarization resistance (R_p) for TCP-coated AA2024, AA6061 and AA7075 in naturally aerated (A) 0.5 M Na_2SO_4 and (B) 0.5 M $\text{Na}_2\text{SO}_4 + 0.05$ M NaCl . R_p values were also recorded for the uncoated alloys (degreased and deoxidized) as controls. Each datum is an average value of no less than 4 samples. The asterisks indicate statistically- significant differences at the 95% confidence level.

Table 5.1 summarizes other electrochemical parameters measured for the bare and TCP-coated alloys in air-saturated 0.5 M Na₂SO₄ and 0.5M Na₂SO₄ + 0.05 M NaCl. Generally, the more aggressive Cl⁻, as compared to SO₄²⁻, leads to more severe attack of the uncoated alloys. For example, i_{corr} is larger by 2x in the NaCl-containing electrolyte than that in Na₂SO₄. Moreover, in the presence of Cl⁻, uncoated alloy samples undergo pitting at E_{pit} . In contrast, the TCP-coated alloys still undergo pitting but more resistant to it as evidenced by a positive shift in E_{pit} resulting in larger difference between E_{corr} and E_{pit} (so called ΔE). The TCP-coated AA2024 exhibits a 200 mV larger ΔE than the bare sample, while ΔE for the coated AA7075 is increased by about 350 mV. Amazingly, the coated AA6061 was not even pitted in the potential window from -1.0 V to 0.5 V vs Ag/AgCl. A smaller i_{corr} is seen for all three coated alloys after coating with TCP: 10x for AA2024, and 100x for both AA6061 and AA7075. These results indicate that the TCP coating provides corrosion protection to all the aluminum alloys even in the aggressive Cl⁻-containing solution, with the greatest level of protection seen for AA6061 and AA7075. Our observation that TCP provides a greater level of corrosion resistance to AA7075, as compared to AA2024, is consistent with data from Nickerson *et al.*⁶⁰ for salt-spray tests.

Table 5.1 Electrochemical parameters for the TCP-coated and bare AA2024, 6061 and 7075 alloys during full immersion in air-saturated 0.5 M Na₂SO₄ and 0.5 M Na₂SO₄ + 0.05 M NaCl. $\Delta E = E_{pit} - E_{corr}$. All statistical data are reported at a 90% confidence level. Each datum is an average measurement for 4 samples.

Alloys		AA2024		AA6061		AA7075	
		Bare	TCP	Bare	TCP	Bare	TCP
0.5 M Na ₂ SO ₄	i_{corr} ($\mu\text{A}/\text{cm}^2$)	0.11 ± 0.03	0.01 ± 0.00	0.19 ± 0.03	0.01 ± 0.00	0.11 ± 0.01	0.01 ± 0.00
	Porosity (%)	-	5.12 ± 2.78	-	0.27 ± 0.09	-	2.62 ± 1.54
0.5 M Na ₂ SO ₄ + 0.05 M NaCl	E_{pit} (V vs Ag/AgCl)	-0.34 ± 0.05	-0.12 ± 0.05	-0.27 ± 0.11	No pitting	-0.35 ± 0.08	0.07 ± 0.06
	ΔE (V)	0.16 ± 0.05	0.35 ± 0.06	0.34 ± 0.10	>1.31	0.26 ± 0.09	0.59 ± 0.08
	i_{corr} ($\mu\text{A}/\text{cm}^2$)	0.28 ± 0.09	0.01 ± 0.00	0.37 ± 0.01	0.01 ± 0.00	0.30 ± 0.01	0.01 ± 0.00
	Porosity(%)	-	7.07 ± 4.58	-	0.40 ± 0.12	-	1.45 ± 0.49

Table 5.1 also presents calculated (apparent) porosity data for the TCP-coated alloys, assessed during full immersion in the two air-saturated electrolyte solutions. The porosity is a structural parameter that is reflective of the presence of hydrated channels and defects in the coating. The calculation was described in Chapter 2, using average values of $R_{p,bare}$, $R_{p,TCP}$, E_{corr} and b_a for the bare and TCP-coated alloys. The TCP coating exhibits the trend of a decreasing porosity in the following order: AA2024 > AA7075 > AA6061 in both electrolyte solutions.

The electrochemical impedance properties were also measured for the three TCP-coated alloys in air-saturated 0.5 M Na₂SO₄. Figure 5.12 presents the typical impedance-frequency and phase shift-frequency plots for the coated alloys. Table 5.2 shows the best fit parameters of the equivalent circuit that was used to analyze the experimental data. In the impedance-frequency profile (Fig. 5.12, left), the high-frequency impedance R_{el} is primarily determined by the resistance through the electrolyte solution (0.5 M Na₂SO₄). Therefore, the values are identical for all three alloys (ca. around 110 Ω). R_{po} , normalized by the geometric area of the exposed sample, represents the electrolyte resistance in the hydrated channels and defects of the coating. The smaller R_{po} value for the TCP-coated AA2024 (525 Ω·cm²) is consistent with a larger porosity or defect density in the coating than on AA6061 (1351 Ω·cm²) and AA7075 (1184 Ω·cm²). The low-frequency impedance may be used to estimate the polarization resistance, R_p , at the coating/metal interface. These values

are consistent with the R_p values determined from linear sweep voltammetric data, as shown in Fig. 5.11. The phase shift-frequency profiles (Fig. 5.12, right) reveal two distinct time constants for all three TCP-coated alloys. The time constant at the higher frequency is usually associated with the coating ($R_{po} \times CPE_{co}$), while the low-frequency time constant is with the coating-metal interface ($R_p \times CPE_{dl}$).⁷⁶⁻⁷⁷ The highest phase angles for both time constants increase from AA2024, AA7075 to AA6061. This indicates a greater heterogeneity on AA2024, AA7075, than AA6061 (Chapter 3). Therefore, the constant phase elements (CPEs) were used to represent the inhomogeneous electrolyte/coating and coating/metal interfaces. Its impedance can be expressed as $Z=(j\omega)^{-n}Q^{-1}$, where n is a ratio that reflects the heterogeneity of the coated alloys.¹¹⁶ The TCP-coated AA6061 exhibited the highest n_{co} (0.93) and n_{dl} (1) values, which reflected a good homogeneity of the coating and coating/metal interface. AA2024 and AA7075 exhibit smaller n_{co} (0.80 for AA2024, 0.86 for AA7075) and n_{dl} (0.86 for AA2024, 0.82 for AA7075) values which are suggestive of more non-uniform coating structures on these two alloys. The differing interfacial properties between three coated alloys are attributed to their respective intermetallic composition. The effective capacitance is determined according to $C_{eff}=Q^{1/n}R^{1/n-1}$.¹¹⁶ C_{eff} for the TCP-coated AA2024 is in a good agreement with values reported by Frankel *et al.*¹⁴⁶

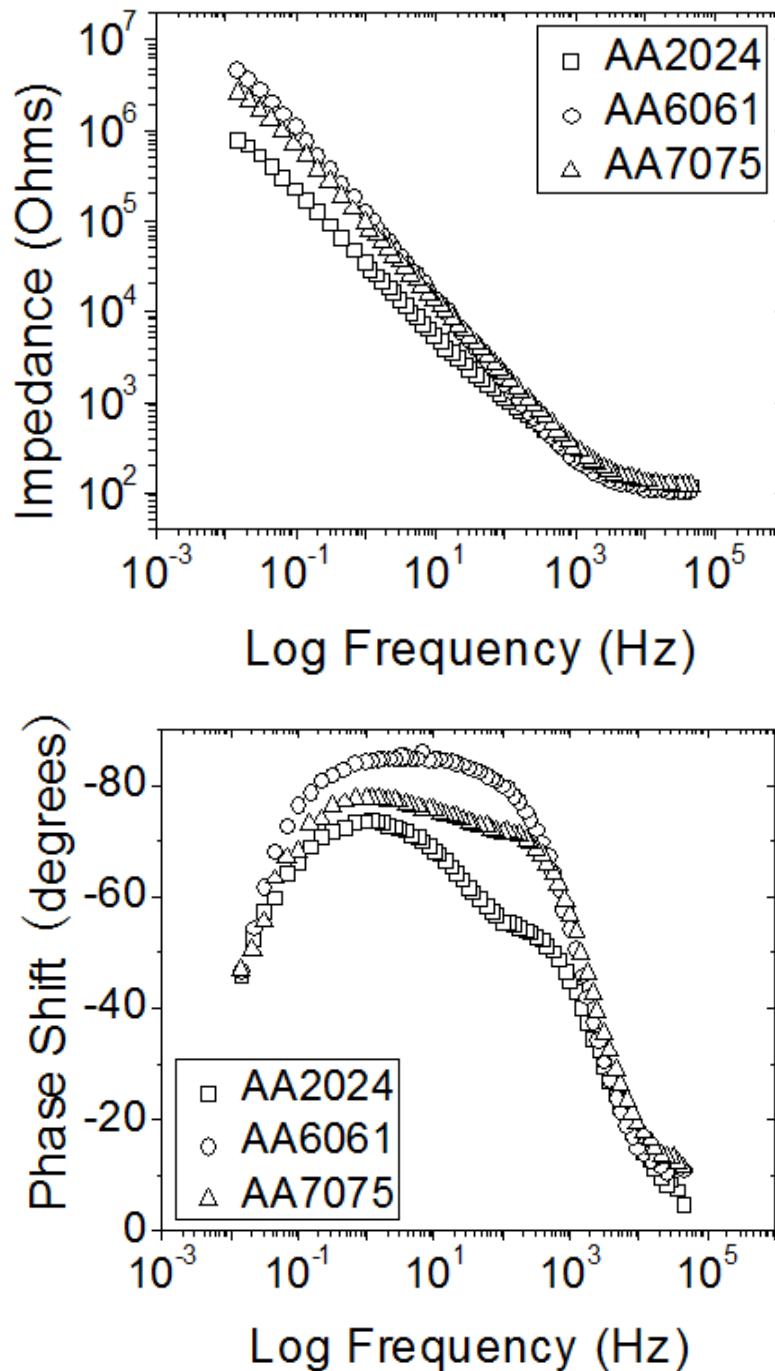


Figure 5.12 Bode plots for the TCP-coated alloys (AA2024, AA6061 and AA7075) at E_{corr} . Measurements were made in naturally aerated 0.5M Na_2SO_4 after the samples were aged in air overnight at room temperature. All samples had a geometric area of 0.2 cm^2 exposed to the electrolyte solution during measurements.

Table 5.2 Best-fit parameters from experimental EIS data for TCP-coated AA2024, AA6061 and AA7075 samples in naturally aerated 0.5 M Na₂SO₄ at room temperature. The equivalent circuit used for data analysis was presented in Chapter 2.

Alloys	R_{el} (Ω)	Q_{co} ($\times 10^{-6}$ $s^n/(\Omega \cdot cm^2)$)	n_{co}	C_{co} ($\mu F/cm^2$)	R_{po} ($\Omega \cdot cm^2$)	Q_{dl} ($\times 10^{-6}$ $s^n/(\Omega \cdot cm^2)$)	n_{dl}	R_p ($\times 10^5$ $\Omega \cdot cm^2$)
AA2024	115	16.04	0.80	2.49	525	11.51	0.86	3.30
AA6061	115	6.16	0.93	3.41	1351	0.15	1	6.46
AA7075	105	9.57	0.86	2.44	1184	1.48	0.82	9.54

5.3 Discussion

5.3.1 Formation mechanism and chemical structure

Similar to AA2024, the formation of the TCP coating occurs in two steps on both alloys. The initial step involves dissolution of the passivating Al oxide layer by H⁺ and F⁻ in the coating bath. This is evidenced by the negative OCP shift (Fig. 5.1). F⁻ in the bath facilitates the metal dissolution by forming soluble AlF₆³⁻ species. K⁺ ions are present at the interface region to compensate the excessive negative ions. However, the minimum OCP for AA6061 during the first 200-s immersion in the TCP bath is more negative and its duration at the minimum value is longer than AA7075. H⁺ and F⁻ attack the alloy surface more severely on AA6061 than AA7075, evidenced by a more negative and longer OCP of AA6061 for the first 200-s immersion in TCP bath. This leads to the thicker interfacial layer (K₃AlF₆) seen on the AA6061 surface than AA7075 (Fig. 5.2). The second step is the hydrolysis of hexafluorozirconate (ZrF₆²⁻) to form the hydrated

zirconia ($\text{ZrO}_2 \cdot 2\text{H}_2\text{O}$) overlayer, which is driven by an increased interfacial pH accompanying the hydrogen evolution and oxygen reduction reactions (ORR) on the metal surface. The zirconia (ZrO_2) layer forms over the K_3AlF_6 interfacial layer, as evidenced by the atomic concentration ratio of O/Zr (2:1) (Fig. 5.1). Since both alloy samples were immersed in the TCP bath for 10 min, no significant difference was seen in the thickness of the ZrO_2 overlayers (~30 nm) on AA6061 or AA7075. Consequently, the TCP coating appears to form a biphasic structure including the ZrO_2 overlayer and a K_3AlF_6 interfacial layer. The apparent coating thickness on AA6061 is about 100 nm and this is slightly greater than the apparent coating thickness on AA2024 (ca. 50 nm) and AA7075 (ca. 80 nm) (Fig. 5.2). In addition, the coating consists of hydrated channels or defects through which dissolved oxygen and electrolyte species can react the underlying surface. In other words, the coating forms a partially blocking layer over the surface. This is evidenced by R_p values ($10^6 \Omega \cdot \text{cm}^2$) that are less than the $10^9 \Omega \cdot \text{cm}^2$ value expected for a full barrier layer (Fig. 5.5). It should be noted that the estimated coating thickness, based on data in Fig. 5.2, is likely less than the true (hydrated) value due to shrinkage of the coating in vacuum (Chapter 3).

The TCP-coated intermetallics exhibit varied morphologies depending on their different composition. For example, a mud-like morphology is seen for the Cu-rich site (Fig. 5.4A) while a smooth morphology is seen for the Fe-rich site (Fig. 5.3A and 5.4A). Compared to Fe-rich intermetallics (e.g. Fe_2Si), Cu-rich intermetallics (e.g. Al_2Cu)

exhibit a faster cathodic ORR kinetics. This leads to a greater level of corrosion in the surrounding metal. This likely is a cause for the differences in morphology around the two intermetallic sites. EDX data revealed that the TCP coating forms on most areas of the two alloys and is enriched around the intermetallics. This was evidenced by the elevated signal intensities of Zr, O and Cr (Fig. 5.3B and 5.4B).

5.3.2 Stability of the TCP coating on AA6061 and AA7075

The TCP coating is designed to protect aluminum alloys from corrosion. To this end, a structurally and chemical stable coating is required for optimum performance. To assess the structural stability of the TCP coating on the two aluminum alloys, we measured pit densities as a function of immersion time. Figure 5.5 shows that the significant pitting occurs during the deoxidization of the metals in the F⁻-rich Alodine® Smut-Go (20% v/v) solution. The surrounding Al matrix is attacked and dissolved to such an extent that dealloying of the intermetallic compounds may occur (e.g. Al₂CuMg). The attacked surface becomes rougher and even exhibits significant pitting as compared to the untreated alloys. The pitting undoubtedly depends on the deoxidizing time, which we did not vary from the recommendation of the coating supplier. The stability of the TCP coating was assessed by measuring how much the pit density changes for the coated alloys during a 14-day full immersion in air-saturated 0.5 M Na₂SO₄ or 0.5 M NaCl. The pit density was unchanged for the coated alloys in both electrolytes (Fig. 5.5 and 5.6). In contrast, the pit density increased for both uncoated alloys, particularly in NaCl. These results indicate the TCP coating functions as a stable

barrier layer for much of the alloy surface. Presumably, dealloying of the intermetallics are also inhibited by the coating.

5.3.3 Transient formation of Cr(VI)

Transient formation of Cr(VI) oxide species was detected in the TCP coating on both AA6061 and AA7075 during full immersion in naturally aerated electrolyte solutions. We have reported how Cr(VI)-O species form transiently in the TCP coating on AA2024-T3 during immersion testing (Chapter 4). We hypothesize the formation mechanism is the same for AA6061 and AA7075 (Figure 5.13). Hydrogen peroxide (H_2O_2), generated from a two-electron oxygen reduction, locally oxidizes Cr(III)-O to Cr(VI)-O near the noble intermetallic sites (e.g., Fe-rich for AA6061, Cu-rich and Fe-rich intermetallics for AA7075). Some chromate (CrO_4^{2-}) combines the corroded Al(III) oxides to form Al(III)/Cr(VI) mixed oxides at the Cu-rich sites. But it is interesting to notice that little Al(III)/Cr(VI) signal is detected at Fe-rich sites because of no significant Al oxidation. Other CrO_4^{2-} or H_2O_2 then diffuses to Al matrix surface and forms Cr(III)/Cr(VI) mixed oxides at the terrace away from pit areas.

Variation in the concentration of Cr(VI)-O species that forms transiently in the TCP coating on AA6061 and AA7075 (Fig. 5.8) is relevant to the composition of their intermetallics. Cu-rich intermetallics have faster oxygen reduction reaction (ORR) kinetics than Fe-rich intermetallics.¹⁴⁰ AA7075 contains a higher percentage of Cu (1.2-2 wt%) than AA6061 (0.15-0.4 wt% Cu). Larger amounts of H_2O_2 are expected to be generated at intermetallic sites in AA7075 than AA6061. Moreover, some defects are

seen in the TCP coating at the intermetallic sites, much more at Cu-rich sites than Fe-rich sites that have a smooth morphology (Fig. 5.3 and 5.4). Cu-rich sites have a larger amount of dissolved O_2 that diffuse through defects to the intermetallics than Fe-rich sites. Therefore, a larger concentration of Cr(VI)-O species form transiently in the TCP coating on AA7075 than AA6061.

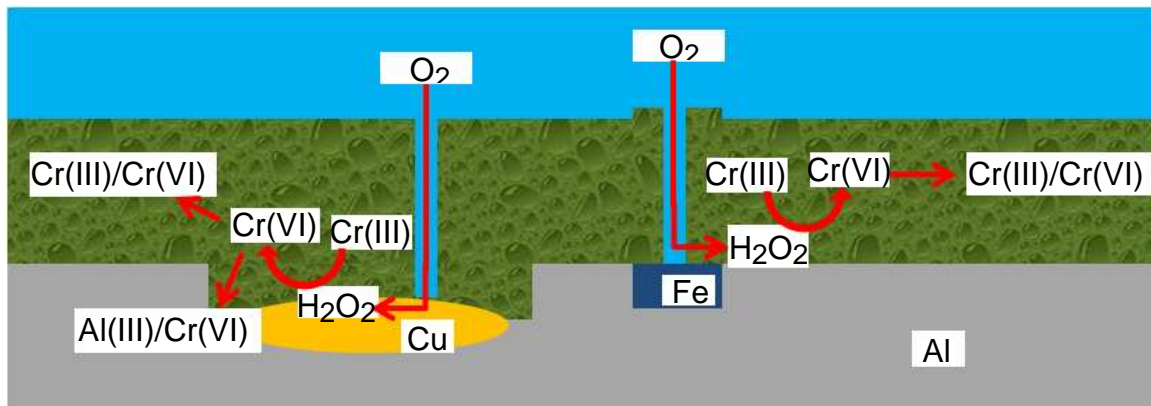


Figure 5.13 Proposed mechanism for transient formation of Cr(VI) on the TCP-coated aluminum alloys during immersion in naturally aerated electrolyte solution.

5.3.4 Corrosion protection

The TCP coating provides modest cathodic and anodic corrosion protection to both aluminum alloys by physical blocking intermetallic sites as well as sites on the Al matrix. This is evidenced by suppressed cathodic and anodic currents at potentials around E_{corr} in both the mild and aggressive electrolyte solutions (Fig. 5.2 and 5.3). The TCP coating provides corrosion protection to both AA6061 and AA7075 (Fig. 6-2C and D) even in the presence of Cl^- . It is well known that Cl^- can induce severe pitting in aluminum alloys.¹⁴⁰ The difference between E_{corr} and E_{pit} (ΔE) is a measure of the

susceptibility to localized pitting corrosion.¹²¹ The more positive E_{pit} is relative to E_{corr} , the more resistant the alloy is to pitting. In the case of the coated alloys, TCP increases ΔE by about 200 mV for AA7075, and more than 1,000 mV for AA6061. Clearly, the TCP coating provides resistance to attack by Cl^- by physically blocking the surface. More quantitative evidence for the corrosion protection is the higher R_p and correspondingly lower i_{corr} values by 10-100x for the TCP-coated alloys as compared to the bare samples (see Fig. 5.4 and Table 5.2). It should be noted, though, that the TCP coating does not provide full barrier protection as such coated metals exhibit R_p values $\geq 10^9 \Omega \cdot cm^2$. The lower R_p values for the TCP-coated metals suggest that the alloy is partially blocked by the coating that consists of hydrated channels and defects through which dissolved O_2 and ions can be transported to the underlying metal surface. However, overall, our results demonstrate that under open-circuit conditions, TCP provides corrosion protection to both AA6061 and AA7075 in both mild and aggressive electrolyte solutions.

How do the three alloys compare in terms of the corrosion resistance provided by TCP? Data available show that the TCP coating provides a higher level of corrosion resistance to AA6061 than AA7075, as evidenced by the higher R_p , smaller i_{corr} and larger ΔE ($E_{pit} - E_{corr}$). The difference in R_p between the coated and uncoated surfaces trended as follows: AA6061 > AA2024 > AA7075. Recalling our previous results for AA2024, the TCP coating provides a greater level of corrosion protection to AA6061

and AA7075 based on the larger R_p values. This variation in passivation is attributed to a combination of the different intermetallic compounds in each alloy, their physical size and the physical nature of the coating on each alloy. For example, we previously reported that the TCP coating has a rougher morphology on and around the Cu-rich sites of AA2024 and AA7075, compared to the smoother morphology on the Fe-rich sites of AA6061 and AA7075. The coating conformally forms over the alloy surface. It is likely, though, that the coating is more defective around the topographically rough Cu-rich intermetallics of AA2024 and AA7075 than the smoother Fe-rich intermetallics of AA6061. The consequence of the rough topographical features is that the Cu-rich sites are not completely coated by TCP. In other words, the coating around these intermetallics contains a greater number of defects and imperfections (Chapter 3). Hydrated channels and defects in the coating can be quantified by the porosity (P). AA2024 exhibits a 10× larger TCP coating porosity than the Fe-rich AA6061 (see Table 5.2). AA7075 has less Cu content than AA2024 and equal Fe content with AA6061. Therefore, it is not surprising that the coating on AA7075 exhibits a roughness and porosity that are between AA2024 and AA6061.

In presence of Cl^- , severe pitting corrosion generally occurs on aluminum alloys E_{pit} . The difference between E_{pit} and E_{corr} , ΔE , was used to evaluate susceptibility of the coated alloy pitting corrosion by Cl^- .¹²¹ ΔE is increased in the presence of TCP for all three alloys. However, AA6061 consists mainly of Fe-rich intermetallics (Fe-Si) and exhibits an increased ΔE for the coated samples to a larger extent compared to AA2024 that has mainly Cu-rich intermetallics. AA7075 has a vast variety of intermetallics that

include both Cu-rich and Fe-rich intermetallics. The TCP-coated AA7075 does not ensure an increased ΔE as large as AA6061, but better than AA2024. In other words, the likelihood of severe pitting corrosion in those coated alloys decreases in the order of AA2024, AA7075 and AA6061. This is attributed to variable porosity of the coatings on the three alloys. In summary, the TCP coating provides protection from pitting corrosion on all three alloys, but much better on AA6061 than on AA7075. The TCP coating can inhibit pitting corrosion in AA2024 but not as effective as AA6061 and AA7075.

5.4 Conclusion

This study focused on the formation, structure and electrochemical properties of the TCP conversion coating on AA6061 and AA7075. The formation of the TCP coating on both alloys is similar to AA2024. The formation of a hydrated zirconia layer ($ZrO_2 \cdot 2H_2O$) is driven by an increase in the interfacial pH caused by the dissolution of the passivating Al oxide layer followed by increased rates of the cathodic reactions (localized oxygen reduction reaction (ORR) and hydrogen evolution on the activated metal. These reactions consume protons and cause the interfacial pH to increase. The coating exhibited a biphasic structure consisting of a hydrated zirconia overlayer and potassium fluoroaluminate interfacial layer. The TCP coating thickness on AA6061 *in vacuo* was about 100 nm, which is greater than the thickness on both AA7075 (ca. 80 nm) and AA2024 (ca. 50 nm). The coating was structurally stable on both alloys during a 14-day full immersion test in both Na_2SO_4 or NaCl. This was evidenced by an unchanging pit density and unchanging R_p values. The transient formation of Cr(VI)-O

species suggests that in addition to passively protecting the aluminum alloy from corrosion, there might also be some active protection similar to the mechanism of chromate conversion coatings.

The coating provides corrosion protection to both alloys as evidenced by the 10-100x increase in R_p and anodic shifts of E_{pit} . The coating provides corrosion protection to both alloys during full immersion tests (room temperature) in both air-saturated Na_2SO_4 and $\text{Na}_2\text{SO}_4 + \text{NaCl}$. Evidence of corrosion protection was the 10-100x increase in R_p to the range of $\sim 10^6 \Omega \cdot \text{cm}^2$ and decrease in i_{corr} to 20-30 nA/cm^2 in both electrolyte solutions for the coated alloys as compared to the bare controls. The coating on AA6061 functions primarily as a cathodic inhibitor while on AA7075 it provides both anodic and cathodic protection. The coating provides corrosion protection even in the presence of Cl^- as no pitting was detected on AA6061 at potentials up to 0.5 V vs. Ag/AgCl and E_{pit} for AA7075 shifted positive by ~ 400 mV. Based on the electrochemical parameters, the coating's dielectric constant was calculated to be about 100. A model is presented that describes the alloy is partially blocked the coating with some hydrated channels and defects through which ions and dissolved oxygen can reach portions of the underlying alloy surface.

CHAPTER 6. STABILITY OF TCP COATINGS DURING ACCELERATED CORROSION TESTS

6.1 Introduction

In many cases, corrosion is the life-limiting factor of aluminum alloys. Corrosive failures can occur unexpectedly during the service. Therefore, corrosion tests are applied to predict the service life of the alloys. They are also used to assess the corrosion inhibition provided by various protection methods. There are three major types of corrosion tests: laboratory, field, and service testing. The service testing provides the highest fidelity results followed by fielding testing. However, the service and field tests can consume enormous time. New systems may be halfway through their lifecycles before real data on the field test would indicate any corrosion problems. The timescales involved in such tests preclude the opportunity for proper materials selection. Accelerated corrosion testing in the laboratory is increasingly more important for predicting material performance as the laboratory environment is better controlled and approaches that of the service environment. Such testing can provide meaningful test data in a reasonable time frame and supports election of the most corrosion resistance materials selection.

Acceleration can be achieved by increasing the salt solution concentration, temperature, UV intensity, pressure for stress corrosion cracking (SCC), relative humidity, and SO₂ concentration, *etc.* To account for the variation of corrosion with configuration, several standardized tests are performed for particular environments, as evidenced by the many ASTM methods. Table 1 shows several common tests under a

variety of environments and the electrochemical methods that are usually used to assess the corrosion and corrosion inhibition properties.

Table 6.1 ASTM standard methods for accelerated corrosion testing and the electrochemical methods that are commonly used to assess the corrosion and corrosion inhibition.

	ASTM Standards	Description
Immersion testing	G-31 ¹⁴⁷	Full immersion
	G-44 ¹⁴⁸	Intermittent immersion
Salt spray (fog) testing	B-117 ¹⁴⁹	Neutral salt spray
	G-85 ¹⁵⁰	Cyclic acidic salt spray
Atmospheric corrosion testing	G-50 ⁹⁶	Humid atmosphere
	G-87 ⁹⁷	Moist SO ₂ exposure
Electrochemical methods	G3 ¹⁵¹	Electrochemical properties including E_{corr} , R_p , and polarization curves
	G-106 ¹⁵²	Electrochemical impedance
	G-71 ¹⁵³	Galvanic corrosion
	D-6208 ¹⁵⁴	Repassivation potential

Accelerated testing does not have to correlate exactly to the service environment as long as the corrosion mechanism remains the same. Therefore, meticulous execution and well control of variables during the testing are necessary to obtain useful results. This goal is to accelerate the test while keeping the corrosion mechanism the same as the service corrosion mechanism. For example, ASTM B-117 is a neutral salt spray test that is accelerated by increasing the NaCl concentration from 3.5% to 20%.

The salt fog produces a severe pitting corrosion in the specimen. This test is commonly used because it is well standardized and easily controllable. However, prediction of performance in service and field environments is not well correlated with the salt spray results when used as stand-alone data. In addition, this salt fog conditions are seldom experienced by airplanes or space shuttles and, thus, the test does not simulate well the service or field environment.

Therefore, several accelerated corrosion tests have been used to better simulate the service environments for the aerospace aluminum alloys. In this chapter, for example, the full immersion test is to mimic the situation where the coated Al alloys are fully immersed in salt solutions (Na_2SO_4 , NaCl); the humid atmosphere corrosion test ($\text{RH}=100\%$) is used to simulate the highly humid environment along the coast or on aircraft carriers; the moist SO_2 atmosphere is used to model the urban environment; and the thin layer mist test is used to model the situation of moisture condensation. . The stability of the conversion coating was assessed by optical observation of corrosion, weight change of the specimen, and basic electrochemical measurements.

6.2 Results and Discussion

6.2.1 Full immersion

Figure 6.1 presents the polarization resistance, R_p , data for the TCP-coated AA2024-T3, AA6061-T6, and AA7075-T6 during full immersion in naturally aerated 0.5 M Na_2SO_4 for 14 days. The samples were taken out from the solution, rinsed with tap water for 30 s, dried in flowing N_2 , and tested electrochemically as described in Chapter

2. It can be seen in Fig. 6.1 that R_p for the TCP-coated AA2024 is in the range of 10^5 - $10^6 \Omega\cdot\text{cm}^2$ that is 10x less than the 10^6 - $10^7 \Omega\cdot\text{cm}^2$ for the coated AA6061 and AA7075. This is consistent with the conclusion in Chapter 5 that the TCP coating provides a better corrosion inhibition on AA6061 and AA7075 relative to AA2024. Moreover, the R_p values for all three alloys are relatively consistent throughout the entire immersion period, which indicates good TCP coating stability.

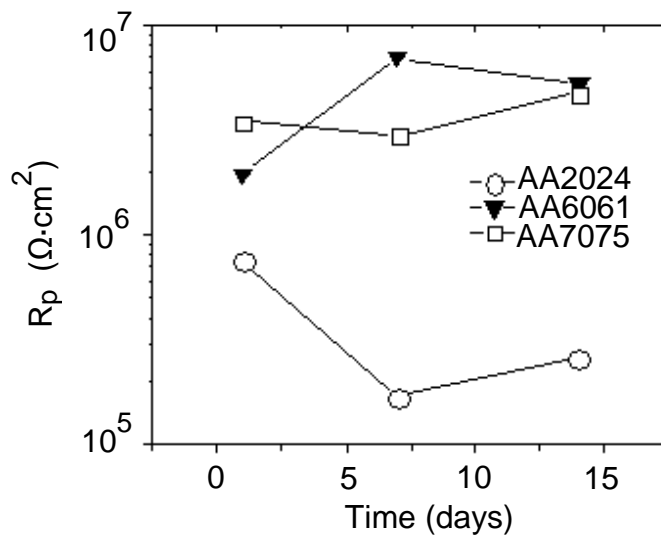
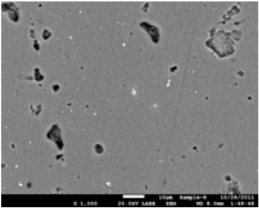
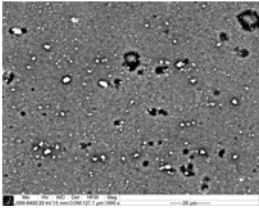
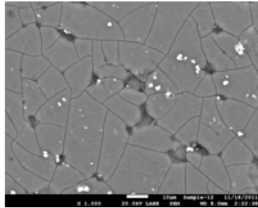
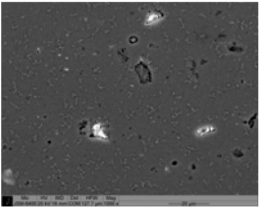
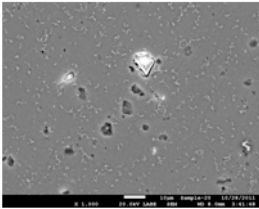
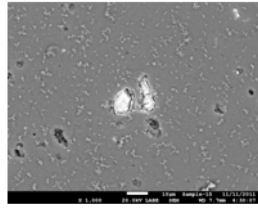
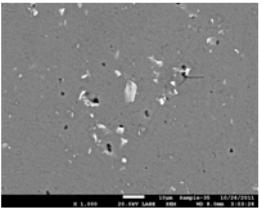
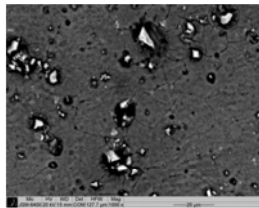
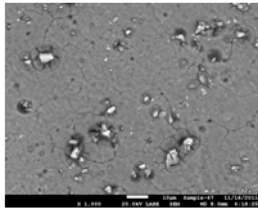
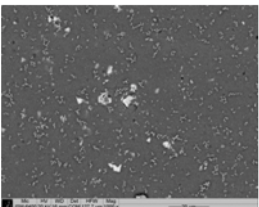
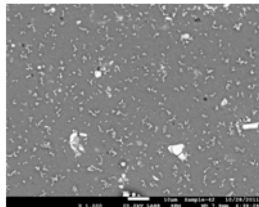
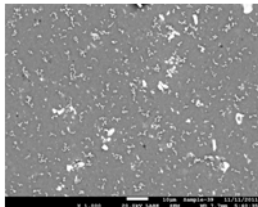
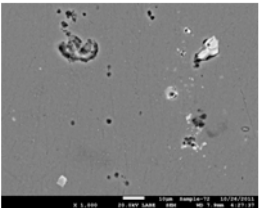
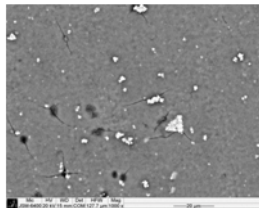
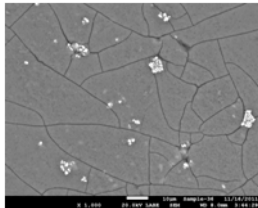
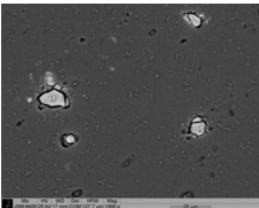
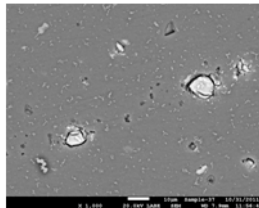
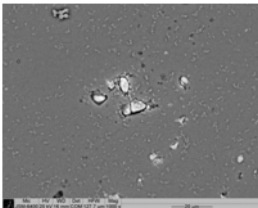


Figure 6.1 Polarization resistance data, R_p , for the TCP-coated AA2024, AA6061, and AA7075 during full immersion in naturally aerated 0.5 M Na_2SO_4 for 14 days.

Table 6.2 shows the SEM images of the TCP-coated Al alloys during the full immersion in air-saturated 0.5 M NaCl that is more aggressive than Na_2SO_4 . Samples were continuously immersed for 14 days. Images for the uncoated samples are also shown as control. The samples were rinsed in ultrapure water for 30 s before imaging. It can be seen that no significant pitting corrosion or morphology change occurs to the

Table 6.2 SEM images of TCP-coated and uncoated AA2024-T3, AA6061-T6, and AA7075-T6 during full immersion in air-saturated 0.5 M NaCl for 14 days.

Alloy	Treatment	Immersion Time (days)		
		1	7	14
2024	Bare			
	TCP			
6061	Bare			
	TCP			
7075	Bare			
	TCP			

coated specimens during the test period immersion in aggressive NaCl. In contrast, there is significant damage on the uncoated specimens as evidenced by the pitting, cracking^{4, 9, 155} and dealloying of Cu-containing intermetallics¹⁵⁶⁻¹⁵⁷. The white precipitates seen in the images for the coated samples are characteristic of the TCP coating. The fact that they are not dissolved in the solution is also an indicator of coating stability.

The full immersion testing was also conducted on the galvanic couple of TCP-coated AA2024 panels and fasteners made of SS 286 CRES and Ti-6Al-4V. The weight loss data and optical images will be shown in the later section.

6.2.2 Atmospheric corrosion

Figure 6.2 shows the R_p data for TCP-coated AA2024, AA6061, and AA7075 during atmospheric exposure to humid air (RH=100%) over a 14-day period at (A) room temperature and (B) 55 °C. R_p for the TCP-coated AA2024 was relatively consistent throughout the exposure period while R_p for the other two alloys increased after 7 and 14 days. First, the non-decreasing R_p values reflect good stability of the coating under these test conditions. Second, the increasing R_p seen for AA6061 and AA7075 results from the formation of a passivating oxide layer in the pores/channels and defects of the coating with the metal are exposed.¹⁵⁸

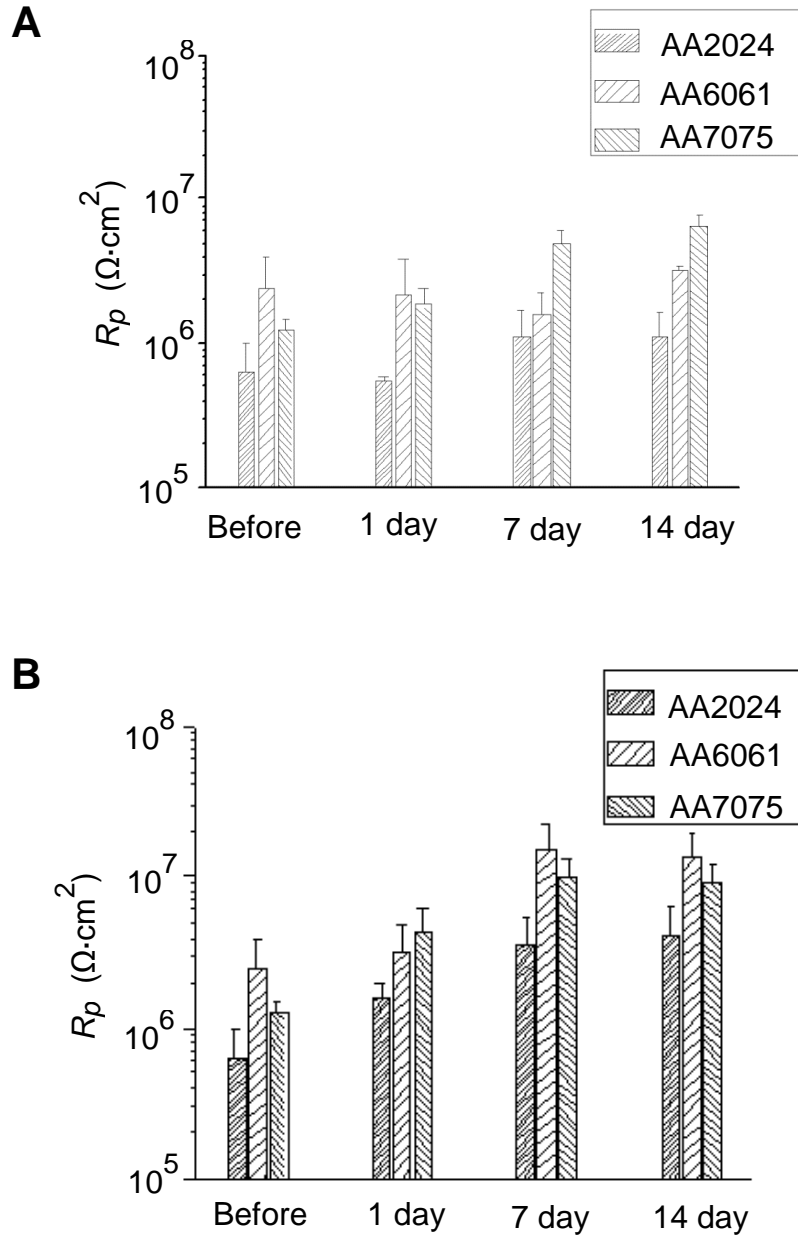


Figure 6.2 R_p for TCP-coated AA2024, AA6061, and AA7075 at different time points during a 14-day atmospheric exposure test in humidified air (RH=100%) at (A) room temperature and (B) 55 °C for 1, 7, and 14 days.

Figure 6.3 shows the optical and SEM images of TCP-coated and uncoated AA2024-T3 specimens after exposure to a moist SO_2 atmosphere for 14 days at 44 °C.

In this test, the alloy panels were galvanically-coupled with a Ti alloy fastener (Chapter

2). Corrosion is clearly seen across the entire uncoated alloy surface (Fig. 6.3D) in the form of pitting (Fig. 6.3E) and subsurface undercutting¹⁵⁹ (Fig. 6.3F). In contrast little change in pitting or surface roughening is seen for the TCP-coated specimens (Fig. 6.3A). Some corrosion products precipitate locally on the coated alloy surface (Fig. 6.3B) but most regions show little evidence for corrosive damage (Fig. 6.3C). These results indicate that the TCP coating provides corrosion inhibition in the moist SO₂ testing environment.

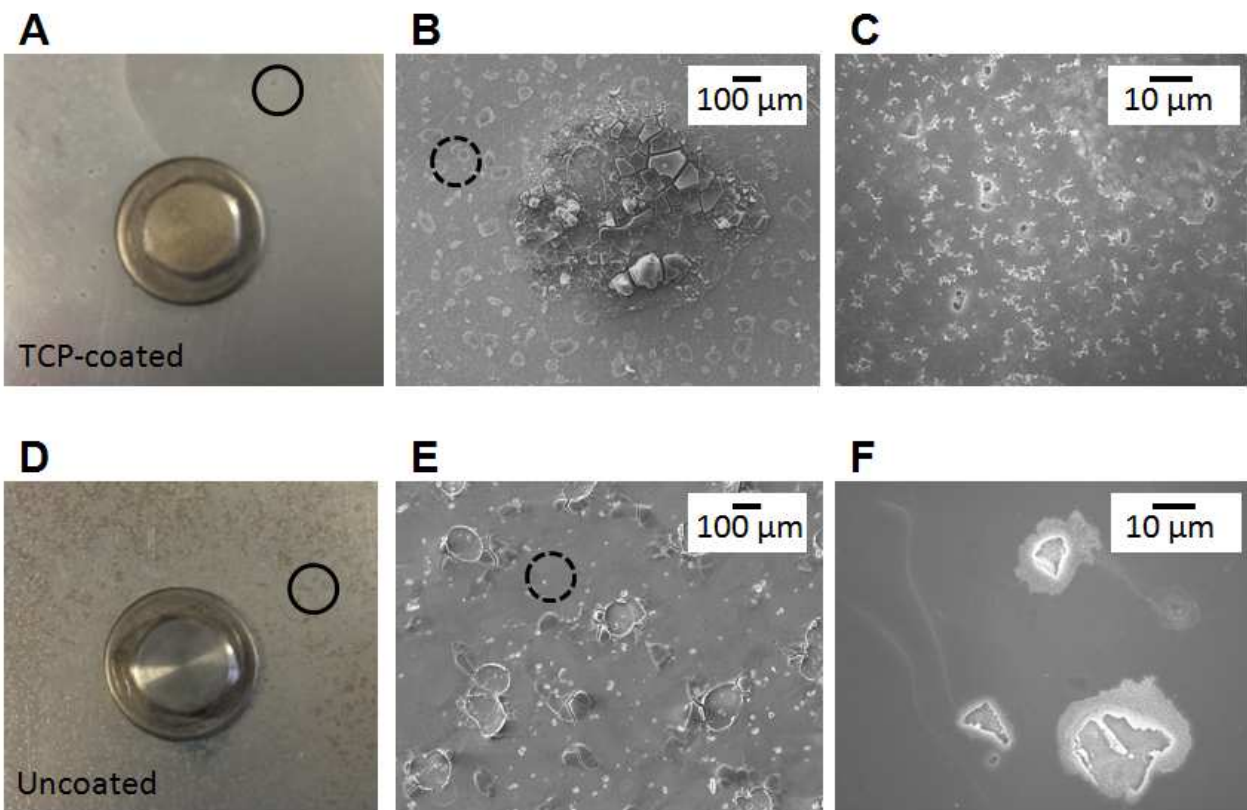


Figure 6.3 Optical images for the (A) TCP-coated and (D) uncoated AA2024-T3 after exposure in moist SO₂ atmosphere (RH=100%) at 40 °C for 14 days. The alloy panels were galvanically coupled with Ti-6Al-4V fasteners. SEM images of the corroded areas (solid black circles) in (A) and (D) are shown in (B) and (E), respectively. Images of the dashed black circles in (B) and (E) are shown in (C) and (F) with a higher magnitude.

6.2.3 Thin layer mist exposure

Table 6.3 shows optical images of the TCP-coated AA2024-T3 specimens after the full immersion test (see above) at room temperature and thin-layer mist (TLM) test at 55 °C in air-saturated 3.5% NaCl, both for 14 days. The alloy panels were galvanically-coupled to either a stainless steel (SS A286 CRES) or Ti alloy (Ti-6Al-4V) fastener (Chapter 2). The areas where the panels are in direct contact with the fasteners (washers) are damaged and show circular-shaped marks around the hole. Comparing the effects of the different fasteners, it can be seen that the specimens coupled with SS fastener underwent a greater level of corrosion than the specimens coupled with the Ti alloy fastener.¹⁶⁰⁻¹⁶¹ In addition, the specimens after the 14-day TLM testing were corroded to a greater extent than those after the full immersion testing, especially for the panels coupled with the SS fastener. This is also seen from the weight loss of the coated AA2024 panels, as shown in Table 6.4. The SS-coupled panels showed a greater weight loss percentage than those coupled with Ti alloy fasteners. This is attributed to the fact that dissolved O₂ has a shorter diffusion pathway through the thin layer of electrolyte solution to the coated alloy surface than that through the bulk solution during the immersion test. Additionally, the salt concentration in the small volume droplets likely progressively increased with droplet evaporation. Therefore, for the same period of testing, a greater amount of O₂ diffuses to the panels in the TLM test and causes a more severe corrosion than that in the full immersion test.

Table 6.3 Optical images of the TCP-coated AA2024-T3 specimens after the thin-layer mist corrosion test at 55 °C for 14 days. The coated alloy panels were galvanically-coupled with either a stainless steel or a Ti alloy fastener. Samples were rinsed in ultrapure water for 30 s and dried in flowing N₂ before images were recorded.

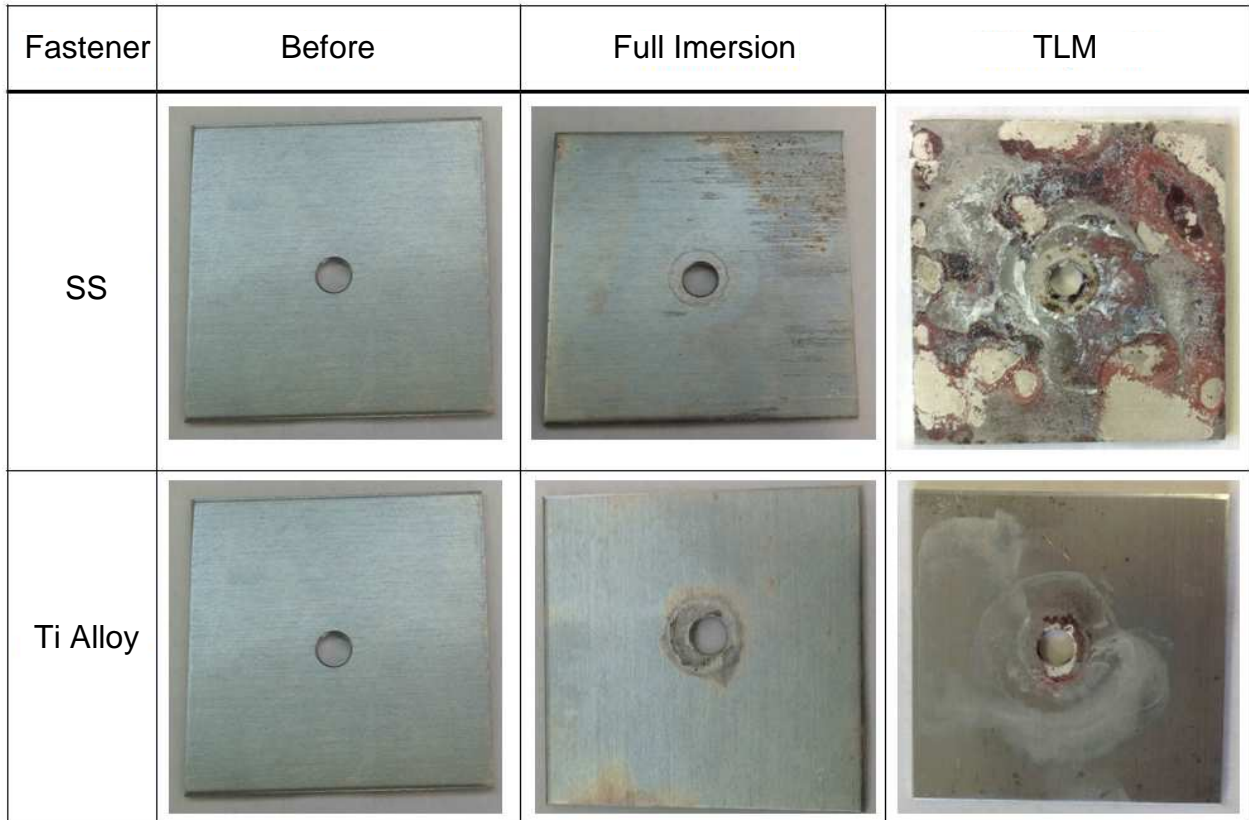


Table 6.4 Weight loss percentage of the TCP-coated AA2024-T3 specimens after the thin-layer mist (TLM) corrosion test at 55 °C for 14 days and full immersion in naturally-aerated 3.5% NaCl at room temperature for 14 days. The coated alloy panels were galvanically-coupled with either a stainless steel or a Ti alloy fastener. Samples were rinsed in ultrapure water for 30 s and dried in flowing N₂ before images were recorded.

Accelerated corrosion tests	Weight loss percentage (%)	
	SS316	Ti-6Al-4V
TLM	30.6 ± 8.7	19.9 ± 9.4
Full immersion	11.4 ± 4.1	3.0 ± 1.6

6.3 Conclusion

The stability and corrosion inhibition provided by the TCP coating on aluminum alloys were assessed by optical/microscopic inspection, weight change, and electrochemical measurements after three different accelerated corrosion tests. The tests included: full immersion at room temperature, atmospheric exposure to humid air at room temperature, moist SO₂ atmospheric exposure, and a thin layer mist (TLM) test. The TCP coating exhibited good physical and chemical stability and provided consistent corrosion protection for at least 14 days during full immersion in air-saturated 0.5 M NaCl and exposure to humidified air. The coating also provided corrosion inhibition to the alloy during the moist SO₂ atmospheric test. For the galvanically-coupled specimens, the degree of corrosion inhibition provided by TCP depended on the fastener type. More extensive corrosion was seen for the SS A286 CRES fastener, presumably because this alloy supports more rapid oxygen reduction reaction kinetics. This is clearly evident in the thin layer mist (TLM) test results, which shows the aluminum alloys coupled with the SS fastener are more extensively corroded than those with Ti alloy fastener.

CHAPTER 7. EFFECTS OF THE DEOXIDATION/DESMUTTING TIME AND SOLUTION CHEMISTRY ON THE CORROSION INHIBITION PROVIDED BY THE TCP COATING ON AA2024

7.1 Introduction

Conversion pretreatment coatings are one component of a multi-layer coating system that is typically used to protect aluminum alloys from corrosion. These coatings are designed to protect an underlying metal surface from corrosion, especially in and around defects, and to provide adhesion with a primer overlayer. The corrosion inhibition provided by the coating depends on its chemical composition, physical structure and thickness, all of which affect oxygen and water/electrolyte accessibility to the metal surface.¹⁶² Conversion coating thicknesses are generally in the 100-500 nm range.

For optimum conversion coating performance, it is essential to properly prepare the metal surface. The preparation or pretreatment typically involves two steps: degreasing and deoxidation/desmutting. Effective cleaning produces a contaminant-free surface on which to form the conversion coating.¹⁶³⁻¹⁶⁴ For aluminum alloys, there are two types of surface contaminants that require removal: cutting and lubrication oils from the processing and shaping of the alloy, and metal oxides (*i.e.*, smut).¹⁶⁴ Degreasers are used to remove the oil contaminants. This is often followed by application of an acidic deoxidizer (also called desmutting or pickling) that is used to dissolve the smut.

Studies have shown that the degreasing and deoxidizing/desmutting pretreatments can affect the performance of conversion coatings on aluminum

alloys.¹⁶⁵⁻¹⁷⁰ The formation and structure of the coating as well as the corrosion inhibition it provides are significantly affected by the temperature used for alkaline cleaning, and the acidic or alkaline nature of the solution used for deoxidation.¹⁷⁰⁻¹⁷¹ In the case of chromate conversion coatings (CCC), the cleanliness and surface chemistry of the alloy strongly influence the coating formation¹⁷¹⁻¹⁷², composition¹⁷³⁻¹⁷⁴ and performance¹⁷⁵. Additionally, the deoxidizing pretreatment can alter the surface copper content and distribution,^{165, 176-177} which can affect the corrosion inhibition provided by the CCC.^{175, 178}

Prior work has shown that the TCP coating inhibits corrosion on aluminum alloys, in part, by serving as a barrier layer.^{114, 118, 146, 179-180} To date though, there has been little work reported on how the substrate pretreatment affects the corrosion inhibition provided by the coating. Guo *et al.* investigated the effect of pretreatment on the TCP coating performance by comparing a commercially-recommended process (degreasing in Turco® 6849 and deoxidizing in Turco® Smut-Go NC) with degreasing in an alkaline Na₂SiO₃ solution and deoxidizing in the HNO₃ + Sanchem 1000 solution.¹⁸¹ At least for these two pretreatments, they found no significant difference in the TCP formation or performance. Wernick *et al.*¹⁸², Buchheit *et al.*¹⁸³, and Mankowski *et al.*¹⁸⁴ reported that the acidic deoxidation step is critical for conversion coating formation as it alters the morphology and chemistry of the alloy surface. Proper

substrate pretreatment is obviously the key for the formation of a continuous, low defect TCP conversion coating.

We hypothesized that the corrosion inhibition provided by a TCP coating would depend on the chemical nature of the deoxidizer and the treatment time due to effects on the substrate's surface roughness, pit density, and pit depth. Figure 7.1A depicts the formation of a low defect, uniform conversion coating on a metal substrate pretreated in a way that minimizes surface roughening and pitting. In contrast, Figure 7.1B depicts the formation of a defective coating that incompletely covers a substrate due to the surface roughening and pitting produced by an aggressive deoxidation pretreatment. The formation of a continuous conversion coating on the steep walls and sharp edges of deep pits is likely a challenge. It is at these sites where initiation of corrosion and coating degradation likely occur. We report herein on the corrosion inhibition provided a TCP coating (Alodine® 5900) on AA2024-T3. Prior to formation of the coating, alloy surfaces were degreased and deoxidized in either an aggressive acidic fluoride medium (Turco® Smut-Go) for different periods of time or in less aggressive 0.1 M NaOH.

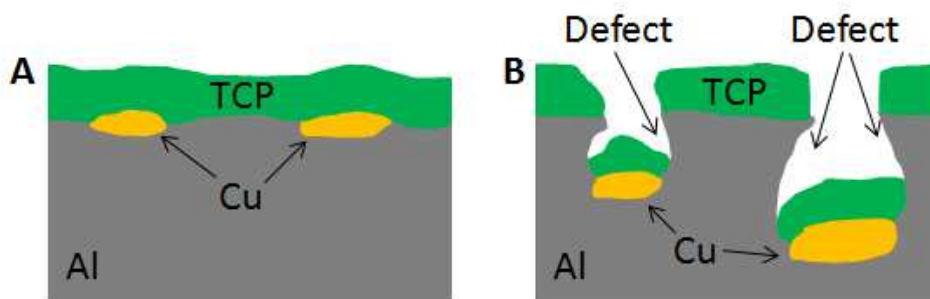


Figure 7.1 Proposed conversion coating structure on (A) an alloy pretreated to minimize surface roughening and pitting and (B) an alloy pretreated in a manner that increases surface roughening and pitting.

7.2 Results

7.2.1 Deoxidizing/desmutting in acidic fluoride Smut-Go.

Figure 7.2 shows profilometry contour plots (left) of AA2024 specimens after treatment times from 0-12 min in Smut-go. Corresponding SEM micrographs (right) of TCP-coated panels that were deoxidized for the same times are also presented. In the contour plots, only a few pits are detected on the alloys after the shorter treatment times (0.5 and 2 min). In contrast, significantly greater roughness and pitting are seen for the longer times (6 and 12 min). Rather deep pits with depths on the order of 1 μm were observed after the 12-min treatment. The increased surface damage with treatment time is also apparent in the SEM micrographs of the TCP-coated substrates. A greater level of roughening and pitting can be seen for the substrates pretreated by longer deoxidation times, particularly the 6 and 12-min treatments. The damage is especially pronounced near the intermetallic inclusions. The elongated precipitates visible in the images are characteristic of this TCP coating.¹¹⁴ The bright collar around the pit mouth is due to the “edge” effect of the electron beam during imaging in the secondary electron mode.¹⁸⁵

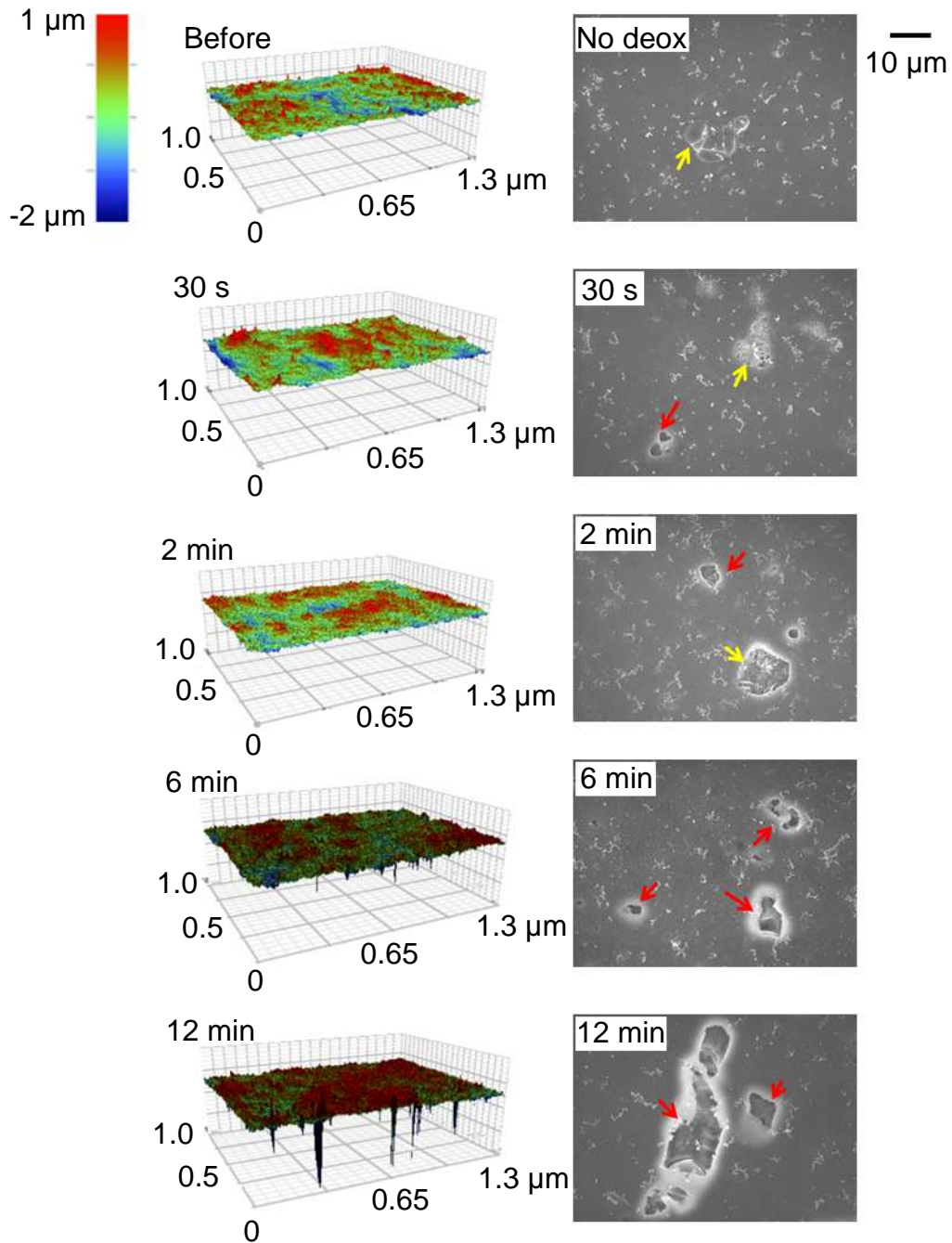


Figure 7.2 Profilometry contour plots (left) of AA2024 specimens before and after deoxidation in Smut-Go for different times. SEM micrographs (right) of TCP-coated AA2024 specimens prepared by deoxidation for different times in Smut-Go. Red arrows indicate the pits and damage sites, whereas yellow ones indicate the visible intermetallics.

Figure 7.3 shows plots of the (A) root mean square (RMS) of the surface roughness, (B) pit density, (C) pit depth, and (D) pit equivalent diameter for the alloy substrates as a function of time in the acidic fluoride deoxidizer. Panel (E) shows the TCP coating thickness on AA2024 specimens deoxidized for the different times. Some pits are not perfectly circular so the software calculates an equivalent diameter assuming a perfect circle with an area to equivalent to that of the irregularly-shaped pits. The data are average values obtained from four 1.3 mm^2 areas on each substrate surface. The plots reveal that the surface roughness increases over the shorter treatment times before leveling off at longer times. The roughness arises primarily from the increased pit density and to a lesser extent from an increased pit depth, as seen in Figures 7.3B and C. It should be noted that the pit density after deoxidation for the 0.5 or 2 min treatment times is not significantly different from that of the alloy before the treatment. However, the pit density increases for treatment times of 2 min or longer. While there is increased pit density, the pit depth and equivalent pit diameter are invariant with treatment time, except for the 12-min treatment time for which there is an increase in pit depth. It could be that the dimensions of the pits subsurface are changing without a measurable change in depth. The limited pit depth could also result from the accumulation of insulating corrosion products within the pits.¹⁸⁶⁻¹⁸⁸ These precipitates would limit further corrosion by preventing electrolyte contact with the metal surface and inhibiting oxygen transport. Figure 7.3E shows ellipsometry data for the TCP coating thickness on AA2024 substrates deoxidized for different times. The results show the thickness is constant at ca. 100 nm for treatment times up to 6 min and then decreases to ca. 60 nm for the 12-min treatment.

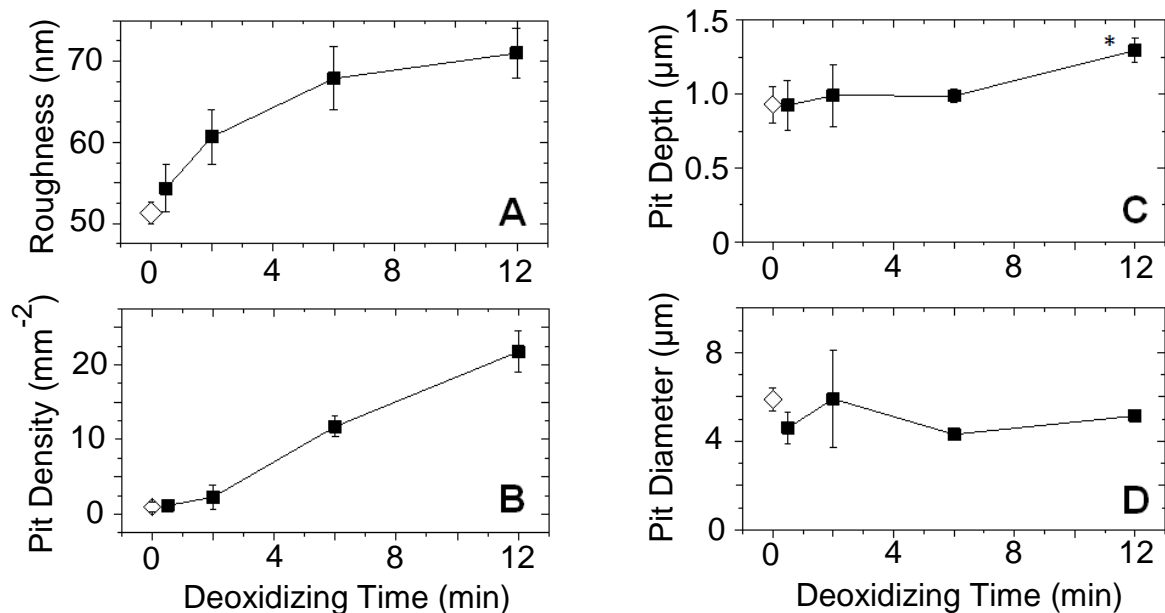


Figure 7.3 Plots of the (A) surface roughness (RMS), (B) pit density, (C) pit depth and (D) equivalent pit diameter for AA2024 specimens treated in Smut-go for different times. Values for the alloy before deoxidation are also shown for comparison (\diamond). Data were obtained from the analysis of profilometry contour plots. Only the pits of $7 \mu\text{m}^2$ or greater in area and $0.5 \mu\text{m}$ or greater in depth were regarded as significant. (E) Plot of the TCP coating thickness, as determined from ellipsometry, on AA2024 specimens treated in Smut-go for different times. Each datum is an average value of 3 spots on each sample. Asterisk indicates significant difference from the values for the untreated controls (0-min treatment).

The surface roughness and pit density both have an effect on the corrosion inhibition provided by the TCP conversion coating as is indicated by the electrochemical data presented in Figure 7.4. Plots of the (A) corrosion potential, E_{corr} , and (B) polarization resistance, R_p , for TCP-coated AA2024 samples deoxidized for periods of time from 0.5-12 min are presented. There was no statistically significant change in E_{corr} for the TCP-coated alloys for all the treatment times (-0.3 to -0.4 V). Interestingly, R_p progressively decreased with treatment time by up to 4x for the 12-min deoxidation

time. Actually, R_p for the sample treated for 12 min, $0.96 (\pm 0.23) \times 10^5 \Omega\text{-cm}^2$, is similar to the value for the degreased and deoxidized but uncoated alloy in the same electrolyte.¹¹⁴ The decreasing R_p suggests that the coating is providing progressively inferior barrier protection. It is likely that the roughness and pitting (density and dimensions) are such that the conversion coating incompletely covers the exposed surface or is more defective, as depicted in Figure 7.1B.

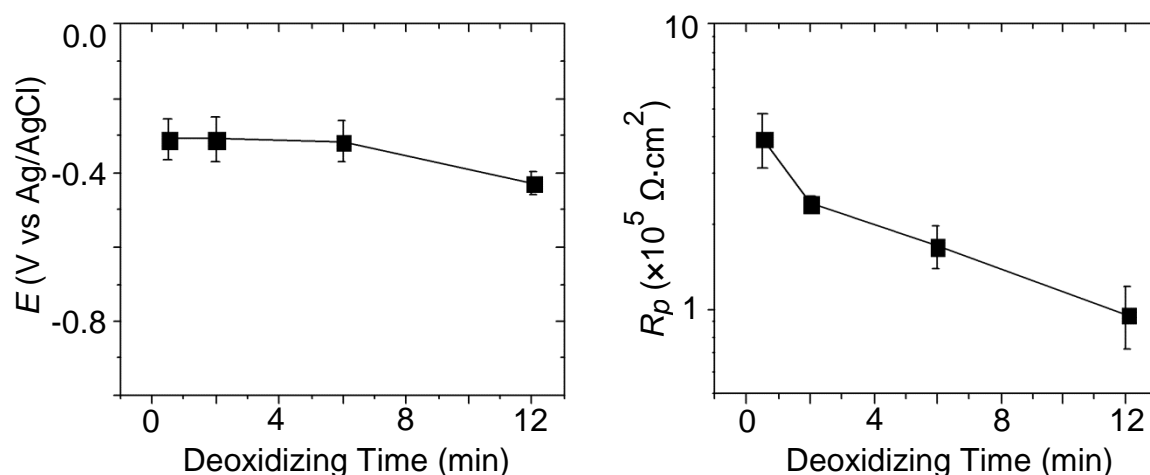


Figure 7.4 (A) Corrosion potential, E_{corr} and (B) polarization resistance, R_p , for TCP-coated AA2024 specimens after deoxidation times of 0.5, 2, 6, and 12 min. All measurements were made in naturally aerated 0.5 M Na_2SO_4 + 0.01 M NaCl . Each datum is an average of three replicates with the standard error revealed by the bars.

7.2.2 Deoxidizing/desmutting in alkaline halide-free 0.1 M NaOH.

Comparison tests were performed TCP-coated specimens that were deoxidized in alkaline (0.1 M NaOH) solution, which etches the aluminum more uniformly as compared to the acidic Smut-Go. Alkaline etch treatments react with the aluminum to

generate hydrogen, and complex oxides and hydroxides of aluminum. For example, the following oxide dissolution/metal corrosion reaction can occur:

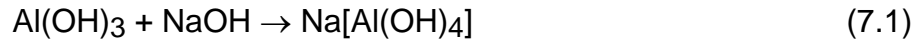


Figure 7.5 presents a comparison of SEM micrographs of AA2024 specimens after (A) degreasing, (B) degreasing and deoxidizing for 2 min in 0.1 M NaOH and (C) degreasing and deoxidizing in Smut-Go for 2 min. The intermetallic inclusion, several micrometers in dimension, after degreasing (Fig. 7.5A), and degreasing and deoxidizing in NaOH (Fig. 7.5B) remained fairly smooth. There was no dissolution of the inclusion or any trenching of the aluminum around the inclusion. In contrast, treatment in Smut-Go caused dissolution of the inclusion such that Al and Mg were removed leaving behind a pitted crater with Cu deposits at the bottom.¹⁸⁴ The crater has steep walls and significant roughening and pitting at the base. It is these features that are likely difficult to completely coat with the TCP (refer to Figure 7.1B).

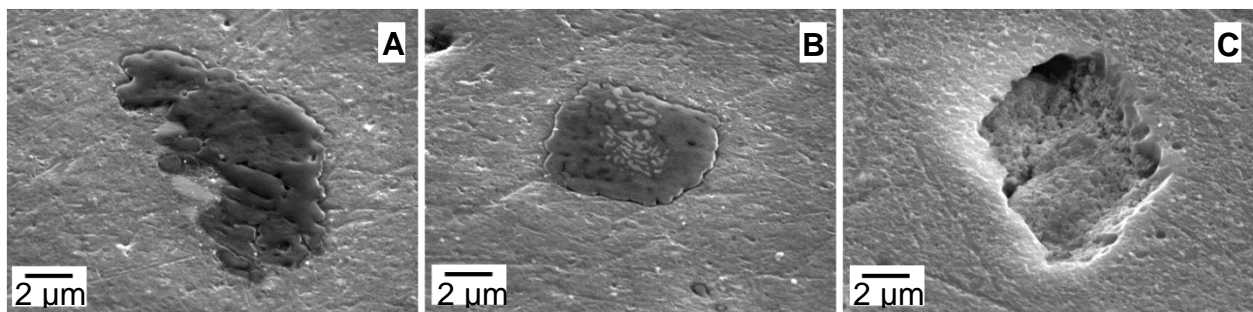


Figure 7.5 SEM micrographs of the uncoated AA2024 after (A) degreasing, (B) degreasing and deoxidizing for 2 min in 0.1 M NaOH and (C) degreasing and deoxidizing for 2 min in Smut-Go. The micrographs were taken with the samples tilted by 54° towards the secondary electron detector. These intermetallic compounds contain Al, Cu, Fe, and Mn according to EDAX analysis data that are not shown here.

Figure 7.6 presents an SEM micrograph of a TCP-coated AA2024 specimen prepared by degreasing and deoxidizing in NaOH for 2 min. EDX elemental line profiling data across an intermetallic inclusion are also presented. First, a much smoother substrate surface is evident in this image as compared to the images shown in Figure 7.2 for the Smut-go treated substrates. Second, it can be seen that the intermetallic inclusion is rich in Cu, Fe, and Mn with no dealloying. The elongated precipitates (white) again are characteristic of this TCP coating are visible in the image. They contain Zr, O, Cr, and F as evidenced by the increased elemental intensities at ca. 20 and 90 μm .¹¹⁴

The intermetallic inclusion in the center of the image is about 10 μm in diameter. The coating is enriched at this site, compared to the surrounding aluminum matrix, as evidenced by the increased signal intensities for Zr, O, Cr, and F at ca. 50 μm . The Zr and O signals arise from the zirconia and the Cr signal comes from Cr(III) oxide in the TCP coating.^{114, 180} The F signal arises, at least in part, from the biphasic structure of the TCP coating.^{114, 180}

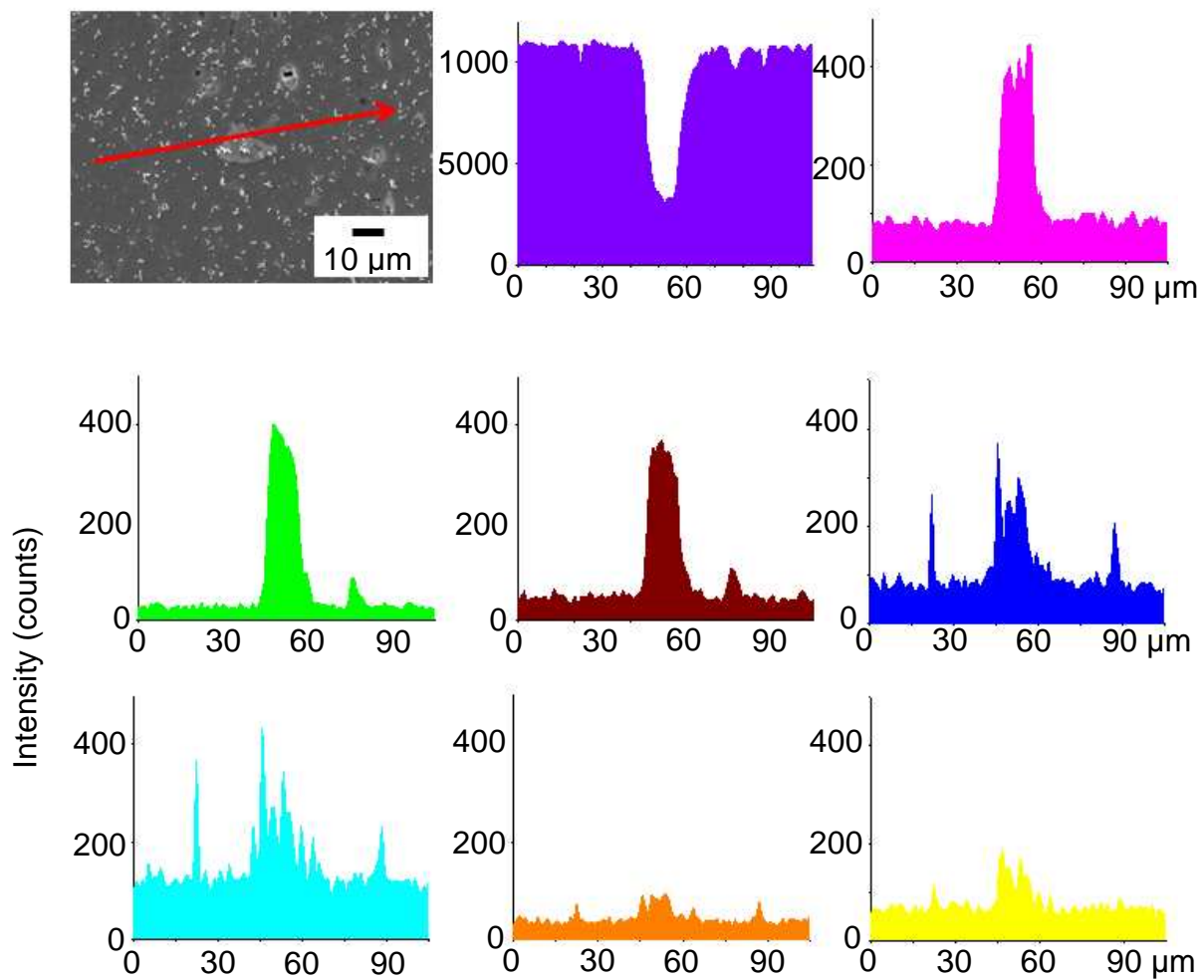


Figure 7.6 SEM micrograph and EDAX elemental line profiling data for the TCP-coated AA2024 formed after degreasing and a deoxidation time of 2 min in 0.1 M NaOH.

Table 7.1 Summary of the physical properties and electrochemical parameters measured for TCP-coated AA2024 specimens degreased and deoxidized for 2 min in either Smut-go or NaOH. The physical properties shown, as determined from optical profilometry, are the surface roughness (RMS), pit density, pit diameter and pit depth. The electrochemical parameters shown are E_{corr} , E_{pit} , and R_p .

Treatments	Physical Properties				Electrochemistry		
	RMS (nm)	Pit density (/mm ²)	Pit diam. (μm)	Pit depth (μm)	E_{corr} (V vs Ag/AgCl)	E_{pit} (V vs Ag/AgCl)	R_p (×10 ⁵ Ω·cm ²)
Without Deox	51.3 ± 1.4	1.0 ± 0.6	5.9 ± 0.5	-0.9 ± 0.1	-0.42 ± 0.02	0.17 ± 0.03	2.15 ± 0.85
Smut-Go	60.7 ± 3.3*	2.3 ± 1.6	5.9 ± 2.2	-0.1 ± 0.2	-0.30 ± 0.06	0.58 ± 0.07*	2.35 ± 0.13
NaOH	58.8 ± 1.0*	1.8 ± 0.7	4.6 ± 0.6	-0.6 ± 0.0*	-0.39 ± 0.01	0.78 ± 0.10*	12.23 ± 4.66*

All measurements were conducted in naturally aerated 0.5 M Na₂SO₄ + 0.01 M NaCl. Data for coated alloys without any deoxidation pretreatment are shown for comparison. Each datum represents a mean value ± S.E.M. (n ≥ 3). Asterisks are used to indicate the statistically significantly different values between the three treatments (t-test at 95% confidence interval). All values are compared to those for the coated samples formed without any deoxidation.

Table 7.1 presents data for the surface roughness (RMS), pit density, pit diameter, and pit depth for alloys after degreasing and a 2-min deoxidation in either Smut-Go or NaOH. The deoxidized alloys exhibit several physical properties that are statistically similar to those for the untreated controls (without deox). The exceptions are the roughness and the pit depth. The surface roughness for the substrates pretreated in both media is slightly greater than the roughness for the control samples. No differences are seen in the pit density or pit diameter of the pretreated samples relative to the controls. The pit depth for the alkaline treated samples is less than that for either the Smut-go treated or the untreated controls due to the more uniform etching of the surrounding aluminum matrix. In short, the 2-min treatment times in both media produce minimal changes in the substrate surface structure, as compared to the longer deoxidation times in Smut-go. The main difference appears to be the reduced pit depth after pretreatment in NaOH.

Table 7.1 presents some electrochemical data recorded for the TCP-coated substrates in naturally aerated 0.5 M Na₂SO₄ + 0.01 M NaCl. Shown are E_{corr} , the breakdown potential for pit initiation, E_{pit} , and R_p for the TCP-coated alloys prepared using a 2-min deoxidation step in the two media. Data for the coated samples without deoxidation are also shown for comparison. No significant difference in E_{corr} is seen for all three sample sets. However, the breakdown or pitting potential, E_{pit} , for the coated samples after either deoxidation treatment is more noble than the value for the coated samples without any deoxidation. For example, E_{pit} is shifted positive by 400 mV (0.58

± 0.07 V vs. Ag/AgCl) for the coated substrates deoxidized in Smut-go and by 600 mV (0.78 ± 0.10 V vs. Ag/AgCl) for coated substrates deoxidized in NaOH, as compared to the potential for the coated samples prepared without any deoxidation. This indicates that deoxidation pretreatment, regardless of the acidic or alkaline nature, is necessary to activate the alloy surface for the formation of a TCP coating. The coating lowers the susceptibility of the alloy to chloride-induced pitting corrosion presumably by physically blocking sites on the surface from contact with the supporting electrolyte solution (Chapter 3 and 5). Finally, the coated alloy deoxidized in Smut-Go has an R_p that is in the same range as that for the coated alloy prepared without deoxidization. However, the coated alloy deoxidized in NaOH exhibits an R_p that is about 6× greater than the value for the coated alloys deoxidized in Smut-Go. In fact, coated samples deoxidized in NaOH exhibited the largest R_p values of any TCP-coated AA2024 specimens we have examined to date.^{114, 180}

Figure 7.7 presents electrochemical impedance data for the TCP-coated AA2024 specimens formed after deoxidation in Smut-Go and NaOH. Data for the coated sample without deoxidation are shown as controls. The phase angle is greater and the capacitive reactance extends over a wider frequency range for the TCP-coated specimens deoxidized in NaOH as compared with the coated specimens deoxidized in Smut-go or not deoxidized at all. This is consistent with greater corrosion inhibition by the coating for the NaOH-treated specimens. All three specimens have phase angle profiles consistent with at least two time constants. One in the higher-frequency region (ca. 10^2 - 10^3 Hz) represents properties of the TCP coating while another in the lower-

frequency region (ca. 0.1-100 Hz) represents the double layer at the exposed metal surface.¹¹⁶ Table 7.2 shows the best-fit parameters of the experimental EIS data to the equivalent circuit for a porous coating (Chapter 2). The data reveal that the coated specimen formed after NaOH treatment exhibits a ~5× greater R_{po} and a ~5× smaller C_{dl} compared to coated specimens formed after Smut-Go treatment. This is attributed to a more continuous and less defective conversion coating, which results from the lower degree of surface roughening and pitting. In other words, less metal is exposed to the electrolyte solution for the coated specimens when the alkaline etch are used. This leads to a ~10× greater R_p for the samples deoxidized in NaOH. This is consistent with the R_p values in Table 7.1, which were determined from linear polarization curves. The TCP-coated samples formed without deoxidation exhibit a greater R_{po} and a smaller C_{dl} as compared to the coated samples formed after deoxidation in Smut-Go. This is attributed to the Al oxide layer that forms during degreasing at 55 °C that is not completely removed during immersion in the coating solution.

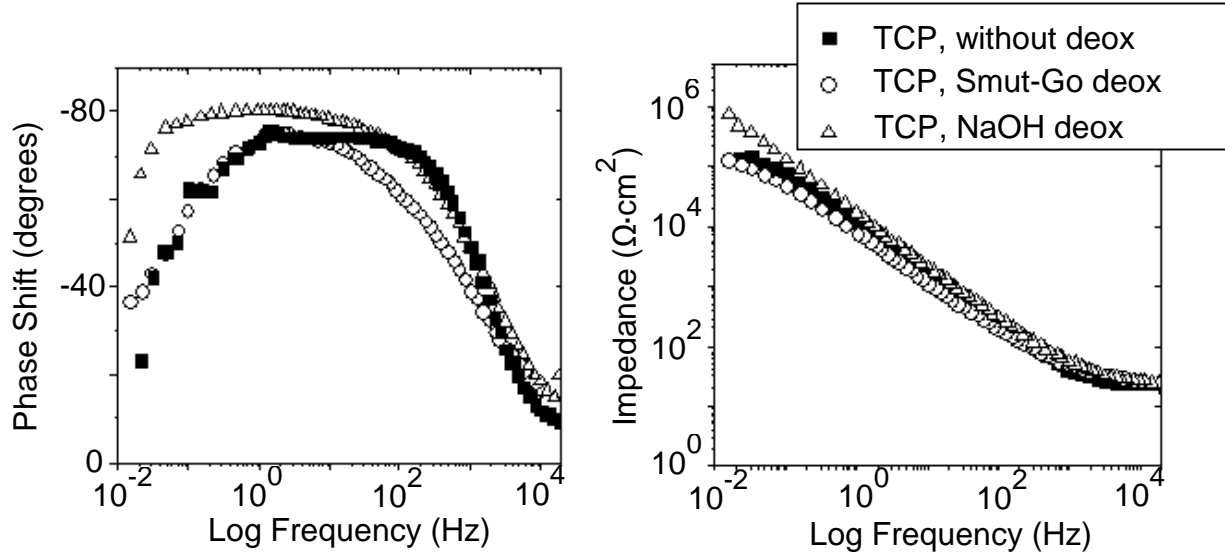


Figure 7.7 Representative electrochemical impedance spectra (EIS) for TCP-coated AA2024 specimens prepared using a 2-min deoxidation in either Smut-Go or NaOH at room temperature. Curves for the TCP-coated sample without deoxidation ($-\Delta-$) are also shown for comparison. Measurements were conducted at E_{CORR} in naturally aerated 0.5 M Na_2SO_4 + 0.01 M NaCl.

Table 7.2 Best-fit parameters, C_{CO} , R_{po} , C_{dl} , and R_p , for the EIS data obtained for TCP-coated AA2024 specimens formed after deoxidation for 2 min in either Smut-Go or NaOH.

Treatment	C_{CO} ($\mu\text{F}/\text{cm}^2$)	R_{po} ($\Omega \cdot \text{cm}^2$)	C_{dl} ($\mu\text{F}/\text{cm}^2$)	R_p ($\times 10^5 \Omega \cdot \text{cm}^2$)
Without deox	5.2 ± 0.7	1740 ± 344	1.9 ± 0.8	2.9 ± 1.4
Smut-Go	4.5 ± 0.9	$217 \pm 44^*$	$9.4 \pm 0.6^*$	1.6 ± 0.5
NaOH	3.4 ± 0.1	1563 ± 490	1.2 ± 0.1	$21.3 \pm 8.3^*$

All measurements were conducted in naturally aerated 0.5 M Na_2SO_4 + 0.01 M NaCl. Data for coated alloys without any deoxidation pretreatment are shown for comparison. R_{el} is the resistance of the bulk electrolyte, R_{po} and R_p represent the resistance of the electrolyte in the pores and the polarization resistance of the metal to corrosion, respectively. Each datum represents a mean value \pm S.E.M. ($n \geq 3$). The rest parameters, e.g., R_{el} , Q_{CO} , n_{CO} , etc., are shown in the supplemental material. Asterisks are used to indicate the significantly different values between the three treatments. All values are compared to those for the coated samples formed without any deoxidation.

Figure 7.8 presents potentiodynamic polarization curves for TCP-coated AA2024 samples prepared by 2-min deoxidation in either Smut-Go or NaOH. Curves for the coated substrates without any deoxidation pretreatment are also shown for comparison. The cathodic current at about *ca.* -0.6 V vs Ag/AgCl results from the reduction of dissolved oxygen that occurs primarily at Cu-rich intermetallic sites. The coated sample deoxidized in NaOH exhibits greater suppression of the cathodic current in this potential region by a factor of about 10x as compared to the coated samples prepared with no deoxidation step or after deoxidation in Smut-go. This is due, at least in part, to the oxide layer that forms on the Cu sites during treatment in NaOH.¹¹⁰ The oxide film appears to be sufficiently thick that it is not completely dissolved in the fluoride-containing TCP bath. Therefore, fewer active copper sites are available for dissolved oxygen reduction as compared to the coated substrates formed without any deoxidation or after deoxidation in Smut-Go. Further evidence for the more passive copper oxide film after deoxidation in NaOH is the suppressed copper stripping peak ($\text{Cu} \rightarrow \text{Cu}^{2+}$) at *ca.* about 0.2 V vs. Ag/AgCl. In contrast, the anodic currents are attenuated at similar levels for deoxidized substrates regardless of the deoxidation treatment. The suppressed currents could also be due to the formation of a magnesium oxide film across the entire alloy surface during immersion in NaOH.¹⁸⁹ For magnesium-containing alloys, such as AA2024-T3 and AA7075-T6, magnesium diffuses to the surface and forms an oxide layer of several tens of nanometers thick.¹⁸⁹⁻¹⁹³ According to the E-pH diagram of Mg, the oxide film contains mainly $\text{Mg}(\text{OH})_2$ that is stable in aqueous solutions of pH greater than about 11.¹⁹⁴⁻¹⁹⁵ This Mg oxide film may be

beneficial in terms of forming a less defective TCP coating.¹⁸⁹ Finally, E_{pit} is shifted to more positive potentials for both deoxidized samples, as compared to the coated sample formed with no deoxidation. The breakdown potential for the substrate deoxidized in NaOH is shifted the most positive consistent with greater corrosion inhibition.

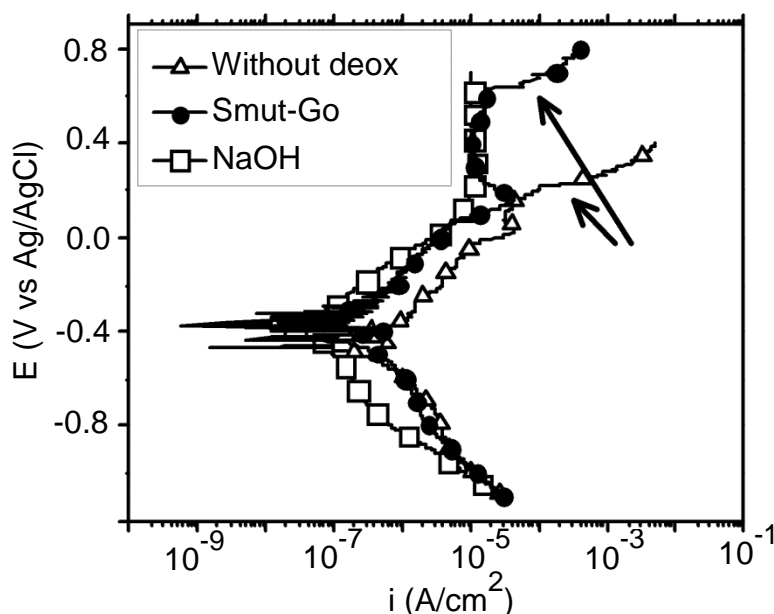


Figure 7.8 Representative potentiodynamic polarization curves for TCP-coated AA2024 formed after deoxidizing (2 min) in Smut-Go (-●-) or NaOH (-□-). Curves for the TCP-coated substrates formed without any deoxidation step (-△-) are shown for comparison. Measurements were conducted in naturally aerated 0.5 M Na₂SO₄ + 0.01 M NaCl. Scan rate = 2 mV/s.

7.3 Discussion

The results indicate that controlling the deoxidation/desmutting chemistry and treatment time is important for achieving optimum TCP-linked corrosion inhibition. This is because the pretreatment can have significant effects on the surface roughness, pit

density and pit depth, all of which impact the conversion coating coverage and corrosion inhibition. Substrate surfaces with less damage (roughening and pitting) support the formation of more continuous and defect-free TCP coatings, and this leads to improved corrosion inhibition. In this work, the improved corrosion inhibition was manifested by positive shifts in the chloride-linked breakdown or pitting potential, E_{pit} , and increases in the polarization resistance, R_p . Achieving such the most protective coating is possible only if the deoxidation/desmutting chemistry and treatment time are controlled in such a way to minimize surface roughening, pitting and the formation of deep (steep-walled) pits.

When AA2024 is deoxidized/desmutted in the acidic fluoride Smut-Go, the fluoride ions adsorb on and are incorporated into the Al oxide film.¹⁹⁶⁻¹⁹⁷ This causes passivation layer breakdown and leads to significant pitting corrosion, particularly around the intermetallic sites (Fig. 7.2). This aggressive solution produces increased surface roughening, pit densities and pit depths. The surface damage becomes more extensive with treatment time, particularly the 6 and 12-min treatments. The deeper pits have steep walls and sharp edges that cannot be effectively passivated by the TCP coating. These are likely the sites where corrosion and coating degradation initiate, as depicted schematically in Figure 7.1B. Dealloying of the intermetallics also occurs during deoxidation in Smut-Go, leaving behind only more noble Cu particles at the bottom of pits. In addition to the inferior corrosion inhibition by TCP coatings formed the more damaged specimens, there is a reduced TCP coating thickness for the 12-min

treatment time. The reason for the coating thinning is unclear at this point. In any event, a thinner coating is likely more defective and as a consequence is less passivating.

As is the case in the acidic fluoride Smut-Go ($\text{pH} < 4$), the passivating aluminum oxide film is also dissolved in NaOH ($\text{pH} > 9$). However, compared to the aggressive localized corrosion mediated by fluoride in Smut-Go (Fig. 7.5C), the aluminum is dissolved more uniformly (Fig. 7.5B) in alkaline media according to Rxn. (7.1). This is evidenced by the unchanged roughness, pit density, and pit diameter for alloy samples treated in 0.1 M NaOH compared to those values prior to treatment (Table 7.1). The uniform dissolution of the Al leads to a decreased pit depth (Table 7.1).

The corrosion inhibition provided by the TCP coating on AA2024 was assessed in naturally aerated 0.5 M Na_2SO_4 + 0.01 M NaCl. The polarization resistance, R_p , for the TCP-coated substrates decreases progressively as a function of the deoxidizing time in Smut-Go (Fig. 7.4B). The breakdown potential for pit initiation was also observed to shift to less positive potentials as a function of the deoxidizing time (data not shown). Both of these trends reflect reduced corrosion inhibition and they correlate with the increased surface roughness and pit density for the substrates after pretreatment. In addition, the reduced coating thickness after the 12-min treatment in Smut-Go (Fig. 7.3E) likely gives rise to more facile mass transport of dissolved O_2 to the underlying metal surface.

In contrast, the best corrosion inhibition we have recorded so far for TCP conversion coatings on aluminum alloys was achieved on specimens deoxidized in NaOH. Due to the fact that the specimen surface is not as roughened and pitted as it is

in Smut-go, the TCP coating presumably forms more uniformly and with fewer defects, hence the improved corrosion inhibition. Additionally, the alkaline treatment forms surface oxides on the Cu intermetallic sites and this serves to inhibit dissolved oxygen reduction. While our results indicate an alkaline deoxidation treatment is preferred for AA2024 in order to achieve the most corrosion inhibitory TCP coating, a limitation is that some “smut” is not dissolved at elevated pH. Therefore for those substrates, significant desmutting is necessary. In this case, the treatment conditions and time should be kept as short as possible to minimize surface roughening and pitting

7.4 Conclusion

Research was conducted to understand the effect of deoxidation/desmutting chemistry and treatment time on the corrosion inhibition provided by TCP coatings on AA2024-T3 surfaces. Key parameters describing the alloy surface condition, such as roughness, pit density, and pit depth, are important to control in order to achieve continuous and low defect conversion coating, which provides the greatest level of corrosion inhibition. Deoxidation/desmutting in the acidic fluoride Smut-Go causes increased surface roughening, pit density and pit depth with increasing treatment time. This aggressive solution causes localized aluminum dissolution around the Cu-rich intermetallic particles. It produces deep pits with the steep walls and sharp edges that are difficult to conformally coat with TCP. Therefore, these sites are likely the location where corrosion and coating degradation initiate. Short immersion times (e.g., 0.5 to 2 min) is recommended for the use with Smut-Go. The most corrosion inhibitory TCP coating was formed on specimens deoxidized in NaOH. This is attributed to more

uniform aluminum dissolution, which leads to less surface roughening and pitting, especially around intermetallic inclusions. A more continuous and lower defect conversion coating forms on the alkaline treated alloy surface and this leads to greater corrosion inhibition as evidenced by a $\sim 10\times$ greater R_p and a more noble E_{pit} . The corrosion inhibition also results from the formation surface oxides on the Cu intermetallic sites, which serve to inhibit the chemisorption of dissolved oxygen, hence its reduction.

CHAPTER 8. EFFECTS OF CURING TEMPERATURE AND TIME ON THE CORROSION INHIBITION PROVIDED BY THE TCP COATING ON AA2024-T3

8.1 Introduction

The TCP coating provides corrosion protection to AA2024 by serving as a barrier layer, as shown in Chapter 5. It is evidenced by that the polarization resistance, R_p , is 10-100× greater for the coated alloys as compared to the uncoated controls (Chapter 6). However, it is noted that the coating appears to possess some hydrated channels and or defects through which solution species and dissolved O_2 can be transported to localized regions of the underlying metal.

A question of interest is, is there any beneficial effect gained by curing the TCP coating after formation? In other words, can the defect density in the coating be reduced through controlled curing? In one of only two reports describing curing effects, Guo and Frankel showed that long-term (48 h) atmospheric curing produces small cracks in the TCP coating.¹⁹⁸ The authors, however, did not report how the corrosion protection was impacted by these coating alterations. We reported an interesting preliminary finding that atmospheric curing of TCP-coated AA2024 at room temperature for 72 h increased R_p from $\sim 10^5$ to $10^9 \Omega\cdot\text{cm}^2$.¹⁹⁹ This significant increase in R_p , reflective of improved barrier properties, was only observed on a few of the coated samples tested.

To date, no systematic study has been conducted on how curing affects the physical structure and corrosion protection of TCP coatings on aluminum alloys. Herein, we address this knowledge gap by focusing on the following two questions:

- (1) Is there any reproducible effect of the curing temperature and time on the physical structure and electrochemical properties (*i.e.*, corrosion protection) of the TCP coating on AA2024?
- (2) If there is a reproducible effect, then what is the associated mechanism?

8.2 Results

8.2.1 Curing temperature.

Figure 8.1 shows the weight loss of a scraped TCP powder sample recorded by thermogravimetric analysis (TGA) during a temperature ramp from 25 to 450 °C under N₂. There is a small but progressive weight loss with temperature up to 290 °C and a more distinct 2% weight loss at temperatures above 290 °C. The first transient is attributed to desorption of water trapped within hydrated channels and or defects of the coating. The distinct weight loss at 290 °C is ascribed to the decomposition of hydroxides (*e.g.* CrOOH, or Cr(OH)₃) that are components of the coating.²⁰⁰ The relatively low weight loss seen for the TCP coating is in contrast to the upwards of 40% weight loss seen for chromate conversion coatings at temperatures greater than 300 °C.²⁰⁰ The dehydration observed at temperatures around 100 °C is of technical interest since this is within the service temperature range that TCP coatings experience in the field. Dehydration during ambient curing is a root cause for the loss of corrosion protection provided chromate conversion coatings on aluminum.²⁰⁰ In contrast, as seen below, dehydration of the TCP coating and the associated physical and chemical changes serve to enhance the corrosion resistance of the coating.

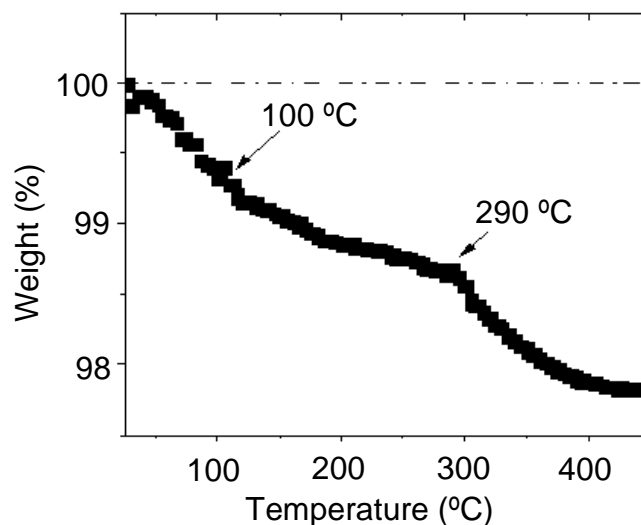


Figure 8.1 Weight loss of a TCP coating during thermogravimetric analysis under an N₂ atmosphere. The sample was obtained by carefully scraping the coatings from three TCP-coated AA2024 specimen surfaces using a sharp blade.

Figure 8.2A and B present polarization resistance (R_p) and corrosion current density (i_{corr}) data, respectively, for TCP-coated and uncoated AA2024 samples. The data were recorded after curing the samples overnight (12-18 h) in ambient air at different temperatures. After overnight curing at RT and 55 °C, R_p for the uncoated samples was $1.94 (\pm 0.23) \times 10^5$ and $1.42 (\pm 0.18) \times 10^5 \Omega\cdot\text{cm}^2$, respectively. These values are in the same range of those for a coated sample, $1.79 (\pm 0.22) \times 10^5 \Omega\cdot\text{cm}^2$ and $2.39 (\pm 0.35) \times 10^5 \Omega\cdot\text{cm}^2$, cured at RT and at 55 °C. This is attributed to formation of a more continuous and defect-free Al oxide layer. After curing at 100 °C, the R_p values for the TCP-coated and uncoated samples became significantly different. The nominal R_p for the coated sample was $3.72 (\pm 0.54) \times 10^5 \Omega\cdot\text{cm}^2$, which was about 2x

greater than that of the uncoated sample, $1.19 (\pm 0.07) \times 10^5 \Omega \cdot \text{cm}^2$. Inversely, i_{corr} decreased by 2x as the temperature increased from RT to 100 °C. A noteworthy difference was observed for samples cured at 150 °C. R_p decreased significantly to ca. $3.02 (\pm 0.22) \times 10^4 \Omega \cdot \text{cm}^2$; a value 2x smaller than the value for uncoated samples after curing at 150 °C and 10x smaller than the values at other temperatures. In contrast, for the uncoated samples, the nominal R_p value decreased by 2x as the curing temperature increased from RT to 150 °C, $0.80 (\pm 0.10) \times 10^5 \Omega \cdot \text{cm}^2$, due to formation of more defective oxide films at high temperatures.²⁰¹ This R_p value after curing at 150 °C is comparable to that for the uncoated samples right after deoxidizing (ca. $3 \times 10^4 \Omega \cdot \text{cm}^2$).¹⁹⁹ Consistent with this, i_{corr} increased by 10x for samples cured at 150 °C as compared to those at RT.

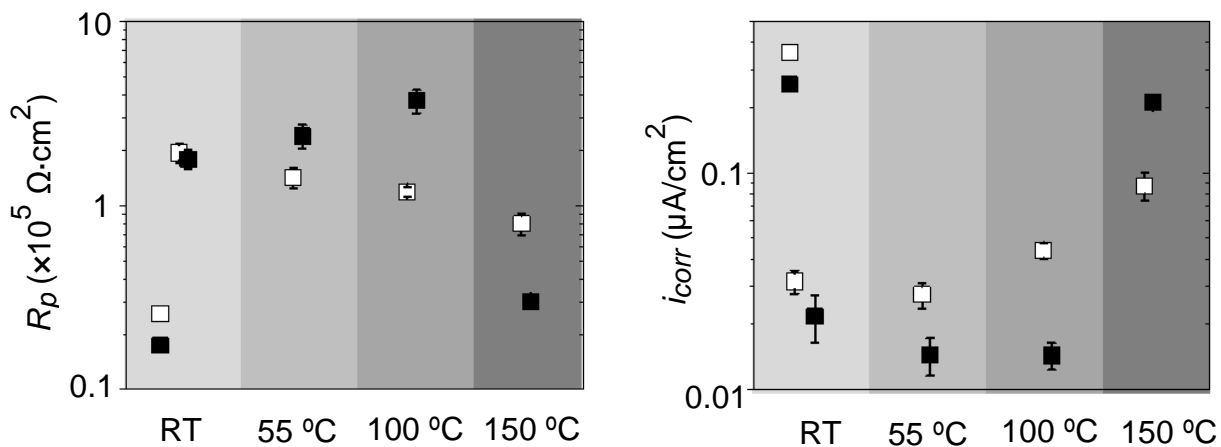


Figure 8.2 (A) Polarization resistance, R_p , and (B) corrosion current density, i_{corr} data for the TCP-coated (■) and uncoated (□) AA2024 after overnight curing in air at varied temperatures: room temperature (RT), 55, 100, and 150 °C. The measurements were conducted in naturally aerated 0.5 M Na_2SO_4 . Each datum is an average value of 3 samples.

Figure 8.3 presents the electrochemical impedance spectra for TCP-coated AA2024 after overnight curing at the different temperatures. Table 9.1 shows the best-fit parameters of the experimental data for RT, 55, and 100 °C to the equivalent circuits shown in Chapter 2. The phase-frequency profiles (Fig. 8.3B) show two distinct time constants (peaks) for the coated AA2024 cured at RT, 55, and 100 °C. The higher-frequency ($\sim 10^3$ Hz) time constant arises from the hydrated channels and defects of the coating (R_{po}), while the lower-frequency (~ 100 Hz) time constant is associated with the corrosion of the underlying exposed metal (R_p) (see Chapter 2). The high-frequency impedance R_{el} , as shown in the impedance-frequency profile (Fig. 8.3A), is essentially the bulk electrolyte resistance that is about $20 \Omega \cdot \text{cm}^2$. R_{po} is the electrolyte resistance in the hydrated channels and or defects of the coating. The fact that that R_{po} increases with temperature up to 100 °C is consistent with a decreasing number of hydrated channels and or defects, or a shrinkage of the dimension of these. The R_p values are consistent with the data in Fig. 8.2A that were obtained from polarization curves. Q_{po} and n_{po} are mathematical parameters that are usually used to calculate the effective coating capacitance by $C_{po} = Q_{po}^{1/n_{po}} R_{po}^{1/n_{po}-1}$.⁷⁶⁻⁷⁷ The C_{po} value decreases as the temperature increases from RT to 100 °C, which is mainly attributed to structural changes as shown in Figure 8.4.

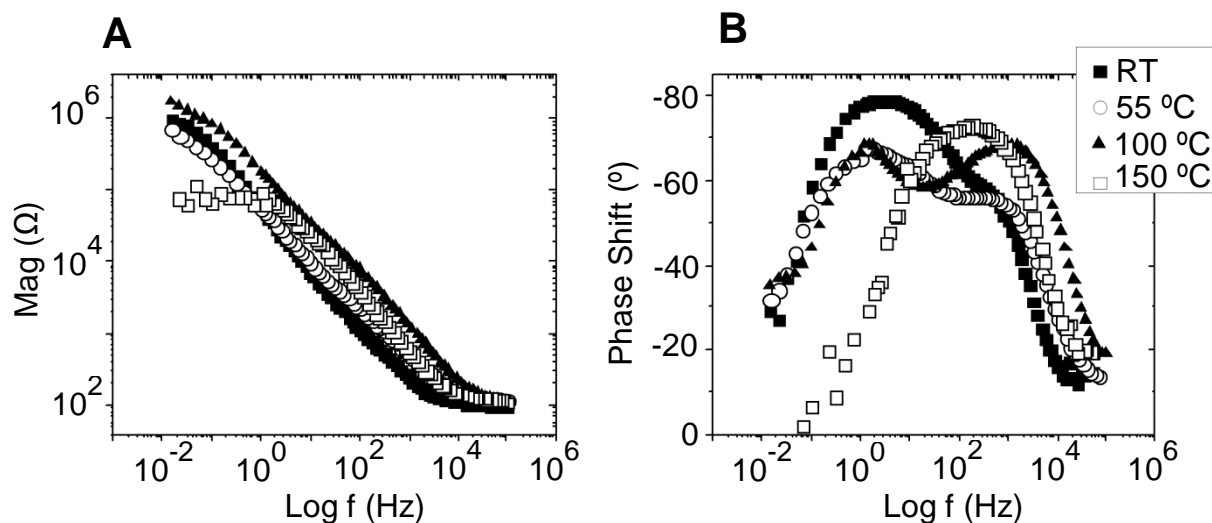


Figure 8.3 Bode plots for the TCP-coated AA2024 at E_{corr} after overnight curing at the various temperature: room temperature (RT, ■), 55 (○), 100 (▲), and 150 °C (□). Three measurements were made in naturally aerated 0.5M Na₂SO₄.

Table 8.1 Best-fit parameters from experimental EIS results of the TCP-coated AA2024 after overnight curing at varied temperatures: room temperature (RT), 55, 100, and 150 °C. The measurements were conducted in naturally aerated 0.5 M Na₂SO₄ at room temperature.

Temp (°C)	R_{el} ($\Omega \cdot \text{cm}^2$)	Q_{po} ($\times 10^{-6} \text{ s}^n / (\Omega \cdot \text{cm}^2)$)	n_{po}	C_{po} ($\mu\text{F} / \text{cm}^2$)	R_{po} ($\Omega \cdot \text{cm}^2$)	Q_{dl} ($\times 10^{-6} \text{ s}^n / (\Omega \cdot \text{cm}^2)$)	n_{dl}	R_{ct} ($\times 10^5 \Omega \cdot \text{cm}^2$)
RT	22	31.05	0.80	1.84	261	20.21	0.93	2.73
55	19	17.92	0.72	0.86	1554	4.22	0.87	3.48
100	20	24.79	0.84	0.21	4717	4.58	0.74	3.95
150	25	-	-	-	-	6.57	0.81	0.29

Figure 8.4A presents data for the apparent porosity or defect parameter change in the coating after overnight curing at the different temperatures. The hypothesis is that curing at elevated temperature dehydrates the coating causing it to shrink and become more continuous over the surface. The dimensions and or number of hydrated channels

and defects are expected to decrease. A more continuous and less defective coating would explain the increased R_p values. The defect parameter, which is reflective of the fraction of hydrated channels and or defects, decreases modestly from 0.25 to 0.13% as the overnight-curing temperature increases from RT to 100 °C. Additionally, a more defect-free Al oxide layer likely forms on the exposed regions of the Al alloy where the channels and defects originally exist. Shrinkage or densification of the coating is evident in the ellipsometric data presented in Figure 8.4B. Clearly, the coating thickness decreases with curing temperature up to 100 °C. Figure 8.4C presents the static water contact angle for the TCP-coated alloy as a function of the curing temperature. The contact angle increases from $7.9 (\pm 1.3)^\circ$ at RT, to $20.1 (\pm 4.3)^\circ$ at 55 °C, and to $102.2 (\pm 2.8)^\circ$ at 100 °C. As the coating becomes less hydrated and shrinks, the coating becomes more hydrophobic.

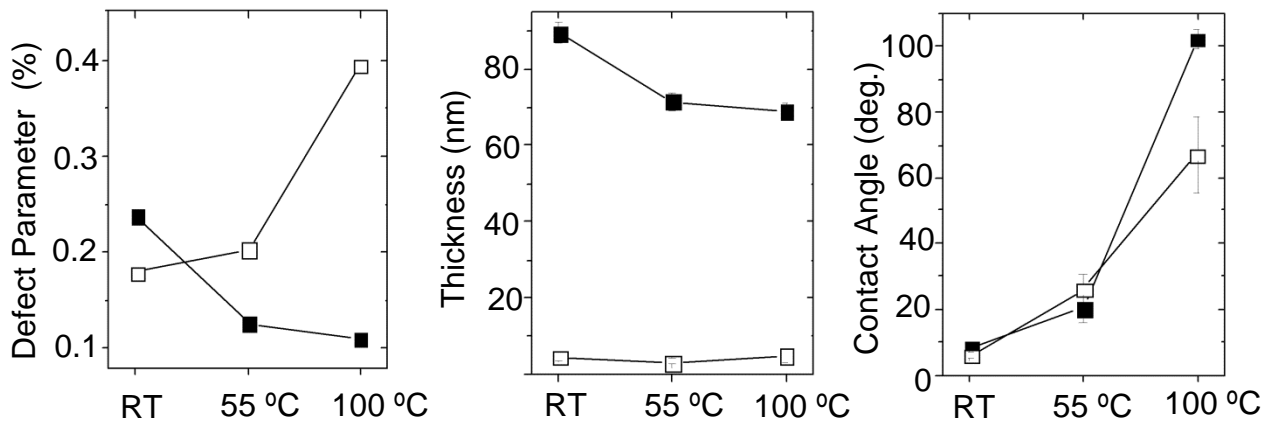


Figure 8.4 (A) Defect parameter, (B) coating thickness, and (C) contact angle of static water on the TCP-coated (■) and uncoated (□) AA2024 after overnight curing in air at various temperatures: room temperature (RT), 55 and 100 °C. Each datum is an average of 3 measurements. The open squares in (B) represent the thickness of Al-oxide layers.

8.2.2 Curing time.

Figure 8.5 presents the effects of curing time at room temperature (RT) on the physical properties of the TCP coating. Fig. 8.5A shows that the coating is about 90 nm thick at formation and remains the same thickness during the 7-day curing period. This thickness is consistent with other published data.^{72, 198-199, 202} However, the static water contact angle increases gradually from 5.6 (± 1.8) ° after overnight curing to 63.1 (± 0.3) ° after 7-day curing, as shown in Fig. 8.5B. Clearly, the coated surface becomes more hydrophobic with time, suggestive of a chemical change. The chemical change is linked to the Cr(III) oxides.²⁰⁰ This is evidenced by the much smaller water contact angle of the non-Cr TCP-coated alloy surface compared to that of the full TCP-coated surface throughout the whole 7-day curing, as seen in Fig. 8.5B. Furthermore, a thin Al oxide film of several nanometers in thickness forms on the uncoated sample during curing at RT, as shown in Fig. 8.5A.

Figure 8.6 shows effects of curing periods on the electrochemical properties of the TCP-coated AA2024 during curing in air at room temperature (RT): (A) E_{corr} and (B) R_p . The E_{corr} value shifts in the positive direction as the samples were cured for a longer period, as shown in Figure 8.6A. This is attributed to formation of Al oxides at the bottom of the channels and defects in the TCP coating on the alloys, but only at the Al matrix sites. A similar trend is also seen for the uncoated samples. Figure 8.6B shows the R_p values for the TCP-coated and uncoated samples as functions of the curing period. The uncoated sample after 1-day curing exhibits an R_p value (ca. $2 \times 10^5 \Omega \cdot \text{cm}^2$)

that is about 10x greater than that right after deoxidization (ca. $3 \times 10^4 \Omega \cdot \text{cm}^2$). This is due to formation of an inert Al oxide film. The R_p value stays relatively constant in this range through the entire 7-day curing period. In contrast, R_p for the TCP-coated alloy increases by about 4x, from ca. $2 \times 10^5 \Omega \cdot \text{cm}^2$ after overnight curing to ca. $8 \times 10^5 \Omega \cdot \text{cm}^2$ after 7-day curing. This is attributed to dehydration of the coating, which reduced the number of defects and hydrated channels, as well as the formation of a more defect-free Al oxide film in those uncoated regions that restricts access of solution species and dissolved O_2 to the metal surface.

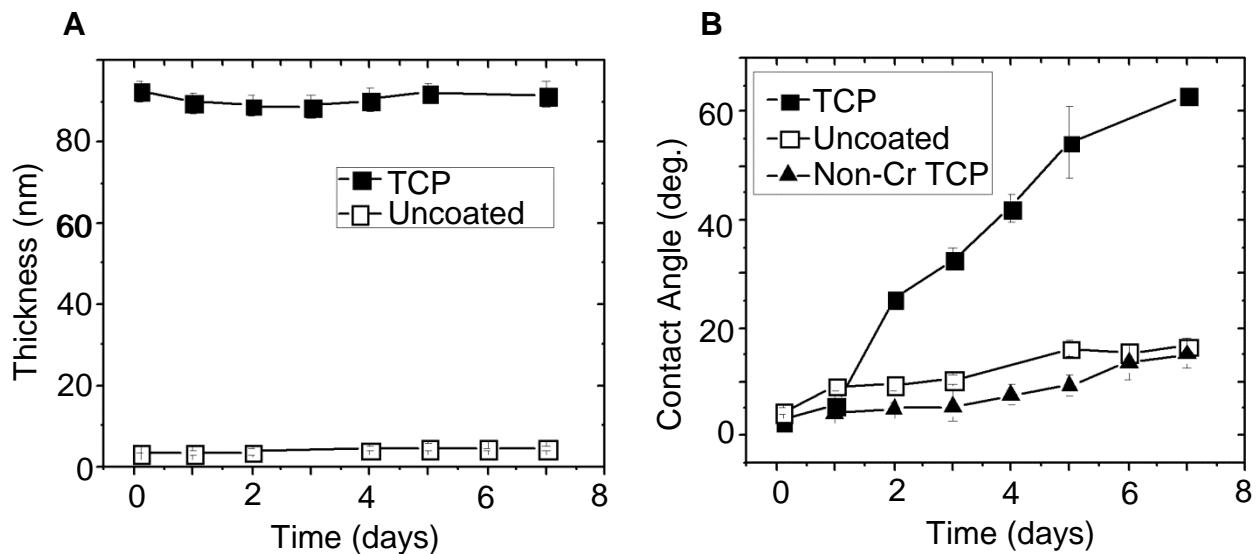


Figure 8.5 Effects of curing period on the physical and chemical properties of the TCP-coated AA2024 during curing in air at room temperature (RT): (A) thickness of TCP coatings for the coated samples (■) and that of Al oxide films for the uncoated samples (□), and (B) contact angle of static water on the uncoated (□), TCP-coated (■) and non-Cr TCP-coated (▲) samples. Each datum is an average of 3 measurements.

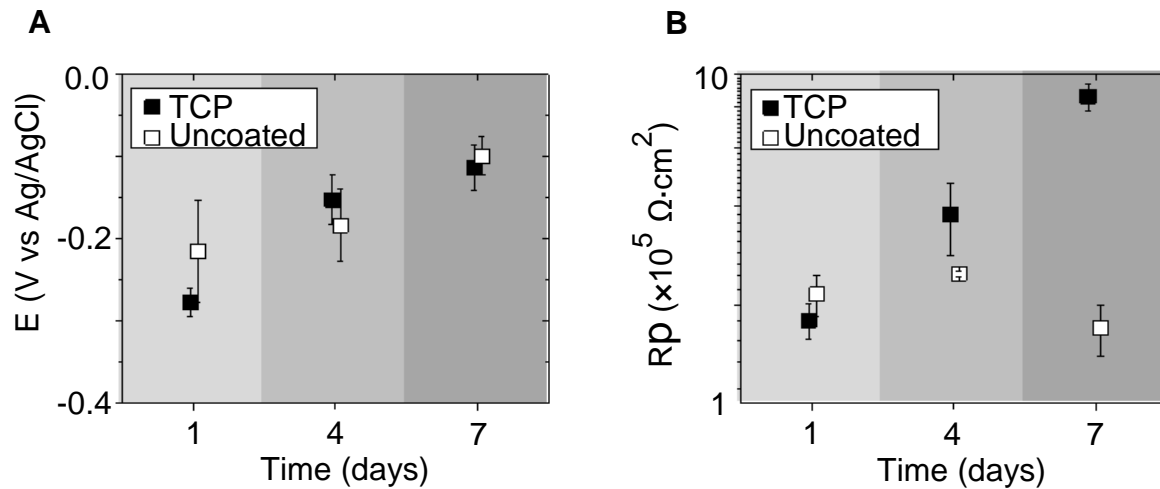


Figure 8.6 Effects of curing periods on the electrochemical properties of the TCP-coated (■) AA2024 during curing in air at room temperature (RT): (A) E_{corr} and (B) R_p . Data of the uncoated (□) is shown as control. Each datum is an average of 3 measurements.

8.3 Discussion

8.3.1 Effect of the curing temperature and time

In summary, some modest reproducible benefits were found for cured TCP coatings. The physical and chemical properties of the coating were found to vary with the curing temperature and time, and both had an effect on the corrosion protection provided by the coating. For temperatures up to 100 °C, R_p increases and i_{corr} decreases for the coated alloys because (i) the coating dehydrates and densifies reducing the number of hydrated channels and defects, and (ii) growth of a more defect-free aluminum oxide layer on those exposed regions of the alloy. The increase in R_p is a factor of 2 when comparing the performance of the coating cured at RT versus the coating cured at 100 °C. Dehydration occurs as the temperature increases (Figs. 9.2 and 9.4). The 1st dehydration step at temperatures centered around 100 °C is likely through evaporation of water trapped within channels and defects of the coating. With

this loss of water, the coating becomes thinner. Consistent with the decrease in the number of hydrated channels and defects, the apparent porosity (*i.e.*, defect parameter measure) of the coating decreases by about 2x after curing at 55 and 100 °C compared to that at room temperature (RT) (Fig. 9.4A). The loss of water leads to shrinkage of the coating as the thickness, determined by ellipsometry, decreases from about 90 nm at RT to about 70 nm at 55 and 100 °C (Fig. 9.4B). In addition, curing at elevated temperature (100 °C) also induces formation of a more defect-free Al oxide layer on the exposed areas of the alloy. This also contributes to a decrease in the apparent coating porosity and the increase R_p . The coating also becomes progressively more hydrophobic with curing temperature as evidenced by the increasing static water contact angle from 7.9 ± 1.3 at RT to 102.2 ± 2.8 degrees at 100 °C (Fig. 9.4C). We showed that this change in contact angle is largely due to the presence of Cr(III) in the coating as the same hydrophobic changes were not observed for hexafluorozirconate coatings devoid of Cr(III). In summary, overnight curing at up to 100 °C produces modest increases in the corrosion resistance of the coatings, as assessed from R_p values, by a factor of two. Unfortunately, we did not observe any of the significantly increased in R_p values ($\sim 10^9 \Omega\cdot\text{cm}^2$) as was previously reported.¹⁹⁹ The decreased apparent porosity is an indication of fewer hydrated channels and defects as pathways for the transport of solution species and dissolved O₂ to the underlying metal surface.

Curing at 150 °C caused deleterious changes in the coating. At this temperature, significant coating dehydration occurs such that cracks form and sections of the coating detach from the surface. This exposes an increased fraction of the alloy surface to

contact with the electrolyte solution. As a consequence, R_p decreases to the same range as that for the bare sample (ca. $3 \times 10^4 \Omega \cdot \text{cm}^2$) right after desmutting. Clearly, curing at this elevated temperature is not recommended.

Besides the curing temperature, the curing time can affect the structure of the TCP coating and the corrosion protection it provides on AA2024. With curing at RT, the coating thickness (Fig. 9.5A) does not appear to change significantly but the wettability does. There is a progressive increase in the static water contact angle from 5.6 ± 1.8 at day 1 to 63.1 ± 0.3 degrees at day 7. Importantly, R_p increases by 4x during this period from 2×10^5 to $8 \times 10^5 \Omega \cdot \text{cm}^2$ (Fig. 9.6B). Frankel *et al.* reported possible shrinkage of the coating for long periods of atmospheric curing (48 h). We did not observe any significant shrinkage, at least under our curing conditions (Fig. 9.5A). Therefore, for curing time at RT, unlike the effects of curing temperature, a thinning or densification of the coating is not the explanation for the increased R_p . We attribute the increased corrosion resistance to (i) growth of a more defect-free aluminum oxide layer on the exposed areas of the alloy and (ii) the increased hydrophobicity of the coating. Changes associated with the Cr(III) species cause the coating to become more hydrophobic over time. The new structure inhibits water from contacting the underlying metal surface.

8.3.2 Effect mechanisms

For the coatings cured at elevated temperature, the 2x increase in R_p is attributed to a reduction in the number of hydrated channels and defects because of (i) thinning of the coating due to dehydration, (ii) changes in the chemical nature of the

Cr(III) species that make the coating more hydrophobic and (iii) growth of a more defect-free aluminum oxide layer on the exposed regions of the alloy surface. For the coatings cured at room temperature for different periods of time, the 4x increase in R_p occurs because of (i) changes in the chemical nature of the Cr(III) species that make the coating more hydrophobic and (ii) growth of a more defect-free Al oxide layer on the exposed regions of the alloy surface. Buchheit *et al.* used the extended x-ray fine structure technique and found a shortening in Cr(III)-Cr(III) nearest neighbor distances upon dehydration of the Cr(III) oxide layer.²⁰⁰ This leads to a short-range structural rearrangement and polymerization of these Cr(III) oxides.^{200, 203} While the corrosion resistance of the coating can be improved with curing, the more hydrophobic coating might be a disadvantage for topcoat adhesion as many of the coatings used are aqueous-based. This point remains to be studied.

8.4 Conclusion

The effects of curing temperature and time on the electrochemical properties (*i.e.*, corrosion resistance) of TCP coatings on AA2024-T3 were investigated. The TCP coating undergoes dehydration and condenses when cured at elevated temperatures. This along with the growth of a more defect-free aluminum oxide layer occurs during curing overnight at elevated temperature (≤ 100 °C). The coating also becomes progressively hydrophobic with the loss of water and associated chemical changes. All three contribute to the improved corrosion protection. However, curing at 150 °C causes excessive dehydration and shrinkage of the coating such that it undergoes severe

cracking and even detachment from the metal surface. A longer curing period at room temperature enhances the corrosion resistance by 4x of the TCP-coated alloy by forming an aluminum oxide layer on the metal sites exposed in the coating channels and defects. The improvement in corrosion inhibition with curing at room temperature is also associated with increasing hydrophobicity of the coating. The best improvement in corrosion resistance was seen for coatings cured at room temperature for 7 days.

CHAPTER 9. CORROSION PROTECTION PROVIDED BY OTHER NON-CHROMIUM CONVERSION COATINGS ON AA2024-T3

9.1 Introduction

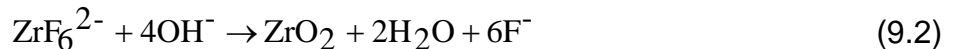
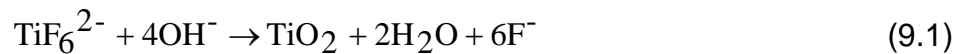
Besides the trivalent chromium process (TCP) coating, several non-chromium conversion coating alternatives have been developed to match the process and technical performance of the chromate conversion coating (CCC). Chapter 1 has introduced the Zr/Ti-based coating that has fluorozirconate and fluorotitanate in the coating bath formula. Henkel developed it in early 1980s as known by Alodine® 5200.⁶² Previous study has showed that Alodine® 5200-coated AA2024 suffered corrosion within 48 hours during a neutral salt fog test (ASTM B 117).⁶⁴ Another member in the fluorozirconate coating family is the Zr/Zn-based conversion coating, namely the non-chromium pretreatment (NCP) coating. This coating contains the soluble inhibitor $ZnSO_4$ in the coating solution⁶⁶ and it is currently under development in NAVAIR.

However, little is known about the formation, structure, and basic electrochemical properties of the 5200 and NCP coatings on AA2024. This chapter addresses this knowledge gap by investigating the formation mechanism, physical structure and basic electrochemical properties of the 5200 and NCP coatings on AA2024. Their corrosion protective properties are compared with the TCP coating. This chapter also reports the coating performance in the galvanic coupled system during two accelerating corrosion tests: (i) full immersion in NaCl-containing electrolyte solutions at room temperature (ASTM D6943) and (ii) exposure in moist SO_2 at 40 °C (ASTM G87).

9.2 Results

9.2.1 Formation of Ti/Zr coatings

Figure 9.1 presents the open circuit potential (OCP) of an AA2024 sample and the pH in the interfacial region, both vs. time, recorded during the formation of the 5200 coating. A tungsten microelectrode was positioned near the alloy surface during the coating formation. The potential of the tungsten microelectrode changes proportionally with the solution pH.^{87-89, 92} For a better recording of the pH change, the immersion was prolonged from the usual 2 to 6 min. Two distinguishable regions are seen. For the first about 10 s, the OCP of the alloy (solid squares) shifted negatively to about ca. -0.9 V vs Ag/AgCl, during which time the alloy surface is activated by F⁻ and H⁺ in the coating bath; the Al oxide layer is dissolved. The consumption of H⁺ by cathodic reactions, such as hydrogen discharge and oxygen reduction, causes the interfacial pH increase, as shown by the open squares in Fig. 9.1. This pH increase initiates hydrolysis of fluorometalates in the coating bath to form metal oxide that deposits on the surface, as shown by the following two chemical reactions:



For the remaining immersion period, OCP stabilizes at about -0.9 V vs Ag/AgCl and the surface pH also stabilizes at about 8. After the 6-min immersion, the microelectrode was removed from the alloy surface and the pH value re-equilibrates to 2.0-3.5, which is the value of the coating bath.

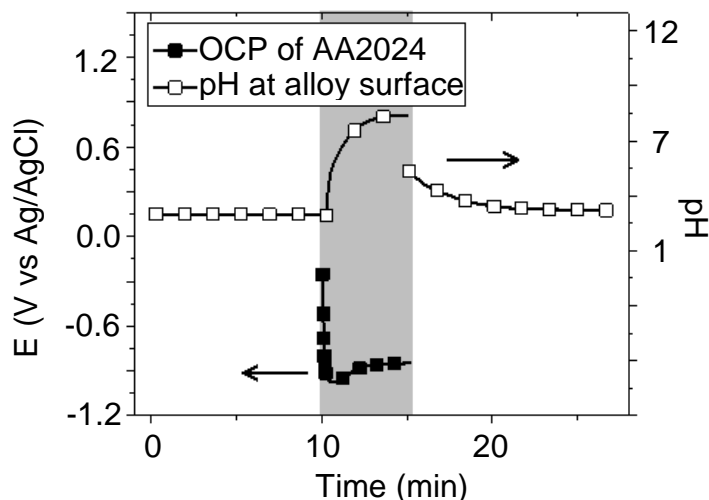


Figure 9.1 Open circuit potential of the AA2024 sample (dark marks) and the interfacial pH (open marks) at the alloy surface recorded during formation of the 5200 coating (grey background). The pH traces with the white background reflect the value of the coating solution. The coating was formed by immersion at room temperature (21-27 °C).

9.2.2 Chemical Structure

Figure 9.2 presents (A) an SEM micrograph of the surface of a 5200-coated AA2024 sample, along with (B) energy-dispersive x-ray (EDAX) spectra collected on the Al terrace site and (C) line profiles across two intermetallic compounds. The alloy surface is relatively clean and features several Cu-rich intermetallic compounds and pits. The diameter of these intermetallic particles ranges from 10 to 15 μm in the long dimension. The x-ray spectrum collected on the Al terrace (within the red box in Fig. 9.2B) shows distinct signals for Zr ($L\alpha_1$), O ($K\alpha_1$), and Ti ($K\alpha_1$), all characteristic components of the 5200 coating. EDAX line profiling across the two intermetallic particles shows that both particles are enriched with Cu, as evidenced by the increased signal at ca. 20 and 70 μm (Fig. 9.2C). Enhanced signals for Zr ($L\alpha_1$), O ($K\alpha_1$), and Ti ($K\alpha_1$) are also seen at the Cu-rich intermetallic sites relative to the surround Al sites (Fig.

9.2D-F). This is a common observation from examining several 5200-coated samples. A greater interfacial pH change is expected near these sites due to the more signal oxygen reduction reaction kinetics and this presumably leads to greater coating deposition. In summary, the 5200 coating appears to form over most of the alloy surface including the intermetallic inclusions.

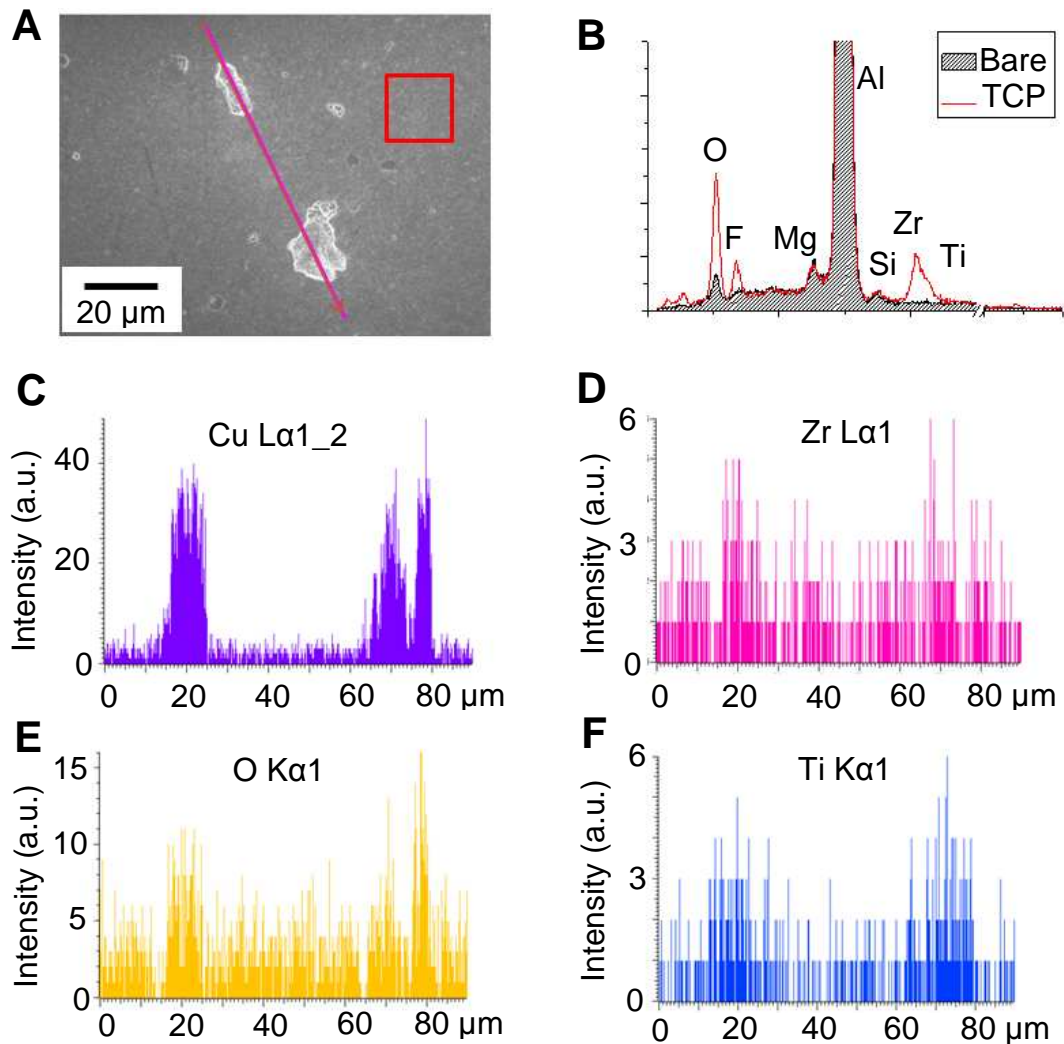


Figure 9.2 An (A) SEM image, (B) EDX spectrum at the Al terrace site (boxed area), and (C) elemental line profiles across two Cu-rich intermetallic compounds in the 5200-coated AA2024. Profiles were recorded after overnight aging in air.

Figure 9.3 presents (A) an SEM micrograph of the surface of a NCP-coated AA2024 sample (no sanding or polishing), along with (B) energy-dispersive x-ray (EDAX) spectra collected on the Al terrace site and (C) line profiles across two intermetallic compounds. Similar to the 5200 and TCP coatings,¹⁹⁹ EDAX line profiling across the Al terrace and the two intermetallic particles shows that the enhanced signals for Zr ($L\alpha_1$), O ($K\alpha_1$), and Ti ($K\alpha_1$) at the Cu-rich intermetallic sites relative to the surround Al sites (Fig. 9.3B-F). This indicates that the NCP coating forms across the alloy surface and enriches at the intermetallic inclusions.

Figure 9.4 presents the XPS depth profiles through the (A) 5200 and (B) NCP coatings on AA2024. The characteristic coating elements, e.g. Zr, Ti, O, and F, are detected for the 5200 coating (Fig. 9.4A). The Ti, Zr and O signals are elevated for the first ca. 30 nm into the coating. They are attributed to titania (TiO_2) and zirconia (ZrO_2), respectively. The O signal does not start to decrease until ca. 60 nm. This decrease is accompanied by an increase in the Al signal. This is the Al-O-F interfacial region. The F signal is virtually constant through the coating. The coating thickness is on the order of about 30 nm with an Al-O-F interfacial region. In contrast, the NCP coating shows a biphasic structure, similar to the TCP coating, with a ZrO_2 top layer and AlF_3/Al_2O_3 interfacial layer (Fig. 9.4B). The top layer is about 40 nm thick and the interfacial layer is about 20 nm, which makes the overall coating thickness of about 60 nm. However, it should be noted that measurements *in vacuo* cause shrinkage of the hydrated coating due to loss of water. The true (hydrated) thickness of the 5200 and NCP coatings on

AA2024 is expected to be somewhat greater than the values estimated from this measurement.

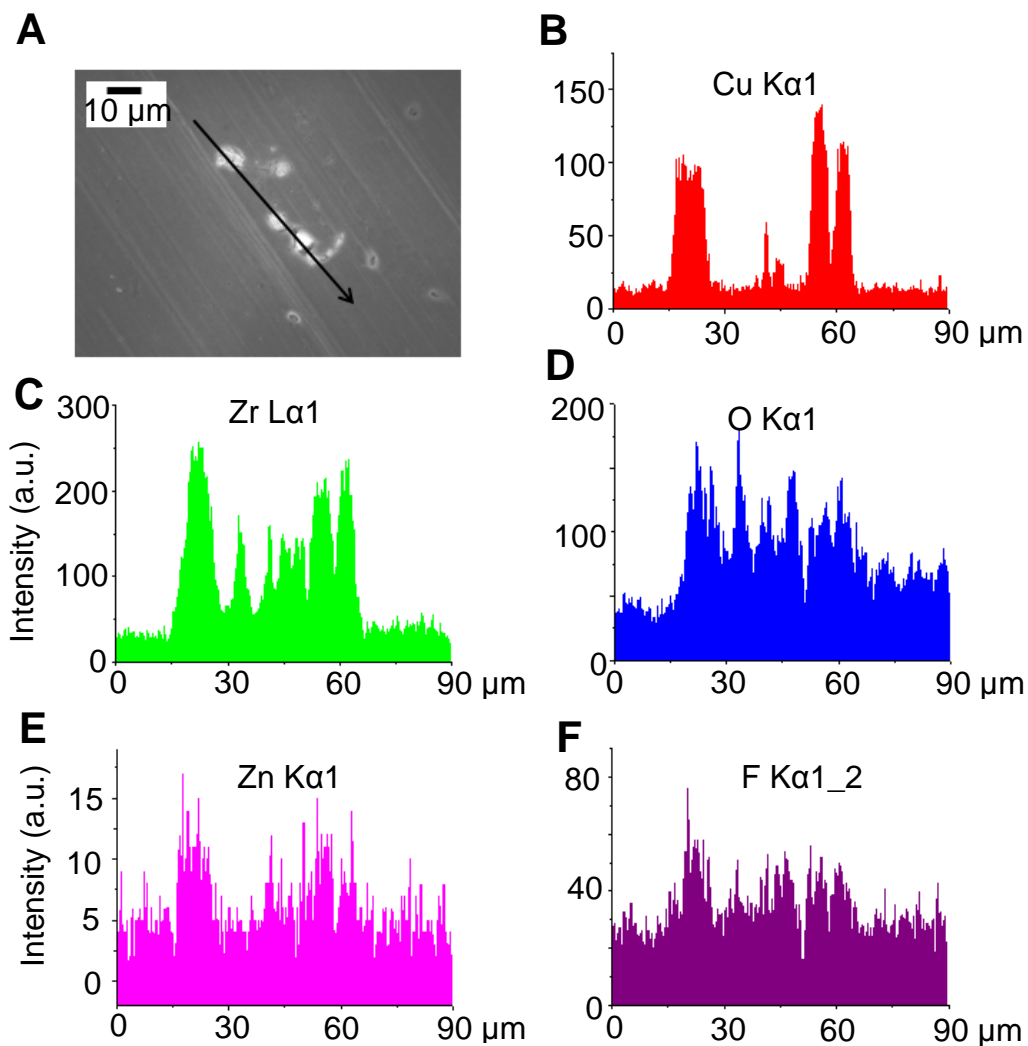


Figure 9.3 An (A) SEM image and (B-F) elemental line profiles for Cu, Zr, O, Zn, and F across the Cu-rich intermetallic compounds in the NCP-coated AA2024. Profiles were recorded after overnight aging in air.

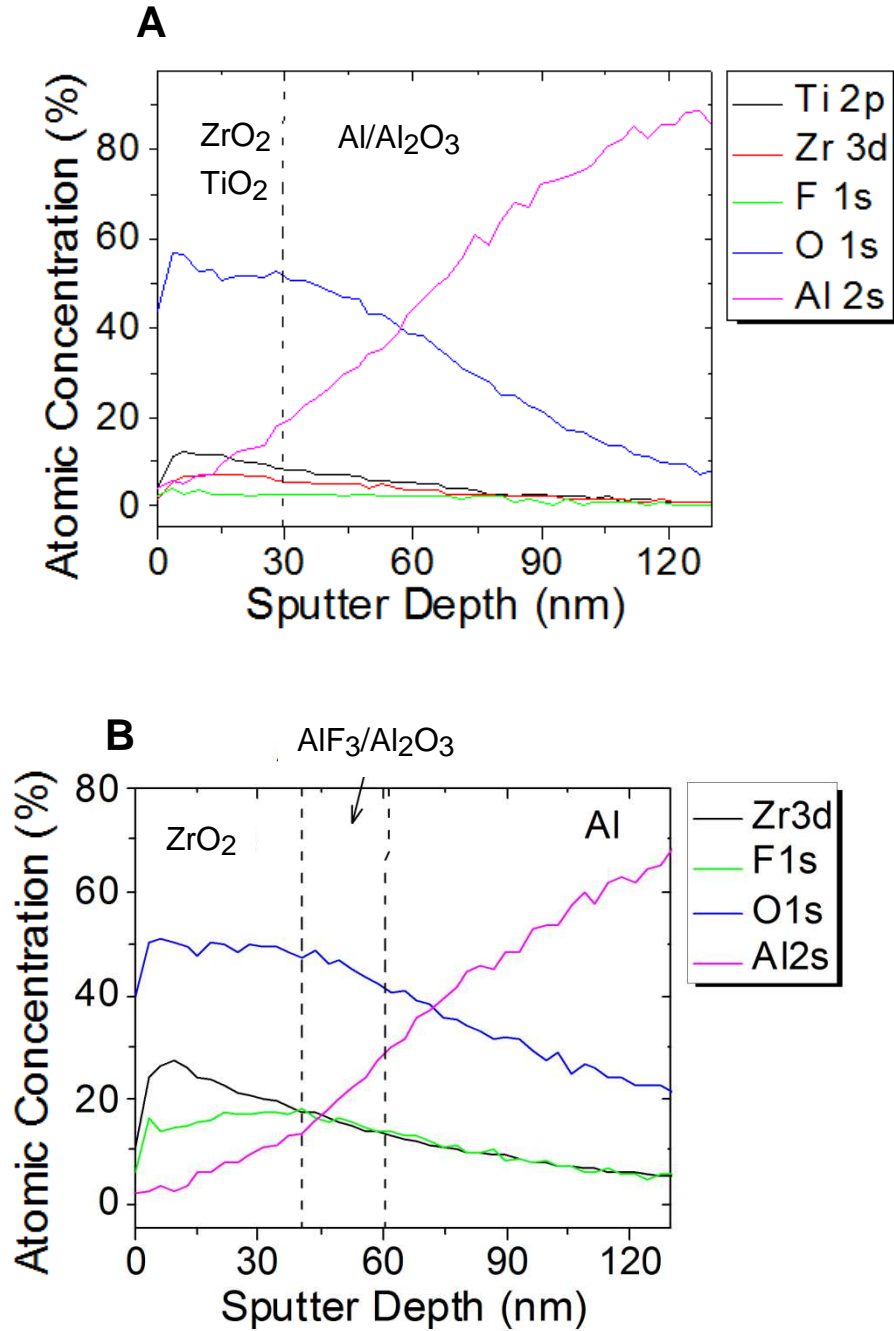


Figure 9.4 Auger depth profiles of several characteristic elements in the (A) 5200 and (B) NCP coatings on AA2024. Dashes lines are approximate boundaries between the coatings and Al matrix at the alloy surface. Data courtesy of Dr. Wayne Jennings from Case Western Reserve University (Swagelok Center for Surface Analysis of Materials).

Figure 9.5 presents TEM images of a cross section the (A) 5200 and (B) NCP coatings at the Al terrace site, and (C) the 5200 coating at the Cu-rich intermetallic sites on AA2024. A layer of Pt was deposited on top of the coating to protect the coating from damage during TEM specimen preparation by focused ion beam (FIB) milling and also to improve the image contrast. Fig. 9.5A shows that the coating is thin ranging from 20 to 30 nm at the Al terrace site (the white arrow and scale bar). There are also places (the black arrow) where the coating appears detached from the metal surface, due to film shrinkage by dehydration *in vacuo*. This is similar to the NCP coating in Fig. 9.5B. Detachment is attributed to the shrinkage of the coating. The NCP coating is about 70 nm thick, which is consistent with the XPS depth profiling data in Fig. 9.4B. Fig. 9.5C shows the 5200 coating at the intermetallic sites. After deoxidation/desmutting in acidic F⁻-rich Smut-Go®, the Al, Mg, and Fe in the Cu-rich intermetallic particles are dissolved leaving only Cu particles resided at the pit bottom. The coating forms in the gaps between particles, which causes the enrichment shown in Fig. 9.2 and 9.3.

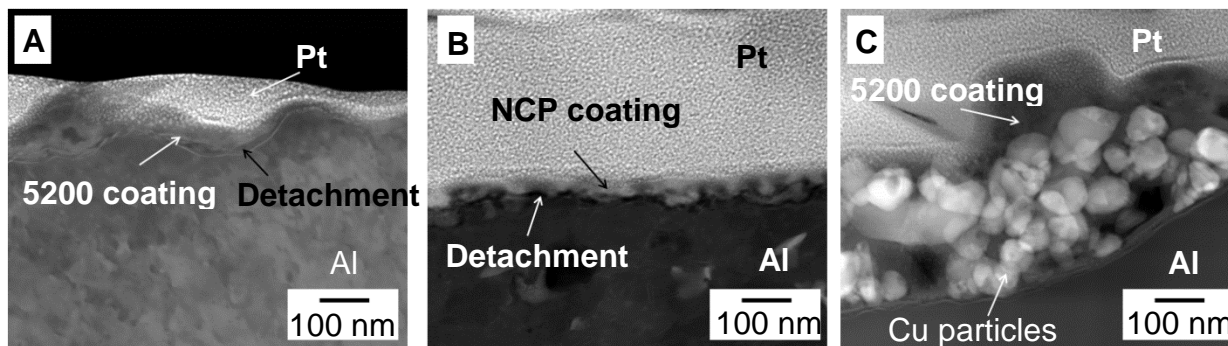


Figure 9.5 TEM images of the cross section of the (A) 5200 and (B) NCP coatings at the Al terrace site, and (C) the 5200 coating at the Cu-rich intermetallic sites on AA2024. The Pt layer is to protect the coating from deformation during TEM specimen preparation using FIB milling. Data courtesy of Mr. Hendrik Colijn from The Ohio State University.

9.2.3 Basic Electrochemical Properties

Figure 9.6 shows typical potentiodynamic polarization curves for 5200-, TCP-, and NCP-coated AA2024 at a slow scan rate of 2 mV/s. Curves for uncoated samples are also shown as control. All the measurements were conducted in air-saturated 0.5 M Na₂SO₄ except for the NCP-coated sample, which was measured in 0.5 M Na₂SO₄ + 0.1 wt% NaCl. It can be seen that no major difference exists in E_{corr} between the uncoated AA2024 and the 5200- and TCP-coated samples, while E_{corr} for the NCP-coated sample shifts in the positive direction. This trend suggests that the 5200 coating affects the kinetics of the anodic and cathodic reactions to similar extents. It is clear that both the anodic and cathodic current densities for the 5200-coated samples are significantly larger than those for the TCP- and NCP-coated samples in the mediums. In fact, the current densities for the 5200-coated sample are nearly identical to those for the uncoated samples (no suppression). The NCP-coated sample exhibits the most reduced anodic current density of the three samples. It should be noted that these NCP-coated alloys were prepared by NAVAIR and then sent via mail to us for electrochemical tests. Thus, the coating may have cured and formed a more stable structure after the 2-week aging before testing. It is also possible that a thicker Al oxide layer forms overfull at Al terrace sites in between the coated regions, which would explain the improved anodic current density suppression.

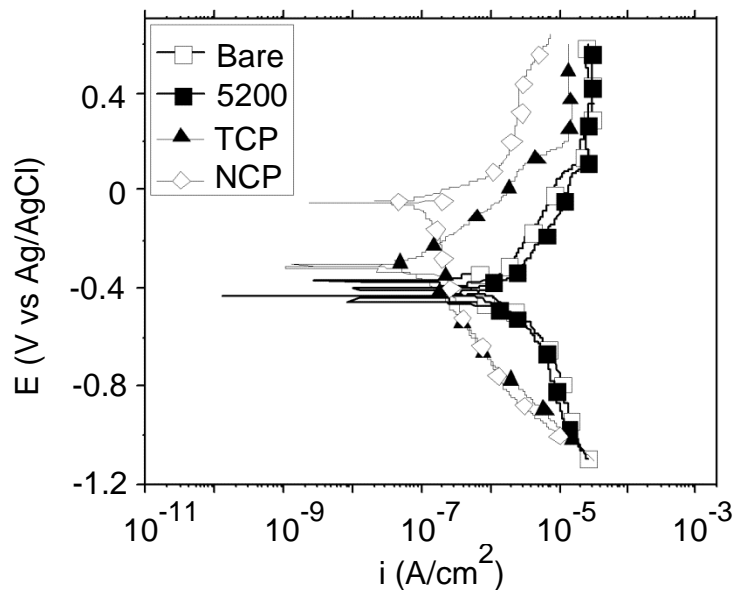


Figure 9.6 Slow-scan potentiodynamic polarization curves recorded for 5200-coated AA2024 in air-saturated 0.5 M Na₂SO₄. Data were also recorded for the uncoated (immediately after degreasing and deoxidation/desmutting) sample, a TCP-coated samples and an NCP-coated sample, for comparison. The scan rate was 2 mV/s. The measurement of the NCP-coated sample was performed in 0.5 M Na₂SO₄ + 0.1% NaCl.

Table 9.1 presents corrosion potential (E_{corr}), polarization resistance (R_p), and defect parameter (P) data for the 5200-coated AA2024. They are compared with the values for TCP- and NCP-coated alloys. Data for the uncoated samples are shown as controls. The R_p values shown here are calculated by taking the inverse of the E vs. i curve at $E_{corr} \pm 30$ mV and they are in an agreement with the values for the 5200-coated AA2024 calculated by the EIS simulation (Table 9.2). Statistical tests show no significant difference in E_{corr} for the 5200-coated (-0.31 ± 0.04 V vs. Ag/AgCl) and uncoated (-0.35 ± 0.04 V) alloys at the 95% confidence level. The TCP-coated samples exhibit an E_{corr} (-0.23 ± 0.03 V) in the same range as the values for uncoated and

5200-coated samples. In contrast, E_{corr} for the NCP-coated samples (-0.15 ± 0.00 V) shifts in the positive direction. The 5200-coated AA2024 specimens exhibit an R_p value ($6.7 \pm 0.6 \times 10^4 \Omega\cdot\text{cm}^2$) that is on the same range as that for the uncoated samples ($6.5 \pm 1.5 \times 10^4 \Omega\cdot\text{cm}^2$). This indicates the coating provides no significant corrosion resistance is on AA2024 in this medium. In contrast, the TCP- and NCP-coated alloys exhibit R_p 's that are $\sim 10\times$ greater than the values for the uncoated and 5200-coated samples. Based on the R_p values, the NCP coating appears to provide comparable corrosion protection to that of the TCP coating on AA2024. This is consistent with the defect parameter data: the 5200 coating exhibits a defect parameter that is $\sim 10\times$ larger than the values for the TCP or NCP coatings. In addition, the 5200 and TCP coatings exhibit β_c and β_a that are in the same range as the uncoated samples, which indicates that these two coatings have no effects on the electrochemical activities (e.g., free energy barrier) for either Al oxidation or O_2 reduction. However, the NCP coating exhibits a greater β_c , which indicates a better passivated surface. This is consistent with the positive shift of E_{corr} for the NCP-coated alloys compared to other treatments. In addition, β_a for the NCP-coated alloy is significantly smaller than that for the other three treatments, which appears to indicate a trend that the NCP-coated alloy is more vulnerable to be attacked on the Al phase. But it should be noted that the NCP-coated samples were tested in a more aggressive Cl^- containing solution that Cl^- causes a more aggressive attack to the anodic Al phase.

Table 9.1 E_{corr} , R_p , and defect parameter for 5200-, TCP- and NCP-coated AA2024. The electrochemical measurements were carried out in air-saturated electrolyte solutions. Data were also recorded for the uncoated alloys (immediately after degreasing and deoxidation/desmutting) as control. The R_p values are calculated by taking the inverse of the slope of the E vs. i curves at E_{corr} (± 30 mV). Each datum is an average value of at least 3 samples.

Treatment	E_{corr} (V vs Ag/AgCl)	R_p ($\times 10^4 \Omega \cdot \text{cm}^2$)	P (%)	β_c (mV/dec)	β_a (mV/dec)	Electrolyte
Bare	-0.31 ± 0.04	5.1 ± 0.7	-	-196 ± 17	218 ± 22	0.5 M Na ₂ SO ₄
5200	-0.35 ± 0.04	6.5 ± 1.0	65 ± 7	-144 ± 10	171 ± 15	0.5 M Na ₂ SO ₄
TCP	-0.23 ± 0.03	64.3 ± 3.3^a	5 ± 3	-190 ± 34	203 ± 24	0.5 M Na ₂ SO ₄
NCP ^b	-0.15 ± 0.01^a	71.3 ± 22.1^a	4 ± 1	-307 ± 93	88 ± 30^a	0.5 M Na ₂ SO ₄ + 0.1% NaCl

^a Significant difference is seen for these values relative to the other unmarked values in the same column.

^b NCP-coated AA2024 were prepared by NAVAIR, Patuxent River, MD.

Figure 9.7 shows the Bode plots of the 5200-coated and uncoated AA2024 in air-saturated 0.5 M Na₂SO₄. Table 9.2 shows the best-fit parameters for the experimental EIS data of the 5200-coated and uncoated AA2024 samples. The equivalent circuits used were shown Chapter 2. In the mag vs log freq plot (Fig. 9.7A), the high-frequency impedance R_{el} is primarily determined by the electrolyte resistance and therefore the values are identical for the coated and uncoated samples. The low-frequency impedance R_p value represents the polarization resistance at the coating/metal interface and it can be seen that there is no significant difference between the coated and uncoated samples. The phase shift vs. log freq plot (Fig. 9.7B) reveals one time constant for the uncoated AA2024, which represents the double layer on the metal surface. In contrast, two distinct time constants are seen for the 5200-coated alloy sample and this indicates a porous structure of the coating. However, it should be noted that the phase shifts for both samples are smaller than 90° that is expected for an ideal capacitor. Therefore, the constant phase elements (CPEs) were used to represent the inhomogeneous electrolyte/coating and coating/metal interfaces. Its impedance can be expressed as $Z=(j\omega)^{-n}Q^{-1}$,⁷⁶ where n is a ratio that reflects the heterogeneity of the coated alloys. The effective capacitance is determined according to $C_{eff}=Q^{1/n}R^{1/n-1}$.⁷⁶

⁷⁷ The C_{eff} for the 5200 coating is much greater than our previously reported value for the TCP coating (2.49 μF/cm²).²⁰⁴ This is attributed to a more porous structure for the 5200 coating that exhibits a greater surface area than the TCP coating.

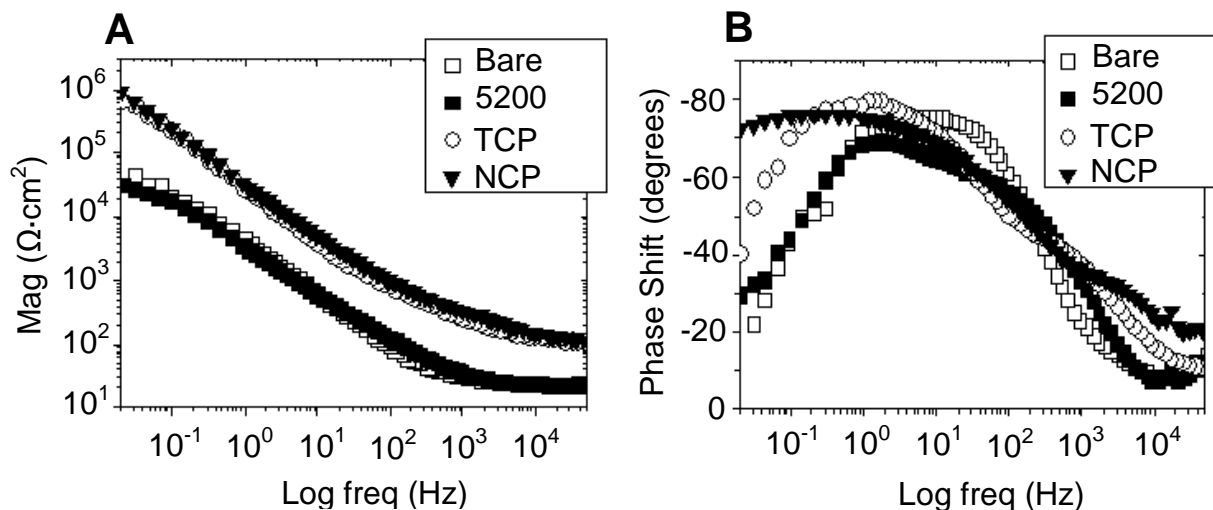


Figure 9.7 Bode plots of the 5200-coated and uncoated AA2024 in air-saturated 0.5 M Na_2SO_4 .

9.2.4 Galvanic Couples of 5200-coated AA2024-T3 and Ti-6Al-4V fasteners.

The corrosion protective property of the 5200 coating is also assessed in the galvanic couples of the 5200-coated AA2024-T3 panels and the Ti-6Al-4V fasteners by investigating the basic electrochemical properties of the couples. Table 9.3 shows E_{corr} , R_p , i_{gal} , β_a , and β_c for the coated alloy panels, fasteners, and the galvanic couples. The couples were assembled with the alloy panel and the fastener isolated as shown in Chapter 2, which ensures the i_{gal} measurement. The Ti-6Al-4V fastener shows a higher E_{corr} and greater R_p than the coated alloy panels, which indicates that the fastener is more noble and acts as the cathode while the alloy panel is the anode. It is noted that i_{gal} is significantly increased when the couples were tested in the more aggressive 3.5% NaCl than that in the 0.5 M $\text{Na}_2\text{SO}_4 + 0.1\%$ NaCl. This is attributed to the more severe attack by a higher concentration of Cl^- on the alloy panels and the fasteners, which is

evidenced by the decreased β_a for the panels, fasteners, and couples. Furthermore, β_a for the alloy panel is reduced to a greater extent than that for the fasteners. This preferential attack on the anodic panel leads to an increased anode/cathode area ratio that causes the increased i_{gal} for the electrolyte solution with a higher Cl^- concentration. In addition, the cathodic reaction is mainly O_2 reduction within this potential window (e.g., from 0 to -1.0 V vs Ag/AgCl) and its rate depends on the concentration of dissolved O_2 rather than the Cl^- concentration. Therefore, β_c for the panels, fasteners, and couples shows no significant difference between these two solutions.

Table 9.2 Best-fit parameters for the experimental EIS data for the 5200-coated and uncoated AA2024 samples in air-saturated 0.5 M Na₂SO₄. The equivalent circuits used for the simulation was presented in Chapter 2.

Treatment	R_{el} (Ω)	Q_{co} ($\times 10^{-6}$ $s^n/(\Omega \cdot cm^2)$)	n_{co}	C_{co} ($\mu F/cm^2$)	R_{po} ($\Omega \cdot cm^2$)	Q_{dl} ($\times 10^{-6}$ $s^n/(\Omega \cdot cm^2)$)	n_{dl}	R_p ($\times 10^4 \Omega \cdot cm^2$)
Uncoated	131±12	-	-	-	-	55.5±7.9	0.8±0.0	4.9±0.2
5200	113±2	41.9±5.1	0.8±0.0	10.4±1.0	1483±259	14.5±2.4	0.8±0.0	6.3±1.2
TCP	118±4	28.9±2.1	0.8±0.0	5.9±0.6	152±57	24.2±3.3	0.9±0.0	18.8±5.1
NCP	103±4	11.5±0.0	0.8±0.0	1.4±0.0	104±16	23.1±1.5	0.8±0.0	427.5±96.9

Table 9.3 Basic electrochemical parameters of the 5200-coated AA2024 panel, Ti-6Al-4V fastener, and the galvanic couples. The coupled samples were set up as shown in Chapter 2. Measurements were carried out in air-saturated 0.5 M Na₂SO₄ + 0.1% NaCl and 3.5% NaCl, respectively. Each datum is an average value of at least 3 samples.

		E_{corr} (V vs Ag/AgCl)	R_p ($\times 10^4 \Omega \cdot cm^2$)	i_{gal} ($\mu A/cm^2$)	β_a (mV/dec)	β_c (mV/dec)
0.5 M Na ₂ SO ₄ + 0.1% NaCl	Panel	-0.51 ± 0.01	23.6 ± 1.9	0.8 ± 0.2	257 ± 5	-383 ± 12
	Fastener	-0.10 ± 0.01	55.0 ± 7.9		691 ± 68	-415 ± 26
	Couple	-0.45 ± 0.02	14.2 ± 7.0	-	368 ± 34	-221 ± 8
3.5% NaCl	Panel	-0.64 ± 0.02	10.6 ± 3.5	2.4 ± 0.2	35 ± 2	-366 ± 18
	Fastener	-0.27 ± 0.04	32.1 ± 9.6		254 ± 79	-462 ± 99
	Couple	-0.57 ± 0.01	1.9 ± 0.5	-	53 ± 8	-290 ± 43

9.2.5 Accelerated Corrosion Tests.

The corrosion inhibition provided by the 5200 coating on AA2024 was assessed by measuring electrochemical parameters, such as E_{corr} , R_p , and i_{gal} , before and after the galvanically coupled samples were exposed to various accelerated environmental tests for 14 days: (i) full immersion in 0.5 M Na_2SO_4 + 0.1% NaCl at room temperature (23-27 °C), and (ii) exposure to moist SO_2 at 40 °C. Table 9.3 shows the basic electrochemical parameters of the 5200-coated AA2024 panel, the Ti-6Al-4V fastener, and the coupled samples. The configuration is shown in Chapter 2. They were measured in both 0.5 M Na_2SO_4 + 0.1% NaCl and 3.5% NaCl.

Figure 9.8 shows optical images of the galvanically-coupled 5200-coated AA2024 samples (A) before accelerated corrosion testing, after (B) full immersion and (C) moist SO_2 exposure tests. Fig. 9.8D shows the uncoated sample after the moist SO_2 exposure testing that exhibits clear damage and corrosion across the entire alloy surface. Similarly, the coated samples after the 14-day accelerated corrosion testing in both environments were severely corroded, evidenced by the localized pitting and damage (indicated by arrows). In addition, it appears that a greater level of damage is seen on the sample after the full immersion testing compared to that after the moist SO_2 exposure testing. These images provide qualitative evidence that the 5200 coating does not provide enough corrosion protection to the alloy, at least in the full immersion and moist SO_2 exposure conditions.

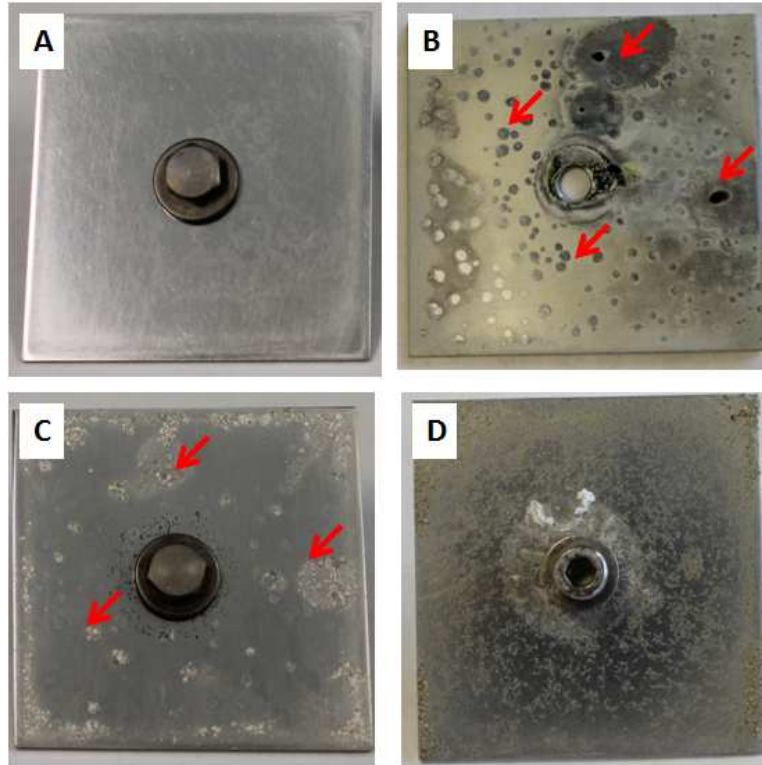


Figure 9.8 Optical images of the 5200-coated AA2024 galvanically coupled with Ti-6Al-4V fasteners (A) before any accelerated corrosion testing, and after 14-day (B) full immersion in air-saturated 0.5 M Na₂SO₄ + 0.1% NaCl and (C) exposure in moist SO₂ at 40 °C. The image of (D) an uncoated AA2024 sample galvanically coupled with the SS fastener is also shown as control.

9.3 Discussion

9.3.1 Formation mechanism and chemical structure

The formation of 5200 coatings on AA2024 is driven by an increase in the interfacial pH (Fig. 9.1). Consumption of H⁺ and F⁻ by dissolution of Al oxide films, along with hydrogen discharge and oxygen reduction reaction, leads to an increased pH at the metal surface. This interfacial pH increase drives hydrolysis of the two fluorometalates to form a mixed oxide layer (Rxn. (9.1) and (9.2)). This layer is about 20-30 nm thick *in vacuo*. EDX analysis revealed that the 5200 coating consists of Zr, Ti and O, which is

consistent with TiO_2 and ZrO_2 that is present over most regions of the alloy surface. The stronger Zr, Ti, and O signals are seen at the Cu-rich intermetallic sites compared to those at Al terrace sites (Fig. 9.2). This is attributed to two reasons. First, besides consumption of H^+ by hydrogen discharge at the Al terrace sites surrounding the Cu-rich intermetallic sites, oxygen reduction reaction (ORR) at the intermetallic sites consumes H^+ and drives the pH increase to a higher level, The pH at Cu-rich intermetallic sites is increased to a higher level that provides a greater driving force for hydrolysis of the fluorometalates to form a thicker $\text{ZrO}_2/\text{TiO}_2$ mixed oxide layer at the intermetallic site (Fig. 9.2). The other reason is that the intermetallic site forms several small Cu particles as the active elements such as Al, Mg and Mn in the compounds are dissolved upon attack by H^+ and F^- . The coating materials fill the pores between these Cu particles (Fig. 9.5C), which is seen as the increased x-ray signals of Zr, Ti and O elements at the intermetallic sites. In addition, the 5200 coating contain hydrated channels and or defects that act as pathways through which dissolved oxygen and ions diffuse to the metals. This is based on the observation that the R_p of 5200-coated AA2024 is on the range of $10^4 \Omega\cdot\text{cm}^2$ that is 5 orders of magnitude smaller than $10^9 \Omega\cdot\text{cm}^2$ for a completely blocking barrier. Shrinkage may occur due to dehydration *in vacuo* (Fig. 9.5A)

9.3.2 Corrosion protection property

Preliminary data in our previous report showed that the 5200 coating provides slightly improved corrosion resistance to AA2024 according to the seemingly increased R_p values.¹⁹⁹ In this work, we found that 5200 coating does not provide any corrosion protection to AA2024 and the increased R_p reported previously was due to the formation of Al oxide layers. Table 9.1 shows that the 5200-coated AA2024 after overnight aging has an R_p that is not statistically different from that of the uncoated samples. Neither cathodic or anodic protection is provided by the 5200 coating seen in the potentiodynamic polarization scans (Fig. 9.6). Additionally, the 5200 coating does not show any corrosion protection to the AA2024 samples that are galvanically coupled with Ti alloy fasteners and severe corrosion is seen on the panels (Fig. 9.8). Therefore, one significant finding in this work is that the 5200 coating does not provide any corrosion protection on AA2024. This is consistent with the findings reported by Smith and Miller based on visual signs of corrosion.²⁰⁵ However, it should be noted that the protective coating system in the field usually contains three layers: (i) conversion coatings, (ii) primers and (iii) top coats. The poor corrosion protection provided by the 5200 coating alone does not indicate the uselessness of this coating. In fact, several studies have shown that some coating systems with the 5200 conversion coating provide a good corrosion protection partially due to its excellent adhesion property.^{65,}

205-206

In contrast, the TCP and NCP coatings significantly improve the corrosion resistance of AA2024 as evidenced by (i) the about 10× greater R_p (Table 9.1) and (ii) suppressed cathodic and anodic currents (Fig. 9.6) for both the TCP- and NCP-coated alloys compared to the uncoated samples. However, it should be noted that all three coatings contain defects and do not completely blocking the alloy surface. These defects allow diffusion of dissolved oxygen and ions to the metals. The 5200 coating obtains a thinner structure (Fig. 9.4 and 9.5) that contains shorter pathways relative to the TCP and NCP coatings.¹⁹⁹ It is evidenced by the relatively greater defect parameter for the 5200 coating and the underlying alloy becomes more susceptible to being attacked, compared to the other two coatings (Table 9.1).

9.4 Conclusion

The results reported herein describe the formation, structure, and electrochemical properties of the 5200 coating on AA2024. Formation of the coating on AA2024 is a pH driven process that leads to hydrolysis of hexafluorometalates (*i.e.* TiF_6^{2-} and ZrF_6^{2-}) to form metal oxide layers (*i.e.* TiO_2 and ZrO_2). The coating forms across the entire alloy surface and enriches at the Cu-rich intermetallic sites. The 5200 coating exhibits a thickness on the range of 20-30 nm *in vacuo*. Hydrated channels and or defects exist in the coating and allow diffusion of dissolved O_2 and ions to the metals. The 5200 coating exhibits a good chemical stability during both full immersion and atmospheric corrosion testing for at least 14 days. However, no significant corrosion protection is provided by

the 5200 coating on AA2024 due to the coating's ultrathin and defective structures.

Severe corrosion occurs after 14-day exposure in the moist SO₂.

CHAPTER 10. EFFECTS OF GALVANIC COUPLING WITH SS A286 CRES AND TI-6AL-4V FASTENERS ON CORROSION INHIBITION PROVIDED BY TRIVALENT CHROMIUM PROCESS (TCP) COATINGS ON AA2024-T3 PANELS

10.1 Introduction

High strength aluminum alloy 2024-T3 is widely used as an aircraft structural component. The metal alloys are joined together by fasteners due to the difficulty of welding.²⁰⁷ Fasteners in the aerospace industry are usually stainless steels or titanium alloys. A benefit of using these two types of fasteners is their ability to function over a wide range service temperatures.²⁰⁸ This is due to their noble nature relative to the aluminum alloys. Two dissimilar conductive materials that are in electrical contact in an electrolyte forms a galvanic couple. This coupling leads to the galvanic corrosion of the more active material (e.g., metal oxidation/corrosion) that acts as the anode, while the more noble material acts as the cathode (e.g., O₂ reduction). A current, called the galvanic current, flows from the anode, through the electrolyte to the cathode. It is a measure of the galvanic corrosion rate. Therefore, when the Al alloy panels are connected with fasteners and exposed to humid air or a salt solution, an ionic connection is made. This coupling can result in severe deterioration of the Al alloy. Studies have shown that galvanic coupling leads to a more severe corrosion damage to a metal than what is observed with the uncoupled metal is exposed to the same conditions.²⁰⁹⁻²¹⁰ A protective coating is one way to inhibit galvanic corrosion. Frankel *et al.* studied the effects of the galvanic coupling on the corrosion protection provided by a multi-coating system on Al alloy panels when coupled with SS A286 CRES or Ti-6Al-

4V fasteners.²⁰⁹⁻²¹⁰ The corrosion inhibition was evidenced by a smaller galvanic current for completely coated panels as compared to coated and scribed panels. Factors that affect the corrosion protection provided by a multi-coating system include the fastener material (SS A286 CRES vs. Ti-6Al-4V), the corrosive environment (full immersion vs. neutral salt spray), and the anode/cathode areas. For example, data showed that coupling with the SS fastener caused more rapid failure of the panel than when coupled with the Ti alloy fastener. However, little was reported on the mechanisms by which the TCP coating provides less corrosion protection to the Al alloy panels when coupled with SS A286 CRES fasteners than with Ti-6Al-4V. In addition, information is lacking about the corrosion inhibition provided by the TCP conversion coating on the Al alloy panels when they are galvanically coupled. Therefore, this chapter focuses on the corrosion inhibition provided by the TCP coating AA2024-T3 panels when coupled with SS A286 CRES and Ti-6Al-4V fasteners. Several electrochemical parameters, e.g., corrosion potential (E_{corr}), polarization resistance (R_p), and galvanic current density (i_{gal}) are reported that serve as benchmarks for the corrosion status of the specimen. The assembling of the galvanic couples was shown in Chapter 2.

10.2 Results

10.2.1 Basic electrochemical properties

Figure 11.1 shows galvanic current density-time transients for the TCP-coated and uncoated AA2024-T3 panels when coupled with SS A286 CRES and Ti-6Al-4V fasteners. Measurements were conducted in naturally aerated 0.5 M Na₂SO₄ + 0.1%

NaCl. The i_{gal} values are positive, which indicates that the galvanic current flows from the anode through the electrolyte solution to the cathode. The currents, which are a direct measure of the corrosion rate, are generally larger for the panels coupled with SS than those coupled with Ti-6Al-4V. Additionally, the currents are less for both fasteners when coated with TCP. . The statistical finding from measurements of 5 samples is that there is not a major difference in i_{gal} for the coated and uncoated AA2024 in this medium, as seen in Table 11.1. Generally, the currents for the SS A286 CRES-coupled panels are $\sim 10\times$ greater than the current densities for the Ti-6Al-4V –coupled panels. This difference in current density is due in part to the more rapid oxygen reduction reaction kinetics on the SS fasteners

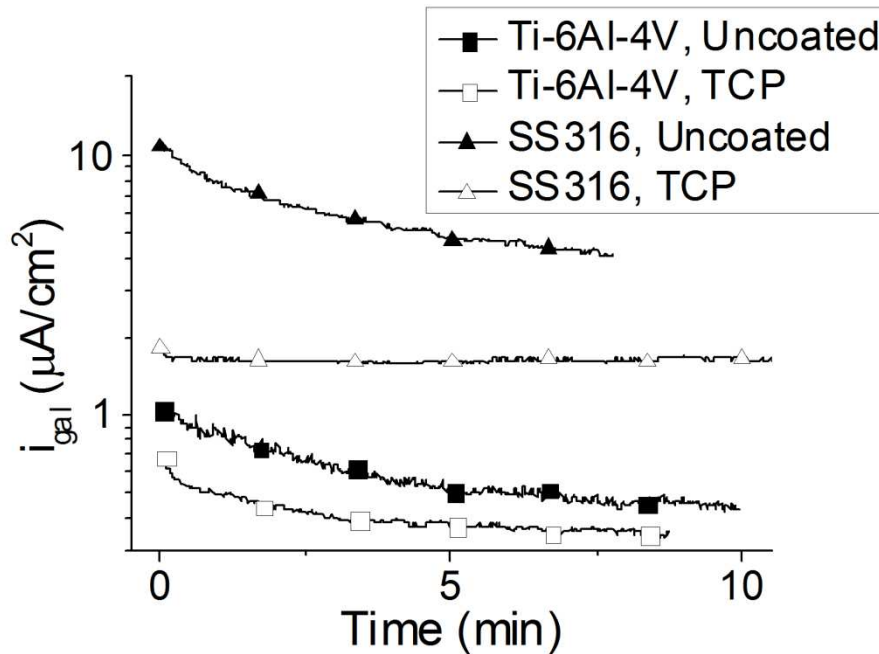


Figure 10.1 Galvanic current density (i_{gal}) vs. time profiles for TCP-coated and uncoated AA2024-T3 panels when coupled with fasteners made of SS A286 CRESSS A286 CRES and Ti-6Al-4V. The current density was normalized to the geometric area of the Al alloy panels. Measurements were conducted in naturally aerated 0.5 M Na_2SO_4 + 0.1% NaCl after 30-min purging with O_2 .

Table 10.1 presents a summary of basic electrochemical parameters, corrosion potential (E_{corr}), polarization resistance (R_p), and galvanic current density (i_{gal}) for the uncoated and TCP-coated AA2024 panels galvanically coupled with Ti-6Al-4V fasteners. E_{corr} was measured after 30-min full immersion of the samples in naturally aerated 0.5 M Na₂SO₄ + 0.1% NaCl solution; and i_{gal} was measured after 2-h immersion in the solution. Average values were calculated from measurements of 5 samples. E_{corr} for the fastener is more positive than that for the panel, which makes the fastener a cathode and the panel an anode. This can also be seen by the positive values for i_{gal} , which indicates a current flowing from the fastener to panel. E_{corr} for the couple falls between the values for the panels and fastener separately, which is consistent with the mixed potential theory. R_p values for the couples are smaller than those for the panels and fasteners. This is due to that the galvanic coupling forms a potential difference between the fastener and panels and drives the current flow between the cathode (fasteners) and anode (panels). Comparing R_p for the couple between uncoated ($0.6 (\pm 0.1) \times 10^4 \Omega \cdot \text{cm}^2$) and coated AA2024 ($4.1 (\pm 2.1) \times 10^4 \Omega \cdot \text{cm}^2$), the TCP coating increases the R_p by about 10x that is consistent with the increase for the individual panels (from $2.0 (\pm 0.5)$ to $26.2 (\pm 1.5) \times 10^4 \Omega \cdot \text{cm}^2$). This indicates that the TCP coating, as a barrier coating, provides some corrosion protection to the galvanically coupled AA2024 panel. However, i_{gal} shows no significant difference with and without the TCP coating. This is because the majority of oxygen reduction occurs at the uncoated

fastener (cathode) and the Al in the panel (anode) is oxidized correspondingly. The electron flows through inside the metals, which is not affected by the coating on the surface.

Comparing E_{corr} for the TCP-coated panels coupled with different fastener, the one with SS fastener (-0.65 ± 0.04 V) is ~ 100 mV lower than that with Ti alloy fastener. R_p for the panel and couple with SS fasteners are both $\sim 5\times$ smaller for that with Ti alloy fasteners. Furthermore, i_{gal} for the coated panel with SS fastener is $\sim 5\times$ greater than that with the Ti alloy fastener. These data indicate that the TCP-coated panels are more vulnerable to corrosion when coupled with SS than with Ti alloy fasteners.

Table 10.1 Basic electrochemical parameters, E_{corr} , R_p , and i_{gal} for the uncoated and TCP-coated AA2024 panels galvanically coupled with Ti-6Al-4V fasteners, and TCP-coated Al alloy panels coupled with SS A286 CRES fasteners. Measurements were conducted in 0.5 M Na_2SO_4 + 0.1% NaCl that was purged with O_2 for 30 min prior to the measurements.

		Uncoated, Ti-6Al-4V	TCP, Ti-6Al-4V	TCP, SS316
E_{corr} (V vs Ag/AgCl)	Panel	-0.50 ± 0.04	-0.46 ± 0.02	-0.65 ± 0.04
	Fastener	-0.11 ± 0.03	-0.07 ± 0.02	-0.01 ± 0.01
	Couple	-0.44 ± 0.02	-0.42 ± 0.01	-0.32 ± 0.05
R_p ($\times 10^4 \Omega \cdot \text{cm}^2$)	Panel	2.0 ± 0.5	26.2 ± 1.5	8.1 ± 1.4
	Fastener	15.1 ± 4.1	13.8 ± 3.2	14.1 ± 1.1
	Couple	0.6 ± 0.1	4.1 ± 2.1	0.5 ± 0.2
$i_{gal} (\mu\text{A}/\text{cm}^2)$		0.48 ± 0.14	0.58 ± 0.15	5.99 ± 2.23

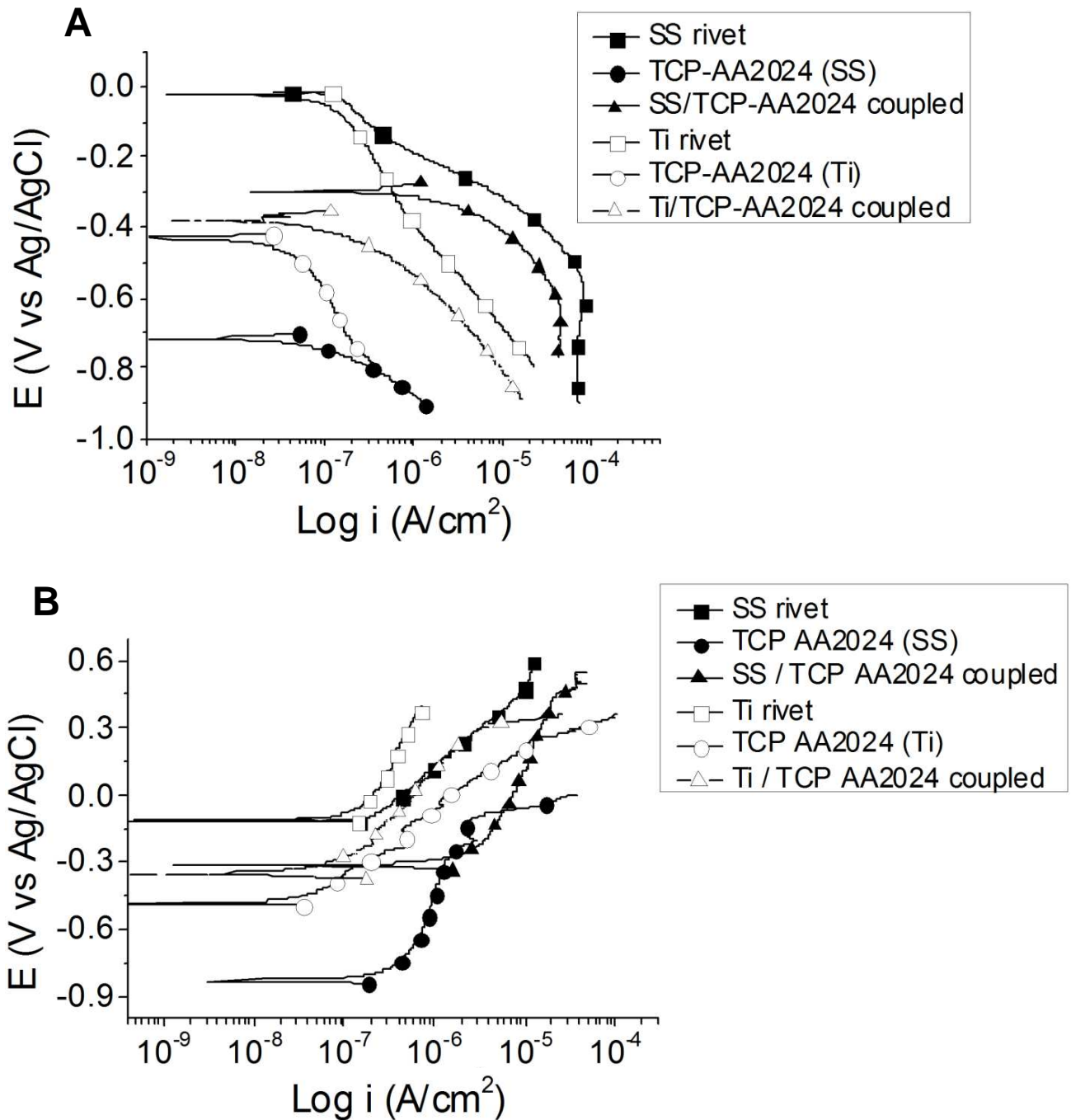


Figure 10.2 (A) Cathodic and (B) anodic polarization curves for the isolated fasteners, the TCP-coated AA2024 panels, and the galvanically-coupled TCP-coated panels. Fasteners include SS A286 CRES and Ti-6Al-4V. The currents were normalized to the geometric area of the fasteners and Al alloy panels. Measurements were conducted in 0.5 M Na₂SO₄ + 0.1% NaCl after a 30-min purge with O₂. The scan rate was 1 mV/s.

Figure 10.2 shows the (A) cathodic and (B) anodic potentiodynamic scans for uncoupled TCP-coated AA2024 panels, the individual SS A286 CRES and Ti-6Al-4V fasteners, and the TCP coated panels when galvanically coupled. Measurements were conducted in 0.5 M Na₂SO₄ + 0.1% NaCl after 30 min purging with O₂. The scan rate was 1 mV/s. The cathodic and anodic current densities for the coupled panels fall between those for the uncoupled panels and the individual fasteners. This applies for both fasteners. Moreover, both fasteners exhibits a greater cathodic but smaller anodic current densities compared to the values for the uncoupled Al alloy panels. This is consistent with the oxygen reduction occurring mainly on the fastener. However, it is interesting to note that the SS fastener exhibits a greater cathodic current density than the Ti alloy fastener. Correspondingly, the anodic current density is greater for the Al alloy panel coupled with the SS fastener than that with Ti alloy fastener. The panel is severely pitted at a lower E_{pit} for the SS than Ti alloy fastener.

10.2.2 Accelerated corrosion tests

Table 10.2 shows the optical images of the TCP-coated AA2024 panels before and after a thin layer mist (TLM) exposure at 55 °C and full immersion at room temperature in 3.5% NaCl for 14 days. The Al alloy panels were galvanically-coupled with SS A286 CRES and Ti-6Al-4V fasteners during the tests. In both accelerated corrosion tests, the panels were more severely corroded across the whole surface when coupled with SS than with Ti. The panels coupled with the Ti alloy fasteners showed only mild corrosion and surface damage, mainly in the region where the fastener was in direct contact with the fastener. This general observation confirms that the TCP-coated panels are more susceptible to corrosion when coupled with SS. These

observations are also consistent with the predictive electrochemical parameters reported in Table 10.1. The localized corrosion and surface damage for the TCP-coated panels coupled with Ti could results from damage to the coating with the fastener is attached. In addition for both fasteners, the TLM causes a more severe corrosion on the panels than the full immersion test. This is because of a greater flux of dissolved O_2 to the metal surface through the thin layer of solution in the TLM test than through the bulk solution in the full immersion test.

Table 10.3 shows the weight loss recorded for the galvanically-coupled the TCP-coated AA2024 panels after the full immersion and thin layer mist (TLM) test. A greater weight loss is seen for the panels after the TLM than the full immersion tests. Also, the panels coupled with the SS fasteners showed greater weight loss than those coupled with the Ti alloy fasteners. This is consistent with the greater level of corrosion seen on the optical micrographs and with the electrochemical parameters shown in Table 11.1 and Figure 11.1.

Table 10.2 Optical images of the TCP-coated AA2024 panels before and after the thin-layer mist exposure at 50 °C and full immersion at room temperature in 3.5% NaCl for 14 days. The Al alloy panels were galvanically-coupled with SS A286 CRES and Ti-6Al-4V fasteners during the tests.

Fasteners	SS316	Ti-6Al-4V
Before		
After TLM test		
After full immersion test		

Table 10.3 Weigh loss data for galvanically-coupled TCP-coated AA2024 panels after full immersion at room temperature and exposure to a thin-layer mist (TLM) test at 40 °C for 14 days. The solution used for both accelerated corrosion tests was naturally aerated 3.5% NaCl. The panels were galvanically coupled with SS A286 CRES and Ti-6Al-4V fasteners.

Accelerated corrosion tests	Weight loss percentage (%)	
	SS316	Ti-6Al-4V
Full immersion	11.4 ± 4.1	3.0 ± 1.6
TLM	30.6 ± 8.7	19.9 ± 9.4

Figure 10.3 shows potentiodynamic scans for galvanically-coupled TCP-coated AA2024 panel and an individual Ti-6Al-4V fastener before and after (A) full immersion in naturally-aerated 3.5% NaCl at room temperature and (B) exposure in moist SO₂ atmosphere at 40 °C, both for 14 days. The electrochemical measurements were conducted in 0.5 M Na₂SO₄ + 0.1% NaCl. The scan rate was 1 mV/s. The cathodic current density indicates the oxygen reduction reaction and shows no significant difference. In contrast, the anodic current density is increased by one order of magnitude after both accelerated corrosion tests. Furthermore, E_{pit} for the samples after full immersion for 14 days is about 700 mV lower than that before the testing.

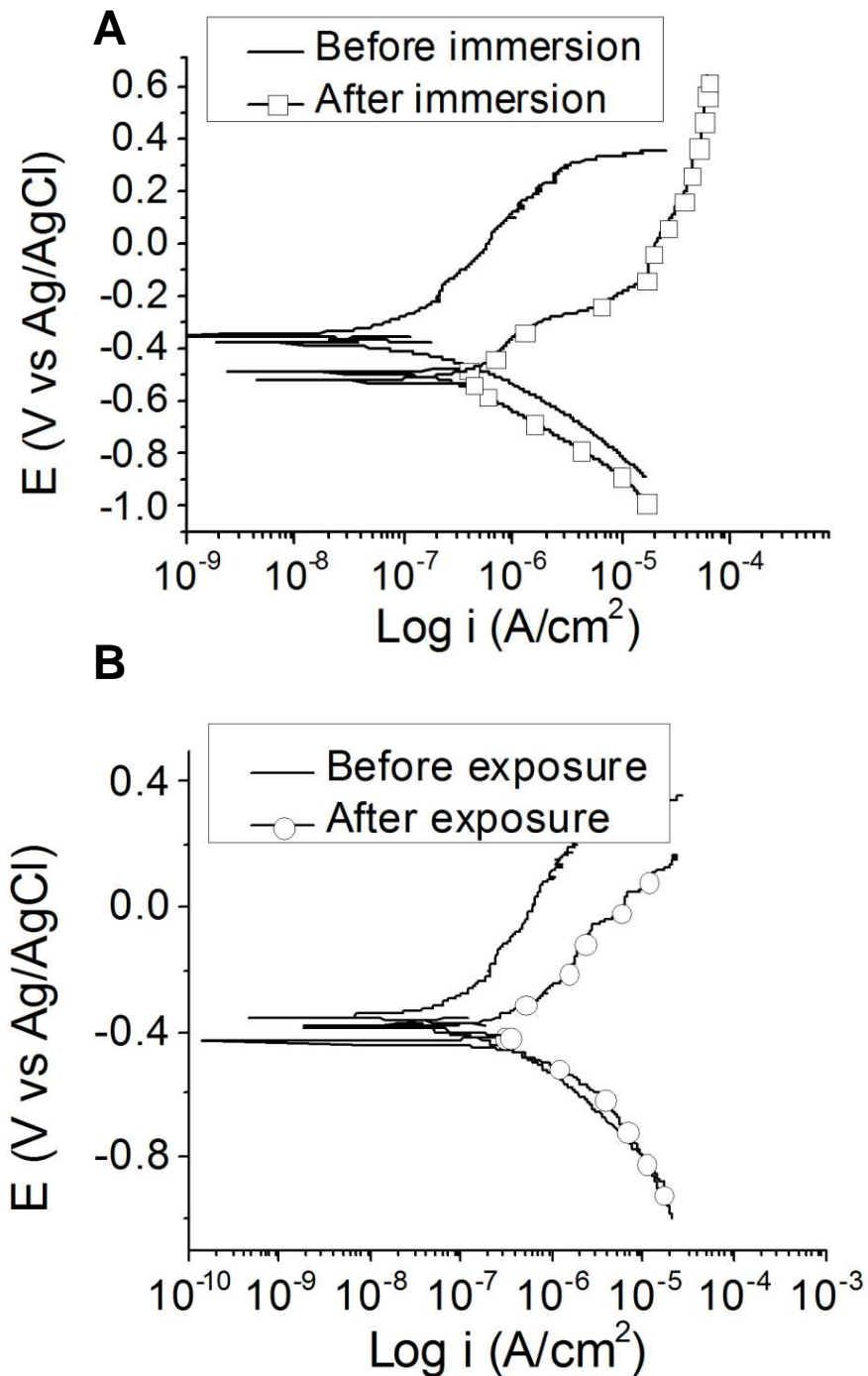


Figure 10.3 Polarization curves for galvanically-coupled TCP-coated AA2024 panels with Ti-6Al-4V fasteners before and after (A) full immersion in 3.5% NaCl at room temperature and (B) exposure to moist SO₂ at 40 °C, both for 14 days. The electrochemical measurements were conducted in naturally aerated 0.5 M Na₂SO₄ + 0.1% NaCl for the samples after full immersion testing while naturally aerated 0.5 M Na₂SO₄ was used for the samples after the moist SO₂ test. The scan rate was 1 mV/s.

Figure 10.4 shows the optical images of the (A) uncoated and (B) TCP-coated AA2024 panels galvanically coupled with Ti-6Al-4V fasteners after exposure to moist SO₂ at 40 °C for 14 days. No significant corrosion is seen on the fasteners for the coated or uncoated panels. This is consistent with the noble nature of the Ti-6Al-4V alloy. However, the uncoated panels are corroded across the entire surface while only a few locally corroded spots are seen on the coated panels. This is consistent with the R_p data in Table 11.1: the TCP coating provides some corrosion protection to the panels in a galvanic couple system with fasteners.

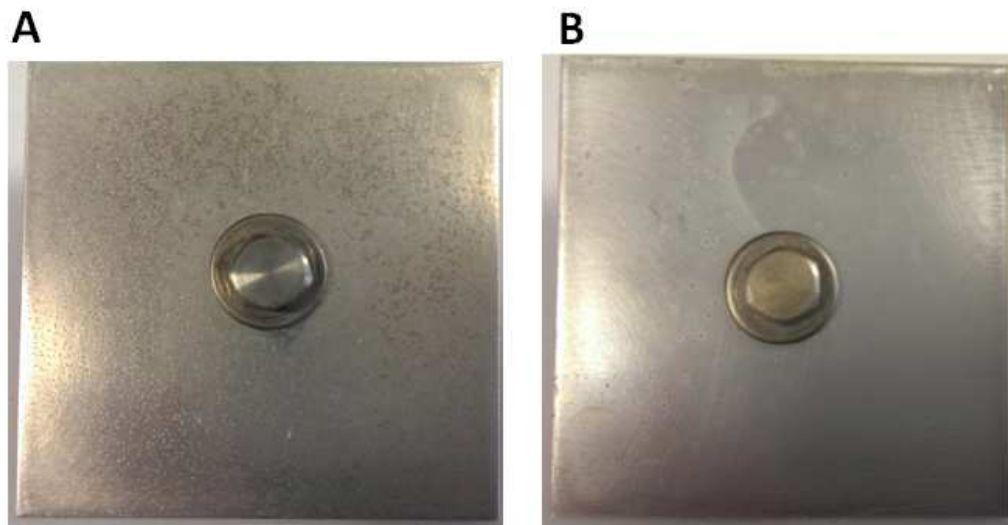


Figure 10.4 (A) Cathodic and (B) anodic polarization curves for the isolated fasteners and TCP-coated AA2024 panels, and the galvanic couples. Fasteners include SS A286 CRES and Ti-6Al-4V. The currents were normalized to the geometric area of the fasteners and Al alloy panels. Measurements were conducted in 0.5 M Na₂SO₄ + 0.1% NaCl that was purged with O₂ for 30 min before measurements. The scan rate was 1 mV/s.

10.3 Discussion

10.3.1 Corrosion protection provided by the TCP coating

The TCP coating provides some corrosion protection to the galvanically coupled AA2024 panels. This is evidenced by the 10x increase in R_p with the coating (Table 11.1). Although the cathodic fasteners were not coated and exposed to the electrolyte solution, it should be noted that the AA2024 panels contain some Cu-rich intermetallic sites that also act as a cathode. Some dissolved O_2 can diffuse to the Cu-rich sites and get reduced. Previous study has shown that the TCP coating partially blocks the diffusion of the dissolved O_2 to the metal. Therefore, the TCP coating functions as a barrier coating on the Al alloy panel and inhibits some O_2 reduction. This can also be seen by the local pitting on the coated panels compared to the severe corrosion across the entire uncoated panels after 14-day exposure in moist SO_2 at 40 °C (Fig. 11.4).

However, the fastener has a greater surface area than the Cu-rich intermetallic sites in the Al alloy panels. Oxygen reduction that occurs at the fastener dominates the cathodic current. Therefore, exposure of the uncoated fastener to the electrolyte solution keeps the overall oxygen reduction unaffected by the coating on the Al alloy panel. This ensures the electron flows through inside the fastener and panel at an unchanged i_{gal} with and without the coating. Even though the TCP coating also inhibits the anodic Al oxidation as a barrier coating, the panel still corrodes as long as the fastener is exposed to the solution.

10.3.2 Effects of Fasteners on Corrosion Protection by TCP

Both SS A286 CRES and Ti-Al6-V4 fasteners are relatively noble than the Al alloy panels and therefore act as the cathode. However, significant difference is seen on the effects of these two types of fasteners on the corrosion protection provided by the TCP coating. The SS fastener has higher O_2 reduction activity, which is evidenced by the greater cathodic current densities on the SS fastener than on Ti alloy fastener (Fig. 11.2). This leads to a more active Al alloy panel evidenced by the negative-shifted E_{corr} (Table 11.1). The panel is oxidized or corroded to a greater extent when coupled with the SS fastener than with the Ti alloy fastener (Fig. 11.2). Through the same accelerated corrosive environments, e.g., full immersion and TLM in 3.5% NaCl, the panels coupled with SS fasteners were corroded more severely than those with Ti alloy fasteners.

10.4 Conclusions

The corrosion protection provided by the TCP coating to the galvanically-coupled AA2024-T3 panels was investigated for the SS A286 CRES and Ti-6Al-4V fasteners. TCP functions as a barrier coating that inhibits diffusion of O_2 and solution species to the underlying metal panel. The extent of galvanic corrosion was greater with the SS than with the Ti alloy fasteners. The TCP coating does provide some corrosion inhibition as the corrosion is more severe on the galvanically-coupled panels without the coating. The more extensive corrosion with the SS fasteners is evidenced by greater i_{gal} and lower R_p values, greater weight loss and the damage seen in the optical micrographs.

For the SS fasteners, the corrosion occurs over most areas of the panels near and removed from the fastener. In contrast, the corrosion with the Ti fasteners is very localized to the region where the fastener head contacts the panel. For the SS A286 CRES fasteners, the greater rate of the oxygen reduction reaction leads to the greater level of metal corrosion. The TCP coating, while providing some barrier protection does consist of pores/channels and defects through which dissolved O₂ and solution species can reach the underlying metal. Finally, the TCP coating provides greater corrosion inhibition under full immersion testing than under the more aggressive thin-layer mist test.

CHAPTER 11. SUMMERY AND FUTURE WORK

11.1 Summery

The trivalent chromium process coating (TCP) is one of the leading replacement of the toxic chromate conversion coating (CCC) in aerospace industry. This dissertation focuses on a fundamental understanding of the formation mechanism, chemical structure, and corrosion protection properties of the TCP coating on three high strength aluminum alloys: AA2024-T3, AA6061-T6, and AA7075-T6. These scientific studies provide information to improve the the corrosion protection property of the TCP coating.

Chapter 3 and 6 showed that the TCP coating exhibits similar formation mechanism and chemical structure on the three aluminum alloys. The formation of the TCP coating is driven by an increase in the interfacial pH caused by (i) dissolution of the oxide layer by H^+ and F^- and (ii) localized oxygen reduction at Cu-rich intermetallic sites. This pH increases leads to hydrolysis of the fluorhexuzirconate to form hydrated ZrO_2 . And precipitation of Cr^{3+} to form $Cr(OH)_3$. Therefore, the coating composition is biphasic consisting of a hydrated $ZrO_2/Cr(OH)_3$ overlayer and a K- and F-rich fluoroalunminate interfacial layer (K_3AlF_6). The thickness of the TCP coating in vacuum is approximately 50 nm on AA2024, 100 nm on AA6061, and 70 nm on AA7075. It coats most of the Al alloy surface and enriches at the intermetallic sites. However, it should be noted that the true coating thickness (e.g., 90-100 nm for AA2024) is greater than these *in vacuo* values.

Chapter 4 and 5 discussed the transient formation of Cr(VI) in the TCP coating on the aluminum alloys using Raman spectroscopy. The Cr(VI) formation occurs when the coated alloy is immersed in air-saturated electrolyte solutions or even after exposure to humid air (curing). The formation involves two steps: (i) oxygen diffuses through the hydrated channels to the Cu-rich intermetallic sites where it gets reduced to H₂O₂; (ii) the H₂O₂ is a strong oxidant and diffuses to nearby sites to oxidize native Cr(III) in the coating to Cr(VI). In samples aged in the laboratory air, the Cr(VI) formation is localized to intermetallic areas where the H₂O₂ is formed. When fully immersed, the locally produced H₂O₂ can diffuse to sites remote from the pits and oxidize the Cr(III). The Cr(VI) exists mainly in the form of chromate (CrO₄²⁻). It combines Al³⁺ or Al(OH)_x to form a mixed oxide of Al(III)/Cr(VI) in the pits. Some chromate (CrO₄²⁻) leaks into the solution, diffuses to the terrace and binds Cr(III) to form a Cr(III)/Cr(VI) mixed oxide. The covalent, polymeric Cr(III)/Cr(VI) mixed oxide accounts for the chemical stability of the TCP coating. Although it is still not clear if the TCP coating provides an active corrosion protection, but the leaking of chromate might occur during the immersion in solutions.

Chapter 3, 5, and 6 investigated the corrosion protection provided by the TCP coating on aluminum alloys. The TCP coating provides both cathodic and anodic protection evidenced by suppressed current density compared to those for the uncoated samples. It can also be seen by the ~10-100x increase in R_p . However, the corrosion protection provided by TCP is much better on AA6061-T6 than on AA7075-T6; and TCP

can inhibit pitting corrosion in AA2024-T3 but not as effective as the other two alloys. The protection mechanisms involve (i) reducing the oxygen reduction kinetics, (ii) partially blocking the mass transfer of dissolved O_2 and ions to the metal, (iii) insulating the electron transfer through the non-conductive $ZrO_2/Cr(OH)_3$ layer, (iv) providing active corrosion protection due to transient formation of Cr(VI), and (v) reducing the likelihood of severe pitting in the Cl^- -containing solution. The corrosion protection provided by the TCP coating is consistent for at least 14 days in various accelerated corrosion tests. The coating exhibits good stability and endures the corrosive environments such as full immersion in salt water, humid atmosphere, moist SO_2 , and thin layer mist (TLM). Some corrosion protection is also provided to the galvanically coupled aluminum alloy panels with SS and Ti alloy fasteners. The protection depends on the types of fasteners.

Chapter 7 discussed the effect of deoxidation/desmutting on the corrosion protection provided by TCP coatings on AA2024-T3. Deoxidation in acidic fluoride Smut-Go was compared with those in alkaline media (NaOH). The alloy surface is more severely pitted around the Cu-rich intermetallic compounds in Smut-Go than in NaOH. The TCP coating becomes defective after deoxidizing in the Smut-Go for a longer period of time (> 2 min), which leads to a decreased corrosion protection. However, a uniform etching of the Al oxide film and the formation of the Cu oxide film at the intermetallic sites occur during the deoxidizing in an alkaline NaOH solution. The recommendation from this work is to use an alkaline etch.

Chapter 8 showed the effects of curing temperature and time on the corrosion protection provided by the TCP coating on AA2024-T3. The TCP coating undergoes dehydration and condenses when cured at elevated temperatures. This along with the growth of a more defect-free aluminum oxide layer occurs during curing overnight at elevated temperature (≤ 100 °C). The coating also becomes progressively hydrophobic with the loss of water and associated chemical changes. All three contribute to the improved corrosion protection. However, curing at 150 °C causes excessive dehydration and shrinkage of the coating such that it undergoes severe cracking and even detachment from the metal surface. A longer curing period at room temperature enhances the corrosion resistance by 4x of the TCP-coated alloy by forming an aluminum oxide layer on the metal sites exposed in the coating channels and defects. The improvement in corrosion protection with curing at room temperature is also associated with increasing hydrophobicity of the coating. The best improvement in corrosion resistance was seen for coatings cured at room temperature for 7 days.

Chapter 9 compared the formation mechanism, chemical structure, and corrosion protection for the TCP coating with other non-chromium conversion coatings, e.g., 5200 (Ti/Zr) and NCP (Zn/Zr). Formation of the 5200 coating on AA2024 is similar to that of the TCP coating: a pH increase drives hydrolysis of hexafluorometalates (*i.e.* TiF_6^{2-} and ZrF_6^{2-}) to form metal oxide layers (*i.e.* TiO_2 and ZrO_2). Both 5200 and NCP coatings form across the entire alloy surface and enriches at the intermetallic sites. The thickness of the 5200 coating is 20-30 nm *in vacuo* that is smaller than that for the TCP (50-60 nm) and NCP (70 nm) coatings. Hydrated channels and or defects exist in the all three

coating and allow diffusion of dissolved O_2 and ions to the metals. No significant corrosion protection is provided by the 5200 coating on AA2024 due to the coating's ultrathin and defective structures; severe corrosion occurs after 14-day exposure in the moist SO_2 . In contrast, the NCP coating provides similar corrosion protection as the TCP coating in terms of basic electrochemical properties.

Chapter 10 studied the corrosion protection provided by the TCP coating to the galvanically-coupled AA2024-T3 panels with the SS A286 CRES and Ti-6Al-4V fasteners. TCP functions as a barrier coating that inhibits diffusion of O_2 and solution species to the underlying metal panel. The extent of galvanic corrosion was greater with the SS than with the Ti alloy fasteners. The TCP coating does provide some corrosion inhibition as the corrosion is more severe on the galvanically-coupled panels without the coating. The more extensive corrosion with the SS fasteners is evidenced by greater i_{gal} and lower R_p values, greater weight loss and the damage seen in the optical micrographs. For the SS fasteners, the corrosion occurs over most areas of the panels near and removed from the fastener. In contrast, the corrosion with the Ti alloy fasteners is very localized to the region where the fastener head contacts the panel. For the SS A286 CRES fasteners, the greater rate of the oxygen reduction reaction leads to the greater level of metal corrosion. The TCP coating, while providing some barrier protection does consist of pores/channels and defects through which dissolved O_2 and solution species can reach the underlying metal. Finally, the TCP coating provides

greater corrosion inhibition under full immersion testing that under the more aggressive thin-layer mist test.

11.2 Future Work

Task 1: While a primary focus of this work was on the corrosion protection provided by the surface pretreatment, it should be noted that it is very rare that a “conversion coating” alone will be the final finish on an assembly. Therefore, these aluminum alloys will be primed (*e.g.*, epoxy matrix loaded with SrCrO_4) with an epoxy or polyurethane enamel topcoat. The corrosion protection will be assessed for the whole multi-coat system. A series of DC and AC electrochemical measurements will be performed in well controlled solution environments to generate a database of polarization resistances (R_p), corrosion potentials (E_{corr}), corrosion currents (i_{corr}), anodic and cathodic potentiodynamic curves to determine the corresponding Tafel slopes (b_a and b_c), pitting potentials (E_{pit}) and repassivation potentials (E_{rep}). Given the multitude of Navy defense assets and the complex environments these assets experience, three types accelerated corrosion tests will be performed: (i) full immersion testing in air-saturated electrolyte solutions as a function of the solution chemistry and temperature, (ii) surface contact by a thin-layer (~500 μL) as a function of the solution chemistry and temperature and (iii) atmospheric exposure to a humidified gaseous environment.

Task 2: The aluminum alloys are usually joined using SS and Ti-6Al-4V fasteners that form galvanic couples with the aluminum alloys. Therefore, the extent and nature of

corrosion in the couples will be assessed by forensic investigation. More detailed studies will be performed on galvanic combinations that do not follow the trends predicted by simple mixed potential theory, e.g. if the galvanic potentials, corrosion rates or pitting tendency is different than the predictions. When possible, the galvanic open circuit potentials (OCPs) and galvanic current measured with a zero resistance ammeter will be recorded in the same solutions used in Task 1. The results will be compared to uniform corrosion rate and pit/no-pit predictions generated from Task 1. Painted samples with scribes exposing the base metal will also be tested to examine how coatings interfere with or alter galvanic corrosion interactions.

Task 3: The electrochemically measured variables will be correlated with the extent of pitting (pit density, pit area and pit depth) and or coating delamination, as assessed by microscopy and weight change, as a function of the solution chemistry, temperature and exposure time. Qualitatively, the degree of corrosion resistance provided by the conversion coatings will be determined based on a pitting or no pitting assessment. Semi-quantitatively, the apparent rate of localized corrosion will be determined by tracking the pit density, pit area, pit depth and weight change as a function of time. The important matrix variables will be the metal type (e.g., aluminum alloys, Ti-6Al-4V alloy, high strength steel and graphite epoxy composite), sample preparation, pretreatment coating, electrolyte composition (mild and aggressive), temperature (25 and 55 °C), and immersion time.

BIBLIOGRAPHY

BIBLIOGRAPHY

1. Davis, J. R. *ASM Specialty Handbook: Aluminum and Aluminum Alloys*. ASM International: Materials Park, OH, **1993**.
2. Kaufman, J. G. *Introduction to Aluminum Alloys and Tempers*. ASM International: Materials Park, OH, **2000**.
3. Campbell, F. C. *Elements of Metallurgy and Engineering Alloys*. ASM International: Materials Park, OH, **2008**.
4. Davis, J. R. *Corrosion of Aluminum and Aluminum Alloys*. ASM International: Materials Park, OH, **1999**.
5. *International Alloy Designations and Chemical Composition Limits for Wrought Aluminum and Wrought Aluminum Alloys*. The Aluminum Association: Arlington, VA, **2009**.
6. *ASM Handbook: Properties and Selection: Nonferrous Alloys and Special-Purpose Materials, Vol. 2*. ASM International: Materials Park, OH, **1990**.
7. Mathers, G. *The Welding of Aluminum and Its Alloys*. Woodhead Publishing: Philadelphia, PA, **2002**.
8. Mandal, N. R. *Aluminum Welding*. Woodhead Publishing: Philadelphia, PA, **2001**.
9. *ASM Handbook, Vol 13A: Corrosion: Fundamentals, Testing, and Protection*. ASM International: Materials Park, OH, **2003**.
10. Stansbury, E. E.; Buchanan, R. A. *Fundamentals of Electrochemical Corrosion*. ASM International: Materials Park, OH, **2000**.
11. *ASTM Standard G46: Standard Guide for Examination and Evaluation of Pitting Corrosion*. ASTM International: West Conshohocken, PA, **2013**.
12. M. H. Larsen, J. C. Walmsley, O. Lunder, R. H. Mathiesen, and K. Nisancioglu *J. Electrochem. Soc.* **2008**, 155, pp C550.

13. *ASTM Standard G110: Standard Practice for Evaluating Intergranular Corrosion Resistance of Heat Treatable Aluminum Alloys by Immersion in Sodium Chloride + Hydrogen Peroxide Solution.* ASTM International: West Conshohocken, PA, **2009**.
14. *ASTM G34: Standard Test Method for Exfoliation Corrosion Susceptibility in 2XXX and 7XXX Series Aluminum Alloys (EXCO Test).* ASTM International: West Conshohocken, PA, **2013**.
15. *ASTM G47: Standard Test Method for Determining Susceptibility to Stress-Corrosion Cracking of 2XXX and 7XXX Aluminum Alloy Products.* ASTM International: West Conshohocken, PA, **2011**.
16. Revie, R. W. *Uhlig's Corrosion Handbook.* 3rd ed.; John Wiley & Sons, Inc.: Hoboken, NJ, **2011**.
17. Riggs, O. L., Jr.; Nathan, C. C. *Corrosion Inhibitors.* NACE: Houston, TX, **1973**; p pp 11.
18. Noack, M. G. *Mater. Perform.* **1982**, 21 (3), pp 26.
19. Mayne, J. E. O. *Official Digest* **1952**, 24 (127), pp 127.
20. Bacon, R. C.; Smith, J. J.; Rugg, R. M. *Ind. Eng. Chem.* **1948**, 40 (1), pp 161.
21. Mayne, J. E. O. *Br. Corros. J.* **1970**, 5, pp 106.
22. Hartley, R. A. *J. Mater.* **1972**, 7 (3), pp 361.
23. Kinsella, E. M.; Mayne, J. E. O. *Br. Polym. J.* **1969**, 1 (4), pp 173.
24. Thomas, N. *JOCCA* **1991**, 53 (8), pp 669.
25. Morcillo, M. *JOCCA* **1990**, 73 (1), pp 24.
26. Leidheiser, H.; Funke, W. *JOCCA* **1987**, 70 (5), pp 121.

27. Funke, W. *JOCCA* **1985**, 68 (9), pp 229.
28. Hare, C. H. *J. Protect. Coat. Linings* **1998**, 15 (7), pp 17.
29. Munger, C. G. *Corrosion Control by Protective Coatings*. NACE International: Houston, TX, **1984**; p 129.
30. Leclercq, M. *J. Protect. Coat. Linings* **1990**, 7 (3), pp 57.
31. Svoboda, M.; Mleziva, J. *Prog. Org. Coat.* **1984**, 12 (3), pp 251.
32. Cubberly, W. H.; Bakerjian, R. *Tool and Manufacturing Engineers Handbook*. SME: Dearborn, MI, **1989**; p 48-1.
33. *Alodine® 1200S*. MSDS 592728; Henkel Corporation: Madison Heights, MI, **2013**.
34. *Iridite® 14-2*. MSDS 78659; MacDermid Industrial Solutions: Waterbury, CT, **2004**.
35. Leggat, R. B.; Taylor, S. R.; Zhang, W.; Buchheit, R. G. *Corrosion* **2002**, 58 (3), pp 283.
36. *MIL-DTL-5541: Military Specification, Chemical Conversion Coatings on Aluminum and Aluminum Alloys*. The U.S. Department of Defense: Washington, DC, **2006**.
37. Zhao, J; Frankel, G; McCreery, R. L. *J. Electrochem. Soc.* **1998**, 145 (7), pp 2258.
38. Sehgal, A.; Lu, D.; Frankel, G. S. *J. Electrochem. Soc.* **1998**, 145 (8), pp 2834.
39. Akiyama, E; Frankel, G. S. *J. Electrochem. Soc.* **1999**, 146 (11), pp 4095.
40. Ramsey, J. D.; McCreery, R. L. *J. Electrochem. Soc.* **1999**, 146 (11), pp 4076-4081, doi: 10.1149/1.1392594.

41. Xia, L.; Akiyama, E.; Frankel, G.; McCreery, R. L. *J. Electrochem. Soc.* **2000**, *147* (7), pp 2556.
42. Lu, D.; Schmutz, P.; Frankel, G. S. *Corrosion* **2002**, *58* (2), pp 137.
43. Akiyama, E.; Markworth, A. J.; McCoy, J. K.; Frankel, G. S.; Xia, L.; McCreery, R. L. *J. Electrochem. Soc.* **2003**, *150* (2), pp B83.
44. Zhao, J.; Xia, L.; Sehgal, A.; Lu, D.; McCreery, R. L.; Frankel, G. S. *Surf. Coat. Technol.* **2001**, *140*, pp 51.
45. Sedman, R. M.; Beaumont, J.; McDonald, T. A.; Reynolds, S.; Krowech, G.; Howd, R. *J. Environ. Sci. Health C Environ. Carcinog. Ecotoxicol. Rev.* **2006**, *24* (1), pp 155.
46. Proctor, D. M.; Otani, J. M.; Finley, B. L.; Paustenbach, D. J.; Bland, J. A.; Speizer, N.; Sargent, E. V. *J. Toxicol. Environ. Health A* **2002**, *65* (10), pp 701.
47. Dayan, A. D.; Paine, A. J. *Human & Experimental Toxicology* **2001**, *20*, pp 439.
48. Occupational Safety & Health Administration. *Occupational Safety and Health Standards: Chromium (VI)*, Part 1910, Standard 1910.1026, **2006**.
49. National Institute for Occupational Safety and Health. *Criteria for a Recommended Standard: Occupational Exposure to Hexavalent Chromium*, NIOSH Publication Number 2013-128, **2013**.
50. Hayes, S. A.; Yu, P.; O'Keefe, T. J.; O'Keefe, M. J.; Stoffer, J. O. *J. Electrochem. Soc.* **2002**, *149* (12), pp C623.
51. Treu, B. L.; Joshi, S.; Pinc, W. R.; O'Keefe, M. J.; Fahrenholtz, W. G. *J. Electrochem. Soc.* **2010**, *157* (8), pp C282.
52. Jones, P. S.; Yu, P.; Pinc, W. R.; O'Keefe, M. J.; Fahrenholtz, W. G.; O'Keefe, T. *J. Int. J. Appl. Ceram. Tec.* **2008**, *5* (1), pp 63.
53. Heller, D. K.; Fahrenholtz, W. G.; O'Keefe, M. J. *Corros. Sci.* **2010**, *52* (2), pp 360.

54. Joshi, S.; Kulp, E. A.; Fahrenholtz, W. G.; O'Keefe, M. J. *Corros. Sci.* **2012**, *60*, pp 290.
55. Cook, R. L.; Taylor, S. R. *Corrosion* **2000**, *53*, pp 321.
56. Kumar, C. S.; Rao, V. S.; Raja, V. S.; Sharma, A. K.; Mayanna, S. M. *Corros. Sci.* **2002**, *44*, pp 387.
57. Guan, H.; Buchheit, R. G. *Corrosion* **2004**, *60* (3), pp 284.
58. Hamdy, A. S.; Beccaria, A. N.; Temtchenko, T. *Surf. Coat. Technol.* **2002**, *155*, pp 184.
59. Pearlstain, F.; Agarwala, V. S. Trivalent Chromium Solutions for Sealing Anodized Aluminum. United States Patent 5,374,347, **1994**.
60. Nickerson, B. C.; Lipnickas, E. Proceedings of the 2003 Tri-Service Corrosion Conference: Las Vegas, NV, Nov. 17-21, 2003; **2003**.
61. *Alodine® T 5900 RTU*. MSDS 756387; Henkel Corporation: Madison Heights, MI, **2011**.
62. *Alodine® 5200 Makeup*. MSDS 594142, Henkel Corporation: Madison Heights, MI, **2012**.
63. *Alodine® 5700 Wipes*. MSDS 869854, Henkel Corporation: Madison Heights, MI, **2013**.
64. B.E. Placzankis, C.E. Miller, and B.D. Mullis *Examination of Nonchromate Conversion Coatings for Aluminum Armor From Three Final Candidates Using Accelerated Corrosion and Adhesion Test Methods*; ARL-TR-2601; Army Research Laboratory: Aberdeen Proving Ground, MD, **2001**.
65. P. Smith, C. Miller *Performance of Chromate-Free Pretreatment Options for CARC Systems*; ARL-TR-4049; Army Research Laboratory: Aberdeen Proving Ground, MD, **2007**.
66. Mahajanam, S. P. V.; Buchheit, R. G. *Corrosion* **2008**, *64* (3), pp 230.

67. *ASM Handbook Vol. 05: Surface Engineering*. ASM International: Materials Park, OH, **1994**.
68. Kutz, M. *Handbook of Environmental Degradation of Materials*. William Andrew Inc.: Norwich, NY, **2012**.
69. Legg, K. O. *Chromate Alternatives for Metal Treatment and Sealing*, DoD Metal Finishing Workshop: Layton, UT, **2007**.
70. *Alodine® T 5900 RTU*. Technical Process Bulletin; Henkel Corporation: Madison Heights, MI, **2008**.
71. *Alodine® 5200*. Technical Data Sheets; Henkel Corporation: Madison Heights, MI, **2007**.
72. Dardona, S.; Jaworowski, M. *Appl. Phys. Lett.* **2010**, *97*, pp 181908.
73. Fujiwara, H. *Spectroscopic Ellipsometry: Principles and Applications*. Wiley: New York, **2007**; p 158.
74. Campestrini, P.; Bohmb; S.; Schram, T.; Terryn, H.; De Wit, J. H. W. *Thin Solid Films* **2002**, *410*, pp 76.
75. Mittal, K. L. *Contact Angle, Wettability and Adhesion*. CRC Press: Boca Raton, **2006**; p 267.
76. Orazem, M. E.; Tribollet, B. *Electrochemical Impedance Spectroscopy*. 1st ed.; Wiley-Interscience: Hoboken, NJ, **2008**.
77. Lai, W.; Haile, S. M. *J. Am. Ceram. Soc.* **2005**, *88*, pp 2979.
78. Bard, A.J.Faulkner, L. R. *Electrochemical Methods*. 2nd ed.; Wiley: Hoboken, NJ, **2000**.
79. Creus, J.; Mazille, H.Idrissi, H. *Surf. Coat. Technol.* **2000**, *130*, pp 224.

80. Liu, C.; Bi, Q.; Leyland, A. Matthews, A. *Corros. Sci.* **2003**, *45*, pp 1257.
81. H. Bohni, and H.H. Uhlig *J. Electrochem. Soc.* **1969**, *116*, pp 906.
82. Galvele, J. R. *J. Electrochem. Soc.* **1976**, *123*, pp 464.
83. Comotti, I. M.; Trueba, M.; Trasatti, S. P. *Surf. Interface. Anal.* **2013**, *Special issue article*, doi: 10.1002/sia.5270.
84. B.N. Stirrup, N.A. Hampson, and I.S. Midgley *J. Appl. Electrochem.* **1975**, *5*, pp 229.
85. M. Asaduzzaman, C.M. Mustafa, and M. Islam *Chemical Industry & Chemical Engineering Quarterly* **2011**, *17*, pp 477.
86. M. Yasudo, F. Weinberg, and D. Tromans *J. Electrochem. Soc.* **1990**, *137*, pp 3708.
87. Fenster, C.; Smith, A. J.; Abts, A.; Milenkovic, S. Hassel, A. W. *Electrochem. Commun.* **2008**, *10*, pp 1125.
88. Anik, M.; Osseo-Asare, K. *J. Electrochem. Soc.* **2002**, *149*, pp B224.
89. Lillard, R. S.; Kanner, G. S.; Butt, D. P. *J. Electrochem. Soc.* **1998**, *145*, pp 2718.
90. Fhaner, M.; Zhao, H.; Bian, X.; Galligan, J. J. Swain, G. M. *Diam. Relat. Mater.* **2011**, *20*, pp 75.
91. MacDonald, D. D.; Liu, J. Lee, D. *J. Appl. Electrochem.* **2004**, *34*, pp 577.
92. Kriksunov, L. B.; MacDonald, D. D.; Millett, P. J. *J. Electrochem. Soc.* **1994**, *141*, pp 3002.
93. Patrik, E.; Orazem, M. S.; Sanchez, J. C.; Nishida, T. *J. Neurosci. Methods* **2011**, *198*, pp 158.

94. Metikoš-Huković, M. Grubač, Z. *J. Electrochem. Soc.* **2003**, 556, pp 167.
95. *ASTM D6943: Standard Practice for Immersion Testing of Industrial Protective Coatings*. ASTM International: West Conshohocken, PA, 2010.
96. *ASTM G50: Standard Practice for Conducting Atmospheric Corrosion Tests on Metals*. ASTM International: West Conshohocken, PA, 2003.
97. *ASTM G87: Standard Practice for Conducting Moist SO₂ Tests*. ASTM International: West Conshohocken, PA, 2013.
98. *ASTM G71: Standard Guide for Conducting and Evaluating Galvanic Corrosion Tests in Electrolytes*. ASTM International: West Conshohocken, PA, 1998.
99. A. Iyer, W. Willis, S. Frueh, W. Nickerson, A. Fowler, J. Barnes, L. Hagos, J. Escarsega, J. La Scala and S. L. Suib *Plat. Surf. Finish.* **2010**, 5, pp 32.
100. E. Akiyama, A. J. Markworth, J. K. McCoy, G. S. Frankel, L. Xia, and R. L. McCreery *J. Electrochem. Soc.* **2003**, 150, pp B83.
101. McCreery, B. L. Hurley and R. L. *J. Electrochem. Soc.* **2003**, 150, pp B367.
102. W. Zhang, B. Hurley, and R. G. Buchheit *J. Electrochem. Soc.* **2002**, 149, pp B357.
103. McCreery, W. J. Clark and R. L. *J. Electrochem. Soc.* **2002**, 149, pp B379.
104. J. Zhao, L. Xia, A. Sehgal, D. Lu, R. L. McCreery, and G. S. Frankel *Surf. Coat. Technol.* **2001**, 140, pp 51.
105. W. R. McGovern, P. Schmutz, R. G. Buchheit, and R. L. McCreery *J. Electrochem. Soc.* **2000**, 147, pp 4494.
106. L. Xia, E. Akiyama, G. Frankel, and R. McCreery *J. Electrochem. Soc.* **2000**, 147, pp 2556.
107. McCreery, J. D. Ramsey and R. L. *J. Electrochem. Soc.* **1999**, 146, pp 4076.

108. J. Zhao, G. Frankel, and R. L. McCreery *J. Electrochem. Soc.* **1998**, *145*, pp 2258.
109. L. Xia, and R.L. McCreery *J. Electrochem. Soc.* **1999**, *146*, pp 3696.
110. M.A. Jakab, D.A. Little, J.R. Scully *J. Electrochem. Soc.* **2005**, *152*, pp B311-B320.
111. M. Kendig, R. Addison, and S. Jeanjaquet *J. Electrochem. Soc.* **1999**, *146*, pp 4419.
112. W.C. Nickerson, E. Lipnickas *Proceedings of the 2003 Tri Service Corrosion Conference*, Las Vegas, NV, 2003.
113. Jaworowski, S. Dardona and M. *Appl. Phys. Lett.* **2010**, *97*, pp 181908.
114. L. Li, G.P. Swain, A. Howell, D. Woodbury, G.M. Swain *J. Electrochem. Soc.* **2011**, *158*, pp C274-C283.
115. L. Li, A.L. Desouza, G.M. Swain *Analyst* **2013**, *138* (15), pp 4398.
116. Tribollet, M.E. Orazem and B. *Electrochemical Impedance Spectroscopy*. 1st ed.; Wiley, John & Sons, Incorporated: 2008.
117. Faulkner, A.J. Bard and L.R. *Electrochemical Methods: Fundamental and Applications*. 2 ed.; Wiley: 2000.
118. X. Dong, P. Wang, S. Argekar, D.W. Schaefer *Langmuir* **2010**, *26*, pp 10833.
119. Berger, R.; Bexell, U.; Grehk, T. M.Hornstrom, S. E. *Surf Coat Tech* **2007**, *202* (2), pp 391-397.
120. McCreery, R. L. *Raman Spectroscopy for Chemical Analysis*. Wiley: New York, 2000.

121. McCreery, L. Xia and R.L. *Journal of Electroanalytical Chemistry* **1998**, 145, pp 3083.
122. J. E. Maslar, W. S. Hurst, W. J. Bowers, Jr., J. H. Hendricks, M. I. Aquino, and i. Levin *App. Surf. Sci.* **2001**, 180, pp 102.
123. McCreery, J. D. Ramsey and R. L. *Corros. Sci.* **2004**, 46, pp 1729.
124. J. D. Ramsey, L. Xia, M. X. Kendig, and R. L. McCreery *Corros. Sci.* **2001**, 43, pp 1557.
125. H. Y. H. Chan, C. G. Takoudis, and M. J. Weaver *J. Phys. Chem. B* **1999**, 103, pp 357.
126. Gewirth, K. L. Stewart and A. A. *Langmuir* **2007**, 23, pp 9911.
127. M. Ivanda, D. Waasmaier, A. Endriss, J. Ihringer, A. Kirfel, and W. Kiefer *J. Raman Spectrosc.* 28, pp 487.
128. G. S. Chen, M. Gao, and R. P. Wei *Corrosion* **1996**, 52, pp 8.
129. R. G. Buchheit, R. P. Grant, P. F. Hlava, B. McKenzie, and G. L. Zender *J. Electrochem. Soc.* **1997**, 144, pp 2621.
130. M. W. Kendig, A. J. Davenport, and H. S. Isaacs *Corros. Sci.* **1993**, 34, pp 41.
131. B. P. Payne, M. C. Biesinger, N. S. McIntyre *J. Electron Spectrosc.* **2011**, 184, pp 29.
132. Rai, L. E. Eary and D. *Environ. Sci. Technol.* **1987**, 21, pp 1187.
133. Millero, M. Pettine and F. J. *Limnol. Oceanogr.* **1990**, 35, pp 730.
134. Millero, M. Pettine and F. J. *Mar. Chem.* **1991**, 34, pp 29.

135. M. A. Jakab, D. A. Little, and J. R. Scully *J. Electrochem. Soc.* **2005**, *152*, pp B311.
136. A. L. Colley, J. V. Macpherson, and P. R. Unwin *Electrochem. Commun.* **2008**, *10*, pp 1334.
137. N. Spanos, S. Slavov, C. Kordulis, and A. Lycourghotis *Langmuir* **1994**, *10*, pp 3134.
138. Polmear, I. J. *Light Alloys*. 3rd ed.; Arnold: London, UK, **1995**.
139. Q. Meng and G. S. Frankel *J. Electrochem. Soc.* **2004**, *151*, pp 271.
140. Buchheit, N. Birbilis and R.G. *J. Electrochem. Soc.* **2005**, *152*, pp B140-B151.
141. Buchheit, R.G. *J. Electrochem. Soc.* **1995**, *142*, pp 3994.
142. Nisancioğlu, K. *J. Electrochem. Soc.* **1990**, *137*, pp 69.
143. M. Buchler, T. Watari, and W. H. Smyrl *Corros. Sci.* **2000**, *42*, pp 1661.
144. G.O. Ilevbare, O. Schneider, R.G. Kelly, and J.R. Scully *J. Electrochem. Soc.* **2004**, *151*, pp 465.
145. L. Li, D.Y. Kim, and G.M. Swain *J. Electrochem. Soc.* **2012**, *159*, pp C326.
146. Frankel, Y. Guo and G.S. *Corrosion* **2012**, *68*, pp 045002-1.
147. *ASTM G31: Standard Practice for Laboratory Immersion Corrosion Testing of Metal*. ASTM International: West Conshohocken, PA, **2004**.
148. *ASTM G44: Standard Practice for Exposure of Metals and Alloys by Alternate Immersion in Neutral 3.5% Sodium Chloride Solution*. ASTM International: West Conshohocken, PA, **2013**.

149. *ASTM B117: Standard Practice for Operating Salt Spray (Fog) Apparatus*. ASTM International: West Conshohocken, PA, **2011**.
150. *ASTM G85: Standard Practice for Modified Salt Spray (Fog) Testing*. ASTM International: West Conshohocken, PA, **2011**.
151. *ASTM G3: Standard Practice for Conventions Applicable to Electrochemical Measurements in Corrosion Testing*. ASTM International: West Conshohocken, PA, **2010**.
152. *ASTM G106: Standard Practice for Verification of Algorithm and Equipment for Electrochemical Impedance Measurements*. ASTM International: West Conshohocken, PA, **2010**.
153. *ASTM G71: Standard Guide for Conducting and Evaluating Galvanic Corrosion Tests in Electrolytes*. ASTM International: West Conshohocken, PA, **2009**.
154. *ASTM D6208: Standard Test Method for Repassivation Potential of Aluminum and Its Alloys by Galvanostatic Measurement*. ASTM International: West Conshohocken, PA, **2007**.
155. Field, D. P.; Weiland, H.; Kunze, K. *Can. Metall. Q.* **1995**, *34* (3), pp 203.
156. Buchheit, R. G.; Martinez, M. A.; Montes, L. P. *J. Electrochem. Soc.* **2000**, *147*, pp 119.
157. Lacroix, L.; Ressler, L.; Blanc, C.; Mankowski, G. *J. Electrochem. Soc.* **2008**, *155* (4), pp C131.
158. Li, L.; Swain, G. M. Proceedings of The 223rd Electrochemical Society Meeting: Toronto, ON, Canada, **2013**.
159. *ASTM G46: Standard Guide for Examination and Evaluation of Pitting Corrosion*. ASTM International: West Conshohocken, PA, **2013**.
160. Feng, Z. C.; Frankel, G. S. *Corrosion* **2013**, doi: <http://dx.doi.org/10.5006/0907>.

161. Matzdorf, C. A.; Nickerson, W. C.; Rincon Troconis, B. C.; Frankel, G. S.; Li, L.; Buchheit, R. G. *Corrosion* **2013**, doi: <http://dx.doi.org/10.5006/0905>.
162. Wit, J.H.W. De *Corrosion Mechanisms in Theory and Practice*. Marcel Dekker: New York, **1995**; p 581-628.
163. Haas, P. L. Hagans and C. M. *Surf. Interface Anal.* **1994**, *21*, pp 65.
164. C.M. Cotell, J.A. Spragues, and F.A. Smidt Jr. *ASM Handbook*. ASM International: **1994**; Vol. 5, p 405-411.
165. R.L. De Rosa, J.T. Grant, L. Katsen, M. Donley, and G.P. Bierwagen *Corrosion (Houston)* **2000**, *56*, pp 395.
166. O. Lunder, and K. Nisancioglu *Corrosion (Houston)* **1988**, *44*, pp 414.
167. L. Fedrizzi, F. Deflorian, R. Canteri, M. Fedrizzi, P.L. Bonora *Progress in Understanding and Prevention of Corrosion*, Proceedings of 10th European Corrosion Congress: London, UK, **1993**.
168. I. Pires, L. Quintino, C.M. Rangel, G.E. Thompson, P. Skeldon, X. Zhou *Trans. Inst. Met. Finish.* **2000**, *78*, pp 179.
169. L. Fedrizzi, A. Bianchi, F. Deflorian, S. Rossi, P.L. Bonora *Electrochim. Acta.* **2002**, *47*, pp 2159.
170. O. Lunder, B. Olsen, K. Nisancioglu *Int. J. Adhes. Adhes.* **2002**, *22*, pp 143.
171. D. Chidambaram, C.R. Clayton, G.P. Halada, M.W. Kendig *J. Electrochem. Soc.* **2004**, *151*, pp B605-B612.
172. P. Campestrini, E.P.M. Van Westing, and J.H.W. De Wit *Electrochim. Acta.* **2001**, *46*, pp 2553-2571.
173. P. Hagans, C.M. Haas *Surf. Interface Anal.* **1994**, *21*, pp 65.
174. A.E. Hughes, R. J. Taylor, B.R.W. Hinton *Surf. Interface Anal.* **1997**, *25*, pp 223.

175. D. Chidambaram, C.R. Clayton, M.W. Kendig, G.P. Halada *J. Electrochem. Soc.* **2004**, *151*, pp B613-B620.
176. G.P. Halada, J.R. Keams, C.R. Clayton, M.W. Kendig, S.L. Jeanjaquest, G.G. Peterson, G. Shea-Mccarthy *The Electrochemical Meeting Abstracts*. Boston, MA, Nov. 1-6, **1998**; Vol. 98-2.
177. X. Sun, R. Li, K.C. Wong, K.A.R. Mitchell, T. Foster *J. Mater. Sci.* **2001**, *36*, pp 3215.
178. P. Campestrini, E.P.M. Van Westing, J.H.W. De Wit *Electrochim. Acta.* **2001**, *46*, pp 2631-2647.
179. S. Dardona, L. Chen, M. Kryzman, D. Goberman, M. Jaworowski *Anal. Chem.* **83**, pp 6127-6131.
180. L. Li, K.P. Doran, G.M. Swain *J. Electrochem. Soc.* **2013**, *160*, pp C1-C6.
181. Y. Guo, and G.S. Frankel *Surf. Coat. Technol.* **2012**, *206*, pp 3895-3902.
182. S. Wernick, R. Pinner, P.G. Sheasby *The Surface Treatment and Finishing of Aluminum and its Alloys*. 5th ed.; ASM International: **1987**.
183. R.G. Buchheit, A.E. Hughes *ASM Handbook*. ASM International: **2003**; Vol. 13A, p 720-735.
184. L. Lacrois, L. Ressler, C. Blanc, and G. Mankowski *J. Electrochem. Soc.* **2008**, *155*, pp C131-C137.
185. S.L. Flegler, J.W. Heckman, K.L. Klomparens *Scanning and Transmission Electron Microscopy: An Introduction*. 1st ed.; Oxford University Press: **1999**; p 77-78.
186. Schweitzer, P.A. *Fundamentals of Metallic Corrosion: Atmospheric and Media Corrosion of Metals*. CRC Press: **2006**; p 500.

187. Baboian, R. *Corrosion Tests and Standards: Application and Interpretation*. ASTM International: 2005; p 552.
188. Davis, J.R. *Corrosion of Aluminum and Aluminum Alloys*. ASM International: **1999**; p 281.
189. S. Joshi, W.G. Fahrenholtz, M.J. O'Keefe *Appl. Surf. Sci.* **2011**, 257, pp 1859.
190. S. Joshi, W.G. Fahrenholtz, M.J. O'Keefe *Surf. Coat. Technol.* **2011**, 205, pp 4312-4319.
191. Hatch, J.E. *Aluminum: Properties and Physical Metallurgy*. ASM International: **1984**.
192. K.J. Holub, L.J. Matienzo *J. Appl. Surf. Sci.* **1981**, 9, pp 22-38.
193. T. Fujita, Z. Horita, T.G. Langdon *Philos. Mag.* **2002**, 82, pp 2249-2262.
194. Revie, R.W. *Uhlig's Corrosion Book*. 2nd ed.; John Wiley & Sons: New York, **2000**; p 815-816.
195. V. Fournier, P. Marcus, I. Olefjord *J. Surf. Interface Anal.* **2002**, 34, pp 494-497.
196. T. Xue, W.C. Cooper, R. Pascual, S. Saimoto *J. Appl. Electrochem.* **1991**, 21, pp 238-246.
197. Szklarska-Smialowska, Z. *Corros. Sci.* **1999**, 41, pp 1743-1767.
198. Guo, Y.; Frankel, G. S. *Surf. Coat. Technol.* **2012**, 206 (19-20), pp 3895-3902.
199. Li, L.; Swain, G. P.; Howell, A.; Woodbury, D.; Swain, G. M. *J. Electrochem. Soc.* **2011**, 158 (9), pp C274-C283.
200. Lcuret, V.; Jeffcoate, C. S.; Issacs, H. S.; Buchheit, R. G. *J. Electrochem. Soc.* **2003**, 250, pp B425.

201. Jeurgens, L. P. H.; Sloof, W. G.; Tichelaar, F. D.; and Mittemeijer, E. J. *J. Appl. Phys.* **1949**, 92.
202. Dong, X. C.; Wang, P.; Argekar, S.; Schaefer, D. W. *Langmuir* **2010**, 26 (13), pp 10833-10841.
203. Lin, X.; McCreery, R. L. *J. Electrochem. Soc.* **1998**, 145, pp 3083.
204. Li, L.; Doran, K. P.; Swain, G. M. *J. Electrochem. Soc.* **2013**, 160 (8), pp C396.
205. Matzdorf, C. *Non-Chromate Aluminum Pretreatments, Phase I Report*, PP0025; Patuxent River, MD, **2003**.
206. Matzdorf, C. *Non-Chromate Aluminum Pretreatments, Phase II Report*, PP0025; Patuxent River, MD, **2004**.
207. C. G. Rhodes, M. W. Mahoney and W. H. Bingel *Scripta Mater.* **1997**, 36, pp 69.
208. Barrett, R. T. *Fastener Design Manual*. NASA Reference Publication: **1990**.
209. C.A. Matzdorf, W. C. Nickerson, B. C. Rincon-Troconis, G. S. Frankel, L. Li, and R. G. Buchheit *Corrosion* **2013**, <http://dx.doi.org/10.5006/0905>.
210. Frankel, Z. Feng and G. S. *Corrosion* **2013**, <http://dx.doi.org/10.5006/0907>.